Statistical transfer matrix-based damage localization and quantification for civil structures

Md Delwar Hossain Bhuyan

ANNÉE 2017

UNIVERSITÉ DE RENNES 1

UNIVERSITE BRETAGNE LOIRE

THÈSE / UNIVERSITÉ DE RENNES 1
sous le sceau de l'Université Bretagne Loire

pour le grade de

DOCTEUR DE L'UNIVERSITÉ DE RENNES 1

Mention : Traitement du Signal et Télécommunications

Ecole doctorale MathSTIC

présentée par

Md Delwar Hossain Bhuyan

préparée à l'unité de recherche Inria
Institut National de Recherche en Informatique et Automatique

---

Statistical transfer matrix-based damage localization and quantification for civil structures

Thèse soutenue à Rennes
le 23 Novembre 2017

devant le jury composé de :

Valérie MONBET
Professeur, Université de Rennes 1, France / président

Dionisio BERNAL
Professeur, Northeastern University, USA / rapporteur

Christian GOGU
Maître de Conférence, Université de Toulouse III / rapporteur

Michael DÖHLER
CR Inria / examinateur

Yann LECIEUX
Maître de Conférence, Université de Nantes / examinateur

Laurent MEVEL
DR Inria / directeur de thèse

Franck SCHOEFS
Professeur, Université de Nantes / co-directeur de thèse

Acknowledgments

First of all, I would like to express my profound gratitude to the director of thesis Dr. Laurent Mevel for all support and guidance throughout my PhD studies. His many thoughts, ideas and conclusive comments were a big source of inspiration. He opened the windows to many collaborations with partners all over the world so that I could learn and work during this thesis. I would also like to extend my sincere gratitude towards my co-director of thesis Professor Dr. Franck Schoefs for his inspiring and enlightening discussions, support and guidance during this thesis.

I would like to give gratefulness to my co-advisor Dr. Michael Döhler for his continuous support, warm encouragements, insightful comments and helps during these three years. He was always available when I needed for any type of discussions. He showed me the excellent way to achieve the best performance in the thesis during the whole three years. In a word, he was an outstanding mentor I had ever met. I would also like to thank to my second co-advisor Dr. Yann Lecieux for his constant support, many fruitful discussions, comments and for an insight into structural engineering. It was an incredible opportunity for me that I worked with them.

I would also like to give thanks to the reviewers, Professor Dr. Dionisio Bernal (Northeastern University Boston) and Dr. Christian Gogu (Université de Toulouse III). They gave their valuable time to read and review it, which is gratefully acknowledged, as well as their helpful remarks to improve the manuscript. I would like to extend my gratitude to Professor Dr. Valérie Monbet (Université de Rennes 1) for accepting to play the role as a president of the jury for the defense and her helpful remarks.

Thanks to the Inria research centre in Rennes to provide an excellent research environment. Also thanks to the PhD students, engineers, researchers, and postdocs of the I4S team for their scientific thoughts exchange and a pleasant atmosphere that they created. Thanks all, for charming lunch times, refreshing coffee breaks, and dinners, that we enjoyed together.

I am gratefully acknowledged to GeM, Bretagne region, and Inria research centre for providing me the financial support during this thesis.

Finally, I wish to express my gratitude to my family. They always supported me in my crucial time at their best possible way. In spite of that, the long distance between me and my family, they were a constant source of love, support, and encouragement in every step of my life.

Md Delwar Hossain Bhuyan
Rennes, November 2017

To my beloved family
and my only daughter Meherima-Arisha

Contents

Introduction

Context of the work

Structural health monitoring (SHM) has gained an increasing attention in the engineering and scientific communities because an unpredicted structural failure may happen catastrophic, economic and human loss. The monitoring of structures has become an important issue, especially in the mechanical, aerospace, automotive and civil structures, while subject to noise and vibration.

There are two kinds of evaluation that are performed such as destructive and non-destructive tests. Destructive tests affect the condition of structure and non-destructive tests do not affect its functionality and it is used to evaluate the properties of a system without causing damage. More researchers have been focussing on the latter approach due to the continuous serviceability of the structure, since it is crucial to maintain the safety and integrity of structures. Currently, performance monitoring of large engineering structures is mainly done on-site by engineers and technicians, who need to have a very specific expertise and knowledge of past hazard events. In the meantime, the number of ageing structures is growing worldwide. Structures are often difficult to reach (e.g. bridges in remote areas, or offshore structures), so inspections are limited. Moreover, visual inspections offer only limited knowledge, not least because only reachable components can be inspected. They are also costly in terms of labor and operation shutdowns. The long term perspective is to replace the inefficient manual inspection procedure by automated robust on-site monitoring with permanently installed sensors.

A promising technique is vibration-based SHM, where structures are equipped e.g. with acceleration sensors that can permanently record structural vibrations data due to ambient excitation. In the last decade, sensor and data acquisition technology have evolved rapidly and have become affordable, allowing a large-scale instrumentation of important structures like bridges, buildings or offshore structures in particular for long term vibration-based monitoring. Thanks to these advances in sensing systems, there is a huge potential to realize an automated and online structural assessment from sensor data, leading to a safe, reliable and cost-efficient structural integrity management. The detection of changes in systems from output-only measured signals is a multidisciplinary research area in the fields of mathematical modeling, automatic control, statistics and signal processing. During the last decades, system identification methods found a special interest in structural engineering for the identification of vibration modes and mode shapes of structures under ambient excitation. Sensors installed

on the structure collect data and then the modal parameters (i.e. natural frequencies, mode shapes and damping ratios) can be estimated e.g. using methods from stochastic system realization theory for linear systems. Those parameters are meaningful for the monitoring of the structure. Moreover, during the last years, huge advances has been made in the development of Operational Modal Analysis, allowing the reliable modal identification of the structures from ambient vibration measurements.

There are two ways to damage assessment that one is fully characterizing the structure with system identification and then comparing the system identification results, and another one is based on damage assessment techniques. Usually, vibration-based structural diagnosis is divided into five subtasks of increasing difficulty: damage detection (level 1), damage localization (level 2), identification of damage type (level 3), quantification of the damage extent (level 4) and prediction of the remaining service life (level 5). When performing these tasks in a cascade fashion, the full structural diagnosis problem is amenable to a solution.

Methods for damage detection have reached some maturity, e.g. with data-driven algorithms adapted from pattern classification and statistical process control. While damage detection can operate purely data-driven, by comparing the current dataset to a reference, damage localization requires some link between the data and the physical properties of the structure, which is often given by a finite element (FE) model of the structure. Physical changes in the structure due to damage induce changes in the modal characteristics of the structure, which can be monitored through output-only vibration measurements. Changes in these parameters indicate damage in a structure, and damage localization is possible when analyzing these changes together with a finite element model of the structure. Damage quantification corresponds to estimating the changes of physical parameter in the faulty elements. For an example, the components of the parameters can be the stiffness of a mass-chain system, Young modulus of beam elements or it can be basically any quantity linked to damage-sensitive properties of the system. However, vibration-based damage localization methods are not very well developed so far, and compared to this, methods for damage quantification are the least developed in the literature. In particular, they lack applicability in practice for automated SHM solutions. Among the promising techniques, the Stochastic Dynamic Damage Locating Vector (SDDLV) and the Influence Lines Damage Location (ILDL) approach have interesting capabilities because they are theoretically sound method in combining both finite element information and modal parameters estimated from output data. This motivates the adaption of the existing damage localization methods in this thesis, and then extend it for damage quantification in a sensitivity-based approach.

The purpose of this thesis is to develop methods for damage localization and quantification from output-only measurements which are needed for the damage assessment for the SHM systems in practice.

Proposed methods

The following methods are developed in the contribution of this thesis:

(1) **Statistical damage localization with stochastic load vectors using multiple mode sets:** The Stochastic Dynamic Damage Location Vector (SDDLV) method is an

output-only damage localization method based on a Finite Element (FE) model of the structure and modal parameters from output-only measurements in the damage and reference state of the system. A vector is obtained in the null space of the changes in the transfer matrix between both states and then applied as virtual load vector to the model. The damage location is related to this resulting stress where it is close to zero. Then, a statistical evaluation of the computed stress is necessary to make a decision if stress is (close to) zero or not, in order to decide if the respective structural element is damaged or not. In previous works [MDBM15] an important theoretical limitation was that the number of modes used could not be higher than number of sensors located on the structure. This is a shortcoming in particular when only few sensors are available, it would be desirable not to discard information from the identification procedure. Here, the SDDLV method has been extended with a joint statistical approach for multiple mode sets, overcoming the restriction on the number of modes. Another problem is that the performance of the method can change considerably depending of the Laplace variable where the transfer function is evaluated. Particular attention is given to this choice and how to optimize it. Therefore, robustness of the damage localization is obtained by taking into account all available information in a joint statistical evaluation.

(2) **Statistical based decision making for damage localization with influence lines:** The Influence Line Damage Location (ILDL) method is complementary to the SDDLV approach. This approach was developed in [Ber14] as a deterministic approach. The objective is to extend it as a stochastic method and investigate its relation to SDDLV. A vector is obtained in the image of the changes in the transfer matrix between healthy and damaged states, instead of null space. It is expected that the image is differently affected by noise than the null space. Then, damage is located at elements where the subspace angle between the image and the influence line computed from the FE model is zero. In previous works [MDBM13], the uncertainty quantification was tempted, where the deterministic aggregation was done for $s = 0$. Here, the damage indicator of the ILDL is considered for arbitrary s and then reconsidered to allow an adequate uncertainty quantification and statistical evaluation for damage localization. In such a way, the ILDL approach is extended with a statistical framework.

(3) **Transfer matrix sensitivity-based output-only statistical damage localization and quantification:** While SDDLV and ILDL exploit directly properties of the null space or image of the transfer matrix, a sensitivity-based approach [DMZ16] is developed in this Chapter, which allows moreover damage quantification. An approach is considered that operates on the transfer matrix difference that is statistically evaluated using the transfer matrix sensitivity with respect to parameters from a FE model. The problems of damage localization and quantification are indeed divided into two separate problems. First, the damaged elements are detected in statistical tests, and then, the damage is quantified only for the damaged elements. Statistical fault isolation and estimation techniques are then used to perform damage localization and quantification in the so-called sensitivity and minmax approaches.

These approaches are derived in depth, and theoretical properties are proven in the con-

tribution chapters. They are validated on structural vibration data in both numerical and real applications.

Outline of the thesis

This thesis is presented in four parts and contains thirteen chapters.
Part I contains preliminaries:

- Chapter 1 presents an overview of state of the art from the literature related to vibration models, system identification, damage detection, localization, and quantification.
- Chapter 2 presents the background on the deterministic damage localization approaches on which this thesis is based, namely the SDDLV and ILDL approaches.
- Chapter 3 explains the background of the statistical signal processing methods used in this thesis. This concerns in particular the subspace-based system identification and uncertainty quantification.
- Chapter 4 presents the statistical approaches for damage localization and quantification, namely a previous statistical framework for SDDLV and ILDL on one side, and a generic sensitivity-based statistical framework for fault isolation and quantification on the other side.

Parts II deals with the theoretical developments:

- Chapter 5 presents the theoretical development of the SDDLV approach using multiple mode sets in a statistical framework. In particular, the effect of removing the limiting restriction on the number of modes is discussed.
- Chapter 6, the ILDL approach is extended with a statistical framework. The damage indicator of the ILDL is considered to allow an adequate uncertainty quantification, before deriving its statistical evaluation for damage localization.
- Chapter 7 presents the theoretical development of the transfer matrix-based residual in a statistical sensitivity-based damage localization and quantification approach. An approach is considered [DMZ16] that operates on a data-driven residual vector that is statistically evaluated using sensitivities with respect to parameters from a FE model. Furthermore, the proposed approach is extended considering a joint statistical evaluation of multiple mode sets.

Part III is devoted to the numerical investigation of the developed damage localization and quantification methods:

- Chapter 8 introduces the performance indicators for the developed methods and presents the numerical models used in this thesis.

- Chapter 9 deals with the applications of the proposed methods of SDDLV using multiple mode sets from Chapter 5. A simple mass-spring chain and a more complex 3D cube beam model are considered as numerical applications. These numerical applications are idealized test cases for the validation of the new developments of this approach, allowing in particular a statistical performance evaluation based on Monte-Carlo simulations. In addition, the damage localization with the SDDLV approach is applied on a beam model for crack propagation as well as the influence of mesh sizes is investigated.

- Chapter 10 presents the application of the statistical evaluation of ILDL approach from Chapter 6. A mass-spring chain model is considered as a numerical simulation for validating the method.

- Chapter 11 deals with the applications of transfer matrix sensitivity-based residual for statistical damage localization and quantification method from Chapter 7. The new approach is validated in numerical simulations of a mass-spring chain and a 2D beam model, where the outcomes for multiple mode sets are compared with only using a single mode set.

- Chapter 12 presents the numerical implementation of the damage localization methods by using Abaqus software for the application of realistic FE models. In Chapters 9, 10, and 11, the localization methods are applied on different numerical simulations, where the FE models are generated using Matlab code. The goal of this chapter is to integrate realistic FE models for more complex structures using Abaqus-Python script for the applicability of the damage localization and quantification methods described in this thesis.

Part IV investigates to real applications of structures for both damage localization and quantification:

- Chapter 13 presents the real case applications on lab structures. In this Chapter, the proposed methods from Chapter 5 and 7 are successfully applied on several real structures for damage localization and quantification. The vibration data of these structures was obtained through numerous collaborations:

  - A cantilever beam, provided by Brüel & Kjær, Denmark.
  - A cantilever beam - by IFSTTAR/COSYS-SII, Bouguenais, France.
  - A four-story steel frame structure, the Yellow Frame at the University of British Columbia, Canada.

Finally, the thesis concludes with an assessment of the developed methods and presents the perspectives for future research.

Notation

Symbols

A^T	Transposed matrix of A
A^H	Transposed conjugated complex matrix of A
A^{-1}	Inverse of A
$A^\dagger$	Pseudoinverse of A
$\stackrel{\text{def}}{=}$	Definition
i	Imaginary unit, $\mathrm{i}^2 = -1$
$\Re(a)$, $\Im(a)$	Real and imaginary part of variable a
A^*, a^*	Complex conjugate
$\operatorname{vec} A$	Column-wise vectorization of matrix A
$A \otimes B$	Kronecker product of matrices or vectors A and B
$\widehat{X}$	Estimate of variable X
$\mathbf{E}(X)$	Expected value of variable X
$\mathcal{N}(M, V)$	Normal distribution with mean M and (co-)variance V
$\mathbb{N}$, $\mathbb{R}$, $\mathbb{C}$	Set of natural, real, complex numbers
I_m	Identity matrix of size $m \times m$
$0_{m,n}$	Matrix of size $m \times n$ containing zeros

Variables

M	Mass matrix
K	Stiffness matrix
C	Damping matrix
n	System order
r	Number of sensors
$r^{(\text{ref})}$	Number of reference sensors
A_c, A_d	State transition matrix for continuous and discrete-time system
C_c, C_d	Observation matrix
x_k	System state at index k
y_k	System output at index k
$\mathcal{H}$	Hankel matrix of output covariances
$\mathcal{J}$	Jacobian matrix
$\mathcal{O}$	Observability matrix
$\mathcal{O}^\uparrow$, $\mathcal{O}^\downarrow$	Matrices, where the last resp. first block row (usually containing r rows) of $\mathcal{O}$ are deleted

Σ	Covariance matrix
N	Number of samples

Abbreviations

DOF	Degree of freedom
FE model	Finite Element model
OMA	Operational modal analysis
SHM	Structural health monitoring
SSI	Stochastic subspace identification
SVD	Singular value decomposition

List of investigated damage localization methods

SDDLV	Stochastic Damage Locating Vector
S-SDDLV	Statistical Stochastic Damage Locating Vector
ILDL	Influence Lines Damage Location
S-ILDL	Statistical Influence Lines Damage Location
R1v-ILDL	Rank 1 for residual vectors with degenerate normal distribution for ILDL
R1v-S-ILDL	Rank 1 for residual vectors with degenerate normal distribution for S-ILDL
R1e-ILDL	Rank 1 for element-wise tests of residual vector for ILDL
R1e-S-ILDL	Rank 1 for element-wise tests of residual vector for S-ILDL
R*-S-ILDL	Arbitrary Rank for S-ILDL

Part I

Preliminaries

Chapter 1

State of the art

1.1 Introduction

The present work focusses on vibration-based damage localization and quantification from output-only measurements for Structural Health Monitoring (SHM). Currently, performance monitoring of large engineering structures is mainly done on-site by engineers and technicians, who need to have a very specific expertise and knowledge of past hazard events. In the meantime, the number of ageing structures is growing worldwide. Even when manpower is available, the inspection task is not easy. Structures are often difficult to reach (e.g. bridges in remote areas, or offshore structures), so inspections are limited. Moreover, visual inspections offer only limited knowledge, not least because only reachable components can be inspected. They are also costly in terms of labor and operation shutdowns. The long term perspective is to replace the inefficient manual inspection procedure by automated robust on-site monitoring with permanently installed sensors. This will allow the engineer to monitor the structures from a centralized facility using robust tools with scientific foundation.

SHM methods have gained an increasing interest of determining the system health since last decades, i.e. the occurrence and characterization of damage in civil, mechanical or aeronautical structures using dynamic response measurements from an array of sensors. Sensors installed on the structure collect data and then the modal parameters (natural frequencies, mode shapes and damping ratios) can be estimated. Those parameters are meaningful for the monitoring of the structure. In the last decade, sensor and data acquisition technology has evolved rapidly and has become affordable, allowing a large-scale instrumentation of important structures like bridges, buildings or offshore constructions in particular for long term vibration-based monitoring [BFG06].

Thanks to these advances in sensing systems, there is a huge potential to realize an automated and online structural assessment from sensor data, leading to a safe, reliable and cost efficient structural integrity management [FW07]. Moreover, during the last years,

huge advances has been made in the development of Operational Modal Analysis, allowing the reliable modal identification of the structures from ambient vibration measurements. Automatic inspection techniques are of enormous value for structures with poor accessibility or in high risk environments such as offshore constructions, large engineering structures or nuclear power plants. Maintenance operations can be optimized and costly downtime kept to a minimum, while the structural safety is increased. Vibration data that is recorded on-site on a structure contains some information about the current condition of the structure.

This thesis related to vibration-based damage localization and quantification in the field of structural health monitoring from the measured data, where the vibration models for modal analysis and the system identification are taken into account as a prerequisite. Therefore, in the following, some contributions from the literature related to vibration models, system identification, and then damage assessment techniques are presented in general which are crucial for the performance monitoring of the SHM systems.

1.2 Vibration models

Typically, experimental identification of structural dynamics models is based on the modal analysis approach which is fundamental in vibration-based monitoring of large civil structures. During the last decades, the experimental verification of design values particularly the modal parameters (eigenfrequencies, damping ratios, mode shapes, and modal scaling factors) have found a special interest under real operation conditions. It is usually performed for the purpose of obtaining accurate experimental estimates of modal parameters, which then can be correlated to the corresponding values numerically estimated from a finite element model of a structure. It is also frequently used for quality control and structural health monitoring purposes. As the modal information is derived from structural response (outputs) while the structure is in operation, this procedure is typically called Operational Modal Analysis (OMA) or Output-only Modal Analysis.

An overview for the application of modal testing and analysis can be found in the literature [Ewi84, MS97, HLS98, Ewi00, BRA+15]. In [HVdA99], the industrial applications of modal testing and analysis of structures is carried-out e.g. family car during road tests, commercial aicraft and the identification of the modes of a concrete bridge under operational conditions. In addition, modal testing of spacecraft during launch [Jam03], modal parameters of wind turbines at different rotation rates [CJ10], and modal testing of engines during startup and shutdown [CSC11], and many more.

First at all, it is important to pay attention that models are always idealization of real dynamic systems that necessarily contains simplifications. The ones adopted throughout this work assume linear time-invariant behaviour of the described system.

Finite element model

Assume that the behavior of a mechanical structure with viscous damping can be described by a linear time-invariant (LTI) dynamic system

$$M\ddot{\mathcal{X}}(t) + C\dot{\mathcal{X}}(t) + K\mathcal{X}(t) = f(t) \tag{1.1}$$

where M, C, $K \in \mathbb{R}^{d\times d}$ are the mass, damping and stiffness matrices, respectively, t indicates continuous time and $\mathcal{X} \in \mathbb{R}^d$ denotes the displacements at the d degrees of freedom (DOF) of the structure. The external force $f(t)$ is not measurable and is modeled as stationary white noise. When measuring accelerations, velocities or displacements at some degrees of freedom of the structure, this measurements yield,

$$y(t) = C_a\ddot{\mathcal{X}}(t) + C_v\dot{\mathcal{X}}(t) + C_d\mathcal{X}(t) + \eta(t) \tag{1.2}$$

where C_a, C_v, and C_d are the matrices indicating at which degrees of freedom acceleration, velocity and displacement measurements are taken, and $\eta(t)$ is the measurement noise.

Continuous-time state-space model

Let the dynamic system (1.1) be observed at r coordinates. Furthermore, defining $x(t) = [\mathcal{X}(t) \;\; \dot{\mathcal{X}}(t)]^T$ which contains the displacement and velocity of the dynamic system, this then leads to the corresponding continuous-time state-space model

$$\begin{cases} \dot{x}(t) = A_c x(t) + B_c f(t) \\ y(t) = C_c x(t) + D_c f(t) + \eta(t) \end{cases} \tag{1.3}$$

with the state vector $x(t) \in \mathbb{R}^n$, the output vector $y(t) \in \mathbb{R}^r$, the state transition matrix $A_c = \begin{bmatrix} 0 & I \\ -M^{-1}K & -M^{-1}C \end{bmatrix} \in \mathbb{R}^{n\times n}$, the input influence matrix $B_c = \begin{bmatrix} 0 \\ -M^{-1} \end{bmatrix} \in \mathbb{R}^{n\times d}$, the output matrix $C_c = \begin{bmatrix} C_d - C_aM^{-1}K & C_v - C_aM^{-1}C \end{bmatrix} \in \mathbb{R}^{r\times n}$ and the direct transmission matrix $D_c = \begin{bmatrix} C_aM^{-1} \end{bmatrix} \in \mathbb{R}^{r\times d}$ where $n = 2d$ is the system order and r is the number of sensor outputs.

The input $f(t)$ (1.3) is not known deterministically but some statistical characteristics are assumed. In particular it is assumed that f is white, stationary, and square integrable. Moreover, experimental data includes measurement noise. Thus, the corresponding continuous-time state-space model in (1.3) writes as

$$\begin{cases} \dot{x}(t) = A_c x(t) + v(t) \\ y(t) = C_c x(t) + w(t) \end{cases} \tag{1.4}$$

with the state noise $v(t) = B_c f(t)$ and output noise $w(t) = D_c f(t) + \eta(t)$.

Once the model has been constructed, the modal parameters of the dynamic system can be extracted from the state matrix A_c [Pee00]. However, only the system matrices A_c and C_c are relevant from output-only system identification, and the non-identified matrices B_c and D_c are only relevant in the derivation of estimates related to the transfer matrix.

Discrete-time state-space model

In a vibration test, the analog signals are recorded by the transducers, and then converted to digital data by an analog to digital converter so that, they can be stored and processed

by a computer for analysis. Since the available information of the dynamic system is discrete in time in practice, a discrete-time state-space model of the previously presented model is more adequate to fit experimental data. Therefore, it is characterized based on the respective stochastic discrete-time state-space model

$$\begin{cases} x_{k+1} = A_d x_k + v_k \\ y_k = C_d x_k + w_k \end{cases}, \tag{1.5}$$

which results from sampling system (1.4) at time steps $t = k\tau$ where τ is the time step. The state vector $x_k = \begin{bmatrix} \mathcal{X}(k\tau)^T & \dot{\mathcal{X}}(k\tau)^T \end{bmatrix}^T \in \mathbb{R}^n$, the measured outputs $y_k \in \mathbb{R}^r$, the state transition matrix

$$A_d = \exp(A_c \tau) \in \mathbb{R}^{n \times n}, \tag{1.6}$$

and the observation matrix $C_d = C_c$ where $n = 2m$ is the model order, r is the total number of measured outputs. Once a discrete-time state-space model has been identified from experimental data, it is possible to estimate the modal parameters of the tested structure. The state noise v_k and output noise w_k are unmeasured and assumed to be centered and square integrable.

In the following Section, some contributions from the literature related to system identification are presented in the context of OMA, which take into account the above features.

1.3 System identification

Identification is the process of developing a mathematical model for a physical system by use of experimental data [Gra75, Lju87, Jua94, Lju99] from measured input and output data. It emerged in the 1960s in the control community. A historical overview of the development of system identification is given in [Gev06]. Some of the important contributions for identification theory in the control community is provided by Ho and Kalman's work on the state-space realization problem [HK66], Aström and Bohlin's work on maximum likelihood methods [AB65], Akaike's work on stochastic realization theory [Aka74, Aka75], Ljung's prediction-error framework [Lju78, LC79] and many more.

In the previous section, the discrete-time state-space model is presented in (1.5) for a stochastic process. In system identification, the problem is to find the system matrices A and C from the outputs y_k and the assumptions on the statistical properties of the driving forces.

The subspace-based system identification algorithms for stochastic inputs has been emerged in the 1970s. The Stochastic subspace identification (SSI) methods are an efficient tool for system identification of mechanical systems in OMA where modal parameters are estimated from measured vibrational data of a structure. In [Kun78], Kung presented the Balanced Realization Algorithm. In 1985, Benveniste and Fuchs [BF85] proved that the Balanced Realization method for linear system eigenstructure identification is consistent under (unmeasured) non-stationary excitation. In [VODM96], Van Overschee and De Moor presented their own formalism and popularized subspace methods in their data-driven form. The Balanced Realization method using a block Hankel matrix of output correlations was also popularized as covariance-driven stochastic subspace identification by Peeters and De Roeck

in [PDR99]. Since then, the family of subspace algorithms is increasing in size and popularity [Lar83, VODM94, Ver94, Vib95], mostly for its capacity to deal with problems of large scale under realistic excitation assumptions. In [MAL96, VODMDS97, Pin02, CGPV06, Akç10], the subspace algorithms for frequency response data are derived. In [BM07], many subspace algorithms from literature are put in a common framework and their consistency for eigenstructure identification under non-stationary noise conditions is proven.

The application of system identification to vibrating structures presented a new research domain in the field of structural engineering, known as modal analysis [Ewi84, POB+91, MS97, HLS98]. Thus, the identified model is the modal model including of eigenfrequencies, damping ratios and mode shapes. Often, the state-space model is used in connection with a system identification method to identify the modal model. For the modal analysis of vibrating structures, the emerging need for reliable identification methods where noise and large system orders of structures under realistic excitation have to be considered, gave another impulse in the development of system identification methods. Experimental Modal Analysis (EMA), where only deterministic inputs are considered, moved to Operational Modal Analysis (OMA) and Operational Modal Analysis with eXogenous inputs (OMAX), where stochastic inputs and combined stochastic-deterministic inputs are considered, respectively [RDR08].

A similar identification approach to subspace identification is the Eigensystem Realization Algorithm (ERA), which was introduced by Juang and Pappa [JP85]. Originally designed for modal analysis using impulse response functions, it was adapted to output-only measurements in [JICL95] and became known as Natural Excitation Technique (NExT-ERA). The latter is closely related to covariance-driven subspace identification. Recently, in [DM12], the authors derived a fast multi-order computation of system matrices with the stochastic subspace-based identification algorithms, and applied to practical test cases where so-called stabilization diagrams are used that contain the system identification results at multiple model orders.

There are also classical identification methods from the structural engineering community, such as Peak Picking method. This is the simplest approach to determine modal parameters, where the eigenvalues are identified as the peaks of a spectrum plot [BG63, BP93]. However, in this method, close modes cannot be distinguished and the accuracy is limited to the frequency resolution. In [STAB88], the Complex Mode Indicator Function (CMIF) method for modal analysis using frequency response functions was introduced. It is based on a singular value decomposition of the frequency response functions (FRF) at each spectral line. Then, a peak in the CMIF indicates the location on the frequency axis that is nearest to the eigenvalue within the accuracy of the frequency resolution. An additional second stage procedure is needed for scaled mode shapes and an accurate eigenvalue estimation. An output-only advancement is the Frequency Domain Decomposition (FDD) method [BVA01, BZA01], where the power spectral density (PSD) functions are used instead of FRFs. Close modes can be identified, but user interaction is required to identify modes from the peaks in the singular values corresponding to the spectral lines.

A non-iterative maximum likelihood approach for frequency-domain identification is the Least-Squares Complex Frequency-domain (LSCF) method [GVV98, VdAGVV01]. The method is a common-denominator transfer function model to measured FRFs in a least squares sense and is the frequency-domain counterpart to the Least Squares Complex Exponential (LSCE) algorithm [BAZM79]. In [GVV+03, PVdAGL04], it was extended to polyref-

erence LSCF, also known as PolyMAX, by fitting a right matrix fraction model on the FRFs. This results in more accurate modal models than LSCF in the multiple inputs case. These are fast and accurate methods and produce very clear stabilization diagrams, where the damping ratios of the modes might be underestimated [CGV+05]. These methods can also be applied to output-only data [GVC+03]. In [DDSG10], an output-only modal analysis approach using transmissibilities under different loading conditions was developed, where the unknown ambient excitation can be arbitrary as long as the modes of interest are excited.

1.4 Context of structural health monitoring

It is clear from the previous discussion that there is a need for a reliable and continuous assessment of the integrity of the structures. Vibration-based structural health monitoring techniques have been actively developed in the last decades [FDN01, CF04, FQ11], for example for the monitoring of bridges, buildings or offshore structures. Generally, there are two kinds of evaluation are performed such as destructive and non-destructive tests. Destructive tests include sampling of the structure, which may affect the condition of structure and non-destructive tests do not involve with any action that can damage the structure or affect its functionality. More researchers have been focussing on the latter approach due to the continuous serviceability of the structure.

Physical changes in the structure due to damage induce changes in the modal characteristics of the structure, which can be monitored through output-only vibration measurements. Currently available methods only cover a small part of monitoring-based structural diagnosis, which can be divided into five subtasks of increasing difficulty [FW07]:

- Level 1: Detection of damage
- Level 2: Localization of damage
- Level 3: Identification of damage type
- Level 4: Quantification of the damage extent
- Level 5: Prediction of the remaining service life.

When performing these tasks in a cascade fashion, the full structural diagnosis problem is amenable to a solution. However, only methods for level 1 have reached (at least limited) maturity for real applications so far, e.g. with data-driven algorithms adapted from the fields of pattern classification and statistical process control. The levels 2-5 of structural diagnosis are much more challenging. One reason for the complexity of these tasks is the requirement of additional information on the monitored structure besides mere measurements, such as large-scale finite element or structural performance models.

In the following, the damage identification methods such as damage detection, localization and quantification approaches are described from the literature of SHM community.

1.4.1 Damage detection methods

The first step of structural diagnosis consists in the detection of damage, before the localization analysis can be performed. Typically, data-driven methods are used for damage detection using only the recorded response of the structure and these methods are generally simpler to be used than the model-based methods, since there is no need of creating and adjusting a model to the structure.

In the late 1970s, the damage detection in structures was proposed by Adams et al. [ACPS78], and was expanded by Crawley & Admas [CA79], where the frequency shifts were used in detecting damage. Salawu [Sal97] also presented an excellent review on the use of modal frequency changes for damage assessment.

A common damage detection method is to compare measurement data to a reference based on statistical hypothesis testing [FW07]. This strategy is to repeatedly estimate current modal parameters by means of system identification, and to compare the result to some reference modal parameters [RML+10, MCC12]. This approach is generic, since it only needs the information from a healthy state of the structure for comparison with the new data, but no a priori information or model of the damaged state is required. An alarm is raised if a corresponding statistical distance measure exceeds a threshold, indicating a significant change within the monitored structure. Other methods are based on model-data matching, where measurement data are directly confronted to a reference model, without resorting to repeated system identification. For instance, such methods include non-parametric change detection based on novelty detection [WMF00, YDBG04], whiteness tests on Kalman filter innovations [Ber13] or other damage-sensitive features [CF04]. Belonging to this method class, the local approach for change detection [BBM87] with subspace-based techniques has a solid theoretical foundation. This approach [DMH14, DHMR14] have led to a mature damage detection method that can be applied to monitor civil structures. Its recent integration into commercial SHM software [ART].

1.4.2 Damage localization methods

Many endeavours to solve the damage localization problem, so far, are based on updating finite element (FE) models, while other approaches use information on the geometry and physical properties of the investigated structure together with measurements to analyse changes in the structure without updating models. Model-based methods update the parameters of an FE model of the healthy structure based on the measurements from the damaged system, and damage is located in the regions of the model where parameters are modified [BXHX01, SDRL15b]. In these methods, there is a need in processing the data and then updating the model based on it. This will delay the identification procedure and makes these methods less appealing for real-time damage detection. However, the model will enhance the damage localization resolution and it helps in evaluating the damage severity.

Using output-only measured data from the damaged structure, these methods try to determine the updated system matrices that reproduce the dynamic response from the data by solving an optimization problem based on the structural equations of motion. Comparing the updated matrices with the original ones provides a damage detection, and this can be used

to determine the damage location and extent [BXHX01]. While these model updating-based approaches are in principle applicable to arbitrary structures, they are often too poorly conditioned to be successful in practice. Real structures may have a large number of structural parameters and the model of the structure may contain a large number of degrees of freedom. The connection of those parameters to the sensor-based information for model updating often turns out to be an ill-posed problem, since the number of identified parameters from measurements are usually small in comparison to the number of model parameters [Fri07]. In this case, the size of the finite element model is much bigger than the dimension of the parameters that can be estimated from sparsely instrumented in-situ SHM systems. In order to circumvent this problem, [BBA14] developed an approach based on selective sensitivities, where a large-scale parameter identification is transferred to a series of reduced order problems with a high parameter sensitivity. This is achieved by exciting the structure with specific loading configurations, each being sensitive to a specific set of parameters. However, this approach is only feasible for relatively small structures, since otherwise the load application is difficult to realize requiring an output-only analysis. An alternative are Bayesian methods such as [YK11, SDRL15a], where structural parameters that are sensitive to the data obtain higher priorities in the updating scheme. A further problem for updating is the requirement of a very accurate FE model of the reference state, otherwise changes due to damage are hidden by model errors. Moreover, user interaction by an experienced engineer is often needed in the updating process, and modal identification is necessary in the damaged state, which both prevent an automation of updating-based methods for SHM. For example, damage localization methods based on FE model updating focus on changes in natural frequencies [CA79], other modal parameters [JR05] and residual functions [JR06], or use a damage function for describing the damage pattern [TMDR02, UTDR06, UTG05]. Details are stated in the following section.

Alternative damage localization methods with a theoretical background combine properties of the data-driven and model-based approaches. They are based on data-driven features from measurements of the reference and damaged states, which are confronted to a FE model of the investigated structure to define damage indicators for the elements of the FE model, without updating its parameters [LCD+16]. In these methods there is no need to update the model continuously and it is only created in the reference state (undamaged condition) of the structure. For example, localization can be performed by sensitivity-based methods on a parametrized residual vector that is computed from measurements [BMG04, BBM+08, DMZ16], or by interrogating changes in the flexibility of a structure [Ber02, Ber10, Ber14], or by statistical methods [DMBM13, MDBM15] through extracting the localization information based on the FE model.

Since the amount of literature related to damage diagnosis is quite large, the identification of damage in a structure can be performed by employing different properties of a system. In the following, the damage identification methods are classified as

- Natural frequency based methods
- Mode shape based methods (mode shape or modal curvature)
- Modal strain energy

- Flexibility methods
- Neural network
- Genetic algorithm
- Wavelet based methods

1.4.2.1 Natural frequency based methods

In many researches [ACPS78, Gud82, KS86, SLL88, HT91, Sal97], structural natural frequency has been found to indicate structural damage.

In [CA79], Cawley and Adams proposed a damage localization method based on FE model updating focus on changes in natural frequencies in a 2D plane structure. Lee and Chung [LC00] also present a method of finding the structural damage size and location using natural frequencies. In this method, the first four natural frequencies are used and the approximate crack location is obtained using Armon's Rank-ordering method. Based on the result of the crack position range, an appropriate FE model is adopted and the crack size is determined by the FE model. Kim et al. [KRCS03] have also presented a methodology to locate and quantify the damage in structures using a few natural frequencies. The authors addressed a damage-localisation algorithm to locate damage from changes in natural frequencies and a damage-sizing algorithm to estimate crack-size from natural frequency perturbation are formulated. In addition [Kul03], the author used the change of the natural frequency as a basis to indentify the existance of the damage in a real bridge structure. In [CF04], the authors addressed that most of the success in use of natural frequencies in damage detection was obtained for single damage in small and simple laboratory structures. In [GNW+17], crack identification is performed based on the analysis of frequency changes in multi-span beams to determine whether the structure is healthy or not. To accurately identify the cracks characteristics for multi-span beam structure, a mathematical model is established, which can predict frequency changes for any boundary conditions, the intermediate supports being hinges.

Based on the natural frequencies, the damage identification is not much accurate due to the low sensitivity of frequency shifts to the damage and for damage, it requires either very precise measurements or large levels of damage. However, the natural frequencies identified in a structure have less statistical variance due to the noise than other modal parameters [FJI97, DFG97]. The other problem that the damage is usually localized in a specific point of structure that affects more on the higher modeshapes and resonant frequencies of the structure. However, the measurement of natural frequency cannot provide enough information for structural damage detection. Usually, this method can only ascertain existence of the large damage, but may not be able to give the damage location because the structural damage in different location may cause the same frequency change.

1.4.2.2 Modeshapes based methods (modeshape and their curvature)

The mode shapes describe the configurations or the pattern in which a structure will naturally displace when excited at the natural frequency. Typically, displacement patterns are of

primary concern. A normal mode of a vibrating system is a pattern of motion in which all parts of the system move sinusoidally with the same frequency and with a fixed phase relation.

Many techniques have been developed over the years based on mode shapes or modal curvature to detect damage. The modeshapes are compared between two states of the structure to detect damage. In [AB82], Allemang and Brown proposed the Modal Assurance Criterion (MAC), which detects mode shape changes over the structure by taking the orthogonality of eigenvectors. Kim et al. [KJL92] presents the MAC in the development of the Coordinate Modal Assurance Criterion (COMAC) method, which utilizes modal node displacement to detect and locate damage. The application of MAC and COMAC in bridge structures can be found [SW95] where these methods could detect most structural changes and locations, but also identified false positives. This was also observed to beam like structures [SCRL06], the authors showed that COMAC was prone to indicating false damage detections.

Pandey et al. [PBS91] first proposed the mode shape monitoring theory to focus on modal curvatures, which are mode shapes' second derivative is known as the Modal Curvature Method (MCM). It utilises the relationship between curvature and flexural stiffness. Since the curvatures are locally sensitive to damage, the authors extend the idea for locating damage by comparing the undamaged mode shapes with the damaged mode shapes. To detect the damage other than the artificial errors from the model construction, a good quality FE model is required that could accurately depict the structure but is often difficult to achieve. Non-model-based damage detection methods, also named as damage index methods, are relatively straightforward. The changes of modal parameters between the undamaged and damaged states of the structure are directly used, or correlated with other relevant information, to develop the damage indicators for localizing damage in the structure [WL04].

The curvature method has some drawbacks. It requires many sensors to define higher modes and its performance is dependent on the number of modes considered. Moreover, to calculate curvatures inherently attains errors due to the application of the central difference approximation method to displacement mode shapes using vibration data. In [YRKO17b], a simple Fourier spectral-based method is proposed to calculate the modal curvature of beams instead of the traditional central difference method and damages in beam-like structures are localized. Zhou et all. [ZWD+17] is proposed a numerical method based on the transfer matrix and mode curvature techniques to detect the damage locations and severities of a drilling riser. Some authors are also addresed the development and application of the curvature method which can be found in [JRWC17, XZ17, FAP17, YRKO17a], and interested for the SHM systems.

Zhang and Aktan stated in [ZA98] that the change in the curvature of the uniform load surface (ULS) can be used in order to locate damage. They comparatively studied the modal flexibility and its derivative, called uniform load surface, for their truncation effect and sensitivity to experimental errosrs. The authors observed that the method has less truncation effect and less sensitive to experimental errors. In [WL04], Wu and Law describe a damage localization method based on changes in ULS curvature where it requires only the frequencies and mode shapes of the first few modes of the plate before and after damage.

Some researchers found that the modal flexibility can be a more sensitive parameter than natural frequencies or mode shapes for structural damage detection. Therefore, the change of

flexibility instead of the change of stiffness is proposed in [PB94] to locate damage of a beam structure. In [WL04], a theoretical sensitivity study is presented comparing the use of natural frequencies, mode shapes, and model flexibility for structural damage detection. In [LRZ02], the authors pointed out that Pandeys method is difficult to locate multiple damages, and they recommended the modal flexibility curvature for multiple damage localization due to its high sensitivity to closely distributed structural damages.

1.4.2.3 Modal strain energy

Modal strain energy has been widely used to quantify the participation of each element in particular vibrating mode and in the selection of a candidate set of elements for damage localization [LK94]. The change of modal strain energy in each structural element before and after the occurrence of damage can also be used for damage localization. An overview of methods is found in [FQ11, JMRC17]. For example, some are based on the change of modal strain energy in connection with a FE model [SK96], requiring as many sensors as degrees of freedom, which is impossible on real structures. In connection with sensitivities from a FE model, changes in the identified frequencies [MWC98] or mode shapes [SLZ00] between the healthy and damaged structure are correlated, which, however, is only feasible for one damaged structural element. Moreover, these methods require a modal identification in the damaged state, which prevents its automation for continuous monitoring, and statistical estimation errors are not taken into account.

In [SLZ98], the ratio of change in the modal strain energy is proposed to detect the damage location. This parameter is based on the estimation of the change of modal strain energy in each element after the occurrence of damage. Information required in the identification are the measured mode shapes and elemental stiffness matrix only without knowledge of the complete stiffness and mass matrices of the structure. A priori, no other information about the structure is required.

As in most other studies, the damaged strain energy mode shapes were compared to the undamaged strain energy mode shapes [YKK99, HWLS06, Sey12]. Statistical methods were employed to jointly analyze information from several mode shapes and to locate damage. In [CDF99], a detailed theoretical explanation is provided on application of the strain energy method to plate-like structures. In [SK05], the author addressed the practical issue of determining the optimal sampling interval that was set to minimize the effects of measurement noise and truncation errors from the calculation of the curvature and strain energy mode shapes, thus providing maximum sensitivity to damage and accuracy of damage localization.

In [VDHHDT+16], a modal strain energy based method and an improved differential evolution (IDE) algorithm are used for damage identification in laminated composite plates, while in [LZL+17] a novel method proposes based on grouping modal strain energy to detect structural damages of offshore platforms. In [TTCAR17] presents a vibration-based technique, using only the first vibration mode, for predicting damage and its location and severity in steel beams where the modal strain energy based damage index was capable of detecting, locating and quantifying damage for single damage scenarios and for multiple damage scenarios, Artificial Neural Network incorporating damage index as the input layer was used.

1.4.2.4 Flexibility methods

Another category of methods use the changes in the flexibility matrix instead of the change of stiffness matrix for damage detection, location and quantification. The flexibility matrix is based on a function of the mode shape and the reciprocal of natural frequency when the structural vibration modes satisfy the normalisation condition. Thus, the effect of high-frequency components in flexibility matrix will rapidly decrease with the increase of natural frequency. Therefore, the flexibility matrix is achieved by only measuring several low-order modes and frequencies in practice and they have higher contribution in the final constructed dynamic flexibility matrix.

Over the last decades, several approaches were investigated for damage assessment based on flexibility that can be found in literature. Pandey and Biswas [PB94] have shown that changes in the flexibility matrix can indicate the presence and location of damage, where the flexibility matrix is estimated from modal parameters of only a few lower frequency modes. Aoki and Byon [AB01] pay attention on localized flexibility properties that can be deduced from the experimentally determined global flexibility matrix, and present the underlying theory that can be viewed as a generalized flexibility formulation in three different generalized coordinates, namely, localized or substructural displacement-basis, elemental deformation-basis and element strain-basis. Yan and Golinval [YG05] proposed a damage diagnosis technique based on changes in dynamically measured flexibility and stiffness of structures, where mass-normalized mode shapes are needed. The flexibility matrices were obtained based on estimated modal parameters by the covariance-driven stochastic subspace identification technique. Damage can be localized from the comparison of these matrices between a reference and damaged state. The merits and the limitations of the technique were tested by the numerical models of a cantilever beam and a three span bridge as well as experiments in the laboratory with an aircraft mock-up. Perera et al.[PRM07] compared experimental and analytical flexibility matrices based on the flexibility matrices obtained from modal parameters in a model updating approach. The proposed algorithm is illustrated for simulated beams and then by experimental data from the vibration tests of a beam. It has been verified that the proposed procedure is very promising for locating and quantifying damaged elements and considerably improves predictions based only on modal flexibility parameters.

Shih et al. [STC09] proposed a multi-criteria approach for damage assessment of beam and plate structures. It includes flexibility matrix, changes in eigenfrequencies and a modal strain energy based damage index. In [NS13], Montazer and Seyedpoor presented a method for damage identification based on the concepts of flexibility and strain energy of a structure. One year later [MS14], the authors introduced a new damage index, called strain change based on flexibility index (SCBFI) to locate damaged elements of truss systems. The principle of SCBFI is based on considering strain changes in structural elements, between healthy and damaged states. Numerical results indicate that the method can provide a reliable tool to accurately identify the multiple-structural damage for truss structures. Reynders and De Roeck [RDR10] presented a method for vibration-based damage localization and quantification, based on quasi-static flexibility. This is a so-called local flexibility method detecting local stiffness variations based on measured modal parameters. This approach for damage assessment was validated in both simulated and laboratory tests.

Assuming that damage occurs, Bernal [Ber10] presents a damage localization technique using both finite element information and modal parameters, namely the Stochastic Dynamic Damage Location Vector (SDDLV) approach. This is a theoretically sound method that evaluates the transfer matrix difference between reference and damaged states of a structure, without updating the FE model. This approach has evolved over the years from being restricted to input/output deterministic systems to handle output-only stochastic systems [Ber02, Ber06, Ber07, Ber10]. In [DMBM13], the deterministic SDDLV approach has been extended with a statistical framework for deciding if an element is damaged, taking into account the uncertainties in the measurement data. Further robustness has been achieved through a statistical aggregation of results for different parameters of the method [MDBM15]. A complementary approach to the SDDLV is the Influence Lines Damage Localization (ILDL) [Ber14], where the damage location is determined from the subspace angle of each position in the structure by computing the column space of the change in flexibility and a known FE model. Using measurement data of the structure in both reference and damaged states together with a FE model leads to a reduced dependence on the model precision, which is also promising for real applications. However, this approach requires a modal identification in the damaged state.

This thesis is focused in the works of Bernal [Ber10, Ber14], described above, as the basis for the damage localization development, and the statistical evaluation works as the basis of the PhD thesis of Luciano Marin [Mar13].

1.4.2.5 Neural networks

Recent studies have introduced artificial neural networks (ANN) to identify damage in a system. In general, the method is used in different application such as artificial intelligence, machine learning, pattern recognition, mathematics, and also vibration-based damage detection analysis [MH99, WZ01, GZ08].

Yun et al. [YYB01] used the natural frequencies and mode shapes as input data for a neural network to detect damage in the joints of framed structures. Using a noise-injection learning algorithm, the neural network was trained to reduce the effects of experimental noise. The authors addressed that the algorithm could estimate damage with reasonable accuracy, while the performance strongly depended on the level of experimental noise. A disadvantage of using mode shape displacements is that the mode shape identification requires many measurement locations. In [WB01], a neural network is used to locate and classify faults and a number of different methods are applied to determine an optimal sensor distribution. In [SS03], the authors developed an ANN combining global (changes in natural frequencies) and local (curvature mode shapes) vibration data as inputs for an ANN for location and severity prediction of damage in a beam-like structures. There, artificial random noise has been generated numerically and added to noise-free data during the training of a trained feed-forward backpropagation ANN. In [MKMB08], a neural network-based system identification approach is presented for the estimation of the damage percentage of joints for truss bridge structures. The technique that was employed to overcome the issues associated with many unknown parameters in a large structural system is the substructural identification. Another localization approach was developed by Gonzalez and Zapico [GZ08] where the inputs of the

ANN are the first flexural modes (frequencies and mode shapes) at each principal direction of the structure and the outputs are the spatial variables (mass and stiffness). In [SMV10], the authors present a subspace-based damage localization using artificial neural network and the effectiveness of this algorithm is studied experimentally by localizing single edge cracks in a thin aluminum plate. In [Li11], the structural damage localization on a simple composite plate specimen is identified using probabilistic neural networks.

Hakim et Razak. [HR14] presents and reviews the technical literature for past two decades on structural damage detection using artificial neural network's with modal parameters such as natural frequencies and mode shapes as inputs. Further in [HRR15], ANNs based damage identification techniques were developed and tested for damage localization in I-beam structures using dynamic parameters. There, experimental modal analysis and numerical simulations were applied to generate dynamic parameters of the first five flexural modes of structures. Recently, in [AAK+17], presents a structural damage detection system using 1D Convolutional Neural Networks (CNNs) that has an inherent adaptive design to fuse both feature extraction and classification blocks into a single and compact learning body. The method performs vibration-based damage detection and localization of the damage in real-time.

1.4.2.6 Genetic algorithms

In the last two decades [Gol89, Hol92, OKC02, GS08], genetic algorithms (GAs) have been developed as promising intelligent search technique for diverse applications in civil engineering and structural identification [CPH03, KCL03]. Friswell and Penny [FP97] stated that GA have been seen as a promising choice for the solution of hard problems in damage identification. The great advantage in using GA is the ability in finding global minimum on a difficult optimization problem where there are many local minima as happens in damage location.

Sazonov et al. [SKGH03] used the GA to produce a sufficiently optimized amplitude characteristic filter to extract damage information from the strain energy mode shapes. There, a FE model was used to generate training data set with the known location. In [OKC02], they used genetic algorithm in order to find the change in the lumped masses in a plate structure based on its fundamental frequencies. Perera et al. [PT06] used structural damage detection via modal data with genetic algorithms. The authors proposed a nonclassical optimization approach involving the use of genetic algorithms to localize damaged areas of the structure. In addition, in [PRM07], the authors developed a model updating method based on GA to locate damage and estimate its severity. Gomes and Silva [GS08] developed a method using GA and a modal sensitivity to identify and evaluate damage cases in a parametric numerical finite element model, where GA is used as an optimization tool. It was summarized that the quantification of the damage could not be obtained accurately. In [PCM09], the authors present a vibration-based damage detection in a uniform strength beam using genetic algorithm.

In [SBBRPF11], a methodology based on genetic algorithms for the crack detection on damaged structural elements was presented where the crack model takes into account the existence of contact between the interfaces of the crack. In [MKGA13], application of genetic algorithm is presented in crack detection of beam-like structures using a new cracked Euler-Bernoulli beam element. In [SIBA15], the authors used the genetic algorithm (GA) for

detecting and locating damage in beam structures. In their study, identification of damage is formulated as an optimization problem using three objective functions (change of natural frequencies, Modal Assurance Criterion and natural frequency). Kim et al. [KKL14] proposed a simple and efficient two-stage optimization procedure to identify the sites and the extent of several damages, and it was tested for numerical case study in truss structures. In [FAMGA16], an algorithm was proposed to detect the damage location using multi-objective genetic algorithm (MOGA) along with modified multi-objective genetic algorithm (MMOGA), and tested for steel beam structure. In this approach natural frequencies are considered as the main dynamic parameters to detect the damage.

1.4.2.7 Wavelets based analysis

Recently, the wavelet transform can be used for damage detection and location by analyzing the signals. The literature review of the research that has been conducted on damage detection by wavelet analysis is given in [KM04, YCWY07, Kat15]. The spectrum graph obtained using wavelet analysis can indicate the damage existence directly. In [RV05], the authors proposed a wavelet based approach for structural damage detection in beams, plate and delamination detection of composite plates. The main idea used is the breaking down of the dynamic signal of a structural response into a series of local basis function called wavelets to detect the special characteristics of the structure using scaling and transformation property of wavelets. In [LW98], the damage is detected on a cracked beam by changes wavelet coefficient.

For damage detection and localization in structures, the applicability of various wavelets has been studied [QWZA01, DLT03, GM03, OS04]. In [HKLL02, DLT03], the authors addressed that the effectiveness of wavelets for damage localization is limited by the measurements precision and the sampling distances. They used the dynamic mode shapes extracted from the acceleration measurements. In [Zab05], the energy components of the wavelet decompositions of impulse response functions and the transmissibility functions is used for damage localization on Z24 Bridge. In [RW06], the estimated mode shapes of the beam structure are analysed by one and two dimensional continuous wavelet transform, where the location of the damage is indicated by a peak in the spatial variation of the transformed response.

In [LDD07], the combination method of empirical mode decomposition (EMD) and wavelet analysis is presented for the detection of changes in the structural response data in which the results demonstrated that the combination method of EMD and continuous wavelet transform can be used to identify the time more sharply and effectively at which structural damage occurs than by using the wavelet transform method alone. Fan and Qiao [FQ09], a 2-D continuous wavelet transform-based damage detection algorithm using Dergauss2d wavelet is presented where an isosurface of 2-D wavelet coefficients is generated to find the location and approximate shape (or area) of the damage, demonstrated by analyzing the numerical and experimental mode shapes of a cantilevered plate. Wei et all [CSQLSHYL17] developed a flexibility-based approach, utilizing the damage locating vectors (DLVs) method, for monitoring the seismic isolation system on a structure. This approach was established through a state-space ARX model to describe the measured responses and

the modal parameters were estimated by applying continuous Cauchy wavelet transform to the time series ARX model. Then they were used to identify the DLVs via the singular value decomposition of the flexibility change of structures before and after damage.

In [SCB17], the damage detection and localization algorithm is presented where the damage detection algorithm used wavelet coefficients to detect anomalies in mode shapes of the beam. In order to obtain a good estimate of the wavelet coefficients and minimize the effects of experimental uncertainties, the measurements were repeated several times for each state of damage. Chen et all [YO17] presents a new damage indicator and a damage estimator based on multiple mode biorthogonal wavelet coefficients are designed to locate and evaluate the internal defects. In [Rak17], the author presents the application of the discrete dyadic wavelet transform (DDWT) that has a fast transform algorithm to detect and localize the response signal features due to cracks in mechanical and civil structures.

Beside this, numerous authors combined the wavelet-based algorithms with artificial neural networks (ANN) for improvement the detection and localization ability. Yam et al. [YYJ03] combined wavelet-based algorithm with ANN to improve the damage identification in sandwich structures, Rucka and Wilde [RW06] proposed a combination of wavelet transform with ANN for the improvement of damage identification ability for structural damage, while Hein and Feklistova [HF11] used such a combination for estimation of damage indices, which describe the delamination occurrence in composite structures.

1.4.3 Damage quantification methods

Compared to detection and localization, methods for damage quantification are the least developed in the literature [FQ11]. Quantification may be carried out together with damage localization in the context of updating FE model parameters [BXHX01, Fri07], but inherits the problem of possible ill-posedness in this case. However, if damage is located first (using any damage localization method) and a precise FE model is available, model updating may be a feasible solution to damage quantification. Further methods include e.g. pattern recognition techniques based on classification principles [AA16]. Alternatively, solving the localization problem first to identify the subset of changed parameters, and estimating their change in a separate second step for damage quantification, yields in general better conditioned methods, for example as is in [Ber14].

In [DMZ16], both damage localization and quantification have been investigated in a sensitivity-based approach based on the local approach using output-only data. A damage-sensitive parameterization of the system is used, referring e.g. to the element stiffnesses in a finite element model. Through sensitivity analysis with respect to this parameterization, damage is first localized by statistical tests, and then damage is quantified only for the localized element. If a parameter is assumed to be changed, i.e. damage is located in the respective element, then damage can finally be quantified based on an estimation of the parameter change. A similar sensitivity-based statistical framework has been shown recently for damage localization using a subspace residual in PhD thesis [All17], where it has been applied in a real test case of a four-story steel frame structure, the Yellow Frame at the University of British Columbia.

1.5 Conclusion

In this chapter, different methods for damage detection, localization and quantification were presented from the literature. In the following chapters, the deterministic damage localization approaches and the statistical damage localization methods with their application to structural vibration analysis are investigated. In chapters 2-4, the background of these methods from existing literature is explained in detail, before developing the new methods in Chapters 5-7 and their applications to vibration analysis are demonstrated in chapters 8-13.

Chapter 2

Background of deterministic damage localization approaches

2.1 Introduction

Vibration based damage localization has become an important issue for Structural Health Monitoring (SHM) such as aerospace, automotive, bridges, buildings, and offshore structures. Sensors installed on the structure collect data and then the modal parameters (damping ratios, natural frequencies and mode shapes) can be estimated. Those parameters are meaningful for the monitoring of the structure and damage localization is possible, when linking these changes in a Finite Element (FE) model of the structure.

Several damage localization methods have been described in the state of art from the literature [Ber02, Ber10, Ber14]. Belonging to the latter category, both the Stochastic Dynamic Damage Locating Vector (SDDLV) [Ber10] and the Influence Line Damage Localization (ILDL) [Ber14] approach is a vibration-based damage localization technique using both finite element information and estimated modal parameters from output data. From estimates of the system matrices in both reference and damaged states, the null space of the difference between the respective transfer matrices is obtained. Then, in the SDDLV, damage is related to a residual derived from this null space and located where the residual is close to zero. This is a theoretically sound method that evaluates the transfer matrix difference between reference and damaged states of a structure, without updating the FE model. A complementary approach to the SDDLV is the Influence Lines Damage Localization (ILDL) [Ber14]. There, damage location is determined from the subspace angle of each position in the structure by computing the column space of the change in flexibility and a known FE model.

In this chapter, the theoretical background of the SDDLV and ILDL approaches is described in details in Sections 2.2 and 2.3 based on [Ber10] and [Ber14].

2.2 The Stochastic Dynamic Damage Location Vector (SDDLV) approach

The Stochastic Dynamic Damage Locating Vector (SDDLV) approach is an output-only damage localization method based on interrogating changes $\delta G(s)$ in the transfer matrix $G(s)$ of a system in both undamaged and damaged states [Ber10]. These changes δG are linked to physical properties of the structure. The structural failure is indicated by losses of stiffness and the consequent damage is confined to some part or a region of the structure, affecting the flexibility of the system, which is linked to δG. A vector is obtained in the null space of $\delta G(s)$ from system identification results using output-only measurements corresponding to both states. Then this load vector is applied to the Finite Element (FE) model of the structure for the computation of a stress field over the structure. The stresses are measures of internal reactions to external forces applied on a deformable body. Damage localization is related to this stress field where the computed stress is zero or close to zero in practice [Ber02, Ber06, Ber07, Ber10]. The property of the vectors in the null space that is relevant for damage localization is the fact that these vectors, when treated as loads on the system, lead to stress fields that it creates in the undamaged system is null over the damaged region. Therefore, the basic idea is that the intersection of the null stress regions corresponding to the load distributions defined by the null space of δG can be used to localize the damage.

In the following section, the deterministic computation of the stress field and the aggregation of results is summarized.

2.2.1 Dynamic modeling of structure

The behavior of a mechanical structure can be described by a linear time-invariant (LTI) dynamic system

$$M\ddot{\mathcal{X}}(t) + C\dot{\mathcal{X}}(t) + K\mathcal{X}(t) = f(t) \tag{2.1}$$

where M, C, $K \in \mathbb{R}^{d\times d}$ are the mass, damping and stiffness matrices, respectively, t indicates continuous time and $\mathcal{X} \in \mathbb{R}^d$ denotes the displacements at the d degrees of freedom (DOF) of the structure. The external force $f(t)$ is not measurable and modeled as white noise. Let the dynamic system (2.1) be observed at r coordinates. Since $f(t)$ is unmeasured (1.1), it can be substituted with a fictive force $e(t) \in \mathbb{R}^r$ acting only in the measured coordinates and that regenerates the measured output. Furthermore, defining $x = [\mathcal{X} \quad \dot{\mathcal{X}}]^T$, this leads to the corresponding continuous-time state-space model

$$\begin{cases} \dot{x}(t) = A_c x(t) + B_c e(t) \\ y(t) = C_c x(t) + D_c e(t) \end{cases} \tag{2.2}$$

with state vector $x \in \mathbb{R}^n$, output vector $y \in \mathbb{R}^r$, the state transition matrix $A_c \in \mathbb{R}^{n\times n}$ and output matrix $C_c \in \mathbb{R}^{r\times n}$, where $n = 2d$ is the system order and r is the number of outputs. Since the input of the system is replaced by the fictive force $e \in \mathbb{R}^r$, the input influence matrix and direct transmission matrix are of size $B_c \in \mathbb{R}^{n\times r}$ and $D_c \in \mathbb{R}^{r\times r}$ respectively. However, only the system matrices A_c and C_c are relevant from output-only system identification, and the non-identified matrices B_c and D_c will only be needed in the

derivation of estimates related to the transfer matrix. From Stochastic Subspace Identification (SSI) [VODM96, PDR99, DM12], estimates $\widehat{A}_c$ and $\widehat{C}_c$ can be obtained from output only measurements, details are given in Chapter 3.

Since $y(t)$ is the output vector of the model in (2.2), it can be measured from displacements $y(t)$, velocities $\dot{y}(t)$ or accelerations $\ddot{y}(t)$ sensors. Hence, it can be simplified for the respective displacements ($disp$), velocity (vel) or acceleration (acc) as

$$y(t) = C_c^{disp} x, \tag{2.3}$$

$$\dot{y}(t) = C_c^{vel} x, \tag{2.4}$$

$$\ddot{y}(t) = C_c^{acc} x + D_c e, \tag{2.5}$$

where the C_c^{disp}, C_c^{vel}, and $C_c^{acc} \in \mathbb{R}^{r \times n}$ are the ouput mapping matrices. By differentiating (2.3) and combining with (2.2) corresponds to

$$\dot{y}(t) = C_c^{disp} \dot{x}(t) = C_c^{disp}(A_c x(t) + B_c e(t)), \tag{2.6}$$

and then, the following expression is obtained by comparing with (2.4)

$$C_c^{vel} = C_c^{disp} A_c, \tag{2.7}$$

Similarly, by taking differentiation of (2.4), and replacing $\dot{x}(t)$ as

$$\ddot{y}(t) = C_c^{vel} \dot{x}(t) = C_c^{disp} A_c (A_c x(t) + B_c e(t)), \tag{2.8}$$

and then follows with (2.5)

$$C_c^{acc} = C_c^{disp} A_c^2. \tag{2.9}$$

Now, taking a Laplace transform of (2.2) and (2.3) and combining the results, the force-displacement transfer matrix of the system (2.2) can be obtained as

$$G(s) = C_c^{disp}(sI - A_c)^{-1} B_c \in \mathbb{C}^{r \times r}. \tag{2.10}$$

Likewise, the transfer matrix of the system (2.2) can be obtained for velocity measurements after taking a Lapalce transform of (2.2) and (2.4), and combining the resutls as

$$G(s) = C_c^{disp} A_c^{-1}(sI - A_c)^{-1} B_c \in \mathbb{C}^{r \times r}, \tag{2.11}$$

and finally, for acceleration measurements, the transfer matrix of the system (2.2) can be obtained by taking a Laplace tranform of (2.2) and (2.5) ,

$$G(s) = C_c^{disp} A_c^{-2}(sI - A_c)^{-1} B_c \in \mathbb{C}^{r \times r}. \tag{2.12}$$

2.2.2 Computation of damage indicator

The damage indicator is based on the transfer matrix difference $\delta G(s)$ between reference and damaged states. However, depending on the output measurements y, the transfer matrix of the system (2.2) derived in (2.10)-(2.12) for the respective ouptut measurements of displacement, velocity or acceleration writes as

$$G(s) = C_c A_c^{-z}(sI - A_c)^{-1} B_c \in \mathbb{C}^{r\times r}, \tag{2.13}$$

where C_c is defined for C_c^{disp}, C_c^{vel}, or C_c^{acc}, and $z = 0, 1$, or 2 respectively. Matrix B_c can be replaced by using the relationships [Ber06, Ber10]. Differentiating (2.3) and (2.4), the following derivation can be found as

$$\dot{y}(t) = C_c^{disp}\dot{x}(t),$$
$$\ddot{y}(t) = C_c^{vel}\dot{x}(t),$$

and then, combining the result with $\dot{x}(t)$ in (2.2) and (2.5) corresponds as

$$C_c^{vel}x(t) = C_c^{disp}(A_c x(t) + B_c e(t)), \tag{2.14}$$

and

$$C_c^{vel}(A_c x(t) + B_c e(t)) = C_c^{acc}x + D_c e. \tag{2.15}$$

Now comparing the term B_c from expression (2.14) separately, and then combination with (2.7) and (2.9) follows

$$C_c^{disp}B_c = 0, \tag{2.16a}$$
$$C_c^{vel}A_c^{-1}B_c = 0, \tag{2.16b}$$
$$C_c^{acc}A_c^{-2}B_c = 0. \tag{2.16c}$$

Similarly, comparing the term B_c from expression (2.15) and then following (2.7) and (2.9), we can write as

$$C_c^{vel}B_c = D_c, \tag{2.17a}$$
$$C_c^{disp}A_c B_c = D_c, \tag{2.17b}$$
$$C_c^{acc}A_c^{-1}B_c = D_c. \tag{2.17c}$$

Following expression (2.16) and (2.17), we can conclude as

$$C_c A_c^{-z} B_c = 0, \tag{2.18}$$
$$C_c A_c^{1-z} B_c = D_c, \tag{2.19}$$

recall that C_c is defined for C_c^{disp}, C_c^{vel}, or C_c^{acc}, and $z = 0, 1$, or 2 for the respective ouptut measurements of displacement, velocity or acceleration, and formulating the least-squares problem with (2.18) and (2.19)

$$\begin{bmatrix} C_c A_c^{1-z} \\ C_c A_c^{-z} \end{bmatrix} B_c = \begin{bmatrix} I \\ 0 \end{bmatrix} D_c,$$

which has a solution for B_c under the condition that the system order satisfies $n \leq 2r$, i.e. the number m of identified modes satisfies $m \leq r$. Then it follows,

$$B_c = \begin{bmatrix} C_c A_c^{1-z} \\ C_c A_c^{-z} \end{bmatrix}^{\dagger} \begin{bmatrix} I \\ 0 \end{bmatrix} D_c,$$

where † denotes the Moore-Penrose pseudoinverse. With the property of $(A^{-z})^{\dagger} = A^{z}$ and based on the relation of $A_c^{-z}(sI - A_c)^{-1}A_c^{z} = (sI - A_c)^{-1}$, the expression of (2.13) can be simplified as [Ber06, Ber10]

$$G(s) = R(s)D_c,$$

where

$$R(s) = C_c(sI - A_c)^{-1} \begin{bmatrix} C_c A_c \\ C_c \end{bmatrix}^{\dagger} \begin{bmatrix} I \\ 0 \end{bmatrix}. \tag{2.20}$$

In (2.20), s is the Laplace variable in the complex plane, I is the identity matrix of size $r \times r$, 0 is the zero matrix of size $r \times r$, and † denotes the Moore-Penrose pseudoinverse.

The computation of $R(s)$ in equation (2.20) holds at the same time for displacement, velocity and acceleration measurements [MDBM15]. The difference between the transfer matrices in both damaged (variables with tilde) and healthy states is $\delta G(s) = \tilde{G}(s) - G(s)$. Damage is considered as changes in the stiffness of system (2.1), while mass remains unchanged. Then, assuming $\delta D_c = \tilde{D}_c - D_c = 0$ (corresponding to no mass change) and D_c being invertible, the matrices $\delta G(s)$ and $\delta R(s)^T = \tilde{R}(s)^T - R(s)^T$ have the same null space [Ber10]. The desired load vector $v(s)$ is obtained from the null space of the $\delta R(s)^T$ from Singular Value Decomposition (SVD)

$$\delta R(s)^T = U\Sigma V^H = \begin{bmatrix} U_1 & U_2 \end{bmatrix} \begin{bmatrix} \Sigma_1 & 0 \\ 0 & \Sigma_2 \end{bmatrix} \begin{bmatrix} V_1 & V_2 \end{bmatrix}^H, \tag{2.21}$$

where $U, \Sigma, V \in \mathbb{C}^{r \times r}$, $\Sigma_2 \approx 0$ and ^{H} indicates the conjugate transpose. Let n_{im} be the dimension of the image U_1 and $(r - n_{\text{im}})$ be the dimension of the null space V_2, where n_{im} depends on the kind and number of damaged elements [Ber02]. For damage localization, the property of the vectors in V_2 is meaningful and it is applied as a loads on the system that yields zero stress fileds over the damaged elements. For example, in a mass-chain system, assume number of damage element is 1 at d DoFs system including r sensors coordinates. In this case, the dimension of the image U_1 is 1 and hence $(r - 1)$ are the column of the null space vectors V_2. The load vector $v(s)$ in the null space of $\delta R(s)^T$ can be chosen as any linear combination of the vectors in V_2, particularly as the vector corresponding to the smallest singular value. Note that only output data is necessary for the computation of an estimate of $v(s)$.

To compute stress field, load vector $v(s)$ is applied to the FE model of the structure (see details in subsection 2.2.3). Let l_k be the number of all stresses that are computed at the elements of the structure. The displacements at all Degrees Of Freedoms (DOFs) are computed from the load vector $v(s)$ at the sensor coordinates and then, stresses are computed at all the elements of the FE model from the displacements. This stress is obtained through

a linear relation to $v(s)$ by the matrix $L_{model}(s) \in \mathbb{C}^{l_k \times r}$ from FE model of the structure [Ber10, DMBM13] and for a chosen s satisfies

$$S(s) = L_{model}(s)v(s). \tag{2.22}$$

Theoretically, the stress vectors $S(s)$ indicate damage [Ber02, Ber10] where entries in $S(s)$ close to zero indicate potentially damaged elements. However, these stresses are not exactly zero but small in practice because of modal truncation, model errors and uncertainties from measurements. While the load vector $v(s)$ is only defined at the sensor coordinates, the damage can be located at any element of the structure because the stress vector computed from load vector $v(s)$ covers the full domain.

2.2.3 Linear relation between load and stress

After Laplace transformation of the mechanical model in (2.1) the model-based transfer matrix can be written as

$$Gmodel(s) = (Ms^2 + Cs + K)^{-1}, \tag{2.23}$$

which relates loads to the displacements of the d Degrees of Freedom (DoFs) of the structure. Define $P \in \mathbb{R}^{d \times r}$ is the sensor mapping matrix that containing zeros and ones from where the row and the column of an entry 1 relate to a sensor position and its corresponding to the degree of freedom (DOF) of the model. Let, $Z(s)$ is the displacement vector which has been obtained after applying load vector $v(s)$ to the model at the sensor coordinate P with (2.23) as

$$Z(s) = Gmodel(s) \times P \times v(s). \tag{2.24}$$

After applying displacements $Z(s)$ at all DoFs, generates the internal stresses $S(s)$ to all elements of the model such as

$$S(s) = \begin{bmatrix} S_1 \\ \vdots \\ S_m \end{bmatrix}, \tag{2.25}$$

where m be the number of element and number of stresses/element depends on kind of the structure. These stresses gives a linear relation with displacements such as $S(s) = QZ(s)$, where Q is a matrix that is not explicitly computed. Then matrix L_{model} is defined as

$$L_{model}(s) = Q \times Gmodel(s) \times P \tag{2.26}$$

and satisfies with (2.22) and (2.24) and links to the computed loads to the desired stress field by $S(s) = L_{model}v(s)$. Now, describing the computation of L_{model} in practice. Define a unit

load vector as

$$v_i = \begin{bmatrix} 0 \\ \vdots \\ 0 \\ 1 \\ 0 \\ \vdots \\ 0 \end{bmatrix} \in \mathbb{R}^{r\times 1},$$

where i-th element is 1. Then compute the nodal displacements as described in (2.24) for each of the unit load vector v_i, $i = 1, ..., r$ and then, the resulting stresses $s(s)_i$ are computed for each of the elements of the FE model from the displacements. This stress satisfies a linear relation to $v_i(s)$ by the matrix $L_{model}(s) \in \mathbb{C}^{l_k\times r}$ from FE model of the structure [Ber10, DMBM13] with

$$S(s)_i = L_{model}(s)v_i. \tag{2.27}$$

Due to this relationship, by applying a unit load vector to the model, the computed stress at the end must be i-th column of the desired matrix L_{model}, and then $L_{model}(s)$ will be the column of the stress resultants $S(s)_i$. Finally, the complete L_{model} of the structure can be obtained from $[S(s)_1, ..., S(s)_r]$ of unit load vector v_i, $i = 1, ..., r$.

2.2.4 Multiple stress vector and aggregation for robustness

Due to truncation and model errors, it is recommended to compute the load vector $v(s)$ and the resulting stress $S(s)$ for several s-values s_w, $w = 1, \ldots, \kappa$, and to aggregate results. To minimize error, the s-values should be chosen in the vicinity of the identified poles of the system but not too close to them [Ber10]. After identification of the system matrices in both states, the computations of (2.21)-(2.22) are repeated for each s_w to get the respective stress vectors $S(s_w)$. For multiple s-values, a deterministic stress aggregation is obtained for each element t as

$$\bar{S}_t = \sum_{w=1}^{\kappa} |S_t(s_w)| \tag{2.28}$$

2.2.5 Example

As a basic sample, the SDDLV approach has been applied on a simple structure of three elements as shown in Figure 2.1. The stiffness parameters are $k_1 = k_2 = k_3 = 1$, and the mass of all elements is 1 in suitable units.

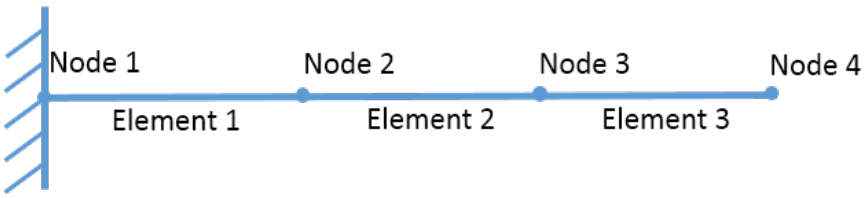

Figure 2.1 – Finite element model with 3 DOFs

The stiffness matrix of the healthy structure can be obtained as follows,

$$K_h^f = \frac{ES}{L}\begin{bmatrix} 1 & -1 & 0 & 0 \\ -1 & 2 & -1 & 0 \\ 0 & -1 & 2 & -1 \\ 0 & 0 & -1 & 1 \end{bmatrix} \tag{2.29}$$

where E, S, L is 1 in suitable units. Considering the damage model of Mazars [MPC89, MBR90], the stiffness matrix of the damaged structure can be obtained as $K_d = (1 - D)K_h$, where D is the damage parameter of the Mazars model $D \in [0, 1]$ in which 0 indicates the safe structure and 1 indicates fully damaged structure. In this sample, damage is simulated at element 2 with factor $D = 0.5$ and then the stiffness matrix K_d of the damaged structure can be obtained as follows,

$$K_d^f = \frac{ES}{L}\begin{bmatrix} 1 & -1 & 0 & 0 \\ -1 & 1.5 & -0.5 & 0 \\ 0 & -0.5 & 1.5 & -1 \\ 0 & 0 & -1 & 1 \end{bmatrix} \tag{2.30}$$

Since the structure is clamped at node 1, the reduced stiffness matrices of the healthy and the damaged states are formulated from (2.29) and (2.30) as follows

$$K_h = \frac{ES}{L}\begin{bmatrix} 2 & -1 & 0 \\ -1 & 2 & -1 \\ 0 & -1 & 1 \end{bmatrix} \tag{2.31}$$

and

$$K_d = \frac{ES}{L}\begin{bmatrix} 1.5 & -0.5 & 0 \\ -0.5 & 1.5 & -1 \\ 0 & -1 & 1 \end{bmatrix} \tag{2.32}$$

In the following, the theoretical stress is computed from the exact modes of the FE model that are related to modal truncation, and the main purpose is to illustrate the difficulties in the stress computation for damage localization.

Considering all modes: All three modes of the structure can be identified from the model of the structure. Using these modes, the transfer matrix difference (2.21) is computed for $s = 0$ from the flexibility matrices in both healthy and damaged states of the structure,

$$\delta R = K_h^{-1} - K_d^{-1} = \begin{bmatrix} 0 & 0 & 0 \\ 0 & 1 & 1 \\ 0 & 1 & 1 \end{bmatrix}.$$

The desired load vector $v(s)$ is obtained in the null space of δR from Singular Value Decomposition (SVD)

$$\delta R = U\Sigma V^H = \begin{bmatrix} 0 & 0.2820 & -0.9594 \\ -0.7071 & -0.6784 & -0.1994 \\ -0.7071 & 0.6784 & 0.1994 \end{bmatrix} \begin{bmatrix} 2 & 0 & 0 \\ 0 & 0 & 0 \\ 0 & 0 & 0 \end{bmatrix} \begin{bmatrix} 0 & 0.0573 & 0.9984 \\ -0.7071 & -0.7059 & 0.0405 \\ -0.7071 & 0.7059 & -0.0405 \end{bmatrix} \tag{2.33}$$

Note that $U, \Sigma, V \in \mathbb{C}^{r\times r}$, $\Sigma_2 \approx 0$ and ^{H} indicates the conjugate transpose. Since the number of damaged element is 1, the dimension of the image $U_1 \in 3 \times 1$ and the dimension of the null space $V_2 \in 3 \times 2$. The load vector $v(s)$ in the null space of $DF(s)$ can be chosen as any linear combination of the vectors in $V_2(s)$, particularly as the vector corresponding to the smallest singular values.

Following Section 2.2.3, the $L_{model}(s)$ is obtained after applying unit load vectors to the FE model at all sensor coordinates,

$$L_{model} = \begin{bmatrix} 1 & 1 & 1 \\ 0 & 1 & 1 \\ 0 & 0 & 1 \end{bmatrix} \tag{2.34}$$

In order to get the stress field, the computed null space vectors $v_2(s)$ can be considered as the desired load vector $v(s)$ and then, it is applied to the L_{model}. Note that stress close to zero indicates the damaged element. To apply the first column vector of the null space V_2 to the L_{model}, yields

$$S(s) = \begin{bmatrix} 1 & 1 & 1 \\ 0 & 1 & 1 \\ 0 & 0 & 1 \end{bmatrix} \begin{bmatrix} 0.0573 \\ -0.7059 \\ 0.7059 \end{bmatrix} = \begin{bmatrix} 0.0573 \\ 0 \\ 0.7059 \end{bmatrix}. \tag{2.35}$$

and similarly, using the last column vector of the null space V_2, yields

$$S(s) = \begin{bmatrix} 1 & 1 & 1 \\ 0 & 1 & 1 \\ 0 & 0 & 1 \end{bmatrix} \begin{bmatrix} 0.9984 \\ 0.0405 \\ -0.0405 \end{bmatrix} = \begin{bmatrix} 0.9984 \\ 0 \\ -0.0405 \end{bmatrix}. \tag{2.36}$$

From results, it is seen that the damage is correctly located at element 2 for any linear combination of the null space vectors in V_2.

For modal truncation, when number of modes < number of sensors: For modal truncation, considering two identified modes out of three from the model. Using two identified modes, first, the transfer matrix (2.20) is computed at $s = 0$ in both healthy and damaged states where the system matrices A_c and C_c are obtained based on modal basis. Then, the transfer matrix difference (2.21) is obtained as follows

$$\delta R(s) = \begin{bmatrix} 0.0432 & -0.0117 & -0.0246 \\ -0.0117 & 0.9343 & 1.0861 \\ -0.0246 & 1.0861 & 0.9226 \end{bmatrix}.$$

Similar to previous section, the desired load vector $v(s)$ is obtained in the null space of δR from Singular Value Decomposition (SVD)

$$\delta R = U\Sigma V^H = \begin{bmatrix} 0.013 & 0.045 & 0.998 \\ -0.708 & -0.704 & 0.041 \\ -0.705 & 0.708 & -0.023 \end{bmatrix} \begin{bmatrix} 2.014 & 0 & 0 \\ 0 & 0.158 & 0 \\ 0 & 0 & 0.043 \end{bmatrix} \begin{bmatrix} 0.013 & -0.045 & 0.998 \\ -0.708 & 0.704 & 0.041 \\ -0.705 & -0.708 & -0.023 \end{bmatrix} \tag{2.37}$$

For the computation of stress, initially, the first column vector of the null space vectors V_2 is applied to the model,

$$S(s) = \begin{bmatrix} 1 & 1 & 1 \\ 0 & 1 & 1 \\ 0 & 0 & 1 \end{bmatrix} \begin{bmatrix} -0.0457 \\ 0.7041 \\ -0.7087 \end{bmatrix} = \begin{bmatrix} 0.0503 \\ 0.0046 \\ 0.7087 \end{bmatrix}. \tag{2.38}$$

and then the last column vector of the null space vector V_2 is applied to the model which yields,

$$S(s) = \begin{bmatrix} 1 & 1 & 1 \\ 0 & 1 & 1 \\ 0 & 0 & 1 \end{bmatrix} \begin{bmatrix} 0.9989 \\ 0.0415 \\ -0.0232 \end{bmatrix} = \begin{bmatrix} 1.0171 \\ 0.0182 \\ 0.0232 \end{bmatrix}. \tag{2.39}$$

For modal truncation $m < r$, it is seen that the smallest stress value corresponds to the damaged element 2.

For modal truncation, when number of modes = number of sensors: In this case, two sensors are located at elements 1 and 2, and therefore, only two identified modes out of three from the model could be used as the number modes cannot be bigger than the number of sensors, $m \leq r$. Based on this criterion, the transfer matrix (2.20) is computed at $s = 0$ in both states where the system matrices A_c and C_c are obtained based on modal basis. Then, the transfer matrix difference (2.21) is obtained as follows

$$\delta R = \begin{bmatrix} 1.0392 & -0.7954 \\ 1.3157 & 0.8609 \end{bmatrix}.$$

Then, the L_{model} computes from Section 2.2.3 after applying unit load vectors to the FE model at sensor coordinates 1 and 2,

$$L_{model} = \begin{bmatrix} 1 & 1 \\ 0 & 1 \\ 0 & 0 \end{bmatrix} \tag{2.40}$$

Similarly, in order to compute the stress field for damage localization, the load vector in the null space of δR is applied to the L_{model}, yields

$$S(s) = \begin{bmatrix} 1 & 1 \\ 0 & 1 \\ 0 & 0 \end{bmatrix} \begin{bmatrix} 0.8620 \\ -0.5069 \end{bmatrix} = \begin{bmatrix} 0.3552 \\ 0.5069 \\ 0 \end{bmatrix}. \tag{2.41}$$

For modal truncation when the number modes are equal to the output sensors, it is seen that the damage position cannot be correctly indicated anymore, which is due to modal truncation error.

2.3 The Influence Line Damage Localization (ILDL) approach

The Influence Line Damage Localization (ILDL) is an output-only damage localization method based on a Finite Element (FE) model of the structure and modal parameters from output-only measurements in the damaged and healthy states. In [Ber14], it is shown that the image of the change in flexibility $\delta F = \delta G(0)$ between damaged and reference states of a structure is a basis for the influence lines of stress resultants at the damaged locations. Damage is thus located at elements where the subspace angle between the image and the influence line computed from the FE model is zero (or small when δF is approximated). This localization approach is complementary to the SDDLV and shows its advantages especially with noisy output-only data from real experiments due to the use of different features for the localization.

An Influence Line (IL) is a plot of a quantity q as a function of the position of a unit load acting (at each position) in a predefined direction. For the ILDL this quantity q is the internal stress resultant S_j of an element j, e.g. the axial force in a truss bar, or the moment at some point in a beam. A classical result in structural analysis theory is the fact that the influence line for quantity q is equal to the deformed shape that the structure takes when the ability of the structure to resist quantity q is removed and a unit discontinuity that is work compatible with q is introduced [MDBM13].

It is shown in [Ber14] that if a structure is loaded by some arbitrary static distribution and damage appears, while the load remains constant, then the change in the deformation field, given some assumptions on the nature of the damage, will be identical to that due to the action of a stress resultant acting on a discontinuity at the damage location. From this result it is concluded that the change in the deformation field due to the damage has the shape of the IL for the stress resultant at the location of the damage, and the deformation field is in the span of the IL's for multiple damage locations. For example, in a beam, the

influence line is always the internal stress resultants (i.e. axial force and moments) S_t of an element t due to apply unit load at the sensors coordinates.

The image of the change in flexibility matrix $\delta F = \delta G(0)$ between damaged and reference states (variables with and without tilde) is the span for all possible differences in the deformation field due to damage on the strucure, and thus the image of δF is identical to the span of the influence lines associated with all the damaged locations. Hence, for the implementation of ILDL, the flexibility matrix δF and the influence lines are required to evaluate for any load in the sensor coordinates on the structure.

Therefore, for damage localization, the influence lines of stress resultants are computed at the sensor coordinates for all elements from a FE model of a reference state and then, the image of δF is obtained from output-only measurement data in both states. The localization is performed by checking each element of the FE model if its respective IL lies in the image of δF. The ILDL does not directly specify the location of the damage. Instead, it provides a scheme for decision, given any postulated damage position, if it is correct or not. This localization approach is complementary to the SDDLV approach, since the image and the null space are complementary subspaces. The damage location information in the null space is also contained in the image of δF.

In the following Section, the model parameters and the principles of ILDL are presented in details.

2.3.1 Modelling of the structure, parameters and flexibility matrix

As similar to subsection 2.2.1, the characteristics of a mechanical structure is assumed to be described by a linear time-invariant (LTI) dynamical system (2.1) and the corresponding continuous-time state-space model are given in details (2.2).

Following (2.20), the transfer matrix $G(s)$ of the system is obtained at $s = 0$ with [Ber14] where the flexibility matrix F is equal to the transfer matrix at $s = 0$,

$$F = G(0) = R(0)D_c, \quad \text{where} \quad R = C_c(sI - A_c)^{-1} \begin{bmatrix} C_c A_c \\ C_c \end{bmatrix}^{\dagger} \begin{bmatrix} I \\ 0 \end{bmatrix} \tag{2.42}$$

for the restriction of the system order $n \leq 2r$, I is the identity matrix of size r, 0 is the zero matrix, and † denotes the Moore-Penrose pseudoinverse.

The difference in the flexibility between damaged (variables with tilde) and reference state (variables without tilde) is $\delta F = \tilde{F} - F$. Since the direct transmission matrix is only a function of the mass and invariant for damage due to stiffness changes, the $\delta D_c = \tilde{D}_c - D_c = 0$ due to no mass change and D_c being invertible [Ber10], it follows that $\delta F = \delta R D$ (with $\delta R = \tilde{R} - R$). Hence, the image of δF is the same as the image of δR. The δR is computed from the output only data in the damage and reference states. After Singular Value Decomposition (SVD) of δR, it follows

$$\delta R = U \Sigma V^T = \begin{bmatrix} U_1 & U_2 \end{bmatrix} \begin{bmatrix} \Sigma_1 & 0 \\ 0 & \Sigma_2 \end{bmatrix} \begin{bmatrix} V_1 & V_2 \end{bmatrix}^T, \tag{2.43}$$

where $U, \Sigma, V \in \mathbb{C}^{r,r}$ and $\Sigma_2 \approx 0$ or closely zero in practice. Let t be the rank of the $\delta R \in \mathbb{R}^{r \times r}$

and $U_1 = [u_1, ...u_t] \in \mathbb{C}^{r\times t}$ be the image of δR in the SVD. Note that U_1 correspond to the nonzero singular values Σ_1, and U_2 corresponds to zero singular values Σ_2.

2.3.2 Computation of influence lines and damage localization

Let $v \in \mathbb{R}^r$ be any load vector at the sensor coordinates of the structure. From such a load, stress resultants can be computed from a FE model. Note that l be the number of all stresses that are computed at the elements of the structure. The relation between loads v and the vector of stress resultants S at the desired elements is linear (2.2.3) and can be expressed by a matrix $L_{model} \in \mathbb{R}^{l\times r}$ based on the FE model of the structure [DMBM13], satisfying $S = L_{model}v$, where $L_{model} = \begin{bmatrix} l_1^T \\ l_2^T \\ \vdots \\ l_l^T \end{bmatrix}$.

In the ILDL approach, the influence line (IL) of each stress resultant S_j (in vector S) is evaluated. IL of this stress resultant is function of the position of a unit load. Such way, applying the respective unit loads at the sensor coordinates to obtain the influence for an element j that corresponds to an entry S_j such as $S_j = l_j^T v$. So, applying v as the unit loads corresponding to the different sensor positions yields the entries of l_j, hence it is clear that l_j is actually the influence line.

For damage localization, the ILDL approach consists of checking if the IL l_j is contained in the subspace U_1. Note that l_j and U_1 are computed based on FE model of the reference state and output-only measurements data, respectively. In [Ber14], the subspace angle (at $s = 0$) is computed as

$$\phi_j = cos^{-1}\left(\frac{||U_1^T l_j||}{||l_j||}\right). \tag{2.44}$$

Therefore, damage is located at the elements where the subspace angle ϕ_j between image U_1 of the flexibility matrix δR and the influence line l_j of the FE model of the reference structure is zero or small in practice.

A slightly different damage indicator was proposed in [MDBM13, Mar13] for the purpose of uncertainty quantification since the subspace angle (2.44) is not derivable at $\phi_j = 0$. There, the indicator

$$\gamma_j = \frac{||U_1^T l_j||^2}{||l_j||^2}\ , \tag{2.45}$$

was used, where $U_1 = [u_1\ \dots\ u_t] \in \mathbb{C}^{r\times t}$, $t < r$ is an orthogonal matrix and $\gamma_j = 1$ indicates the perfect fit for the damage localization.

Chapter 3

Stochastic system identification and uncertainty quantification

3.1 Introduction

The Stochastic subspace identification has become very popular for the identification of linear time-invariant (LTI) systems from output only measurements taken from a system. In the past literature [BF85, VODM96, PDR99, BM07], an overview of subspace identification methods has been described. The subspace methods established a special interest in the field of aeronautical, civil and mechanical engineering during the last decade for modal analysis, particularly the identification of the modal parameters (frequency, damaping, and mode shapes) of structures. Therefore, in the context of vibration monitoring [HVdA99, MBG03, MGB03, MBB+06, BMCC10, DHMR14, MDBM15, DMZ16], the identification of an LTI system from output-only measurements is a basic requirement that allows particularly Finite Element Model updating and Structural Health Monitoring.

In Operational Modal Analysis, the identified modes does not contain only true modes of the structure but also spurious modes appear because of non-white noise and non-stationary excitation, low signal-to-noise ratio, or a bad selection of the model order. Using the stabilization diagram, the true system modes remain quite constant at different model orders while spurious modes change. However, when estimating the modal parameters for different system orders, the structural modes are assumed to stabilize when the model order increases and thus can be distinguished from these spurious noise modes in the well-known stabilization diagram procedure [PDR01, Bak11].

When estimated from a limited number of data samples using Stochastic Subspace Identification (SSI), not the "true" parameters of the system matrices are obtained, but estimates are naturally subject to variance errors depending on the data and the estimation method because of unknown noise inputs, measurement noise and finite data length. The uncer-

tainties in the estimates are penalizing the quality and precision of the damage localization results. The uncertainty analysis of the estimates from stochastic subspace identification are stated in the literature [RPDR08, DRDRK08, DLM13, DM13]. Measurements from aircraft load calibration are also subjected to uncertainties. In [GGB+13b, GGB+13a], the authors proposed that these uncertainties need to be taken into account to analyse impacts of uncertainties on the calibration. In this Chapter, the Stochastic subspace indentification algorithm is introduced from the background of literature and then, a variance analysis are described based on a sensitivity approach.

This chapter is organized as follows. In Section 3.2, the subspace identification algorithm is presented, and in Section 3.3, the derivations of the sensitivity for the estimated system matrices are explained.

3.2 The Stochastic Subspace Identification (SSI) algorithm

Consider the LTI systems described by a discrete-time state-space model from (1.5)

$$\begin{cases} x_{k+1} = A_d x_k + v_k \\ y_k = C_d x_k + w_k \end{cases}, \tag{3.1}$$

where the state $x \in \mathbb{R}^n$, the output vector $y \in \mathbb{R}^r$, $A_d = \exp(A_c\tau)$, $C_d = C_c$, τ is the time step, and v_k and w_k are the unobserved process and measurement noise, respectively. The parameter n defines the system order and r is the number of sensors output.

Throughout this work, the system matrices A_d and C_d are only interested to identify from the output-only measurements data, y_k. In Operational Modal Analysis, no observed inputs are available ($B = 0$, $D = 0$) and the identification of system is done using the output-only data (y_k). When some inputs (e_k) are observed, the deterministic-stochastic subspace identification algorithms can be used. In the literature [PDR99, BM07, DM12], there are exists several algorithm for Stochastic Subspace Identication (SSI). For the identification of the system matrices A_c and C_c of (2.2) and its eigenstructure, the following general framework has been described. Initially, we identify estimates of the system matrices $\widehat{A}_d$ and $\widehat{C}_d$ at different model orders from the measurements using covariance-driven subspace identification. Using noisy system, these model orders require to be relatively high and additionally noise modes appear in the results. From these results r identified mode pairs are selected in a so-called stabilization diagram, so that the condition of the system order $n \leq 2r$ is satisfied. After rejecting the noise modes, finally the corresponding eigenvalues of the continuous-time system and the mode shapes are used to get the desired estimates $\widehat{A}_c$ and $\widehat{C}_c$.

3.2.1 System identification

A sensor subset of so-called reference sensors or projection channels can be used to reduce the computational burden and to improve identification [PDR99], denoted by $y_k^{(\mathrm{ref})}$. Let the theoretical cross-covariance between the state and the reference outputs be $\mathcal{G} = \mathbf{E}(x_{k+1} y_k^{(\mathrm{ref})T})$ and the output covariance be $\mathcal{R}_i = \mathbf{E}(y_k y_{k-i}^{(\mathrm{ref})T}) = C_d A_d^{i-1} \mathcal{G}$, then the block Hankel matrix is

formulated as

$$\mathcal{H} = \begin{bmatrix} \mathcal{R}_1 & \mathcal{R}_2 & \dots & \mathcal{R}_q \\ \mathcal{R}_2 & \mathcal{R}_3 & \dots & \mathcal{R}_{q+1} \\ \vdots & \vdots & \ddots & \vdots \\ \mathcal{R}_{p+1} & \mathcal{R}_{p+2} & \dots & \mathcal{R}_{p+q} \end{bmatrix} = \text{Hank}(\mathcal{R}_i). \tag{3.2}$$

It has the factorization property $\mathcal{H} = \mathcal{O}\mathcal{C}$ into the matrices of observability and controllability

$$\mathcal{O} = \begin{bmatrix} C_d \\ C_d A_d \\ \vdots \\ C_d A_d^p \end{bmatrix} \quad \text{and} \quad \mathcal{C} = \begin{bmatrix} \mathcal{G} & A_d\mathcal{G} & \dots & A_d^{q-1}\mathcal{G} \end{bmatrix},$$

respectively. From $\mathcal{O}$, the observation matrix C_d is obtained in its first block row. Using the shift-invariance property of $\mathcal{O}$, the matrix A_d is obtained based on least squares solution

$$A_d = \mathcal{O}^{\uparrow\dagger}\mathcal{O}^{\downarrow}, \tag{3.3}$$

where the last and the first block row has been eliminated in $\mathcal{O}^{\uparrow}$ and $\mathcal{O}^{\downarrow}$, and † denotes the Moore-Penrose pseudoinverse.

Using measurement data, the output covariance estimates $\widehat{\mathcal{R}}_i = 1/N \sum_{k=1}^{N} y_k y_{k-i}^{(\text{ref})T}$, $i = 1, \dots, p+q$, are computed to get the estimation of the Hankel matrix $\widehat{\mathcal{H}} = \text{Hank}(\widehat{\mathcal{R}}_i)$ in (3.2). From singular value decomposition (SVD) of $\widehat{\mathcal{H}}$, the observability matrix $\widehat{\mathcal{O}}$ is estimated and the system matrices $\widehat{A}_d$ and $\widehat{C}_d$ are obtained as above.

3.2.2 Modes

For the discrete-time system, the eigenvalues $\lambda_{d,l}$ and mode shapes φ_l are obtained from the system matrices A_d and C_d for each mode l, $l = 1, \dots, m$ as

$$\det(A_d - \lambda_{d,l} I) = 0, \quad A_d\phi_l = \lambda_{d,l}\phi_l, \quad \varphi_l = C_d\phi_l. \tag{3.4}$$

The respective eigenvalues of system matrix A_c (1.6) in the continuous-time system are retrieved as

$$\lambda_{c,l} = \frac{1}{\tau} \log(\lambda_{d,l}) \tag{3.5}$$

and the natural frequencies f_l and damping ratios ξ_l yield

$$f_l = \frac{|\lambda_{c,l}|}{2\pi\tau}, \quad \xi_l = \frac{-\Re(\lambda_{c,l})}{|\lambda_{c,l}|}. \tag{3.6}$$

In practice, the set of identified modes does not contain only true modes of the structure but also spurious modes because of non-white noise and non-stationary excitation, low signal-to-noise ratio, or a bad selection of the model order. In the stabilization diagram, the true system modes remain quite constant at different model orders while spurious modes change. Therefore, when estimating the modal parameters for different system orders, the structural modes can be distinguished from these spurious noise modes in the well-known stabilization diagram procedure.

3.2.3 Final system matrices

Let m be the number of mode pairs selected from the stabilization diagram, where number of modes $m \leq r$ to satisfy the restriction $n \leq 2r = 2m$. Let the identified modes are $(\lambda_{c,l}, \varphi_l)$ and $(\overline{\lambda_{c,l}}, \overline{\varphi}_l)$, $l = 1, \ldots, m$. Then, the system matrices can be written in the modal basis as $A_c = \text{diag}(\lambda_c^1, \ldots, \lambda_c^m, \overline{\lambda_c^1}, \ldots, \overline{\lambda_c^m})$ and $C_c = [\varphi_1 \ \ldots \ \varphi_m \ \overline{\varphi}_1 \ \ldots \ \overline{\varphi}_m]$ and defined up to a change of basis $(T^{-1}A_cT, C_cT)$. Finally, the system matrices in the real-valued modal basis can be written as

$$A_c = \begin{bmatrix} \Re(\Lambda_c) & \Im(\Lambda_c) \\ -\Im(\Lambda_c) & \Re(\Lambda_c) \end{bmatrix}, \quad C_c = \begin{bmatrix} \Re(\Phi) & \Im(\Phi) \end{bmatrix}, \tag{3.7}$$

where $\Lambda_c = \text{diag}(\lambda_c^1, \ldots, \lambda_c^m)$ and $\Phi = [\varphi^1 \ \ldots \ \varphi^m]$, obtained from the chosen modes.

3.3 Uncertainty quantification

In order to analyze the statistical uncertainty of identified parameters, it is essential to assess the quality of the estimates from the measurements. There are different kinds of uncertainty that can be considered, such as aleatory uncertainty that cannot be reduced, e.g. variability in a production process, and epistemic uncertainty that can be reduced by collecting more measurements [DKD09]. Throughout this thesis, epistemic uncertainty is considered that could indeed be reduced by analyzing longer datasets of vibration measurements. Note that the considered uncertainty is not linked to any uncertain parameters of a model, but stems directly from an estimation problem using finite and noisy measurements. In detail, the uncertainty of estimates based on a finite set of measurements y_k, $k = 1, ..., N$ modelled in (3.1) is due to measurement noise (related to w_k) and unknown excitation inputs (related to v_k and w_k). We analyze the resulting variance errors. Thus, when estimated from a limited number of data samples using Stochastic Subspace Identification (SSI), not the "true" parameters of the system matrices are obtained, but estimates are naturally subject to variance errors depending on the data and the estimation method because of unknown noise inputs, measurement noise and finite data length. The uncertainty analysis of the estimates from stochastic subspace identification are stated in the literature [RPDR08, DRDRK08, DLM13, DM13].

In this section, the variance analysis of the system matrices is done by a sensitivity analysis, starting from the covariance of the Hankel matrix. The expressions of the covariances of the Hankel matrix and observability matrix have been derived in [PGS07, RPDR08] and are recalled here for the sake of clarity.

3.3.1 Definitions of covariance computation

Define a covariance estimate $\hat{\Sigma}_{\mathcal{H}} = \text{cov}(\text{vec}(\mathcal{H}))$ of the Hankel matrix $\mathcal{H}$ from where $\text{vec}(\cdot)$ indicates the column stacking vectorization operator. Estimates of $\hat{\Sigma}_{\mathcal{H}}$ can be directly computed from the dataset by separating the available data length into several blocks of length. Let, the total data length N_t turned into n_b blocks of length $\mathcal{N}_b$. The Hankel matrix $\hat{\mathcal{H}}^{(k)} = \text{Hank}(\hat{\mathcal{R}}_i^{(k)})$ is computed on the output-correlations $\hat{R}_i^{(k)} = 1/\mathcal{N}_b \sum_{k=1+(k-1)\mathcal{N}_b}^{k\mathcal{N}_b} y_k y_{k-i}^{(\text{ref})T}$ on

each block, while the Hankel matrix on the entire dataset yields $\hat{\mathcal{H}} = \frac{1}{n_b}\sum_{k=1}^{n_b}\hat{\mathcal{H}}^{(k)}$. Finally, the covariance $\hat{\Sigma}_{\mathcal{H}}$ is estimated by the sample covariance

$$\hat{\Sigma}_{\mathcal{H}} = \frac{1}{n_b - 1}\sum_{k=1}^{n_b}\text{vec}\left(\hat{\mathcal{H}}^{(k)} - \hat{\mathcal{H}}\right)\text{vec}\left(\hat{\mathcal{H}}^{(k)} - \hat{\mathcal{H}}\right)^T.$$

Let $g(\widehat{\mathcal{H}})$ be a vector valued function of the parameter and its covariance can be obtained with Taylor approximation as

$$g(\widehat{\mathcal{H}}) = g(\mathcal{H}) + \mathcal{J}_{g,\mathcal{H}}\text{vec}(\widehat{\mathcal{H}} - \mathcal{H}) + O(||\text{vec}(\widehat{\mathcal{H}} - \mathcal{H})||^2)$$

and then, it can be simplified as

$$\text{cov}(g(\widehat{\mathcal{H}})) \approx \mathcal{J}_{g,\mathcal{H}}\widehat{\Sigma}_{\mathcal{H}}\mathcal{J}_{g,\mathcal{H}}^T, \tag{3.8}$$

where $\mathcal{J}_{g,\mathcal{H}} = \partial g(\mathcal{H})/\partial\text{vec}(\mathcal{H})$ is the sensitivity of the function g. Since the output covariances and the Hankel matrix are asymptotically Gaussian variables [Han70] (when number of measurements is large), the statistical delta method [CB02] ensures that expression (3.8) is asymptotically exact. The required sensitivity can be obtained analytically through a first-order perturbation $\triangle g$ of the function g, which yields

$$\triangle g = \mathcal{J}_{g,\mathcal{H}}\text{vec}(\triangle\mathcal{H}). \tag{3.9}$$

With this strategy, the covariance $\Sigma_{\mathcal{H}}$ of an estimate of Hankel matrix $\mathcal{H}$ can be propagated to any function of $\mathcal{H}$, particularly to the modal parameters and to the stress estimate $S(s)$.

Note that some of the matrices and vectors in the derivation of the damage localization approach are complex-valued variables. The following notation will be used. Define $\otimes$ is the Kronecker product with the property of $\text{vec}(AXB) = (B^T \otimes A)\text{vec}(X)$. I_a defines the identity matrix of size $a \times a$, and $0_{a,b}$ defines the zero matrix of size $a \times b$. Let $e_j^a \in \mathbb{R}^a$ is the j-th unit vector such as column j of I_a. For any matrix $X \in \mathbb{R}^{a\times b}$ [DM13], the permutation matrix $\mathcal{P}_{a,b} \overset{\text{def}}{=} \begin{bmatrix} I_a \otimes e_1^b & I_a \otimes e_2^a & \dots & I_a \otimes e_b^b \end{bmatrix} \in \mathbb{R}^{ab\times ab}$ is defined as

$$\text{vec}(X^T) = \mathcal{P}_{a,b}\,\text{vec}(X). \tag{3.10}$$

Finally, to deal with their uncertainties, define an equivalent real-valued notation for any matrix Q as

$$Q_{\text{Re}} \overset{\text{def}}{=} \begin{bmatrix} \Re(Q) & -\Im(Q) \\ \Im(Q) & \Re(Q) \end{bmatrix}, \quad Q_{\text{re}} \overset{\text{def}}{=} \begin{bmatrix} \Re(Q) \\ \Im(Q) \end{bmatrix}, \tag{3.11}$$

where $\Re(\cdot)$ and $\Im(\cdot)$ denote the real and imaginary parts, respectively.

3.3.2 Sensitivities on singular values and singular vectors

For real and complex values, the pertubation propagation to the singular values and vectors are described in [DM13].

For real case [DMBM13, Lemma.6], consider $X \in \mathbb{R}^{a\times b}$. Let $\sigma_i > 0$, u_i and v_i be the i-th singular value, left and right singular vector of the real matrix $X \in \mathbb{R}^{a\times b}$, and $\triangle X$ is a small perturbation on X. For the same X, then

$$\triangle\sigma_i = (v_i \otimes u_i)^T \text{vec}(\triangle X), \begin{bmatrix}\triangle u_i \\ \triangle v_i\end{bmatrix} = B_i^{\dagger} C_i \text{vec}(\triangle X),$$

where

$$B_i = \begin{bmatrix} I_a & (-X/\sigma_i \\ (-X^T)/\sigma_i & I_b \end{bmatrix}, C_i = 1/\sigma_i \begin{bmatrix} {v_i}^T \otimes (I_a - u_i {u_i}^T) \\ ({u_i}^T \otimes (I_b - v_i {v_i}^T))\mathcal{P}_{a,b} \end{bmatrix}$$

where I_a is identity matrix of size $a \times a$ and $\mathcal{P}_{a,b}$ is the permutation matrix as defined in (3.10).

For complex case [DMBM13, Lemma.7], consider $X \in \mathbb{C}^{a\times b}$. Let $\sigma_i > 0$, u_i and v_i be the i-th singular value, left and right singular vector of complex matrix $X \in \mathbb{C}^{a\times b}$ for rank t. After SVD of X,

$$X = U\Sigma V^H = \sum_{i=1}^{r} \sigma_i \bar{u}_i \bar{v}_i^H = \sum_{i=1}^{r} \sigma_i (e^{\mathrm{i}\phi_i} u_i)(e^{\mathrm{i}\phi_i} v_i)^H.$$

Let H be the Hermitian and ϕ_i be chosen such that the imaginary part of the first entry of $e^{\mathrm{i}\phi_i}\bar{v}_i$ and define the respective singular vectors by $u_i = e^{\mathrm{i}\phi_i}\bar{u}_i$ and $v_i = e^{\mathrm{i}\phi_i}\bar{v}_i$. The sensitivity of the singular vector yields as follows

$$\begin{bmatrix}\triangle(u_i)_{\text{re}} \\ \triangle(v_i)_{\text{re}}\end{bmatrix} = B_i^{\dagger} C_i \text{vec}(\triangle X)_{\text{re}},$$

$$\text{Where } B_i \overset{\text{def}}{=} \begin{bmatrix} I_{2a} & (-X)_{\text{Re}}/\sigma_i \\ (-X^T)_{\text{Re}}/\sigma_i) & I_{2b} \end{bmatrix} (I_{4r} - E^{4r,4r}_{3r+1,3r+1}),$$

$$C_i \overset{\text{def}}{=} 1/\sigma_i \begin{bmatrix} ({v_i}^T \otimes I_a)_{\text{Re}} - (u_i)_{\text{re}}((\bar{v}_i \otimes u_i)_{\text{re}})^T \\ (({u_i}^T \otimes I_b)_{\text{Re}} - (v_i)_{\text{re}}((\bar{u}_i \otimes v_i)_{\text{re}})^T)P_1 \end{bmatrix},$$

$$P_1 \overset{\text{def}}{=} \begin{bmatrix} \mathcal{P}_{a,b} & 0 \\ 0 & -\mathcal{P}_{a,b} \end{bmatrix}.$$

It is noted that the multiplication by $(I_{4r} - E^{4r,4r}_{3r+1,3r+1})$ sets the column in B_i to zero that corresponds to the imaginary part of the first entry of v_i.

3.3.3 Covariance estimation of the identified system matrices

For uncertainty computation, the covariance of the identified system matrices are necessary. In this section, the covariance estimation of the system matrices A_d and C_d using the covariance of the subspace matrix, $\mathcal{H}$ is recalled from [RPDR08, DM13]. The covariance estimation of the system matrices is derived in the following steps. Intially, a perturbation $\triangle\mathcal{H}$ of the

subspace matrix (3.2) is propagated to a perturbation $\triangle\mathcal{O}$ of the observability matrix. Then, a perturbation $\triangle\mathcal{O}$ is propagated to perturbations $\triangle A_d$ and $\triangle C_d$ on system matrices A_d and C_d. Finally, the covariances of the vectorized system matrices are computed. To obtain $\triangle\mathcal{O}$, the sensitivities of the singular values and vectors in (3.2) are necessary, details are stated in Section 3.3.2 with [PGS07, DMBM13].

In [RPDR08], the sensitivity of the observability matrix $\mathcal{O}$ is derived and the perturbation $\triangle\mathcal{O} = U_1 \triangle \Sigma_1^{1/2} + \triangle U_1 \Sigma_1^{1/2}$. Then, a perturbation $\triangle\mathcal{H}$ of the subspace matrix is propagated to a perturbation $\triangle\mathcal{O}$ of the observability matrix as

$$\mathrm{vec}(\triangle\mathcal{O}) = \mathcal{J}_{\mathcal{O},\mathcal{H}}\mathrm{vec}(\triangle\mathcal{H}),$$

where

$$\mathcal{J}_{\mathcal{O},\mathcal{H}} \overset{\text{def}}{=} \tfrac{1}{2}(I_n \otimes U_1\Sigma_1^{-1/2})S_4 \begin{bmatrix} (v_1 \otimes u_1)^T \\ \vdots \\ (v_n \otimes u_n)^T \end{bmatrix} + (\Sigma_1^{1/2} \otimes \begin{bmatrix} I_{(p+1)r} & 0_{(p+1)r\times qr} \end{bmatrix}) \begin{bmatrix} B_1^\dagger C_1 \\ \vdots \\ B_n^\dagger C_n \end{bmatrix}, \quad (3.12)$$

with $S_4 \overset{\text{def}}{=} \sum_{(k-1)n+k,k}^{n^2,n}$ and $\mathcal{J}_{\mathcal{O},\mathcal{H}} \in \mathbb{R}^{(p+1)rn\times(p+1)rqr_0}$. Note that B_i and C_i is already stated in Section 3.3.2.

The system matrix A_d is obtained from $\mathcal{O}$ (3.3) and C_d is obtained from the first block row of $\mathcal{O}$ in Section 3.2.1. Then, a perturbation $\triangle\mathcal{O}$ in $\mathcal{O}$ is propagated to the system matrices A_d and C_d where the respective sensitivities are obtained through [RPDR08]

$$\mathrm{vec}(\triangle A_d) = \mathcal{J}_{A_d,\mathcal{O}}\mathrm{vec}(\triangle\mathcal{O}), \quad \mathrm{vec}(\triangle C_d) = \mathcal{J}_{C_d,\mathcal{O}}\mathrm{vec}(\triangle\mathcal{O}),$$

where

$$\begin{aligned} \mathcal{J}_{A_d,\mathcal{O}} &\overset{\text{def}}{=} (I_n \otimes \mathcal{O}^{\uparrow\dagger}S_2) - (A_d^T \otimes \mathcal{O}^{\uparrow\dagger}S_1) + ((\mathcal{O}^{\uparrow\dagger}S_2 - A_d^T\mathcal{O}^{\uparrow T}S_2) \otimes (\mathcal{O}^{\uparrow T}\mathcal{O}^{\uparrow})^{-1})\mathcal{P}_{(p+1)r,n}, \\ \mathcal{J}_{C_d,\mathcal{O}} &\overset{\text{def}}{=} I_n \otimes \begin{bmatrix} I_r & 0_{r,pr} \end{bmatrix}, \end{aligned} \quad (3.13)$$

with $\mathcal{J}_{A_d,\mathcal{O}} \in \mathbb{R}^{n^2\times(p+1)rn}$ and $\mathcal{J}_{C_d,\mathcal{O}} \in \mathbb{R}^{rn\times(p+1)rn}$.

By using the product rule, the sensitivity of $A_d = \mathcal{O}^{\uparrow\dagger}\mathcal{O}^{\downarrow} = (\mathcal{O}^{\uparrow T}\mathcal{O}^{\uparrow})^{-1}\mathcal{O}^{\uparrow T}\mathcal{O}^{\downarrow}$ and the Kronecker algebra leads to the assertion. Note that $\mathcal{J}_{A_d,\mathcal{O}} = A_1$ and $\mathcal{J}_{C_d,\mathcal{O}} = A_2$ in [RPDR08]. Then, the covariances of the estimated system matrices (A_d, C_d) are obtained from (3.12) and (3.13) as

$$\hat{\Sigma}_{A_d,C_d} \overset{\text{def}}{=} \mathrm{cov}\left(\begin{bmatrix} \mathrm{vec}(A_d) \\ \mathrm{vec}(C_d) \end{bmatrix}\right) = \begin{bmatrix} \mathcal{J}_{A_d,\mathcal{O}} \\ \mathcal{J}_{C_d,\mathcal{O}} \end{bmatrix} \mathcal{J}_{\mathcal{O},\mathcal{H}}\hat{\Sigma}_{\mathcal{H}}\mathcal{J}_{\mathcal{O},\mathcal{H}}^T \begin{bmatrix} \mathcal{J}_{A_d,\mathcal{O}} \\ \mathcal{J}_{C_d,\mathcal{O}} \end{bmatrix}^T = \begin{bmatrix} \mathcal{J}_{A_d,\mathcal{H}} \\ \mathcal{J}_{C_d,\mathcal{H}} \end{bmatrix} \hat{\Sigma}_{\mathcal{H}} \begin{bmatrix} \mathcal{J}_{A_d,\mathcal{H}} \\ \mathcal{J}_{C_d,\mathcal{H}} \end{bmatrix}^T, \quad (3.14)$$

where $\hat{\Sigma}_{\mathcal{H}}$ is the covariance of the subspace matrix in Section 3.3.1.

3.3.4 Covariance estimation of the modal parameters

In [RPDR08], the derivation of the sensitivity for the eigenvalues and eigenvectors of a matrix and subsequently for the modal parameters are described, details are derived in [GVL96, PGS07].

Assume that $\lambda_{d,l}$, ϕ_l, and χ_l be the l-th eigenvalue, left and right eigenvector of A_d with

$$A_d\phi_l = \lambda_{d,l}\phi_l, \chi^* A_d = \lambda_{d,l}\chi_l^*, \tag{3.15}$$

where * defines the complex conjugate transponse. Then, a perturbation $\triangle A$ of A is propagated to $\lambda_{d,l}$ and ϕ_l,

$$\triangle\lambda_{d,l} = \mathcal{J}_{\lambda_{d,l},A_d}\text{vec}(\triangle A_d), \quad \triangle\phi_l = \mathcal{J}_{\phi_l,A_d}\text{vec}(\triangle A_d),$$

where

$$\mathcal{J}_{\lambda_{d,l},A_d} \overset{\text{def}}{=} \frac{1}{\chi_l^*\phi_l}(\phi_l^T \otimes \chi_l^*), \mathcal{J}_{\phi_l,A_d} \overset{\text{def}}{=} (\lambda_{d,l}I_n - A)^\dagger(\phi_l^T \otimes (I_n - \frac{\phi_l\chi_l^*}{\chi_l^*\phi_l})), \tag{3.16}$$

with $\mathcal{J}_{\lambda_{d,l},A_d} \in \mathbb{C}^{1\times n^2}$ and $\mathcal{J}_{\phi_l,A_d} \in \mathbb{C}^{n\times n^2}$.

The relationship between discrete and continuous time system is given in (3.5). Now, the continuous eigenvalue is recalled as

$$\lambda_{c,l} \overset{\text{def}}{=} \log(\lambda_{d,l})/\tau,$$

where τ is time step. Then, a perturbation $\triangle\lambda_{d,l}$ in $\lambda_{d,l}$ is propagated to $\lambda_{c,l}$,

$$\triangle\lambda_{c,l} = \mathcal{J}_{\lambda_{c,l},A_d}\triangle\lambda_{d,l},$$

where

$$\mathcal{J}_{\lambda_{c,l},A_d} \overset{\text{def}}{=} \frac{1}{\triangle t|\lambda_{d,l}|^2}\begin{bmatrix}\Re(\mathcal{J}_{\lambda_{d,l}}) & -\Im(\mathcal{J}_{\lambda_{d,l}})\\ \Im(\mathcal{J}_{\lambda_{d,l}}) & \Re(\mathcal{J}_{\lambda_{d,l}})\end{bmatrix} \tag{3.17}$$

Therefore, the natural frequency f_l and the damping ratio ζ_l is recalled from (3.5)-(3.6), assume that the element t of the mode shape φ_l is scaled to unity that $\varphi_l = \frac{C_d\phi_l}{(C_d\phi_l)_t}$. Then, its sensitivity is derived as a perturbation $\triangle A_d$, $\triangle C_d$ is propagated to φ_l,

$$\triangle\varphi_l = \mathcal{J}_{\varphi_l,A_d,C_d}\begin{bmatrix}\text{vec}(\triangle A_d)\\ \text{vec}(\triangle C_d)\end{bmatrix}$$

where

$$\mathcal{J}_{\varphi_l,A_d,C_d} \overset{\text{def}}{=} \frac{1}{(C_d\phi_l)_t}(I_r - \begin{bmatrix}0_{r,t-1} & \varphi_l & 0_{r,r-t}\end{bmatrix})\begin{bmatrix}C_d\mathcal{J}_{\phi_l,A_d} & \phi_l^T \otimes I_r\end{bmatrix}. \tag{3.18}$$

with $\mathcal{J}_{\varphi_l,A_d,C_d} \in \mathbb{C}^{r\times(n^2+rn)}$.

Finally, the covariances estimation of the modal parameters (i.e. eigenvalues and mode-shapes) can be computed from (3.14), (3.16), (3.17) and (3.18) as

$$\begin{aligned}\hat{\Sigma}_{\lambda_{c,l}} &= (\mathcal{J}_{\lambda_{c,l}}\mathcal{J}_{\lambda_{d,l},A_d})_{\text{Re}}\hat{\Sigma}_{A_d}((\mathcal{J}_{\lambda_{c,k}}\mathcal{J}_{\lambda_{d,l},A_d})_{\text{Re}})^T,\\ \hat{\Sigma}_{\varphi_l,A_d,C_d} &= (\mathcal{J}_{\varphi_l,A_d,C_d})_{\text{re}}\hat{\Sigma}_{A_d,C_d}((\mathcal{J}_{\varphi_k A_d,C_d})_{\text{re}})^T\end{aligned} \tag{3.19}$$

3.3.5 Covariance of system matrices A_c and C_c from subspace identification

For the covariance computation of A_c and C_c in (3.7), a perturbation $\Delta\mathcal{H}$ of the Hankel matrix in (3.2) is propagated to a perturbation $\Delta\lambda_{c,l}$ and $\Delta\varphi_l$ in the selected modes $l = 1, \dots, m$, yielding

$$\Delta\lambda_{c,l} = \mathcal{J}_{\lambda_{c,l},\mathcal{H}} \operatorname{vec}(\Delta\mathcal{H}), \quad \Delta\varphi_l = \mathcal{J}_{\varphi_l,\mathcal{H}} \operatorname{vec}(\Delta\mathcal{H}),$$

where the sensitivities $\mathcal{J}_{\lambda_{c,l},\mathcal{H}} \in \mathbb{C}^{1\times h}$ and $\mathcal{J}_{\varphi_l,\mathcal{H}} \in \mathbb{C}^{r\times h}$ with $h = (p+1)rqr_0$ has been derived in the combination of (3.17), (3.16), (3.18), (3.13), and (3.12), respectively, detailed in [RPDR08, DM13]. Now, plugging these expressions into (3.7) and vectorizing the system matrices corresponds to

$$\operatorname{vec}(\Delta A_c) = \mathcal{J}_{A_c,\mathcal{H}} \operatorname{vec}(\Delta\mathcal{H}), \quad \operatorname{vec}(\Delta C_c) = \mathcal{J}_{C_c,\mathcal{H}} \operatorname{vec}(\Delta\mathcal{H}), \tag{3.20}$$

where

$$\mathcal{J}_{A_c,\mathcal{H}} = P_1 \begin{bmatrix} \Re(\mathcal{J}_{\lambda_{c,1},\mathcal{H}}) \\ \vdots \\ \Re(\mathcal{J}_{\lambda_{c,m},\mathcal{H}}) \\ \Im(\mathcal{J}_{\lambda_{c,1},\mathcal{H}}) \\ \vdots \\ \Im(\mathcal{J}_{\lambda_{c,m},\mathcal{H}}) \end{bmatrix}, \; \mathcal{J}_{C_c,\mathcal{H}} = \begin{bmatrix} \Re(\mathcal{J}_{\varphi_1,\mathcal{H}}) \\ \vdots \\ \Re(\mathcal{J}_{\varphi_m,\mathcal{H}}) \\ \Im(\mathcal{J}_{\varphi_1,\mathcal{H}}) \\ \vdots \\ \Im(\mathcal{J}_{\varphi_m,\mathcal{H}}) \end{bmatrix}, \; P_1 = \begin{bmatrix} E_1 \\ \vdots \\ E_m \\ F_1 \\ \vdots \\ F_m \end{bmatrix},$$

and the selection matrix P_1 is defined in the following the matrices

$$E_j = \begin{bmatrix} e_j^m e_j^{m\,T} & 0_{m,m} \\ 0_{m,m} & -e_j^m e_j^{m\,T} \end{bmatrix}, \; F_j = \begin{bmatrix} 0_{m,m} & e_j^m e_j^{m\,T} \\ e_j^m e_j^{m\,T} & 0_{m,m} \end{bmatrix}.$$

Therefore, the covariance of the system matrices can be computed from (3.20) as

$$\Sigma_{A_c,C_c} \overset{\text{def}}{=} \operatorname{cov}\left(\begin{bmatrix} \operatorname{vec}(A_c) \\ \operatorname{vec}(C_c) \end{bmatrix} \right) = \begin{bmatrix} \mathcal{J}_{A_c,\mathcal{H}} \\ \mathcal{J}_{C_c,\mathcal{H}} \end{bmatrix} \Sigma_{\mathcal{H}} \begin{bmatrix} \mathcal{J}_{A_c,\mathcal{H}} \\ \mathcal{J}_{C_c,\mathcal{H}} \end{bmatrix}^T. \tag{3.21}$$

3.3.6 Sensitivity of the transfer matrix $R(s)$

In this section, the sensitivity $\mathcal{J}_{R(s),(A_c,C_c)}$ of the matrix $R(s)$ (2.20) with respect to the system matrices A_c and C_c (3.7) is recalled from [MDBM15], which is needed for the stress computation in (2.21)–(2.22). In the following, the sensitivity computation of $R(s)$ in (2.20) is derived. Define

$$Z(s) = C_c(sI - A_c)^{-1}, \quad H = \begin{bmatrix} C_c A_c \\ C_c \end{bmatrix}, \quad L = \begin{bmatrix} I \\ 0 \end{bmatrix},$$

such that $R(s) = Z(s)H^\dagger L$. Using the product rule, a perturbation $\Delta R(s)$ of $R(s)$ yields as

$$\Delta R(s) = [\Delta Z(s)]H^\dagger L + Z(s)[\Delta(H^\dagger)]L. \tag{3.22}$$

Now both terms $\Delta Z(s)$ and $\Delta(H^\dagger)$ are developed as functions of ΔA_c and ΔC_c, which are already stated in Section (3.3.3).

With the property $\Delta(X^{-1}) = -X^{-1}[\Delta X]X^{-1}$, the first term yields

$$\begin{aligned}\Delta Z(s) &= [\Delta C_c](sI - A_c)^{-1} - C_c(sI - A_c)^{-1}[\Delta(sI - A_c)](sI - A_c)^{-1} \\ &= [\Delta C_c](sI - A_c)^{-1} + Z(s)[\Delta A_c](sI - A_c)^{-1}. \end{aligned} \tag{3.23}$$

For the second term, a perturbation $\Delta(H^\dagger)$ of the pseudoinverse $H^\dagger$ yields

$$\operatorname{vec}(\Delta(H^\dagger)) = \mathcal{J}_{H^\dagger}\operatorname{vec}(\Delta H), \tag{3.24}$$

where the sensitivity $\mathcal{J}_{H^\dagger}$ is derived in [DMBM13, Lemma 8]. Denotes the selection matrices $S_1 \overset{\text{def}}{=} I_n \otimes [I_r \;\; 0_{r,r}]$, $S_2 \overset{\text{def}}{=} I_n \otimes [0_{r,r} \;\; I_r]$ such that

$$\operatorname{vec}(\Delta H) = \begin{bmatrix} S_1^T & S_2^T \end{bmatrix} \begin{bmatrix} \operatorname{vec}(\Delta(C_c A_c)) \\ \operatorname{vec}(\Delta C_c) \end{bmatrix} = S_1^T \operatorname{vec}(\Delta(C_c A_c)) + S_2^T \operatorname{vec}(\Delta C_c),$$

and then follows with (4.7)

$$\operatorname{vec}(\Delta(H^\dagger)) = \mathcal{J}_{H^\dagger} S_1^T \operatorname{vec}(\Delta(C_c A_c)) + \mathcal{J}_{H^\dagger} S_2^T \operatorname{vec}(\Delta C_c),$$

where $\Delta(C_c A_c) = [\Delta C_c]A_c + C_c[\Delta A_c]$. By combining this result with (4.5) and (4.6) yields

$$\operatorname{vec}(\Delta R(s)) = \begin{bmatrix} \mathcal{J}_{R(s),A_c} & \mathcal{J}_{R(s),C_c} \end{bmatrix} \begin{bmatrix} \operatorname{vec}(\Delta A_c) \\ \operatorname{vec}(\Delta C_c) \end{bmatrix},$$

where

$$\begin{aligned} \mathcal{J}_{R(s),A_c} &\overset{\text{def}}{=} \left(M(s)^T \otimes Z(s)\right) + \left(L^T \otimes Z(s)\right) \mathcal{J}_{H^\dagger} S_1^T (I_n \otimes C_c), \\ \mathcal{J}_{R(s),C_c} &\overset{\text{def}}{=} \left(M(s)^T \otimes I_r\right) + \left(L^T \otimes Z(s)\right) \mathcal{J}_{H^\dagger} \left(S_1^T (A_c^T \otimes I_r) + S_2^T\right), \end{aligned}$$

with $M(s) \overset{\text{def}}{=} (sI - A_c)^{-1} H^\dagger L$. After stacking the real and imaginary parts of $\operatorname{vec}(\Delta R(s)^T)$, it follows from (3.10) and (3.11)

$$(\operatorname{vec}(\Delta R(s)^T)) = \mathcal{J}_{R(s),A_c C_c} \begin{bmatrix} \operatorname{vec}(\Delta A_c) \\ \operatorname{vec}(\Delta C_c) \end{bmatrix}, \tag{3.25}$$

where

$$\mathcal{J}_{R(s),A_c,C_c} = \begin{bmatrix} \mathcal{P}_{r,r} & 0_{r^2,r^2} \\ 0_{r^2,r^2} & \mathcal{P}_{r,r} \end{bmatrix} \begin{bmatrix} \Re(\mathcal{J}_{R(s),A_c}) & \Re(\mathcal{J}_{R(s),C_c}) \\ \Im(\mathcal{J}_{R(s),A_c}) & \Im(\mathcal{J}_{R(s),C_c}) \end{bmatrix}.$$

Chapter 4

Statistical damage localization and quantification

4.1 Introduction

This Chapter presents the statistical damage localization and quantification based on the previous works [MDBM15, Mar13] and [DMZ16]. Firstly, the statistical damage localization method with the SDDLV approach is described. A full description of the SDDLV is available in Chapter 2 in Section 2.2. Particularly, the Stochastic Dynamic Damage Location Vector (SDDLV) method is an output-only damage localization method based on a Finite Element (FE) model of the structure and modal parameters from output-only measurements in the reference and damaged states of the system. A vector is obtained in the null space of the changes in the transfer matrix between both states and then applied as a load vector to the model. The damage location is related to this stress where it is close to zero. In [MDBM15, Mar13], the SDDLV method was extended with a statistical framework, where the robustness of the localization information was proposed by aggregating results at different s-values in the Laplace domain where the number of modes used could not be higher than number of sensors located on the structure.

Using noisy measurement data, the computed stresses are naturally afflicted with uncertainties. Then, a statistical evaluation of the computed stress is necessary to make a decision if stress is (close to) zero or not, in order to decide if the respective structural element is damaged or not. At the same time it allows a joint evaluation of the stress vectors computed on different s-values in statistical tests. For such an evaluation, the modal parameter covariance is propagated to the obtained stress vectors in a sensitivity-based approach. Robustness of the damage location is obtained by taking into account the information from multiple s-values in a joint statistical evaluation. Finally, all stress values corresponding to an element are being tested for damage in a hypothesis test where the computed stresses are evaluated

with their joint covariance.

Secondly, a sensitivity-based approach has been described for damage localization and quantification which operates on a data-driven residual vector that is statistically evaluated using information from a finite element (FE) model [DMZ16]. We consider the case of output-only vibration measurements of a structure subject to ambient excitation. Damages are considered as changes in the structural stiffness. The problems of damage localization and quantification are classified into two separate problems. First, the damaged elements are detected in statistical tests, and second, the damage is quantified only for the damaged elements.

This chapter is proposed as follows. In Section 4.2, the statistical damage localization approach with SDDLV is described based on [MDBM15] and a statistical framework is presented for both damage localization and quantification in Section 4.3 based on [DMZ16].

4.2 Statistical damage localization approach with SDDLV

The Stochastic Dynamic Damage Locating Vector (SDDLV) method is an output-only damage localization method based on both a Finite Element (FE) model of the structure and modal parameters estimated from output-only measurements in the damage and reference states of the system. A vector is obtained in the null space of the changes in the transfer matrix from both states at the sensor positions for some s-values in the Laplace domain and then applied as a load vector to the model. The damage location is related to this stress where it is close to zero. In [MDBM15, Mar13], the damage localization method is extended with a statistical framework, where the robustness of the localization information is proposed by aggregating results at different s-values in the Laplace domain. Then the uncertainty in the output-only measurements is propagated to the stress estimates at different values of the Laplace variable and these estimates are aggregated based on statistical principles.

In the following, the SDDLV approach is introduced as an output-only method for damage localization in Section 4.2.1 and then, the robust statistical approach for the aggregation of damage localization results is derived in Section 4.2.2 based on [MDBM15].

4.2.1 The SDDLV approach

In Section 2.2, the SDDLV approach is described in details. There, the transfer function $G(s) \in \mathbb{C}^{r\times r}$ of the system (2.1) at the sensor coordinates can be derived as from Section 2.2

$$G(s) = R(s)D_c,$$

where

$$R(s) = C_c(sI - A_c)^{-1}\begin{bmatrix} C_cA_c \\ C_c \end{bmatrix}^{\dagger}\begin{bmatrix} I \\ 0 \end{bmatrix}, \tag{4.1}$$

under the condition that the system order satisfies $n \leq 2r$, i.e. the number m of identified modes satisfies $m \leq r$. Note that $R(s)$ can be computed from output-only system identification, e.g. using stochastics subspace identification methods in Section 3.2. The difference between the transfer matrices in both damaged (variables with tilde) and healthy states is

$\delta G(s) = \tilde{G}(s) - G(s)$. The matrices $\delta G(s)$ and $\delta R(s)^T = \tilde{R}(s)^T - R(s)^T$ have the same null space [Ber10]. The desired load vector $v(s) \in \mathbb{C}^r$ is obtained from the null space of the $\delta R(s)^T$ using a Singular Value Decomposition (SVD)

$$\delta R(s)^T = U\Sigma V^H = \begin{bmatrix} U_1 & U_2 \end{bmatrix} \begin{bmatrix} \Sigma_1 & 0 \\ 0 & \Sigma_2 \end{bmatrix} \begin{bmatrix} V_1 & V_2 \end{bmatrix}^H, \tag{4.2}$$

where $U, \Sigma, V \in \mathbb{C}^{r \times r}$, $\Sigma_2 \approx 0$ and ^{H} indicates the conjugate transpose. Let n_{im} be the dimension of the image U_1 and $(r - n_{\text{im}})$ be the dimension of the null space V_2, where n_{im} depends on the kind and number of damaged elements. The load vector $v(s)$ in the null space of $\delta R(s)^T$ can be chosen as any linear combination of the vectors in V_2, particularly as the vector corresponding to the smallest singular value. Thus it can be estimated entirely on measurements in healthy and damaged states.

Finally, the load $v(s)$ is applied to the FE model of the healthy structure to compute stress field at all structural elements, stacked in vector $S(s)$, which yields a linear relationship and can be expressed by a matrix $L_{model}(s) \in \mathbb{C}^{l \times r}$ (2.2.3) based on the FE model of the structure, satisfying

$$S(s) = L_{model}(s)v(s). \tag{4.3}$$

The stress vector $S(s)$ indicates potential damage for elements with corresponding entries in $S(s)$ that are close to zero. When estimated, these stresses are not exactly zero but small in practice because of modal truncation, model errors and variance errors from measurements. Note that while the load vector $v(s)$ is only defined at the sensor coordinates, the damage can be located at any element of the structure because the stress vector computed from load vector $v(s)$ covers the full domain.

In the following, the deterministic aggregation (2.28) has been replaced by a statistical aggregation based on [MDBM15], where the intrinsic uncertainty of the stress estimation from finite measurement data is taken into account.

4.2.2 Uncertainty quantification and robust statistical approach

In the SDDLV approach, estimates of the modal parameters and then estimates of system matrices A_c and C_c are obtained in the damaged and undamaged states using SSI, derived in Section 3.2. Their identification is subject to variance errors because of unknown excitation, measurement noise and limited data length. The uncertainties in the estimates are penalizing the quality and precision of the damage localization results. For making decisions about damaged elements of the structure, these uncertainties need to be taken into account to decide whether stress of an element is significantly close to zero or not. In [DMBM13], the uncertainty propagation from system identification results generally to the stress $\widehat{S}(s_w)$ for a single value of the Laplace variable s_w was analyzed. In addition [MDBM15], the expressions for the uncertainty propagation to the stress vector $\widehat{S}(s_w)$ derived at multiple values s_w, $w = 1, \ldots, \kappa$.

In this section, the aggregation of the results and the joint evaluation of the different stress results is derived for each structural element in a statistical test. For the purpose of variance analysis, the definitions of the covariance computation is derived in Section 3.3.1. Therefore,

in the following, the sensitivity and covariance computation is derived for the theoretical values (e.g. $\mathcal{H}$, A_c, C_c, $S(s_w)$). Then estimates of the sensitivities and covariances are obtained by plugging in the estimates obtained from the data (e.g. $\widehat{\mathcal{H}}$, $\widehat{A}_c$, $\widehat{C}_c$, $\widehat{S}(s_w)$).

4.2.2.1 Covariance of system matrices A_c and C_c from subspace identification

In this section, the covariance of the system matrices A_c and C_c is computed for each selected mode $l = 1, \ldots, m$, starting from the identified eigenvalues $\lambda_{c,l}$ and mode shapes φ_l. Based on the SSI approach, their perturbation is linked to the Hankel matrix $\mathcal{H}$ by

$$\begin{aligned} \triangle\lambda_{c,l} &= \mathcal{J}_{\lambda_{c,l},\mathcal{H}}\mathrm{vec}(\triangle\mathcal{H}), \\ \triangle\varphi_l &= \mathcal{J}_{\varphi_l,\mathcal{H}}\mathrm{vec}(\triangle\mathcal{H}), \end{aligned}$$

where the sensitivity matrices $\mathcal{J}_{\lambda_{c,l},\mathcal{H}} \in \mathbb{C}^{1\times h}$ and $\mathcal{J}_{\varphi_l,\mathcal{H}} \in \mathbb{C}^{r\times h}$ with $h = \dim(\mathrm{vec}(\mathcal{H}))$ are detailed in Section 3.3.4. The system matrices A_c and C_c are assembled from the eigenvalues and mode shapes for each mode l as derived in Section 3.2.3. Then the sensitivities of the vectorized system matrices yield accordingly

$$\mathrm{vec}(\triangle A_c) = \mathcal{J}_{A_c,\mathcal{H}}\mathrm{vec}(\triangle\mathcal{H}), \tag{4.4a}$$

$$\mathrm{vec}(\triangle C_c) = \mathcal{J}_{C_c,\mathcal{H}}\mathrm{vec}(\triangle\mathcal{H}), \tag{4.4b}$$

where the sensitivities $\mathcal{J}_{A_c,\mathcal{H}}$ and $\mathcal{J}_{C_c,\mathcal{H}}$ are obtained from the eigenvalue and mode shape sensitivities $\mathcal{J}_{\lambda_{c,l},\mathcal{H}}$ and $\mathcal{J}_{\varphi_l,\mathcal{H}}$ as derived

$$\mathcal{J}_{A_c,\mathcal{H}} = P\begin{bmatrix} \Re(\mathcal{J}_{\lambda_{c,1},\mathcal{H}}) \\ \vdots \\ \Re(\mathcal{J}_{\lambda_{c,m},\mathcal{H}}) \\ \Im(\mathcal{J}_{\lambda_{c,1},\mathcal{H}}) \\ \vdots \\ \Im(\mathcal{J}_{\lambda_{c,m},\mathcal{H}}) \end{bmatrix}, \mathcal{J}_{C_c,\mathcal{H}} = \begin{bmatrix} \Re(\mathcal{J}_{\varphi_1,\mathcal{H}}) \\ \vdots \\ \Re(\mathcal{J}_{\varphi_m,\mathcal{H}}) \\ \Im(\mathcal{J}_{\varphi_1,\mathcal{H}}) \\ \vdots \\ \Im(\mathcal{J}_{\varphi_m,\mathcal{H}}) \end{bmatrix}, P = \begin{bmatrix} E_1 \\ \vdots \\ E_m \\ F_1 \\ \vdots \\ F_m \end{bmatrix},$$

and the selection matrix P is obtained with the following matrices

$$E_l = \begin{bmatrix} e_m^l e_m^{l^T} & 0_{m,m} \\ 0_{m,m} & -e_m^l e_m^{l^T} \end{bmatrix}, F_l = \begin{bmatrix} 0_{m,m} & e_m^l e_m^{l^T} \\ e_m^l e_m^{l^T} & 0_{m,m} \end{bmatrix}.$$

4.2.2.2 Sensitivity of the transfer matrix $R(s)$

In this section, the sensitivity $\mathcal{J}_{R(s),(A_c,C_c)}$ of the matrix $R(s)$ (2.20) with respect to the system matrices A_c and C_c (3.7) is recalled from [MDBM15], which is needed for the stress computation in (2.21)–(2.22). In the following, the sensitivity computation of $R(s)$ in (2.20) is derived. Define

$$Z(s) = C_c(sI - A_c)^{-1}, \quad H = \begin{bmatrix} C_c A_c \\ C_c \end{bmatrix}, \quad L = \begin{bmatrix} I \\ 0 \end{bmatrix},$$

such that $R(s) = Z(s)H^\dagger L$. Using the product rule, a perturbation $\Delta R(s)$ of $R(s)$ yields as

$$\Delta R(s) = [\Delta Z(s)]H^\dagger L + Z(s)[\Delta(H^\dagger)]L. \tag{4.5}$$

Now both terms $\Delta Z(s)$ and $\Delta(H^\dagger)$ are developed as functions of ΔA_c and ΔC_c, which are already stated in Section (3.3.3).

With the property $\Delta(X^{-1}) = -X^{-1}[\Delta X]X^{-1}$, the first term yields

$$\begin{aligned} \Delta Z(s) &= [\Delta C_c](sI - A_c)^{-1} - C_c(sI - A_c)^{-1}[\Delta(sI - A_c)](sI - A_c)^{-1} \\ &= [\Delta C_c](sI - A_c)^{-1} + Z(s)[\Delta A_c](sI - A_c)^{-1}. \end{aligned} \tag{4.6}$$

For the second term, a perturbation $\Delta(H^\dagger)$ of the pseudoinverse $H^\dagger$ yields

$$\operatorname{vec}(\Delta(H^\dagger)) = \mathcal{J}_{H^\dagger}\operatorname{vec}(\Delta H), \tag{4.7}$$

where the sensitivity $\mathcal{J}_{H^\dagger}$ is derived in [DMBM13, Lemma 8]. Denotes the selection matrices $S_1 \overset{\text{def}}{=} I_n \otimes [I_r \;\; 0_{r,r}]$, $S_2 \overset{\text{def}}{=} I_n \otimes [0_{r,r} \;\; I_r]$ such that

$$\operatorname{vec}(\Delta H) = \begin{bmatrix} S_1^T & S_2^T \end{bmatrix} \begin{bmatrix} \operatorname{vec}(\Delta(C_c A_c)) \\ \operatorname{vec}(\Delta C_c) \end{bmatrix} = S_1^T \operatorname{vec}(\Delta(C_c A_c)) + S_2^T \operatorname{vec}(\Delta C_c),$$

and then follows with (4.7)

$$\operatorname{vec}(\Delta(H^\dagger)) = \mathcal{J}_{H^\dagger} S_1^T \operatorname{vec}(\Delta(C_c A_c)) + \mathcal{J}_{H^\dagger} S_2^T \operatorname{vec}(\Delta C_c),$$

where $\Delta(C_c A_c) = [\Delta C_c]A_c + C_c[\Delta A_c]$. By combining this result with (4.5) and (4.6) yields

$$\operatorname{vec}(\Delta R(s)) = \begin{bmatrix} \mathcal{J}_{R(s),A_c} & \mathcal{J}_{R(s),C_c} \end{bmatrix} \begin{bmatrix} \operatorname{vec}(\Delta A_c) \\ \operatorname{vec}(\Delta C_c) \end{bmatrix},$$

where

$$\begin{aligned} \mathcal{J}_{R(s),A_c} &\overset{\text{def}}{=} \left(M(s)^T \otimes Z(s)\right) + \left(L^T \otimes Z(s)\right) \mathcal{J}_{H^\dagger} S_1^T (I_n \otimes C_c), \\ \mathcal{J}_{R(s),C_c} &\overset{\text{def}}{=} \left(M(s)^T \otimes I_r\right) + \left(L^T \otimes Z(s)\right) \mathcal{J}_{H^\dagger} \left(S_1^T (A_c^T \otimes I_r) + S_2^T\right), \end{aligned}$$

with $M(s) \overset{\text{def}}{=} (sI - A_c)^{-1} H^\dagger L$. After stacking the real and imaginary parts of $\operatorname{vec}(\Delta R(s)^T)$, it follows from (3.10) and (3.11)

$$(\operatorname{vec}(\Delta R(s)^T)) = \mathcal{J}_{R(s),A_c C_c} \begin{bmatrix} \operatorname{vec}(\Delta A_c) \\ \operatorname{vec}(\Delta C_c) \end{bmatrix}, \tag{4.8}$$

where

$$\mathcal{J}_{R(s),A_c,C_c} = \begin{bmatrix} \mathcal{P}_{r,r} & 0_{r^2,r^2} \\ 0_{r^2,r^2} & \mathcal{P}_{r,r} \end{bmatrix} \begin{bmatrix} \Re(\mathcal{J}_{R(s),A_c}) & \Re(\mathcal{J}_{R(s),C_c}) \\ \Im(\mathcal{J}_{R(s),A_c}) & \Im(\mathcal{J}_{R(s),C_c}) \end{bmatrix}.$$

4.2.2.3 Sensitivity of the stress vector $S(s)$

For stress variance computation, the sensitivity $\mathcal{J}_{R(s),(A_c,C_c)}$ of the transfer matrix $R(s)$ in (4.1) with respect to the system matrices A_c and C_c is derived from Section 4.2.2.2. Then, the covariance of the matrices $R(s)$ and $\tilde{R}(s)$ are computed in the healthy and damaged states of the structure for a chosen s-value.

Now, the uncertainty of the system matrices is propagated to matrix $R(s)$ (4.1) for both healthy and damaged states, then to the load vector $v(s)$ in the null space of $\delta R(s)^T = \tilde{R}(s)^T - R(s)^T$ and finally to the stress vector $S(s)$. It holds that

$$\mathrm{vec}(\triangle R(s)^T)_{\mathrm{re}} = \mathcal{J}_{R(s)^T,(A_c,C_c)} \begin{bmatrix} \mathrm{vec}(\triangle A_c) \\ \mathrm{vec}(\triangle C_c) \end{bmatrix}, \tag{4.9a}$$

$$\triangle v(s)_{\mathrm{re}} = \mathcal{J}_{v(s),\delta R(s)^T}(\mathrm{vec}(\triangle \delta R(s)^T))_{\mathrm{re}}, \tag{4.9b}$$

$$\triangle S(s)_{\mathrm{re}} = (\mathcal{L}_{\mathrm{model}}(s))_{\mathrm{Re}}\ \triangle v(s)_{\mathrm{re}}, \tag{4.9c}$$

where the respective sensitivity matrices have been derived in detail in Section 4.2.2.2. The sensitivity $\mathcal{J}_{v(s),\delta R(s)^T}$ of the load vector $v(s)$ with respect to $\delta R(s)^T$ is computed with [DMBM13, Proposition 4]. Combining (4.4) and (4.9), it follows

$$\triangle S(s)_{re} = \mathcal{J}_{S(s),\delta R(s)^T}(vec(\triangle \delta R(s)^T(s)))_{\mathrm{re}},$$

where $\mathcal{J}_{S(s),\delta R(s)^T} \overset{\mathrm{def}}{=} (L_{model(s)})_{Re} \mathcal{J}_{v(s),\delta R(s)^T}$. Together with (4.9), it follows

$$\begin{aligned} \triangle S(s)_{re} &= \mathcal{J}_{S(s),\delta R(s)^T} \mathcal{J}_{\tilde{R}(s),(\tilde{A}_c,\tilde{C}_c)} \begin{bmatrix} vec(\triangle \tilde{A}_c) \\ vec(\triangle \tilde{C}_c) \end{bmatrix} - \mathcal{J}_{S(s),\delta R(s)^T} \mathcal{J}_{R(s),(A_c,C_c)} \begin{bmatrix} vec(\triangle A_c) \\ vec(\triangle C_c) \end{bmatrix} \\ &= \tilde{\mathcal{J}}_{S(s),(\tilde{A}_c,\tilde{C}_c)} \tilde{\mathcal{J}}_{(\tilde{A}_c,\tilde{C}_c),\tilde{\mathcal{H}}} vec(\triangle \tilde{\mathcal{H}}) - \mathcal{J}_{S(s),(A_c,C_c)} \mathcal{J}_{(A_c,C_c),\mathcal{H}} vec(\triangle \mathcal{H}) \end{aligned} \tag{4.10}$$

where

$$\tilde{\mathcal{J}}_{S(s),(\tilde{A}_c,\tilde{C}_c)} \overset{\mathrm{def}}{=} \mathcal{J}_{S(s),\delta R(s)^T} \mathcal{J}_{\tilde{R}(s),(\tilde{A}_c,\tilde{C}_c)},\ \tilde{\mathcal{J}}_{(\tilde{A}_c,\tilde{C}_c),\tilde{\mathcal{H}}} \overset{\mathrm{def}}{=} \begin{bmatrix} \mathcal{J}_{\tilde{A}_c,\tilde{\mathcal{H}}} \\ \mathcal{J}_{\tilde{C}_c,\tilde{\mathcal{H}}} \end{bmatrix}$$

$$\text{and} \quad \mathcal{J}_{S(s),(A_c,C_c)} \overset{\mathrm{def}}{=} \mathcal{J}_{S(s),\delta R(s)^T} \mathcal{J}_{R(s),(A_c,C_c)},\ \mathcal{J}_{(A_c,C_c),\mathcal{H}} \overset{\mathrm{def}}{=} \begin{bmatrix} \mathcal{J}_{A_c,\mathcal{H}} \\ \mathcal{J}_{C_c,\mathcal{H}} \end{bmatrix}.$$

As the system matrices are computed on two different datasets from the damage and undamaged sates, hence they are statistically independent [DMBM13, Theorem. 5].

4.2.2.4 Statistical aggregation and evaluation of stress results at multiple s-values

Since the computation of the stress $S(s_w)$ at multiple Laplace variables s_w, $w = 1, \ldots, \kappa$ increases the information content about damaged or healthy element on structure, a joint evaluation of these stresses increases the robustness of the statistical approach in [DMBM13],

where only one Laplace variable s was considered. The joint statistical evaluation requires the covariance computation of the stacked (real-valued) stress results.

$$S \overset{\text{def}}{=} \begin{bmatrix} S(s_1)_{\text{re}} \\ \vdots \\ S(s_\kappa)_{\text{re}} \end{bmatrix}, \tag{4.11}$$

and its uncertainty follows from (4.10) as

$$\triangle S(s) = \begin{bmatrix} \tilde{\mathcal{J}}_{S(s_1),(\tilde{A}_c,\tilde{C}_c)} \tilde{\mathcal{J}}_{(\tilde{A}_c,\tilde{C}_c),\tilde{\mathcal{H}}} \\ \vdots \\ \tilde{\mathcal{J}}_{S(s_\kappa),(\tilde{A}_c,\tilde{C}_c)} \tilde{\mathcal{J}}_{(\tilde{A}_c,\tilde{C}_c),\tilde{\mathcal{H}}} \end{bmatrix} vec(\triangle\tilde{\mathcal{H}}) - \begin{bmatrix} \mathcal{J}_{S(s_1),(A_c,C_c)} \mathcal{J}_{(A_c,C_c),\mathcal{H}} \\ \vdots \\ \mathcal{J}_{S(s_\kappa),(A_c,C_c)} \mathcal{J}_{(A_c,C_c),\mathcal{H}} \end{bmatrix} vec(\triangle\mathcal{H}) \ . \tag{4.12}$$

Note that vector S contains the stress information for different s-values at all elements of the structure. Following from (3.8) and (4.12), the covariance $\Sigma_S \overset{\text{def}}{=} \text{cov}(\text{vec}(S))$ of the total stress yields

$$\begin{aligned} \Sigma_S = &\begin{bmatrix} \tilde{\mathcal{J}}_{S(s_1),(\tilde{A}_c,\tilde{C}_c)} \tilde{\mathcal{J}}_{(\tilde{A}_c,\tilde{C}_c),\tilde{\mathcal{H}}} \\ \vdots \\ \tilde{\mathcal{J}}_{S(s_\kappa),(\tilde{A}_c,\tilde{C}_c)} \tilde{\mathcal{J}}_{(\tilde{A}_c,\tilde{C}_c),\tilde{\mathcal{H}}} \end{bmatrix} \Sigma_{\tilde{\mathcal{H}}} \begin{bmatrix} \tilde{\mathcal{J}}_{S(s_1),(\tilde{A}_c,\tilde{C}_c)} \tilde{\mathcal{J}}_{(\tilde{A}_c,\tilde{C}_c),\tilde{\mathcal{H}}} \\ \vdots \\ \tilde{\mathcal{J}}_{S(s_\kappa),(\tilde{A}_c,\tilde{C}_c)} \tilde{\mathcal{J}}_{(\tilde{A}_c,\tilde{C}_c),\tilde{\mathcal{H}}} \end{bmatrix}^T + \\ &\begin{bmatrix} \mathcal{J}_{S(s_1),(A_c,C_c)} \mathcal{J}_{(A_c,C_c),\mathcal{H}} \\ \vdots \\ \mathcal{J}_{S(s_\kappa),(A_c,C_c)} \mathcal{J}_{(A_c,C_c),\mathcal{H}} \end{bmatrix} \Sigma_{\mathcal{H}} \begin{bmatrix} \mathcal{J}_{S(s_1),(A_c,C_c)} \mathcal{J}_{(A_c,C_c),\mathcal{H}} \\ \vdots \\ \mathcal{J}_{S(s_\kappa),(A_c,C_c)} \mathcal{J}_{(A_c,C_c),\mathcal{H}} \end{bmatrix}^T . \end{aligned} \tag{4.13}$$

since the datasets from reference and damaged states can be regarded as statistically independent. The covariance expression (4.13) leads to a statistical approach for damage localization using multiple s-values based on a statistical test for each element t of the structure. In this approach, all stress components corresponding to a structural element t are collected in a subvector S_t of S. Accordingly, the respective parts of the covariance matrix Σ_S (4.13) that correspond to element t are collected in Σ_t, such that $\Sigma_t = \text{cov}(S_t)$. Then, vector S_t is tested for being zero in a hypothesis test. Since an estimate of the stress vector S_t is asymptotically Gaussian distributed, a joint statistical evaluation of the computed stresses is derived in a χ^2-test as

$$\chi_t^2 = S_t^T \Sigma_t^{-1} S_t \tag{4.14}$$

for each structural element t. Since stress over damaged elements is zero in theory, potential damage is located in elements t corresponding to the lowest values of χ_t^2 among all elements.

4.3 Sensitivity-based statistical damage localization and quantification

4.3.1 Framework

Assume that measurements are collected from stochastic system depending on the parameter of the system and typically, parameter changes affect measurements output. For damage localization and quantification we assume that damage is linked to stiffness changes. Let $\theta \in \mathbb{R}^{l_{par}}$ be a parameter vector that describes the monitored system in the current state, and $\theta_0 \in \mathbb{R}^{l_{par}}$ its value in the reference system. In a hypothesis test, assume that

$$\begin{aligned} \text{reference} \quad \text{system}, H_0 : \ \theta{=}\theta_0 \\ \text{faulty} \quad \text{system}, H_1 : \ \theta{\neq}\theta_0. \end{aligned}$$

Each components of the parametric vector θ corresponds to the physical properties of one element of the FE model. Then, each element is tested for damage localization using sensitivity and minmax approaches, while the quantification of the damage extents corresponds to estimating the changes of δ in the damaged elements. For an example, the components of θ can be the stiffnesses of a mass-chain system, Young modulus of beam elements or it can be basically any quantity linked to damage-sensitive properties of the system. For testing of the system in the reference or faulty states, the faulty system is analyzed in the Gaussian framework of residuals.

In [DMZ16], a statistical framework has been set up for Gaussian residual vectors parametrized by θ with the purpose to decide which parts of θ have changed (for damage localization) and then to estimate this change (for damage quantification). The Gaussian residual vector $\zeta \in \mathbb{R}^h$ is computed from the measurements of the system and needs to satisfy the following properties

$$\zeta \sim \begin{cases} \mathcal{N}(0, \Sigma) & \text{for hypothesis } H_0 \\ \mathcal{N}(\mathcal{J}\delta, \Sigma) & \text{for hypothesis } H_1, \end{cases} \tag{4.15}$$

with constant mean $\mathcal{J}\delta$ from where $\delta = \sqrt{N}(\theta - \theta_0) \in \mathbb{R}^{l_{par}}$ is the unknown change in parameter vector for $\delta{\neq}0$ in the hypothesis H_1, N is the data length used for the computation of ζ, the sensitivity matrix $\mathcal{J} \in \mathbb{R}^{h \times l_{par}}$ has full column rank and the residual covariance matrix $\Sigma \in \mathbb{R}^{h \times h}$ is positive definite. It is assumed that the sensitivity and covariance matrices $\mathcal{J}$ and Σ are known or estimated somehow in practice. In detail, the following problems are considered in this framework:

- Fault detection indicates to change detection in θ, corresponds to deciding if $\delta \neq 0$;
- Fault isolation indicates which components of the δ are non-zero in the faulty system
- Fault quantification estimates the changes δ between θ and θ_0 in the faulty components of the system

Therefore, an appropriate subspace-based residual vector [BAB00] has been derived based on output measurements $\mathcal{Y}_N = \{y_k\}_{k=1,\dots,N}$ of system (1.5) as

$$\zeta(\theta_0, \mathcal{Y}_N) \stackrel{\text{def}}{=} \sqrt{N}\,\text{vec}(S(\theta_0)^T \widehat{\mathcal{H}}_{p+1,q}), \tag{4.16}$$

where $\widehat{\mathcal{H}}_{p+1,q}$ is an estimate computed on $\mathcal{Y}_N$ of the block Hankel matrix (3.2)

$$\mathcal{H}_{p+1,q} \stackrel{\text{def}}{=} \begin{bmatrix} \mathcal{R}_1 & \mathcal{R}_2 & \dots & \mathcal{R}_q \\ \mathcal{R}_2 & \mathcal{R}_3 & \dots & \mathcal{R}_{q+1} \\ \vdots & \vdots & \ddots & \vdots \\ \mathcal{R}_{p+1} & \mathcal{R}_{p+2} & \dots & \mathcal{R}_{p+q} \end{bmatrix} = \text{Hank}(\mathcal{R}_i),$$

containing $\mathcal{R}_i = \mathbf{E}(y_k y_{k-i}^T)$ is the output correlations, and $S(\theta_0)$ is the left null space of $\mathcal{H}_{p+1,q}$ from the reference system.

Based on the expression (4.15), the considered problems can be solved in a standard Gaussian framework with statistical tests and parameter estimation methods, as described in the following sections.

4.3.2 Basic damage detection tests

In the literature, many methods have been proposed for statistical damage detection and localization in the framework of such a Gaussian residual vector ζ [BN93, Bas97]. In the following, the appropriate generalized likelihood ratio (GLR) tests is recalled.

4.3.2.1 Damage detection: global test

Based on residual vector ζ in (4.15), the global test is intended to make a decision between $\delta = 0$ and $\delta \neq 0$. The GLR test applied to this problem corrsponds to the test statistic [Bas97]

$$t_{\text{global}} = \zeta^T \Sigma^{-1} \mathcal{J} \left(\mathcal{J}^T \Sigma^{-1} \mathcal{J}\right)^{-1} \mathcal{J}^T \Sigma^{-1} \zeta, \tag{4.17}$$

which follows a χ^2 distribution of l degrees of freedom and the non-centrality parameter $\delta^T F \delta$, where $F = \mathcal{J}^T \Sigma^{-1} \mathcal{J}$ is the Fisher information matrix. To make a decision between H_0 and H_1, the test variable t_{global} is compared to a threshold for damage detection. Generally, the threshold is chosen so that the probability of false alarms is below some chosen level. In theory, the choice of threshold can be made according to the χ^2 distribution of t_{global} from the healthy system.

4.3.3 Damage localization: sensitivity and minmax tests

From the previous section, the sensitivity $\mathcal{J}$ and covariance expression Σ are known that are estimated based on the parametric Gaussian residual vector containing the faulty components of the system. Recall that θ be the parameters of the structure. In the statistical tests, the damage localization corresponds to which components of the $\delta = \theta - \theta_0$ are non-zero (i.e.

$\delta \neq 0$) and the damage quantification corresponds to estimate the changes of δ in the damaged elements.

For making decision about damage localization, it has to be known which components of δ are non-zero by testing each components of δ separately. Assuming that different partitions of the vector δ into 2 subvectors,

$$\delta = \begin{bmatrix} \delta_a \\ \delta_b \end{bmatrix}, \tag{4.18}$$

where one of the sub-vectors are tested. For damage localization, $\delta_a = 0$ is tested against $\delta_a \neq 0$. Following (4.18), the sensitivity $\mathcal{J}$ and the Fisher information matrix $F = \mathcal{J}^T \Sigma^{-1} \mathcal{J}$ are analogously derived as follows

$$\mathcal{J} = \begin{bmatrix} \mathcal{J}_a & \mathcal{J}_b \end{bmatrix}, F = \begin{bmatrix} F_{aa} & F_{ab} \\ F_{ba} & F_{bb} \end{bmatrix} = \begin{bmatrix} \mathcal{J}_a^T \Sigma^{-1} \mathcal{J}_a & \mathcal{J}_a^T \Sigma^{-1} \mathcal{J}_b \\ \mathcal{J}_b^T \Sigma^{-1} \mathcal{J}_a & \mathcal{J}_b^T \Sigma^{-1} \mathcal{J}_b \end{bmatrix}, \tag{4.19}$$

details are given in [Bas97, DMZ16]. In the following subsections, the sensitivity and minmax tests have taken into account for damage localization.

4.3.3.1 Sensitivity test

In this approach, for damage localization, assuming that $\delta_b = 0$ for testing the components of $\delta_a = 0$ against $\delta_a \neq 0$, where $\zeta \sim \mathcal{N}(\mathcal{J}_a \delta_a, \Sigma)$. The generalized likelihood ratio (GLR) test follows as

$$t_{sens} = \zeta^T \Sigma^{-1} \mathcal{J}_a (\mathcal{J}_a^T \Sigma^{-1} \mathcal{J}_a)^{-1} \mathcal{J}_a^T \Sigma^{-1} \zeta, \tag{4.20}$$

which is called sensitivity test, and details are stated in [Bas97, DMZ16]. The test statistic t_{sens} is the χ^2 distribution of $dim(\delta_a)$ with non-centrality parameter $\delta_a^T F_{aa} \delta_a$. For making decision about faulty components, the test variable is compared to a threshold. Generally, a threshold is chosen for a given probability of false alarms according to the χ^2 distribution of the nominal system.

If the assumption $\delta_b = 0$ does not satisfy, the non-centrality parameter of t_{sens} yields from the properties of $\tilde{\zeta} \sim \mathcal{N}(\mathcal{J}_a^T \Sigma^{-1} \mathcal{J}_a)^{-1/2} \mathcal{J}_a^T \Sigma^{-1} \zeta$ as

$$\delta_a^T F_{aa} \delta_a + 2\delta_a^T F_{ab} \delta_b + \delta_b^T F_{ba} {F_{aa}}^{-1} F_{ab} \delta_b. \tag{4.21}$$

Since $\zeta \sim \mathcal{N}(\mathcal{J}\delta, \Sigma)$ and $\mathcal{J}\delta = \mathcal{J}_a \delta_a + \mathcal{J}_b \delta_b$,

$$\tilde{\zeta} \sim \mathcal{N}(F_{aa}^{1/2} \delta_a + F_{aa}^{-1/2} F_{aa} \delta_b, I)$$

following the properties of (4.19). From this normal distribution with the non-centrality parameter of (4.21), the statistical χ^2 distribution yields as $t_{sens} = \tilde{\zeta}^T \tilde{\zeta}$.

4.3.3.2 Minmax test

Rather than assuming the components of $\delta_b = 0$, the variable δ_b is substituted by its least favorable value for making a decision about δ_a, which leads to the minmax test [Bas97] as presented in the following. For the different subvectors of δ_a and δ_b, the partial residuals are

$$\zeta_a = \mathcal{J}_a^T \Sigma^{-1} \zeta \tag{4.22a}$$

$$\text{and } \zeta_b = \mathcal{J}_b^T \Sigma^{-1} \zeta, \tag{4.22b}$$

respectively. For the faulty components, the $\delta_a = 0$ is tested against $\delta_a \neq 0$ based on residual vector ζ and the GLR test statistic writes as

$$t_{mm} = \zeta_a^* F_a^{*-1} \zeta_a^*, \tag{4.23}$$

where the robust residual $\zeta_a^* = \zeta_a - F_{aa} F_{bb}^{-1} \zeta$ and $F_a^* = F_{aa} - F_{ab} F_{bb}^{-1} F_{ba}$. The mean of the robust residual ζ_a^* is sensitive to changes δ_a but blind to $\delta_b = 0$, which holds the distributed Gaussian properties of $\zeta_a^* \sim \mathcal{N}(F_a^* \delta_a, F_a^*)$, details are given in [DMZ16]. Note that t_{mm} is called the minmax test. For making a decision about faulty components, the test variables is compared to a threshold level, which is obtained for a given probability of fasle alarms from the χ^2 distribution of the the nomial system.

4.3.4 Damage quantification: sensitivity and minmax estimates

In the previous sections, a decision is made for the faulty system between $\delta_a = 0$ and $\delta_a \neq 0$ for the components of δ based on the sensitivity and the minmax tests. In both tests, the test variables is compared to a threshold level to make a decision about faulty components when $\delta_a \neq 0$. When the respective test exceeds a threshold and it is decided that the component is faulty, $\delta_a \neq 0$, the question about actual value of δ_a arises. In this section, estimates of the change $\delta = \theta - \theta_0$ are derived based on the properties of the sensitivity and minmax approaches, respectively.

4.3.4.1 Sensitivity approach

In the sensitivity approach, an estimate of the δ_a can be derived from the residual vector ζ for the damage quantification. Together with (4.19) and (4.20), the following expression can be derived

$$\hat{\delta}_a^{sens} = \left(\mathcal{J}_a^T \Sigma^{-1} \mathcal{J}_a\right)^{-1} \mathcal{J}_a^T \Sigma^{-1} \zeta, \tag{4.24}$$

where $\hat{\delta}_a^{sens} \sim \mathcal{N}(\delta_a, F_{aa}^{-1})$ for the assumption $\delta_b = 0$, details are given in [DMZ16].

4.3.4.2 Minmax approach

Similarly, an estimate of the δ_a can be derived based on minmax approach in the previous section follows

$$\hat{\delta}_a^{mm} = F_a^{*-1} \zeta_a^*, \tag{4.25}$$

with $\hat{\delta}_a^{mm} \sim \mathcal{N}(\delta_a, F_a^{*-1})$, where details are given in [DMZ16].

In the following, the summary of the statistical damage localization approach for SD-DLV and the sensitivity-based approach have been presented shortly in Figures 4.1 and 4.2, respectively.

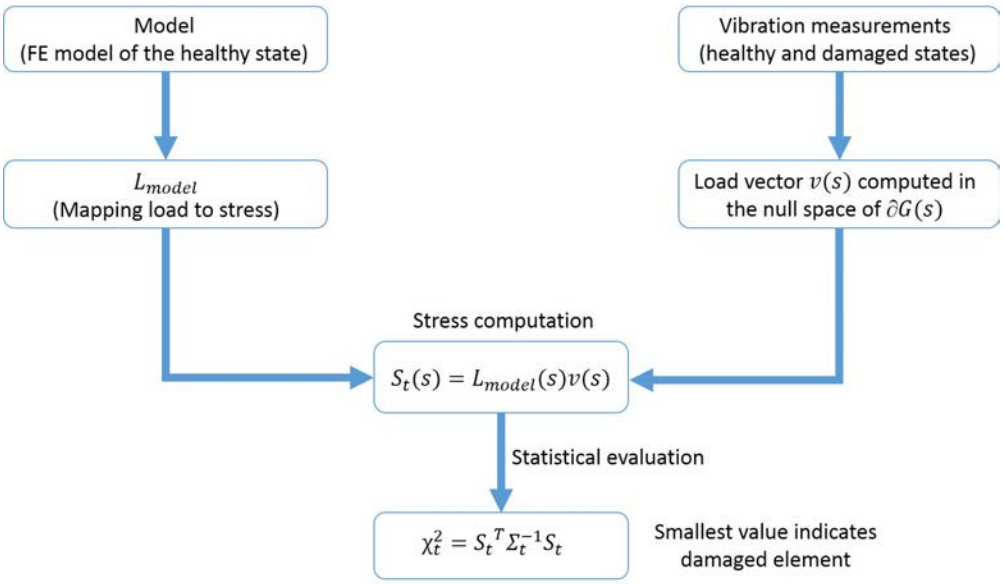

Figure 4.1 – Statistical damage localization for SDDLV (S-SDDLV) using different s-values.

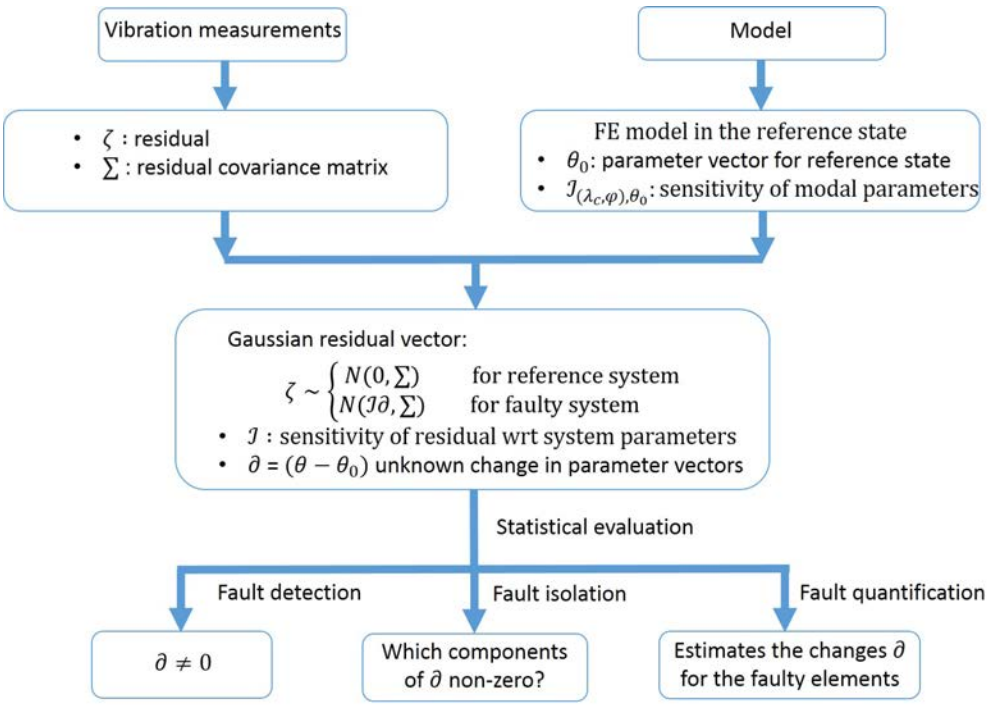

Figure 4.2 – Sensitivity-based statistical fault detection, isolation and quantification approach.

Part II

Contributions

Chapter 5

Statistical damage localization with stochastic load vectors using multiple mode sets

5.1 Introduction

This Chapter presents the statistical damage localization with stochastic load vector using multiple mode sets based on the SDDLV approach (Chapter 2, Section 2.2) which is a vibration based damage localization technique using both finite element information and modal parameters estimated from output data. The estimates of the modal parameters are subject to variance errors (see Chapter 3, Section 3.3). Based on that uncertainty information, a statistical extension of the SDDLV method was developed in [DMBM13, MDBM15] for deciding if an element is damaged using one or different s-values (see Chapter 4 in Section 4.2).

In [DMBM13, MDBM15], the number of modes used in the computation could not be bigger than the number of sensors located on the structure. This is a restriction when there are more modes describing on the structure than the available sensors. Here, the SDDLV method is developed with a joint statistical evaluation using multiple mode sets. It overcomes this limitation. It is demonstrated that the computation of stress for multiple mode sets increases the information content about the damaged or non-damaged elements of the structure. Finally, all stress values corresponding to each element are being tested for damage in a hypothesis test where the computed stresses are evaluated with their joint covariance. To derive such a test, the computation of the covariance of the resulting stress is necessary. Following Chapter 3 [DM13], the necessary covariance scheme is developed and extended for a joint statistical evaluation using multiple mode sets for the same or different Laplace variables.

This chapter is organized as follows. In Section 5.2, the SDDLV method is presented as

a vibration-based damage localization method and the removal of the limiting restriction on the number of modes is discussed using multiple mode sets in Section 5.3. In Section 5.4, the statistical damage localization approach is derived using these multiple mode sets. Finally, the new approach is applied on numerical simulations and experimental data to evaluate the performance of the approach in Chapter 9 and 13.

5.2 The SDDLV approach

The SDDLV approach is already described in details in Chapter 2. In this Chapter, to obtain the robustness of the damage localization results, the stress field is computed for multiple mode sets instead of using one limited mode set [MDBM15] for same or different one-Laplace variable s of the transfer matrix and then results are aggregated in a sensible way.

In this section, the deterministic computation of the stress field and the aggregation of the results is summarized shortly, before deriving its statistical evaluation in Section 5.4.

5.2.1 Modeling

The characteristics of a mechanical structure (2.1) and the corresponding continuous-time state-space model is recalled from (2.2)

$$\begin{cases} \dot{x}(t) = A_c x(t) + B_c e(t) \\ y(t) = C_c x(t) + D_c e(t) \end{cases} \tag{5.1}$$

with state vector $x \in \mathbb{R}^n$, output vector $y \in \mathbb{R}^r$, the state transition matrix $A_c \in \mathbb{R}^{n \times n}$ and output matrix $C_c \in \mathbb{R}^{r \times n}$, where $n = 2d$ is the system order and r is the number of outputs. Since the input of the system is replaced by the fictive force $e \in \mathbb{R}^r$, the input influence matrix and direct transmission matrix are of size $B_c \in \mathbb{R}^{n \times r}$ and $D_c \in \mathbb{R}^{r \times r}$ respectively.

However, only the system matrices A_c and C_c are relevant from output-only system identification, and the non-identified matrices B_c and D_c will only be needed in the derivation of estimates related to the transfer matrix. From Stochastic Subspace Identification (SSI), modal parameter estimates and subsequently the estimates $\widehat{A}_c$ and $\widehat{C}_c$ can be obtained from output only measurements, details are given in Section 3.2.3.

5.2.2 Computation of damage indicator

The damage indicator is based on the transfer matrix difference $\delta G(s)$ between reference and damaged states. From Section 2.2, the transfer matrix of the model from (5.1) is obtained as

$$G(s) = R(s) D_c,$$

where

$$R(s) = C_c (sI - A_c)^{-1} \begin{bmatrix} C_c A_c \\ C_c \end{bmatrix}^{\dagger} \begin{bmatrix} I \\ 0 \end{bmatrix}, \tag{5.2}$$

In (5.2), recall that s is the Laplace variable in the complex plane, I is the identity matrix of size $r \times r$, 0 is the zero matrix of size $r \times r$, and † denotes the Moore-Penrose pseudoinverse.

Note that $R(s)$ can be computed from output-only system identification, e.g. using stochastic subspace identification methods in Section 3.2, while matrices B and D cannot be identified for the computation of $G(s)$.

The difference between the transfer matrices in both damaged (variables with tilde) and healthy states is $\delta G(s) = \tilde{G}(s) - G(s)$. Assume that damage is due to changes in stiffness and mass is constant, then the matrices $\delta G(s)$ and $\delta R(s)^T = \tilde{R}(s)^T - R(s)^T$ have the same null space. The desired load vector $v(s)$ is obtained from the null space of the $\delta R(s)^T$ from Singular Value Decomposition (SVD)

$$\delta R(s)^T = U\Sigma V^H = \begin{bmatrix} U_1 & U_2 \end{bmatrix} \begin{bmatrix} \Sigma_1 & 0 \\ 0 & \Sigma_2 \end{bmatrix} \begin{bmatrix} V_1 & V_2 \end{bmatrix}^H, \tag{5.3}$$

where $U, \Sigma, V \in \mathbb{C}^{r\times r}$, $\Sigma_2 \approx 0$ and ^{H} indicates the conjugate transpose. Let n_{im} be the dimension of the image U_1 and $(r - n_{\text{im}})$ be the dimension of the null space V_2, where n_{im} depends on the kind and number of damaged elements. The load vector $v(s)$ in the null space of $\delta R(s)^T$ can be chosen as any linear combination of the vectors in V_2, particularly as the vector corresponding to the smallest singular value. Note that only output data is necessary for the computation of an estimate of $v(s)$. Finally, the load $v(s)$ is applied to the FE model of the healthy structure to compute stress field at all structural elements, stacked in vector $S(s)$, which yields a linear relationship and can be expressed by a matrix $L_{model}(s) \in \mathbb{C}^{l\times r}$ based on the FE model of the structure, satisfying

$$S(s) = L_{model}(s)v(s). \tag{5.4}$$

The stress vector $S(s)$ indicates potential damage for elements with corresponding entries in $S(s)$ that are close to zero. When estimated, these stresses are not exactly zero but small in practice because of modal truncation, model errors and variance errors from measurements.

5.2.3 Stress aggregation for robustness

Due to truncation and model errors, it is recommended to compute the load vector $v(s)$ and the resulting stress $S(s)$ for several s-values s_w, $w = 1, \ldots, \kappa$, and to aggregate results. To minimize error, the s-values should be chosen in the vicinity of the identified poles of the system but not too close to them [Ber10]. After identification of the system matrices in both states, the computations of (5.3)-(5.4) are repeated for each s_w to get the respective stress vectors $S(s_w)$. For multiple s-values, a deterministic stress aggregation is obtained for each element t as

$$\bar{S}_t = \sum_{w=1}^{\kappa} |S_t(s_w)| \tag{5.5}$$

In the previous works [MDBM15] (see Chapter 4, Section 4.2), this deterministic aggregation has been replaced by a statistical aggregation, where the intrinsic uncertainty of the stress estimation from finite measurement data is taken into account.

In the following, we address the restriction on the number of modes in the computation of the load vector by using multiple mode sets. The resulting stress from each mode set will be statistically aggregated for damage localization.

5.3 Multiple mode sets for SDDLV

In practice, there may be more modes available from identification than number of sensors on the structure. It will be meaningful to utilize this information completely from the identification procedure. In the SDDLV [Ber10], it was not possible to use all modes in this case for the stress computation due to the theoretical restriction $n \leq 2r$, where $n = 2m$ is the system order and r is the number of sensors. Note that m is the number of conjugated complex mode pairs identified from datasets where m has to satisfy the constraint $m \leq r$.

This constraint is due to the fact that system matrix B_c in (5.1) cannot be estimated from output-only measurements for the computation of the transfer matrix. Under this constraint, expression (5.2) is available, which allows the computation of the load vector in the null space of $\delta G(s)$ from output-only measurements.

In order to remove the restriction $m \leq r$ on the number of modes, the computation of stress from different mode sets is investigated in the following, where the current restriction is satisfied for the number of modes in each mode set. This allows considering more than r modes in the analysis. By taking into account more of the identified modes, it is expected that the information content for damage localization should increase. Load vectors and the respective stress are computed for each mode set, using one or several s-values.

Denote $\mathcal{M} = \{(\lambda_i, \varphi_i) : i = 1, \ldots, n\}$ the set of all identified modes. To take all these modes into account, we propose to use subsets $\mathcal{M}_j$, $j = 1, \ldots, n_s$, containing m_j modes each, where the condition $m_j \leq r$ is satisfied for each mode set, and $\mathcal{M} = \bigcup_{j=1}^{n_s} \mathcal{M}_j$. It is recommended to group modes with neighbouring frequencies together for each mode set in order to reduce truncation errors when evaluating the respective transfer matrices associated to each mode set. Then, the new method of this paper takes into account the identified data from *all* mode sets as follows.

The modal parameters of the structure are identified from SSI using measurement data of the healthy and damaged state. From the modal parameters corresponding to each mode set $\mathcal{M}_j$, the system matrices A_c^j and C_c^j are assembled in the healthy and damaged states as detailed in Section 3.2.3. Then, the computation of the load vector $v^j(s)$ is carried out separately for each mode set, i.e. the "transfer matrix" resultant $R^j(s)$ is computed from both states as in (5.2) and the load vector $v^j(s)$ is obtained in the null space of $R^j(s)$ from the SVD as in (5.3). The stress vectors $S^j(s) = L_{model}(s)v^j(s)$ are computed for each mode set and s-value, together with their uncertainty. Finally, damage localization is performed based on a joint statistical evaluation of the computed stresses.

5.4 Uncertainty propagation and covariance computation of damage localization residuals

For the damage localization algorithm, estimates of the modal parameters are needed in the damaged and undamaged states using SSI, detailed in Section 3.2. For each mode set, they are the starting point of the computations of the load vectors and associated stresses for damage localization. Their identification is subject to variance errors because of unknown excitation, measurement noise and limited data length. The uncertainties in the estimates are

penalizing the quality and precision of the damage localization results. For making decisions about damaged elements of the structure, these uncertainties need to be taken into account to decide whether stress of an element is significantly close to zero or not. In previous works (Chapter 4, Section 4.2.2), the uncertainty of the stress vector $S(s)$ in (5.4) was quantified for a single mode set at one or several s-values.

In this section, the uncertainty computation of the stress vector $S^j(s)$ is derived for different mode sets $\mathcal{M}_j$, $j = 1, \ldots, n_s$, for any choice of s, and the joint evaluation of the different stress results is described for each structural element in a statistical test.

5.4.1 Definitions of covariance computation

The definitions of covariance computation is stated in Section 3.3.1 and recalled here for the sake of clarity. Let $\widehat{\Sigma}_{\mathcal{H}}$ be the covariance of $\text{vec}(\widehat{\mathcal{H}})$, where $\text{vec}(\cdot)$ defines the column stacking vectorization operator. This covariance can easily be estimated from the measurement data, details are given in Section 3.3.1.

Let $g(\widehat{\mathcal{H}})$ be a vector valued function of the parameter and its covariance can be obtained with Taylor approximation as

$$g(\widehat{\mathcal{H}}) = g(\mathcal{H}) + \mathcal{J}_{g,\mathcal{H}}\text{vec}(\widehat{\mathcal{H}} - \mathcal{H}) + O(||\text{vec}(\widehat{\mathcal{H}} - \mathcal{H})||^2),$$

and then, it can be simplified as

$$\text{cov}(g(\widehat{\mathcal{H}})) \approx \mathcal{J}_{g,\mathcal{H}}\widehat{\Sigma}_{\mathcal{H}}\mathcal{J}_{g,\mathcal{H}}^T, \tag{5.6}$$

where $\mathcal{J}_{g,\mathcal{H}} = \partial g(\mathcal{H})/\partial\text{vec}(\mathcal{H})$ is the sensitivity of the function g. Since the output covariances and the Hankel matrix are asymptotically Gaussian variables [Han70] (when number of measurements is large), the statistical delta method [CB02] ensures that expression (5.6) is asymptotically exact. The required sensitivity can be obtained analytically through a first-order perturbation $\triangle g$ of the function g, which yields

$$\triangle g = \mathcal{J}_{g,\mathcal{H}}\text{vec}(\triangle\mathcal{H}). \tag{5.7}$$

With this strategy, the covariance $\Sigma_{\mathcal{H}}$ of an estimate of Hankel matrix $\mathcal{H}$ can be propagated to any function of $\mathcal{H}$, particularly to the modal parameters and to the stress estimate $S(s)$.

Note that some of the matrices and vectors in the derivation of the damage localization approach are complex-valued variables. To deal with their uncertainties, define an equivalent real-valued notation for any matrix Q as

$$Q_{\text{Re}} \overset{\text{def}}{=} \begin{bmatrix} \Re(Q) & -\Im(Q) \\ \Im(Q) & \Re(Q) \end{bmatrix}, Q_{\text{re}} \overset{\text{def}}{=} \begin{bmatrix} \Re(Q) \\ \Im(Q) \end{bmatrix},$$

where $\Re(\cdot)$ and $\Im(\cdot)$ denote the real and imaginary parts, respectively.

For multiple mode sets $\mathcal{M}_j$, $j = 1, \ldots, n_s$, the sensitivities of the stress estimate $S^j(s)$ are derived with respect to estimates A_c^j, C_c^j and subsequently to the Hankel matrix $\mathcal{H}$ in both the damaged and healthy states. Then, the covariance of $S^j(s)$ can be obtained as in (5.6).

5.4.2 Sensitivity of the system matrices A_c and C_c from subspace identification

In this section, the covariance of the system matrices A_c^j and C_c^j is computed for each mode set $\mathcal{M}_j$, starting from the identified eigenvalues $\lambda_{c,l}^j$ and mode shapes φ_l^j, $l = 1, \ldots, m_j$, for each mode set. Based on the SSI approach, their perturbation is linked to the Hankel matrix by

$$\triangle\lambda_{c,l}^j = \mathcal{J}_{\lambda_{c,l}^j,\mathcal{H}}\text{vec}(\triangle\mathcal{H}),$$
$$\triangle\varphi_l^j = \mathcal{J}_{\varphi_l^j,\mathcal{H}}\text{vec}(\triangle\mathcal{H})$$

where the sensitivity matrices $\mathcal{J}_{\lambda_{c,l}^j,\mathcal{H}} \in \mathbb{C}^{1\times h}$ and $\mathcal{J}_{\varphi_l^j,\mathcal{H}} \in \mathbb{C}^{r\times h}$ with $h = \dim(\text{vec}(\mathcal{H}))$ are detailed in Section 3.3.4. The system matrices A_c^j and C_c^j are assembled from the eigenvalues and mode shapes for each mode set $\mathcal{M}_j$ as derived in Section 3.2.3. Then the sensitivities of the vectorized system matrices yield accordingly

$$\text{vec}(\triangle A_c^j) = \mathcal{J}_{A_c,\mathcal{H}}^j\text{vec}(\triangle\mathcal{H}), \tag{5.8a}$$
$$\text{vec}(\triangle C_c^j) = \mathcal{J}_{C_c,\mathcal{H}}^j\text{vec}(\triangle\mathcal{H}), \tag{5.8b}$$

where the sensitivities $\mathcal{J}_{A_c,\mathcal{H}}^j$ and $\mathcal{J}_{C_c,\mathcal{H}}^j$ are obtained from the eigenvalue and mode shape sensitivities $\mathcal{J}_{\lambda_{c,l}^j,\mathcal{H}}$ and $\mathcal{J}_{\varphi_l^j,\mathcal{H}}$ as derived

$$\mathcal{J}_{A_c,\mathcal{H}}^j = P\begin{bmatrix} \Re(\mathcal{J}_{\lambda_{c,1}^j,\mathcal{H}}) \\ \vdots \\ \Re(\mathcal{J}_{\lambda_{c,m_j}^j,\mathcal{H}}) \\ \Im(\mathcal{J}_{\lambda_{c,1}^j,\mathcal{H}}) \\ \vdots \\ \Im(\mathcal{J}_{\lambda_{c,m_j}^j,\mathcal{H}}) \end{bmatrix}, \mathcal{J}_{C_c,\mathcal{H}}^j = \begin{bmatrix} \Re(\mathcal{J}_{\varphi_1^j,\mathcal{H}}) \\ \vdots \\ \Re(\mathcal{J}_{\varphi_{m_j}^j,\mathcal{H}}) \\ \Im(\mathcal{J}_{\varphi_1^j,\mathcal{H}}) \\ \vdots \\ \Im(\mathcal{J}_{\varphi_{m_j}^j,\mathcal{H}}) \end{bmatrix}, P = \begin{bmatrix} E_1 \\ \vdots \\ E_{m_j} \\ F_1 \\ \vdots \\ F_{m_j} \end{bmatrix},$$

and the selection matrix P is obtained with the following matrices

$$E_l = \begin{bmatrix} e_{m_j}^l e_{m_j}^{l^T} & 0_{m_j,m_j} \\ 0_{m_j,m_j} & -e_{m_j}^l e_{m_j}^{l^T} \end{bmatrix}, F_l = \begin{bmatrix} 0_{m_j,m_j} & e_{m_j}^l e_{m_j}^{l^T} \\ e_{m_j}^l e_{m_j}^{l^T} & 0_{m_j,m_j} \end{bmatrix}.$$

5.4.3 Sensitivity of the stress vector $S^j(s)$

For stress variance computation, the sensitivity $\mathcal{J}_{R(s),(A_c,C_c)}$ of the matrix $R(s)$ in (5.2) with respect to the system matrices A_c and C_c was derived in Section 4.2.2.2. For each mode set, the covariance of the matrices $R(s)$ and $\tilde{R}(s)$ are computed in the healthy and damaged states of the structure for a chosen s-value. Now, the uncertainty of the system matrices is

propagated to matrix $R^j(s)$ in (5.2) for both healthy and damaged states, then to the load vector in the null space of $\delta R^j(s)^T = \tilde{R}^j(s)^T - R^j(s)^T$ and finally to the stress vector $S^j(s)$. It holds that

$$\mathrm{vec}(\triangle R^j(s)^T)_{\mathrm{re}} = \mathcal{J}^j_{R(s)^T,(A_c,C_c)} \begin{bmatrix} \mathrm{vec}(\triangle A_c^j) \\ \mathrm{vec}(\triangle C_c^j) \end{bmatrix}, \tag{5.9a}$$

$$\triangle v^j(s)_{\mathrm{re}} = \mathcal{J}^j_{v(s),\delta R(s)^T}(\mathrm{vec}(\triangle \delta R^j(s)^T))_{\mathrm{re}}, \tag{5.9b}$$

$$\triangle S^j(s)_{\mathrm{re}} = (\mathcal{L}_{\mathrm{model}}(s))_{\mathrm{Re}}\ \triangle v^j(s)_{\mathrm{re}}, \tag{5.9c}$$

where the respective sensitivity matrices have been derived in detail in Section 4.2.2.2. The sensitivity $\mathcal{J}^j_{v(s),\delta R(s)^T}$ of the load vector $v(s)$ with respect to $\delta R(s)^T$ is computed with [DMBM13, Proposition 4]. Combining (5.8) and (5.9), it holds

$$\triangle S^j(s)_{\mathrm{re}} = \mathcal{J}^j_{S(s),\delta R(s)^T}(vec(\triangle \delta R(s)^T(s)))^j_{\mathrm{re}},$$

where $\mathcal{J}^j_{S(s),\delta R(s)^T} \overset{\mathrm{def}}{=} (L_{model(s)})_{\mathrm{Re}} \mathcal{J}^j_{v(s),\delta R(s)^T}$. For a joint evaluation of the stress for multiple mode sets, the uncertainty of the stress needs to be related to a common factor, which is the uncertainty of the Hankel matrix. Following above expression,

$$\begin{aligned} \triangle S^j(s)_{\mathrm{re}} &= \mathcal{J}^j_{S(s),\delta R(s)^T} \mathcal{J}^j_{\tilde{R}(s),(\tilde{A}_c,\tilde{C}_c)} \begin{bmatrix} vec(\triangle \tilde{A}_c^j) \\ vec(\triangle \tilde{C}_c^j) \end{bmatrix} - \mathcal{J}^j_{S(s),\delta R(s)^T} \mathcal{J}^j_{R(s),(A_c,C_c)} \begin{bmatrix} vec(\triangle A_c^j) \\ vec(\triangle C_c^j) \end{bmatrix} \\ &= \tilde{\mathcal{J}}^j_{S(s),(\tilde{A}_c,\tilde{C}_c)} \tilde{\mathcal{J}}^j_{(\tilde{A}_c,\tilde{C}_c),\tilde{\mathcal{H}}} vec(\triangle \tilde{\mathcal{H}}) - \mathcal{J}^j_{S(s),(A_c,C_c)} \mathcal{J}^j_{(A_c,C_c),\mathcal{H}} vec(\triangle \mathcal{H}) \end{aligned} \tag{5.10}$$

where

$$\tilde{\mathcal{J}}^j_{S(s),(\tilde{A}_c,\tilde{C}_c)} \overset{\mathrm{def}}{=} \mathcal{J}^j_{S(s),\delta R(s)^T} \mathcal{J}^j_{\tilde{R}(s),(\tilde{A}_c,\tilde{C}_c)},\ \tilde{\mathcal{J}}^j_{(\tilde{A}_c,\tilde{C}_c),\tilde{\mathcal{H}}} \overset{\mathrm{def}}{=} \begin{bmatrix} \mathcal{J}_{\tilde{A}_c^j,\tilde{\mathcal{H}}} \\ \mathcal{J}_{\tilde{C}_c^j,\tilde{\mathcal{H}}} \end{bmatrix}$$

$$\text{and} \quad \mathcal{J}^j_{S(s),(A_c,C_c)} \overset{\mathrm{def}}{=} \mathcal{J}^j_{S(s),\delta R(s)^T} \mathcal{J}^j_{R(s),(A_c,C_c)},\ \mathcal{J}^j_{(A_c,C_c),\mathcal{H}} \overset{\mathrm{def}}{=} \begin{bmatrix} \mathcal{J}_{A_c^j,\mathcal{H}} \\ \mathcal{J}_{C_c^j,\mathcal{H}} \end{bmatrix}.$$

As the system matrices are computed on two different datasets from the damage and undamaged sates, hence they are statistically independent [DMBM13, Theorem. 5].

Since the computation of stress using multiple mode sets $\mathcal{M}_j$ increases the information content about damaged or healthy element on structure, a joint stress evaluation has been proposed to increase the robustness of the damage localization method. The joint statistical evaluation needs to compute the covariance of the stress results with respect to multiple mode sets including real and imaginary parts of the stress value. Assume that the stress vector $S^j(s)$ is evaluated at a possibly different s-value $s = s^j$ for each mode set $\mathcal{M}_j$, $j = 1, \ldots, n_s$. After stacking the real and imaginary parts of the stress vectors, the total stress vector is derived as

$$S \overset{\mathrm{def}}{=} \begin{bmatrix} S^1(s^1)_{\mathrm{re}} \\ \vdots \\ S^{n_s}(s^{n_s})_{\mathrm{re}} \end{bmatrix}, \tag{5.11}$$

and its uncertainty follows from (5.10) as

$$\triangle S(s) = \begin{bmatrix} \tilde{\mathcal{J}}^1_{S(s^1),(\tilde{A}_c,\tilde{C}_c)}\tilde{\mathcal{J}}^1_{(\tilde{A}_c,\tilde{C}_c),\tilde{\mathcal{H}}} \\ \vdots \\ \tilde{\mathcal{J}}^{n_s}_{S(s^{n_s}),(\tilde{A}_c,\tilde{C}_c)}\tilde{\mathcal{J}}^{n_s}_{(\tilde{A}_c,\tilde{C}_c),\tilde{\mathcal{H}}} \end{bmatrix} vec(\triangle\tilde{\mathcal{H}}) - \begin{bmatrix} \mathcal{J}^1_{S(s^1),(A_c,C_c)}\mathcal{J}^1_{(A_c,C_c),\mathcal{H}} \\ \vdots \\ \mathcal{J}^{n_s}_{S(s^{n_s}),(A_c,C_c)}\mathcal{J}^{n_s}_{(A_c,C_c),\mathcal{H}} \end{bmatrix} vec(\triangle\mathcal{H}) \ . \tag{5.12}$$

Note that vector S contains the stress information for all mode sets at all elements of the structure.

5.5 Statistical evaluation for SDDLV (S-SDDLV) using Multiple mode sets

5.5.1 Joint statistical evaluation of stress

Following from (5.6) and (5.12), the covariance $\Sigma_S \overset{\text{def}}{=} \text{cov}(\text{vec}(S))$ of the total stress yields

$$\begin{aligned} \Sigma_S = &\begin{bmatrix} \tilde{\mathcal{J}}^1_{S(s^1),(\tilde{A}_c,\tilde{C}_c)}\tilde{\mathcal{J}}^1_{(\tilde{A}_c,\tilde{C}_c),\tilde{\mathcal{H}}} \\ \vdots \\ \tilde{\mathcal{J}}^{n_s}_{S(s^{n_s}),(\tilde{A}_c,\tilde{C}_c)}\tilde{\mathcal{J}}^{n_s}_{(\tilde{A}_c,\tilde{C}_c),\tilde{\mathcal{H}}} \end{bmatrix} \Sigma_{\tilde{\mathcal{H}}} \begin{bmatrix} \tilde{\mathcal{J}}^1_{S(s^1),(\tilde{A}_c,\tilde{C}_c)}\tilde{\mathcal{J}}^1_{(\tilde{A}_c,\tilde{C}_c),\tilde{\mathcal{H}}} \\ \vdots \\ \tilde{\mathcal{J}}^{n_s}_{S(s^{n_s}),(\tilde{A}_c,\tilde{C}_c)}\tilde{\mathcal{J}}^{n_s}_{(\tilde{A}_c,\tilde{C}_c),\tilde{\mathcal{H}}} \end{bmatrix}^T + \\ &\begin{bmatrix} \mathcal{J}^1_{S(s^1),(A_c,C_c)}\mathcal{J}^1_{(A_c,C_c),\mathcal{H}} \\ \vdots \\ \mathcal{J}^{n_s}_{S(s^{n_s}),(A_c,C_c)}\mathcal{J}^{n_s}_{(A_c,C_c),\mathcal{H}} \end{bmatrix} \Sigma_{\mathcal{H}} \begin{bmatrix} \mathcal{J}^1_{S(s^1),(A_c,C_c)}\mathcal{J}^1_{(A_c,C_c),\mathcal{H}} \\ \vdots \\ \mathcal{J}^{n_s}_{S(s^{n_s}),(A_c,C_c)}\mathcal{J}^{n_s}_{(A_c,C_c),\mathcal{H}} \end{bmatrix}^T . \end{aligned} \tag{5.13}$$

since the datasets from reference and damaged states can be regarded as statistically independent. The covariance expression (5.13) leads to a new statistical approach for damage localization using multiple mode sets based on a statistical test for each element t of the structure. In this approach, all stress components corresponding to a structural element t are collected in a subvector S_t of S, containing the information of all mode sets. Accordingly, the respective parts of the covariance matrix Σ_S in (5.13) that correspond to element t are collected in Σ_t, such that $\Sigma_t = \text{cov}(S_t)$. Then, vector S_t is tested for being zero in a hypothesis test. Since an estimate of the stress vector S_t is asymptotically Gaussian distributed, a joint statistical evaluation of the computed stresses is derived in a χ^2-test as

$$\chi^2_t = S_t^T \Sigma_t^{-1} S_t \tag{5.14}$$

for each structural element t. Since stress over damaged elements is zero in theory, potential damage is located in elements t corresponding to the lowest values of χ^2_t among all elements.

5.5.2 Joint stress evaluation for different s-values

In the previous section, the computation of stress (5.11) was derived using only one Laplace variable for each mode set, while there is a possibility to use several Laplace variables. The

computation of stress $S^j(s_w^j)$ can be easily generalized for several s-values for each mode set $\mathcal{M}_j$, denoted by s_w^j, where $w = 1, ..., \kappa^j$ and κ^j is the number of s-values used for mode set $\mathcal{M}_j$. After stacking the real and imaginary parts of the stress vectors for multiple s-values and mode sets, the joint stress vector writes analogously as

$$S = \begin{bmatrix} S^1(s_1^1)_{\mathrm{re}} \\ \vdots \\ S^1(s_{\kappa^1}^1)_{\mathrm{re}} \\ \vdots \\ S^{n_s}(s_1^{n_s})_{\mathrm{re}} \\ \vdots \\ S^{n_s}(s_{\kappa^{n_s}}^{n_s})_{\mathrm{re}} \end{bmatrix}. \tag{5.15}$$

Then covariance of the stress (5.15) with respect to different s-values can be derived together with (5.13) for mode sets $\mathcal{M}_j$, $j = 1, \ldots, n_s$, as

$$\begin{aligned} \Sigma_{S(s)} = &\begin{bmatrix} \tilde{\mathcal{J}}^1_{S(s_1^1),(\tilde{A}_c,\tilde{C}_c)}\tilde{\mathcal{J}}^1_{(\tilde{A}_c,\tilde{C}_c),\tilde{\mathcal{H}}} \\ \vdots \\ \tilde{\mathcal{J}}^1_{S(s_{\kappa^1}^1),(\tilde{A}_c,\tilde{C}_c)}\tilde{\mathcal{J}}^1_{(\tilde{A}_c,\tilde{C}_c),\tilde{\mathcal{H}}} \\ \vdots \\ \tilde{\mathcal{J}}^{n_s}_{S(s_1^{n_s}),(\tilde{A}_c,\tilde{C}_c)}\tilde{\mathcal{J}}^{n_s}_{(\tilde{A}_c,\tilde{C}_c),\tilde{\mathcal{H}}} \\ \vdots \\ \tilde{\mathcal{J}}^{n_s}_{S(s_{\kappa^{n_s}}^{n_s}),(\tilde{A}_c,\tilde{C}_c)}\tilde{\mathcal{J}}^{n_s}_{(\tilde{A}_c,\tilde{C}_c),\tilde{\mathcal{H}}} \end{bmatrix} \Sigma_{\tilde{\mathcal{H}}} \begin{bmatrix} \tilde{\mathcal{J}}^1_{S(s_1^1),(\tilde{A}_c,\tilde{C}_c)}\tilde{\mathcal{J}}^1_{(\tilde{A}_c,\tilde{C}_c),\tilde{\mathcal{H}}} \\ \vdots \\ \tilde{\mathcal{J}}^1_{S(s_{\kappa^1}^1),(\tilde{A}_c,\tilde{C}_c)}\tilde{\mathcal{J}}^1_{(\tilde{A}_c,\tilde{C}_c),\tilde{\mathcal{H}}} \\ \vdots \\ \tilde{\mathcal{J}}^{n_s}_{S(s_1^{n_s}),(\tilde{A}_c,\tilde{C}_c)}\tilde{\mathcal{J}}^{n_s}_{(\tilde{A}_c,\tilde{C}_c),\tilde{\mathcal{H}}} \\ \vdots \\ \tilde{\mathcal{J}}^{n_s}_{S(s_{\kappa^{n_s}}^{n_s}),(\tilde{A}_c,\tilde{C}_c)}\tilde{\mathcal{J}}^{n_s}_{(\tilde{A}_c,\tilde{C}_c),\tilde{\mathcal{H}}} \end{bmatrix}^T + \\ &\begin{bmatrix} \mathcal{J}^1_{S(s_1^1),(A_c,C_c)}\mathcal{J}^1_{(A_c,C_c),\mathcal{H}} \\ \vdots \\ \mathcal{J}^1_{S(s_{\kappa^1}^1),(A_c,C_c)}\mathcal{J}^1_{(A_c,C_c),\mathcal{H}} \\ \vdots \\ \mathcal{J}^{n_s}_{S(s_1^{n_s}),(A_c,C_c)}\mathcal{J}^{n_s}_{(A_c,C_c),\mathcal{H}} \\ \vdots \\ \mathcal{J}^{n_s}_{S(s_{\kappa^{n_s}}^{n_s}),(A_c,C_c)}\mathcal{J}^{n_s}_{(A_c,C_c),\mathcal{H}} \end{bmatrix} \Sigma_{\mathcal{H}} \begin{bmatrix} \mathcal{J}^1_{S(s_1^1),(A_c,C_c)}\mathcal{J}^1_{(A_c,C_c),\mathcal{H}} \\ \vdots \\ \mathcal{J}^1_{S(s_{\kappa^1}^1),(A_c,C_c)}\mathcal{J}^1_{(A_c,C_c),\mathcal{H}} \\ \vdots \\ \mathcal{J}^{n_s}_{S(s_1^{n_s}),(A_c,C_c)}\mathcal{J}^{n_s}_{(A_c,C_c),\mathcal{H}} \\ \vdots \\ \mathcal{J}^{n_s}_{S(s_{\kappa^{n_s}}^{n_s}),(A_c,C_c)}\mathcal{J}^{n_s}_{(A_c,C_c),\mathcal{H}} \end{bmatrix}^T. \end{aligned} \tag{5.16}$$

Analogously to the previous section, the covariance expression (5.16) leads to a new statistical aggregation scheme for multiple mode sets using several s-values. For each structural element t, the corresponding stress subvector S_t of S in (5.15) is selected together with its covariance components Σ_t of Σ in (5.16). The stress vector S_t is tested for being zero in a statistical hypothesis test as in (5.14) for each structural element t.

5.6 Conclusions

In this chapter, the damage localization with the SDDLV approach has been extended considering multiple mode sets based on a joint statistical evaluation that takes into account the information from all identified modes of the structure. The stress computation using multiple mode sets increases the information content about the damaged or non-damaged elements of the structure, compared to evaluation from a limited number of modes due to a previous constraint of the approach on the number of modes. With the new approach, this constraint is lifted, which allows damage localization with fewer sensors at the same time. While the stress evaluation for each mode set is naturally subject to modal truncation errors that depend on the choice of the Laplace variable s, the joint statistical evaluation for several mode sets seems to mitigate these errors.

The method has been successfully applied to vibration measurements on both numerical and real applications in Chapter 9 and 13 respectively, where damage was correctly localized with a small number of sensors, while the previous approach with a limited number of modes failed.

5.7 Dissemination

Parts of this chapter have been published or are submitted to:

[BDL+17] M.D.H. Bhuyan, M. Döhler, Y. Lecieux, L. Mevel, and F. Schoefs. Statistical damage localization with stochastic load vectors using multiple mode sets. *International Journal of Structural Health Monitoring (IJSHM)*, 16(5):518–535, 2017.

[BAD+SA] M.D.H. Bhuyan, S. Allahdadian, M. Döhler, Y. Lecieux, L. Mevel, F. Schoefs, and C. Ventura. Transfer matrices-based output-only statistical damage localization and quantification. In *11th International Workshop on Structural Health Monitoring (IWSHM)*, September 12-14, 2017, Stanford, CA, USA.

[BGD+ce] M.D.H. Bhuyan, G. Gautier, M. Döhler, L. Mevel, Y. Lecieux, and F. Schoefs. Statistical damage localization in mechanical systems based on load vectors. In *International Federation of Automatic Control (IFAC), World Congress*, 9-14 July, 2017, Toulouse, France.

[GBDMia] G. Gautier, M.D.H. Bhuyan, M. Döhler, and L. Mevel. Comparison of damage localization in mechanical systems based on stochastic subspace identication method. In *European Geosciences Union, General Assembly*, 23-28 April, 2017, Vienna, Austria.

[BDMin] M.D.H. Bhuyan, M. Döhler, and L. Mevel. Statistical damage localization with stochastic load vectors using multiple mode sets. In *8th European Workshop on Structural Health Monitoring (EWSHM)*, July 4-7, 2016, Bilbao, Spain.

Chapter 6

Statistical based decision making for damage localization with influence lines

6.1 Introduction

This Chapter presents the statistical evaluation with influence lines damage location (ILDL) approach which is complementary to the SDDLV approach. In ILDL approach, the image of the flexibility matrix between reference and damaged states of a structure is a basis for the influence line (IL) of the stress resultants at damaged locations. Damage is thus located at the elements where the subspace angle between image of the flexibility matrix and the influence line of the FE model of the structure is zero or small in practice [Ber14]. Since the image and the null space are complementary subspaces, the information on the damage location in the null space is also contained in the image of δG. In theory, the null space and the image contain the same complementary information from δG, though in practice only an estimate of this matrix is available.

Since an estimate of the image is computed from noisy measurement data, it is naturally afflicted with uncertainties. Hence, a statistical evaluation of the subspace angle is necessary for making a decision about damaged or healthy elements. For such an evaluation, the modal parameter covariance is propagated to the obtained subspace angles in a sensitivity-based approach. Finally, all computed values corresponding to an element are being tested for damage in a hypothesis test where the computed subspace angles are evaluated with their individual covariance.

In previous works [Ber14], empirical thresholds are used in the ILDL approach (at $s = 0$) for deciding at which elements damage is located (i.e. where subspace angles are close to zero). In addition [MDBM13], the ILDL approach was extended in a statistical approach

for $s = 0$, where the uncertainty quantification was tempted on the damage indicator, the subspace angle. However, it can be shown that it has a non-Gaussian distribution at the damaged element, while the image of δG is asymptotically Gaussian and thus its theoretical validation is questionable due to this issue. This motivates a revision of the approach and the following extension of the ILDL approach.

In this chapter, a statistical framework is developed and demonstrated in a numerical application, where its advantages are shown comparing to a deterministic ILDL evaluation for damage localization. This Chapter is organized as follows. In Section 6.2, the ILDL approach is presented for damage localization on structures from output-only measurements data. In Section 6.2.2, the computation of the ILDL approach is generalized to $s \neq 0$ and the difficulties for the distribution of the damage indicator is described in Section 6.2.3, and then the damage indicator of the ILDL is reconsidered to allow an adequate uncertainty quantification, before deriving its statistical evaluation of damage localization in Section 6.3. Finally, the statistical evaluation of the ILDL approach has been demonstrated on a numerical application in Chapter 10.

6.2 The ILDL approach

The ILDL approach is described in details in Section 2.3 (Chapter 2). In the following, the modeling of the structure, the deterministic computation of the damage localization residuals, the generalization of the ILDL approach for arbitrary s-value and the difficulties of the damage localization indicator are summarized shortly, before deriving its statistical evaluation in Section 6.3.

6.2.1 Damage indicator with influence lines

The characteristics of a mechanical structure (2.1) and the corresponding continuous-time state-space model is recalled from (2.2)

$$\begin{cases} \dot{x}(t) = A_c x(t) + B_c e(t) \\ y(t) = C_c x(t) + D_c e(t) \end{cases} \tag{6.1}$$

with state vector $x \in \mathbb{R}^n$, output vector $y \in \mathbb{R}^r$, the state transition matrix $A_c \in \mathbb{R}^{n \times n}$ and output matrix $C_c \in \mathbb{R}^{r \times n}$, where $n = 2d$ is the system order and r is the number of outputs. Since the input of the system is replaced by the fictive force $e \in \mathbb{R}^r$, the input influence matrix and direct transmission matrix are of size $B_c \in \mathbb{R}^{n \times r}$ and $D_c \in \mathbb{R}^{r \times r}$ respectively.

From Section 2.3.1, the transfer matrix $G(s)$ of system is obtained at $s = 0$ with [Ber14]

$$G(0) = R(0) D_c, \quad \text{where} \quad R(0) = C_c (sI - A_c)^{-1} \begin{bmatrix} C_c A_c \\ C_c \end{bmatrix}^{\dagger} \begin{bmatrix} I \\ 0 \end{bmatrix} \tag{6.2}$$

for the restriction of the system order $n \leq 2r$. Note that $R(0)$ can be computed from output-only system identification, e.g. using stochastic subspace identification methods in Section 3.2, while matrices B and D cannot be identified for the computation of $G(0)$.

The difference in the transfer matrices between damaged (variables with tilde) and reference state (variables without tilde) is $\delta G(0) = \tilde{G}(0) - G(0)$. Since the direct transmission matrix is only a function of the mass and invariant for damage due to stiffness changes, the $\delta D_c = \tilde{D}_c - D_c = 0$ due to no mass change and D_c being invertible [Ber10], it follows that $\delta G(0) = \delta R(0)D$ (with $\delta R(0) = \tilde{R}(0) - R(0)$). Hence, the image of $\delta G(0)$ is the same as the image of $\delta R(0)$. The $\delta R(0)$ is computed from the output only data in the damage and reference states. After Singular Value Decomposition (SVD) of $\delta R(0)$, it follows

$$\delta R(0) = U\Sigma V^T = \begin{bmatrix} U_1 & U_2 \end{bmatrix} \begin{bmatrix} \Sigma_1 & 0 \\ 0 & \Sigma_2 \end{bmatrix} \begin{bmatrix} V_1 & V_2 \end{bmatrix}^T , \tag{6.3}$$

where $U, \Sigma, V \in \mathbb{C}^{r,r}$ and $\Sigma_2 \approx 0$ or closely zero in practice. Let t be the rank of the $\delta R(0) \in \mathbb{R}^{r\times r}$ and $U_1 = [u_1, ...u_t] \in \mathbb{R}^{r\times t}$ be the image of δR in the SVD. Note that U_1 correspond to the nonzero singular values Σ_1, and U_2 corresponds to zero singular values Σ_2.

For the ILDL approach, the influence line of each stress resultant S is evaluated at the sensor coordinates. Such way, to apply the respective unit loads at the sensor coordinates to get the influence for an element j that corresponds to an entry S_j in vector S. It is noted that the row vector l_j^T of L_{model} (see Section 2.2.3) is the influence line (IL) of the stress resultant for element j, which is denoted by the column vector l_j.

For damage localization, the ILDL approach consists of checking if the IL l_j is contained in the subspace U_1. Note that l_j and U_1 are computed based on FE model of the reference state and output-only measurements data, respectively. The quantity used in [Ber14] that measures how well l_j fits into the image U_1 is the subspace angle

$$\phi_j = cos^{-1}\left(\frac{||U_1^T l_j||}{||l_j||}\right). \tag{6.4}$$

where $\phi_j = 0$ indicates the perfect fit. If j is the damaged element, ϕ_j will be close to zero. Therefore, damage is located at the elements where the subspace angle ϕ_j between image U_1 of the flexibility matrix δR and the influence line l_j of the FE model of the reference structure is zero or small in practice.

For uncertainty quantification, the subspace angle is not derivable at $\phi_j = 0$. Then the following damage indicator was proposed in [Mar13, MDBM13] as

$$\gamma_j = \frac{||U_1^T l_j||^2}{||l_j||^2} , \tag{6.5}$$

where $\gamma_j = 1$ indicates the perfect fit for the damage localization.

In the following, first, the computation of the ILDL approach is generalized for any arbitrary s-value ($s \neq 0$) in subsection 6.2.2 and the difficulties for the distribution of the damage indicator are described in subsection 6.2.3, and finally the damage indicator $\gamma_j(s)$ of the ILDL is reconsidered to allow an adequate uncertainty quantification, before deriving its statistical evaluation for damage localization.

6.2.2 Generalization to arbitrary s

As recalled in the previous section, the ILDL approach has been derived for $s = 0$ from where the transfer matrix difference (6.3) is recalled as follows

$$\delta R(0) = \begin{bmatrix} U_1 & U_2 \end{bmatrix} \begin{bmatrix} \Sigma_1 & 0 \\ 0 & \Sigma_2 \end{bmatrix} \begin{bmatrix} V_1 & V_2 \end{bmatrix}^H. \tag{6.6}$$

For damage localization, the ILDL approach consists of checking if the IL l_j is contained in the subspace U_1. This is the case, if and only if

$$l_j = U_1 U_1^H l_j. \tag{6.7}$$

The computation above can also be generalized to $s \neq 0$ from (6.6) by showing that the SDDLV [Ber10], which is defined for arbitrary s, yields an equivalent criterion as (6.7) for the damaged elements. Following [Ber10], for any arbitrary s-value, the transfer matrix difference is recalled here from (2.21)

$$\delta R(s)^T = \tilde{U}\Sigma\tilde{V}^H = \begin{bmatrix} \tilde{U}_1 & \tilde{U}_2 \end{bmatrix} \begin{bmatrix} \Sigma_1 & 0 \\ 0 & \Sigma_2 \end{bmatrix} \begin{bmatrix} \tilde{V}_1 & \tilde{V}_2 \end{bmatrix}^H, \tag{6.8}$$

where $\tilde{U}_1 = V_1$, $\tilde{U}_2 = V_2$, $\tilde{V}_1 = U_1$ and $\tilde{V}_2 = U_2$ in comparison to (6.6), but now for arbitrary s. In SDDLV approach, damage locating vector in the null space of $\delta R(s)^T$ is applied to the finite element (FE) model of the structure for the computation of a stress field over the structure. For arbitrary s, matrix L_{model} is complex-valued, and the influence lines are found in its rows as $L_{model} = \begin{bmatrix} l_1^H \\ l_2^H \\ \vdots \\ l_l^H \end{bmatrix}$. A damaged element j yields zero stress

$$l_j^H(s)\tilde{V}_2(s) = 0,$$

and follows

$$\tilde{V}_2(s)\tilde{V}_2^H(s)l_j(s) = 0.$$

Since $I = \tilde{V}_1\tilde{V}_1^H + \tilde{V}_2\tilde{V}_2^H$, the above expression can be replaced as

$$(I - \tilde{V}_1(s)\tilde{V}_1(s)^H)l_j(s) = 0.$$

Replacing now $U_1 = \tilde{V}_1$, it follows

$$(I - U_1 U_1^H)l_j(s) = 0 \tag{6.9a}$$

$$\text{or, } l_j(s) = U_1 U_1^H l_j(s) \tag{6.9b}$$

This expression is purely based on the SDDLV properties for a damaged element j, holding for arbitrary s. It also means that the influence line of a damaged element j is contained in

the image of the transfer matrix difference for arbitrary s, analogous to ILDL property (6.7) that was previously derived for $s = 0$. In such a way, the damage localization with the ILDL approach is generalized for any arbitrary choice of s-value, where the IL lies on the image U_1 in the SVD.

In previous works [MDBM13], a statistical evaluation of $\gamma_j(s)$ was done (for $s = 0$). The range of γ_j is bounded between $0 \leq \gamma_j \leq 1$, and in theory $\gamma_j = 1$ at the damaged element, at the border of the range. While U_1 is asymptotically Gaussian, the distribution of γ_j is thus clearly non-Gaussian. In this context, the uncertainty quantification was tempted in [MDBM13] but its theoretical validation is questionable due to this issue. This motivates the following extension of the ILDL approach.

6.2.3 Difficulties for the distribution of damage indicator $\gamma_j(s)$

With U_1 being an asymptotically Gaussian estimate, the following problems are encountered to characterize the distribution of damage indicator, γ_j:

- The range of γ_j (2.45) is bounded between $0 \leq \gamma_j \leq 1$, and in theory $\gamma_j = 1$ at the damaged element, at the border of the range. While U_1 is asymptotically Gaussian, the distribution of γ_j is thus clearly non-Gaussian. In this context, the uncertainty quantification was tempted in [MDBM13] but its theoretical validation is questionable due to this issue.

- Even for the simplest case when u has only one column (a Gaussian vector), the distribution of γ_j is difficult to handle. There are expressions for the distribution for the case where u is centered and its covariance is of shape $\sigma^2 I$, leading to a uniform distribution on the sphere, which is not our case. In this case, the distribution of γ_j is known when u has two components (i.e. 2 sensors) - "projected normal distribution" [MJ00]. The probability density function (pdf) of this distribution is already quite complicated, and a more general case has not been found.

Due to this issue, we reconsider the damage indicator of the ILDL to allow an adequate uncertainty quantification. We can reformulate in the following way:
For the case when U_1 has more than one column, it is checked that l_j is a linear combination of the columns of U_1 with the subspace angle:

$$\frac{l_j}{||l_j||} = \sum_i \alpha_i u_i, \quad \alpha_i = \frac{u_i^H l_j}{||l_j||}$$

If this relation is satisfied, $\sum \alpha_i^2 = 1$ which is actually the same as γ_j. This is what we want to test with the subspace angle, ($\gamma_j = 1$). Then, we could equivalently test

$$\sum_{i=1}^{t} \frac{u_i^H l_j}{||l_j||} u_i - \frac{l_j}{||l_j||} = 0.$$

But the same problems for characterizing the distribution of this residual remain: one of the terms $\frac{u_i^H l_j}{||l_j||}$ may be at the border of the range between -1 and 1, the distribution of these

scalar products are difficult to characterize and the dependence between the terms containing u_i's is even more difficult. So, the above equation can be simplified as

$$l_j = U_1 U_1^H l_j.$$

as shown in (6.9). Since $U_1 {U_1}^H$ projects into the subspace spanned by U_1, we indeed check with this equation if l_j lies in the subspace spanned by U_1. We hence can test

$$(I - U_1 U_1^H) l_j = 0.$$

This expression is asymptotically Gaussian and it is not at a border for the damaged element at 0. The following two cases are considered

Case-1:

For rank$(\delta R) = t = 1$, to make a test that checks directly if $u_1 = \pm \frac{l_j}{||l_j||}$.

Case-2:

For general case, consider an arbitrary rank of δR. Then make a such test that checks $(I - U_1 U_1^H) l_j = 0$.

In the following Section 6.3, first the uncertainty quantification of the respective damage indicator is computed and then, a statistical damage localization approach has been proposed.

6.3 Uncertainty computation of damage localization residuals

For the damage localization approach, estimates of the modal parameters are obtained in the damaged and undamaged states using SSI, detailed in Section 3.2. Due to unknown excitation, measurement noise and limited data length, their identification is subject to variance errors. The uncertainties in the estimates are penalizing the quality and precision of the damage localization results. For making decisions about damaged elements of the structure, these uncertainties need to be taken into account to decide whether the damaged element or not. Therefore, the uncertainty of the estimation of the system matrix is propagated to the uncertainty of the damage localization residuals that derives based on a sensitivity-based approach.

Note that the derivation of the covariance computation has already stated in Section 3.3.1 and recalled here for simplicity. Let Δf be a first-order perturbation of function $f(\mathcal{H})$, then it follows

$$\triangle f = \mathcal{J}_{f,\mathcal{H}} vec(\triangle \mathcal{H}),\ cov(f(\mathcal{H})) \approx \mathcal{J}_{f,\mathcal{H}} \hat{\Sigma}_{\mathcal{H}} \mathcal{J}_{f,\mathcal{H}}^T$$

Note that $\mathcal{J}_{f,\mathcal{H}} = \partial f(\mathcal{H}) / \partial vec(\mathcal{H})$ is the sensitivity of f with respect to $\mathcal{H}$ in the above derivation.

The following notation and properties will be used. $\otimes$ denotes the Kronecker product, having the property $\text{vec}(AXB) = (B^T \otimes A)\text{vec}(X)$. I_a denotes the identity matrix of size $a \times a$, and $0_{a,b}$ denotes the zero matrix of size $a \times b$. $e_j^a \in \mathbb{R}^a$ denotes the j-th unit vector (being

column j of I_a). The permutation matrix $\mathcal{P}_{a,b} \overset{\text{def}}{=} \begin{bmatrix} I_a \otimes e_1^b & I_a \otimes e_2^b & \dots & I_a \otimes e_b^b \end{bmatrix} \in \mathbb{R}^{ab \times ab}$ is defined with the property

$$\text{vec}(X^T) = \mathcal{P}_{a,b}\,\text{vec}(X) \tag{6.10}$$

for any matrix $X \in \mathbb{R}^{a \times b}$. Note that some of the matrices are complex-valued variables in $\delta R(s)$ in section 6.3.1. To deal with uncertainties of the complex-valued matrices, we define an equivalent real-valued notation for any matrix Q as follows

$$Q_{\text{Re}} \overset{\text{def}}{=} \begin{bmatrix} \Re(Q) & -\Im(Q) \\ \Im(Q) & \Re(Q) \end{bmatrix}, Q_{\text{re}} \overset{\text{def}}{=} \begin{bmatrix} \Re(Q) \\ \Im(Q) \end{bmatrix} \tag{6.11}$$

With this notation, it holds

$$(Ab)_{\text{re}} = A_{\text{Re}} b_{\text{re}}, \quad (A^H b)_{\text{re}} = (A_{\text{Re}})^T b_{\text{re}} \tag{6.12}$$

for matrix $A \in \mathbb{C}^{a \times b}$ and vector $b \in \mathbb{C}^b$. Details are given in Chapter 3.

6.3.1 Covariance of the system matrices and δR

The identification of the system matrix has computed from datasets using subspace identification procedure, details are given in Section 3.2.3. The covariance of the identified system matrices for the damage and undamaged states are derived as follows

$$\Sigma_{A_c,C_c} = \begin{bmatrix} \mathcal{J}_{A_c,\mathcal{H}} \\ \mathcal{J}_{C_c,H} \end{bmatrix} \Sigma_{\mathcal{H}} \begin{bmatrix} \mathcal{J}_{A_c,\mathcal{H}} \\ \mathcal{J}_{C_c,\mathcal{H}} \end{bmatrix}^T, \Sigma_{\tilde{A}_c,\tilde{C}_c} = \begin{bmatrix} \mathcal{J}_{\tilde{A}_c,\tilde{\mathcal{H}}} \\ \mathcal{J}_{\tilde{C}_c,\tilde{\mathcal{H}}} \end{bmatrix} \Sigma_{\tilde{\mathcal{H}}} \begin{bmatrix} \mathcal{J}_{\tilde{A}_c,\tilde{\mathcal{H}}} \\ \mathcal{J}_{\tilde{C}_c,\tilde{\mathcal{H}}} \end{bmatrix}^T \tag{6.13}$$

In thw following section, for real and complex cases, the covariance of the transfer matrices $R(s)$ and $\tilde{R}(s)$ are computed in the healthy and damaged states for a chosen s-value, and details are stated in Section 4.2.2.2.

Real case: $s = 0$**,** $\delta R \in \mathbb{R}^{r \times r}$
Consider the real case where $\delta R \in \mathbb{R}^{r \times r}$. For healthy state, the sensitivity of $R(s) \in \mathbb{R}^{r \times r}$ with respect to the system matrix A_c and C_c is derived as follows

$$vec(\Delta R(s)) = \mathcal{J}_{R(s),A_c,C_c} \begin{bmatrix} vec(\Delta A_c) \\ vec(\Delta C_c) \end{bmatrix}, \tag{6.14}$$

with $\mathcal{J}_{R(s),A_c,C_c} = [\mathcal{J}_{R(s),A_c}\ \mathcal{J}_{R(s),C_c}] \in \mathbb{R}^{r^2 \times (n^2+nr)}$ where all details are derived in Section 4.2.2.2. Similarly, for damaged case, the sensitivity of $\tilde{R}(s)$ with respect to the system matrix $\tilde{A}_c$ and $\tilde{C}_c$ is derived as

$$vec(\Delta \tilde{R}(s)) = \mathcal{J}_{\tilde{R}(s),\tilde{A}_c,\tilde{C}_c} \begin{bmatrix} vec(\Delta \tilde{A}_c) \\ vec(\Delta \tilde{C}_c) \end{bmatrix}, \tag{6.15}$$

where $\mathcal{J}_{\tilde{R}(s),\tilde{A}_c,\tilde{C}_c} = [\mathcal{J}_{\tilde{R}(s),\tilde{A}_c}\ \mathcal{J}_{\tilde{R}(s),\tilde{C}_c}] \in \mathbb{R}^{r^2\times(n^2+nr)}$. The system matrices are computed from the damage and undamaged sates on different independent measurements. So, combining this results with (6.3), the following covariance expression of $\delta R(s)$ is obtained as

$$\Sigma_{\delta R(s)} = cov(\delta R(s)) = \mathcal{J}_{R(s),A_c,C_c}\Sigma_{A_c,C_c}\mathcal{J}^T_{R(s),A_c,C_c} + \mathcal{J}_{\tilde{R}(s),\tilde{A}_c,\tilde{C}_c}\Sigma_{\tilde{A}_c,\tilde{C}_c}.\mathcal{J}^T_{\tilde{R}(s),\tilde{A}_c,\tilde{C}_c}. \quad (6.16)$$

Complex case: $\delta R \in \mathbb{C}^{r\times r}$

Consider the complex case where $\delta R \in \mathbb{C}^{r\times r}$. For healthy state, the sensitivity of $R(s) \in \mathbb{C}^{r\times r}$ with respect to the system matrix A_c and C_c is derived as follows

$$vec(\Delta R(s)) = \mathcal{J}^c_{R(s),(A_c,C_c)}\begin{bmatrix} vec(\Delta A_c) \\ vec(\Delta C_c) \end{bmatrix}, \quad (6.17)$$

with $\mathcal{J}^c_{R(s),(A_c,C_c)} = [\mathcal{J}^c_{R(s),A_c}\ \mathcal{J}^c_{R(s),C_c}] \in \mathbb{C}^{r^2\times(n^2+nr)}$. After stacking the real and imaginary parts of $\mathrm{vec}(\Delta R(s))$, it follows from (6.11)

$$\mathrm{vec}(\Delta R(s))_{\mathrm{re}} = \mathcal{J}_{R(s),(A_c,C_c)}\begin{bmatrix}\mathrm{vec}(\Delta A_c)\\ \mathrm{vec}(\Delta C_c)\end{bmatrix}, \quad (6.18)$$

where

$$\mathcal{J}_{R(s),(A_c,C_c)} = \begin{bmatrix}\Re(\mathcal{J}^c_{R(s),A_c}) & \Re(\mathcal{J}^c_{R(s),C_c})\\ \Im(\mathcal{J}^c_{R(s),A_c}) & \Im(\mathcal{J}^c_{R(s),C_c})\end{bmatrix}.$$

Similarly, for damaged case, the sensitivity of $\tilde{R}(s)$ with respect to the system matrix $\tilde{A}_c$ and $\tilde{C}_c$ is derived as

$$vec(\Delta \tilde{R}(s)) = \mathcal{J}^c_{\tilde{R}(s),(\tilde{A}_c,\tilde{C}_c)}\begin{bmatrix} vec(\Delta \tilde{A}_c) \\ vec(\Delta \tilde{C}_c) \end{bmatrix}, \quad (6.19)$$

where $\mathcal{J}^c_{\tilde{R}(s),(\tilde{A}_c,\tilde{C}_c)} = [\mathcal{J}^c_{\tilde{R}(s),\tilde{A}_c}\ \mathcal{J}^c_{\tilde{R}(s),\tilde{C}_c}] \in \mathbb{C}^{r^2\times(n^2+nr)}$. After stacking the real and imaginary parts of $\mathrm{vec}(\Delta\tilde{R}(s))$, then it follows from (6.11)

$$\mathrm{vec}(\Delta \tilde{R}(s))_{\mathrm{re}} = \mathcal{J}_{\tilde{R}(s),(\tilde{A}_c,\tilde{C}_c)}\begin{bmatrix}\mathrm{vec}(\Delta \tilde{A}_c)\\ \mathrm{vec}(\Delta \tilde{C}_c)\end{bmatrix}, \quad (6.20)$$

where

$$\mathcal{J}_{\tilde{R}(s),(\tilde{A}_c,\tilde{C}_c)} = \begin{bmatrix}\Re(\mathcal{J}^c_{\tilde{R}(s),\tilde{A}_c}) & \Re(\mathcal{J}^c_{\tilde{R}(s),\tilde{C}_c})\\ \Im(\mathcal{J}^c_{\tilde{R}(s),\tilde{A}_c}) & \Im(\mathcal{J}^c_{\tilde{R}(s),\tilde{C}_c})\end{bmatrix}.$$

Since the system matrices are computed from the damage and undamaged states on different statistically independent measurements, the covariance of $\delta R(s)$ follows with (6.3)

$$\Sigma_{\delta R(s)} = cov(\delta R(s)) = \mathcal{J}_{R(s),(A_c,C_c)}\Sigma_{A_c,C_c}(\mathcal{J}_{R(s),(A_c,C_c)})^T + \mathcal{J}_{\tilde{R}(s),(\tilde{A}_c,\tilde{C}_c)}\Sigma_{\tilde{A}_c,\tilde{C}_c}.(\mathcal{J}_{\tilde{R}(s),(\tilde{A}_c,\tilde{C}_c)})^T. \quad (6.21)$$

6.4 Case-1: Statistical tests for rank 1

In this case, u_1 being the first left singular vectors constitutes the image of the transfer matrix δR. The Influence Line (IL) l_j is computed from the Finite Element(FE) model of the structure. In the ILDL it is checked if the IL l_j lies in the image of δR, i.e. in the span of u_1 in the rank 1-case. Estimates of u_1 vectors are random variables. The uncertainties in the data are afflicted to the damage localization results. To distinguish between random variables that are estimated from data and their expected values, we use the notation with " $\hat{}$ " for the estimates.

In the following, the uncertainty expressions are first derived for the case when u_1 is real-valued, i.e. for the case when $s = 0$. In a second step, the results are generalized to the case where u_1 is complex-valued for arbitrary s.

6.4.1 Real case, rank 1

Consider the case $s = 0$ where $\delta R \in \mathbb{R}^{r\times r}$ is a rank 1 matrix. The SVD of its estimates

$$\widehat{\delta R} = \begin{bmatrix} \hat{u}_1 & \hat{U}_2 \end{bmatrix} \begin{bmatrix} \hat{\sigma}_1 & 0 \\ 0 & 0 \end{bmatrix} \begin{bmatrix} \hat{v}_1^T \\ \hat{V}_2^T \end{bmatrix}.$$

In this case, we can check directly if the influence line l_j corresponds to the image u_1 of the change in flexibility. Since the singular vectors are defined up to a sign change, we need to check if

$$\gamma_{j-} \stackrel{\text{def}}{=} \hat{u}_1 - l_j/||l_j|| = 0, \tag{6.22}$$

or if

$$\gamma_{j+} \stackrel{\text{def}}{=} \hat{u}_1 + l_j/||l_j|| = 0, \tag{6.23}$$

for each element j.

In the following, we start with an analysis of the statistical properties of $\hat{u}_1$.

6.4.1.1 Statistical properties of image estimate

The asymptotic covariance associated to δR yields

$$\sqrt{N}\text{vec}(\widehat{\delta R} - \delta R) \xrightarrow{d} \mathcal{N}(0, \Sigma_{\delta R}),$$

where $\widehat{\delta R}$ is estimated on N data samples. Consider an estimate $\hat{u}_1$ of u_1. Application of the delta method yields with Section 3.3

$$\sqrt{N}(\hat{u}_1 - u_1) \xrightarrow{d} \mathcal{N}(0, \Sigma_{u_1}), \tag{6.24}$$

where, since δR has rank 1, [LLM08]

$$\Sigma_{u_1} = \mathcal{J}_{u_1,\delta R}\, \Sigma_{\delta R}\, \mathcal{J}_{u_1,\delta R}^T \in \mathbb{R}^{r\times r}, \quad \mathcal{J}_{u_1,\delta R} = \sigma_1^{-1} v_1^T \otimes (I_r - u_1 u_1^T) \in \mathbb{R}^{r\times r^2}.$$

Proposition 6.1 *The rank of $\mathcal{J}_{u_1,\delta R}$ is $r-1$, and it holds in particular $u_1^T \mathcal{J}_{u_1,\delta R} = 0$.*

Proof: It holds

$$\mathcal{J}_{u_1,\delta R} = \sigma_1^{-1} v_1^T \otimes U_2 U_2^T = U_2(\sigma_1^{-1} v_1^T \otimes U_2^T), \tag{6.25}$$

thus $u_1^T \mathcal{J}_{u_1,\delta R} = 0$ and $\text{rank}(\mathcal{J}_{u_1,\delta R}) \leq r-1$.

On the other side, let w be a vector in the left null space of $\mathcal{J}_{u_1,\delta R}$, thus

$$w^T(v_1^T \otimes (I_r - u_1 u_1^T)) = v_1^T \otimes (w^T - w^T u_1 u_1^T) = 0.$$

Since $v_1 \neq 0$ it follows

$$w = u_1 u_1^T w,$$

and plugging in $w = \alpha u_1 + U_2 \beta$ for some scalar α and vector $\beta \in \mathbb{R}^{r-1}$, it follows $w = \alpha u_1$ since u_1 and U_2 are orthogonal. Hence, u_1 is the only vector in the left null space of $\mathcal{J}_{u_1,\delta R}$, so the rank of $\mathcal{J}_{u_1,\delta R}$ is $r-1$. □

Corollary 6.2 *The image vector u_1 is in the null space of Σ_{u_1}, as well as in the null space of $\Sigma_{u_1}^\dagger$.*

Proof: Since $\Sigma_{u_1} = \mathcal{J}_{u_1,\delta R} \Sigma_{\delta R} \mathcal{J}_{u_1,\delta R}^T$, the relation $\Sigma_{u_1} u_1 = 0$ follows directly from Proposition 6.1.

It follows with (6.25)

$$\Sigma_{u_1} = U_2(\sigma_1^{-1} v_1^T \otimes U_2^T) \Sigma_{\delta R} (\sigma_1^{-1} v_1 \otimes U_2) U_2^T, \tag{6.26}$$

and since U_2 has orthogonal columns (and U_2^T orthogonal rows),

$$\Sigma_{u_1}^\dagger = U_2 \left((\sigma_1^{-1} v_1^T \otimes U_2^T) \Sigma_{\delta R} (\sigma_1^{-1} v_1 \otimes U_2) \right)^\dagger U_2^T, \tag{6.27}$$

thus $\Sigma_{u_1}^\dagger u_1 = 0$.

□

Since $\mathcal{J}_{u_1,\delta R}$ is not full row rank, Σ_{u_1} is rank deficient. Assuming that $\Sigma_{\delta R}$ is positive definite and thus full rank, the rank of Σ_{u_1} is $r-1$, following Proposition 6.1. Hence, the normal distribution (6.24) is degenerate and special care needs to be taken for its evaluation in a hypothesis test in the following sections. Two versions are presented in the following. First, the degenerate distribution is directly taken into account in evaluating (6.22) and (6.23), and second, the degenerate distribution of these vectors is circumvented by comparing their elements separately.

6.4.1.2 Version 1: residual vectors with degenerate normal distribution for Statistical ILDL (R1v-S-ILDL)

Based on (6.22) and (6.23), define the asymptotical Gaussian residuals from the estimates of u_1,

$$\zeta_{j-} \stackrel{\text{def}}{=} \sqrt{N}(\hat{u}_1 - l_j / ||l_j||) \tag{6.28}$$

and

$$\zeta_{j+} \stackrel{\text{def}}{=} \sqrt{N}(\hat{u}_1 + l_j/||l_j||) \tag{6.29}$$

for each element j.

If j is the damaged element, l_j is in the image of δR. Thus, either ζ_{j-} or ζ_{j+} converge to a Gaussian variable with zero mean in this case, yielding either

$$\zeta_{j-} \xrightarrow{d} \mathcal{N}(0, \Sigma_{u_1}) \tag{6.30}$$

or

$$\zeta_{j+} \xrightarrow{d} \mathcal{N}(0, \Sigma_{u_1}), \tag{6.31}$$

following from (6.24).

If j is not the damaged element, the CLT's

$$\sqrt{N}(\hat{u}_1 - l_j/||l_j|| - (u_1 - l_j/||l_j||)) \xrightarrow{d} \mathcal{N}(0, \Sigma_{u_1}) \tag{6.32}$$

and

$$\sqrt{N}(\hat{u}_1 + l_j/||l_j|| - (u_1 + l_j/||l_j||)) \xrightarrow{d} \mathcal{N}(0, \Sigma_{u_1}) \tag{6.33}$$

hold, so the respective residuals can be approximated for a sufficiently large, fixed N by

$$\zeta_{j-} \approx \mathcal{N}(\mu_{j-}, \Sigma_{u_1}), \tag{6.34}$$

where $\mu_{j-} = \sqrt{N}(u_1 - l_j/||l_j||)$, and

$$\zeta_{j+} \approx \mathcal{N}(\mu_{j+}, \Sigma_{u_1}), \tag{6.35}$$

where $\mu_{j+} = \sqrt{N}(u_1 + l_j/||l_j||)$.

Based on distributions (6.30)–(6.31) and (6.34)–(6.35), it can be tested if element j is damaged or not with a generalized likelihood ratio test. Since Σ_{u_1} is rank deficient, the respective test statistics write as

$$t_{j-} = \zeta_{j-}^T \Sigma_{u_1}^\dagger \zeta_{j-}, \tag{6.36}$$

and

$$t_{j+} = \zeta_{j+}^T \Sigma_{u_1}^\dagger \zeta_{j+}, \tag{6.37}$$

respectively. With [RM71, Thm. 7.3] it follows that t_{j-} and t_{j+} are asymptotically χ^2 distributed with $\text{rank}(\Sigma_{u_1}) = r - 1$ degrees of freedom.

Consider now the non-centrality parameter of t_{j-}. Both cases $u_1 = l_j/||l_j||$ and $u_1 \neq l_j/||l_j||$ can be considered at the same time for the evaluation of the non-centrality parameter, since the mean of (6.34) for the latter case is indeed zero for $u_1 = l_j/||l_j||$, as in (6.30). Following [RM71, Thm. 7.3], the non-centrality parameter of t_{j-} is $\delta_{j-} = \mu_{j-}^T \Sigma_{u_1}^\dagger \mu_{j-}$, where $\mu_1 = \sqrt{N}(u_1 - l_j/||l_j||)$ is the mean of the underlying Gaussian vector. From Corollary 6.2, $\Sigma_{u_1}^\dagger u_1 = 0$, it follows

$$\delta_{j-} = \frac{N}{||l_j||^2} l_j^T \Sigma_{u_1}^\dagger l_j. \tag{6.38}$$

Note that in the case, where j is actually the damaged element, either $u_1 = l_j/||l_j||$ or $u_1 = -l_j/||l_j||$ holds, and since $\Sigma_{u_1}^{\dagger} u_1 = 0$ it follows $\Sigma_{u_1}^{\dagger} l_j = 0$ in *both* cases. Hence, $\delta_{j-} = 0$ for *either* case when j is the damaged element.

Analogously, consider the non-centrality parameter of t_{j+}. Both cases $u_1 = -l_j/||l_j||$ and $u_1 \neq -l_j/||l_j||$ can be considered at the same time, since the mean of (6.35) for the latter case is indeed zero for $u_1 = -l_j/||l_j||$, as in (6.31). Following [RM71, Thm. 7.3], the non-centrality parameter of t_{j+} is $\delta_{j+} = \mu_{j+}^T \Sigma_{u_1}^{\dagger} \mu_{j+}$, where $\mu_{j+} = \sqrt{N}(u_1 + l_j/||l_j||)$ is the mean of the underlying Gaussian vector. From Corollary 6.2 it follows

$$\delta_{j+} = \frac{N}{||l_j||^2} l_j^T \Sigma_{u_1}^{\dagger} l_j. \tag{6.39}$$

Note that when j is actually the damaged element and either $u_1 = l_j/||l_j||$ or $u_1 = -l_j/||l_j||$ holds, it follows $\delta_{j+} = 0$ for *either* case.

From these properties, specifically from (6.38) and (6.39), it follows that both test statistics (6.36) and (6.37) are actually equivalent. Their non-centrality parameter $\delta_{j-} = \delta_{j+}$ is zero when j is the damaged element, and

$$\delta_j \overset{\text{def}}{=} \delta_{j-} = \delta_{j+} = \frac{N}{||l_j||^2} l_j^T \Sigma_{u_1}^{\dagger} l_j \tag{6.40}$$

when j is undamaged.

Remark 6.3 *Consistent estimates of the tests are achieved by replacing Σ_{u_1} by its estimate,*

$$t_{j-} = \zeta_{j-}^T \widehat{\Sigma}_{u_1}^{\dagger} \zeta_{j-}, \quad t_{j+} = \zeta_{j+}^T \widehat{\Sigma}_{u_1}^{\dagger} \zeta_{j+}.$$

When $\widehat{\Sigma}_{u_1}$ is obtained from the same realization $\hat{u}_1$ that is used in the computation of the residuals, it actually holds $t_{j-} = t_{j+}$ due to Corollary 6.2, besides the asymptotic equivalence of both tests. In this case, the test variables boil down to

$$t_{j-} = t_{j+} = \frac{N}{||l_j||^2} l_j^T \widehat{\Sigma}_{u_1}^{\dagger} l_j.$$

Note that this is still a random variable due to the random nature of estimate $\widehat{\Sigma}_{u_1}$, and is asymptotically χ^2 distributed as described above.

6.4.1.3 Version 2: element-wise tests of residual vector for Statistical ILDL (R1e-S-ILDL)

In this section, the damage localization indicators are derived for real case for rank 1, to check if $\frac{l_j}{||l_j||} = u_1$ or $\frac{l_j}{||l_j||} = -u_1$ element-wise.

As the singular vectors are defined up to a sign change, the following expression is recalled from (6.22)-(6.23) as

$$\gamma_{j-} \overset{\text{def}}{=} u_1 - l_j/||l_j||$$

and

$$\gamma_{j+} \stackrel{\text{def}}{=} u_1 + l_j/||l_j||$$

for each element j. In the following, version-1 is modified separately as an element-wise tests of the residual vector, such as

$$\gamma^i_{j-} = \begin{bmatrix} \gamma^1_{j-} \\ \vdots \\ \gamma^r_{j-} \end{bmatrix}, \; i = 1 \cdots r. \tag{6.41}$$

and

$$\gamma^i_{j+} = \begin{bmatrix} \gamma^1_{j+} \\ \vdots \\ \gamma^r_{j+} \end{bmatrix}. \tag{6.42}$$

In damaged case, the expected values of all these components are zero for one of both vectors. The deterministic evaluation of this indicator is proposed as follows. We consider the maximum value of $\{\gamma^i_{j-}\}$ and $\{\gamma^i_{j+}\}$ for the positive and negative direction of the image vectors u_1, then take the minimum value between the maximum of $\{\gamma^i_{j-}\}$ and $\{\gamma^i_{j+}\}$ for each element j.

So, compute

$$\gamma^{max}_{j-} = max\{\gamma^1_{j-}, \cdots, \gamma^r_{j-}\} \text{ and } \gamma^{max}_{j+} = max\{\gamma^1_{j+}, \cdots, \gamma^r_{j+}\}$$

and then take the least value between them as

$$\text{damage indicator} = min\{\gamma^{max}_{j-}, \gamma^{max}_{j+}\}. \tag{6.43}$$

Statistical tests for damage indicator

Following (6.2), all components in ζ^i_{j-} (6.28) and ζ^i_{j+} (6.29), $i = 1 \cdots r$ corresponding to an element j are evaluated in a statistical test separately with (6.3)

$$t^i_{j-} = {\zeta^i_{j-}}^T \widehat{\Sigma}^{i\dagger}_{u_1} \zeta^i_{j-} = (\zeta^i_{j-})^2 / \widehat{\Sigma}^i_{u_1} \tag{6.44}$$

and

$$t^i_{j+} = {\zeta^i_{j+}}^T \widehat{\Sigma}^{i\dagger}_{u_1} \zeta^i_{j+} = (\zeta^i_{j+})^2 / \widehat{\Sigma}^i_{u_1}, \tag{6.45}$$

where $\widehat{\Sigma}^i_{u_1}$ is i-th diagonal element of $\widehat{\Sigma}_{u_1}$. Similar to previous expression (6.43), consider the maximum value of t^i_{j-} and t^i_{j+} for each element j respectively since $\gamma_{j-} \in \mathbb{R}^{r\times 1}$ and $\gamma_{j+} \in \mathbb{R}^{r\times 1}$,

$$t^{max}_{j-} = max\{t^1_{j-}, \cdots, t^r_{j-}\}$$

and

$$t^{max}_{j+} = max\{t^1_{j+}, \cdots, t^r_{j+}\}$$

and then take the least value between them as a damage indicator for

$$\text{statistical test} = min\{t_{j-}^{max}, t_{j+}^{max}\}. \tag{6.46}$$

In the damaged case, the expected values of all components of either γ_{j-} or γ_{j+} are zero for one of both vectors, so we pick-out the maximum value for each of χ^2-values. To choose in the worst case scenarios for each of those vectors which the damaged case should be zero, and we then take the minimal value from them (t_{j-}^{max} and t_{j+}^{max}).

6.4.2 Complex case, rank 1

The results of the previous section are now generalized to the case where s is arbitrary and u_1 is complex-valued. Consider the case where $\delta R \in \mathbb{C}^{r\times r}$ is a rank 1 matrix, with SVD

$$\delta R = \begin{bmatrix} u_1 & U_2 \end{bmatrix} \begin{bmatrix} \sigma_1 & 0 \\ 0 & 0 \end{bmatrix} \begin{bmatrix} v_1^H \\ V_2^H \end{bmatrix}.$$

Since u_1 is a complex-valued vector from the SVD of δR, it is defined up to some phase angle ϕ. Thus, testing if influence line l_j corresponds to the estimated image $\hat{u}_1$, we need to check if

$$\gamma_j \overset{\text{def}}{=} u_1 e^{\mathrm{i}\phi} - l_j/||l_j|| = 0 \tag{6.47}$$

for any element j and phase angle ϕ.

6.4.2.1 Statistical properties of image estimate

The asymptotic covariance associated to an estimate of δR yields

$$\sqrt{N}\text{vec}(\widehat{\delta R} - \delta R)_{\text{re}} \xrightarrow{d} \mathcal{N}(0, \Sigma_{\delta R})$$

where $\Sigma_{\delta R} \in \mathbb{R}^{2r^2\times 2r^2}$. Since δR has rank 1, it follows from [LLM08]

$$\Delta u_1 = \mathcal{J}^c_{u_1,\delta R}\text{vec}(\Delta\delta R), \quad \mathcal{J}^c_{u_1,\delta R} = \sigma_1^{-1} v_1^T \otimes (I_r - u_1 u_1^H) \in \mathbb{C}^{r\times r^2}$$

and thus, in real terms,

$$\Delta(u_1)_{\text{re}} = \mathcal{J}_{u_1,\delta R}\text{vec}(\Delta\delta R)_{\text{re}}, \quad \mathcal{J}_{u_1,\delta R} = (\mathcal{J}^c_{u_1,\delta R})_{\text{Re}} \in \mathbb{R}^{2r\times 2r^2}.$$

Consider an estimate $\hat{u}_1$ of u_1. Application of the delta method yields, hence,

$$\sqrt{N}(\hat{u}_1 - u_1)_{\text{re}} \xrightarrow{d} \mathcal{N}(0, \Sigma_{u_1}), \quad \Sigma_{u_1} = \mathcal{J}_{u_1,\delta R}\Sigma_{\delta R}\mathcal{J}^T_{u_1,\delta R} \tag{6.48}$$

Analogous to Proposition 6.1 and Corollary 6.2, it follows:

Proposition 6.4 *The rank of $\mathcal{J}^c_{u_1,\delta R}$ is $r-1$, and it holds in particular $u_1^H\mathcal{J}^c_{u_1,\delta R} = 0$ and equivalently $(u_1)^T_{\text{re}}\mathcal{J}_{u_1,\delta R} = 0$. The image vector $(u_1)_{\text{re}}$ is in the null space of Σ_{u_1}, as well as in the null space of $\Sigma^\dagger_{u_1}$.*

Hence, the normal distribution (6.48) is degenerate and special care needs to be taken for its evaluation in a hypothesis test in the following sections, where in addition the non-uniqueness due to any phase angle ϕ needs to be considered. Analogously, two versions are presented in the following. First, the degenerate distribution is directly taken into account in evaluating (6.47), and second, the degenerate distribution of these vectors is circumvented by comparing their elements separately.

6.4.2.2 Version 1: residual vectors with degenerate normal distribution for Statistical ILDL (R1v-S-ILDL)

Based on (6.47), define the asymptotical real-valued Gaussian residual from the estimate of u_1,

$$\zeta_j \stackrel{\text{def}}{=} \sqrt{N}(\hat{u}_1 e^{\mathrm{i}\phi} - l_j/||l_j||)_{\text{re}} \tag{6.49}$$

for any ϕ. Analogously to the results in (6.30), (6.32), (6.34) and (6.36), it follows that the test statistic

$$t_j \stackrel{\text{def}}{=} \zeta_j^T \Sigma_{u_1}^{\dagger} \zeta_j \tag{6.50}$$

is χ^2 distributed. It follows with Proposition 6.4 that its non-centrality parameter is

$$\delta_j = \frac{N}{||l_j||^2} (l_j)_{\text{re}}^T \Sigma_{u_1}^{\dagger} (l_j)_{\text{re}},$$

independently of ϕ. Hence, the residual (6.49) can be written with any phase angle ϕ, in particular with $\phi = 0$, since the resulting test statistic (6.50) is independent from it.

Analogously to Remark 6.3, when estimating the covariance Σ_{u_1} with the estimate $\hat{u}_1$ that is also used in the test statistic, its computation boils down to

$$t_j = \frac{N}{||l_j||^2} (l_j)_{\text{re}}^T \widehat{\Sigma}_{u_1}^{\dagger} (l_j)_{\text{re}} \tag{6.51}$$

due to Proposition 6.4.

6.4.2.3 Version 2: element-wise tests of residual vector for Statistical ILDL (R1e-S-ILDL)

In this case, the following expression is recalled from (6.47) to check if

$$\gamma_j \stackrel{\text{def}}{=} u_1 e^{\mathrm{i}\phi} - l_j/||l_j|| = 0$$

for any element j and phase angle ϕ. In the following, version 1 is modified separately as an element-wise tests of the residual vector, such as

$$\gamma_j^i = \begin{bmatrix} \gamma_j^1 \\ \vdots \\ \gamma_j^r \end{bmatrix}, i = 1 \cdots r.$$

In damaged case, the expected values of all these components are zero for the appropriately chosen phase angle ϕ. To ensure the correct phase angle in the damaged case, so that γ_j can actually become zero, ϕ needs to be chosen such that $l_j/||l_j|| = u_1 e^{\mathrm{i}\phi}$. It follows $u_1^H l_j/||l_j|| = e^{\mathrm{i}\phi}$, so ϕ can be computed as

$$\phi = \arctan(\Im(u_1^H l_j/||l_j||)/\Re(u_1^H l_j/||l_j||)).$$

For a deterministic evaluation, we consider the maximum value of γ_j^i for each element j. Since $\gamma_j \in \mathbb{R}^{r\times 1}$, consider the maximum value of γ_j^i for each element j respectively,

$$\gamma_j^{max} = max\{\gamma_j^1, \cdots, \gamma_j^r\}. \tag{6.52}$$

Statistical tests for damage indicator

Following (6.2), all components in ζ_j^i (6.49), $i = 1 \cdots r$ corresponding to an element j are evaluated in a statistical test with (6.50)

$$t_j^i = {\zeta_j^i}^T (\widehat{\Sigma}_{u_1}^i)^\dagger \zeta_j^i = (\zeta_j^i)^2/(\widehat{\Sigma}_{u_1}^i) \tag{6.53}$$

where $\widehat{\Sigma}_{u_1}^i$ is i-th diagonal element of $\widehat{\Sigma}_{u_1}$. Similar to previous expression (6.52), consider the maximum value of t_j^i for each element j as a statistical test since $\gamma_j \in \mathbb{R}^{r\times 1}$,

$$t_j^{max} = max\{t_j^1, \cdots, t_j^r\} \tag{6.54}$$

This statistical expression is meaningful, since in the damaged case the expected values of all components of γ_j are zero, so we pick-out the maximum value for each of χ^2-values. To choose in the worst case scenarios for each of those vectors which the damaged case should be zero.

6.5 Case-2: Arbitrary rank case with damage indicator, $\gamma_j = (I - U_1 {U_1}^H) l_j$ for Statistical ILDL (R*-S-ILDL)

For general case, the damage localization indicator can be defined as follows

$$\gamma_j = (I - U_1 {U_1}^H) l_j, \tag{6.55}$$

recall that U_1 is the image of the $\delta R(s)$ and l_j is the Influence Line (IL) computed from the Finite Element (FE) model of the structure.
For real case, the damage indicator (6.55) can be expressed as

$$\gamma_j = (I_{r,r} - U_1 {U_1}^T) l_j, \tag{6.56}$$

where I is the identity matrix of size $r \times r$, $U_1 \in \mathbb{R}^{r\times t}$ is the image of the $\delta R(0) \in \mathbb{R}^{r\times r}$ and $l_j \in \mathbb{R}^{r\times 1}$.

Let t be the rank of $\delta R(s)$. In the following sections, the uncertainty propagation to the damage localization results (6.56) are computed for the respective real $U_1 \in \mathbb{R}^{r\times t}$ and complex matrices $U_1 \in \mathbb{C}^{r\times t}$.

6.5.1 Real case

Consider the real case where $\delta R \in \mathbb{R}^{r \times r}$. Now, the covariance propagation to U_1 in the image of $\delta R(s) \in \mathbb{R}^{r \times r}$ is computed based on the the following expression

$$vec(\Delta U_1) = \mathcal{J}_{U_1} vec(\Delta \delta R(s)), \tag{6.57}$$

where the sensitivity $\mathcal{J}_{U_1}$ is derived in Proposition 2.

Proposition 6.5 *For real case, consider $\delta R(s) \in \mathbb{R}^{r \times r}$. Let $\sigma_i > 0$, u_i and v_i be the i-th singular value, left and right singular vector of the real matrix $\delta R(s) \in \mathbb{R}^{r \times r}$. The sensitivity of U_1 in the image of $\delta R(s) \in \mathbb{R}^{r \times r}$ is derived with [DMBM13, Lemma.6]*

$$\mathcal{J}_{U_1} = 1/\sigma_i \begin{bmatrix} I_r & (-\delta R)/\sigma_i \\ (-\delta R^T)/\sigma_i & I_r \end{bmatrix}^{\dagger} \begin{bmatrix} {v_i}^T \otimes (I_r - u_i {u_i}^T) \\ ({u_i}^T \otimes (I_r - v_i {v_i}^T)) \mathcal{P}_{r,r} \end{bmatrix}, \tag{6.58}$$

where I_r is identity matrix of size $r \times r$ and $\mathcal{P}_{r,r}$ is the permutation matrix defined in (6.10).

Applying the product rule in (6.56), a first-order perturbation ΔU_1 is propagated to a perturbation, γ_j, yields

$$\Delta \gamma_j = vec(-U_1^T \Delta U_1^T l_j - I \Delta U_1^T U_1^T l_j).$$

With the property of $\text{vec}(AXB) = (B^T \otimes A)\text{vec}(X)$ for any matrix X, the above expression can be written as

$$\Delta \gamma_j = (-{l_j}^T \otimes U_1) vec(\Delta {U_1}^T) - (({U_1}^T l_j)^T \otimes I) vec(\Delta U_1)$$

From (6.10), it follows that $vec(\Delta {U_1}^T) = \mathcal{P}_{r,t}(vec(\Delta U_1))$. Hence, the covariance of γ_j can be formulated as follows

$$\Delta \gamma_j \quad = \quad \mathcal{J}_{\gamma_j}(vec(\Delta U_1)). \tag{6.59}$$

with sensitivity $\mathcal{J}_{\gamma_j} = (-{l_j}^T \otimes U_1)\mathcal{P}_{r,t} - {l_j}^T U_1 \otimes I_{r,r}$. The system matrices are obtained on different statistically independent measurements from healthy and damaged states. So, combining this results with (6.16), the following covariance expression yields

$$\Sigma_{\gamma_j} = cov(\gamma_j) = \mathcal{J}_{\gamma_j} \mathcal{J}_{U_1} \mathcal{J}_{R(s)} \Sigma_{A_c, C_c} \mathcal{J}_{R(s)}^T \mathcal{J}_{U_1}^T \mathcal{J}_{\gamma_j}^T + \mathcal{J}_{\gamma_j} \mathcal{J}_{U_1} \mathcal{J}_{\tilde{R}(s)} \Sigma_{\tilde{A}_c, \tilde{C}_c} \mathcal{J}_{\tilde{R}(s)}^T \mathcal{J}_{U_1}^T \mathcal{J}_{\gamma_j}^T. \tag{6.60}$$

Statistical evaluation of χ_j^2-test for γ_j :

All components in (6.56) corresponding to an element j are being tested for a hypothesis test where all computed values depends on their covariance. For each element j, a scaler χ_j^2 test is derived as

$$\chi_j^2 = \gamma_j^T \Sigma_j^{-1} \gamma_j. \tag{6.61}$$

Finally, if tested element is being 0 then it's potentially damaged element.

6.5.2 Complex case

For complex case, let $U_1 \in \mathbb{C}^{r\times t}$ is a singular vector in the image of $\delta R(s) \in \mathbb{C}^{r\times r}$ with $t = \text{rank}(\delta R(s))$. Then damage localization indicator (6.55) can be rewritten together with (6.11) as follows

$$\gamma^c_{j_{\text{re}}} = (I_{2r,2r} - U_{1_{\text{Re}}} {U_{1_{\text{Re}}}}^T) l_{j_{\text{re}}} \tag{6.62}$$

In order to compute, the variance of damage localization residual, the covariance of the image u are needed, which is a singular vector in the image of $\delta R(s) \in \mathbb{C}^{r\times r}$. After stacking the real and imaginary parts of vec$(\Delta\delta R)$, it follows from (6.10) and (6.11)

$$vec(\Delta U_{1_{\text{Re}}}) = \mathcal{J}_{U_{1_{\text{Re}}}} (vec(\Delta\delta R(s)))_{\text{re}}. \tag{6.63}$$

Where the sensitivity $\mathcal{J}_{U_{1_{\text{Re}}}}$ is derived in Proposition 3.

Proposition 6.6 *For complex case, $\delta R(s) \in \mathbb{C}^{r\times r}$. Let $\sigma_i > 0$, u_i and v_i be the i-th singular value, left and right singular vector of complex matrix $\delta R \in \mathbb{C}^{r\times r}$ for rank t. After SVD of δR,*

$$\delta R(s) = U\Sigma V^T = \sum_{i=1}^{r} \sigma_i \bar{u}_i \bar{v}_i^H = \sum_{i=1}^{r} \sigma_i (e^{\mathrm{i}\phi_i} u_i)(e^{\mathrm{i}\phi_i} v_i)^H. \tag{6.64}$$

Let H be the Hermitian and ϕ_i be chosen such that the imaginary part of the first entry of $e^{\mathrm{i}\phi_i}\bar{v}_i$ and define the respective singular vectors by $\bar{u}_i = e^{\mathrm{i}\phi_i} u_i$ and $\bar{v}_i = e^{\mathrm{i}\phi_i} v_i$. Where $u_i = [u_1, ...u_t] \in \mathbb{C}^{r\times t}$ be the image of $\delta R(s) \in \mathbb{C}^{r\times r}$ in the SVD. The sensitivity of U_{1re} are derived for complex case as follows with [DMBM13, Lemma.7]

$$\mathcal{J}_{U_{1_{re}}} = B_i^{\dagger} C_i \tag{6.65}$$

$$\text{Where } B_i^{\dagger} \overset{\text{def}}{=} \begin{bmatrix} I_{2r} & (-\delta R)_{\text{Re}}/\sigma_i \\ (-\delta R^T)_{\text{Re}}/\sigma_i) & I_{2r} \end{bmatrix} (I_{4r} - E^{4r,4r}_{3r+1,3r+1}),$$

$$C_i \overset{\text{def}}{=} 1/\sigma_i \begin{bmatrix} ({v_i}^T \otimes I_r)_{\text{Re}} - (u_i)_{\text{re}}((\bar{v}_i \otimes u_i)_{\text{re}})^T \\ (({u_i}^T \otimes I_r)_{\text{Re}} - (v_i)_{\text{re}}((\bar{u}_i \otimes v_i)_{\text{re}})^T) P_1 \end{bmatrix},$$

$$P_1 \overset{\text{def}}{=} \begin{bmatrix} \mathcal{P}_{r,r} & 0 \\ 0 & \mathcal{P}_{r,r} \end{bmatrix}.$$

$$\mathcal{J}_{U_{1_{\text{Re}}}} \overset{\text{def}}{=} \begin{bmatrix} I_{2rt} \\ I_t \otimes \begin{bmatrix} 0_{r,r} & -I_{r,r} \\ I_{r,r} & 0_{r,r} \end{bmatrix} \end{bmatrix} \mathcal{J}_{U_{1_{\text{re}}}}.$$

Applying the product rule in (6.55), a first-order perturbation of vec$(\Delta U_{1\text{Re}})$ is propagated to a perturbation on $\Delta\gamma_{j_{\text{re}}}$, yields

$$\Delta\gamma_{j_{\text{re}}} = vec(-U_{1_{\text{Re}}}^T \Delta U_{1_{\text{Re}}}^T l_{j_{re}} - I\Delta U_{1_{\text{Re}}}^T U_{1_{\text{Re}}}^T l_{j_{\text{re}}}).$$

With the property of $\text{vec}(AXB) = (B^T \otimes A)\text{vec}(X)$ for any matrix X, the above expression can be written as

$$\Delta\gamma_{j_{\text{re}}} = (-{l_{j_{\text{re}}}}^T \otimes U_{1_{\text{Re}}})vec(\Delta {U_{1_{\text{Re}}}}^T) - (({U_{1_{\text{Re}}}}^T l_{j_{\text{re}}})^T \otimes I)vec(\Delta U_{1_{\text{Re}}})$$

From (6.10), it follows that $vec(\Delta {U_{1_{\text{Re}}}}^T) = \mathcal{P}_{2r,2t}(vec(\Delta U_{1_{\text{Re}}}))$. Then, the covariance of $\gamma_{j_{\text{re}}}$ can be simplified as

$$\Delta\gamma_{j_{\text{re}}} \quad = \quad \mathcal{J}_{\gamma_{j_{\text{re}}}}(vec(\Delta U_{1_{\text{Re}}})), \tag{6.66}$$

with $\mathcal{J}_{\gamma_{j_{\text{re}}}} = (-{l_{j_{\text{re}}}}^T \otimes U_{1_{\text{Re}}})\mathcal{P}_{2r,2t} - {l_{j_{\text{re}}}}^T U_{1_{\text{Re}}} \otimes I_{2r,2r}$. Combining this results with (6.21), the following covariance expression is obtained

$$\begin{aligned}\Sigma_{\gamma_j^c} = cov(\gamma_{j_{\text{re}}}^c) = \mathcal{J}_{\gamma_{j_{\text{re}}}}\mathcal{J}_{U_{1_{\text{Re}}}}\mathcal{J}^c_{\tilde{R}(s),A_c,C_c}\Sigma_{A_c,C_c}(\mathcal{J}^c_{\tilde{R}(s),A_c,C_c})^T\mathcal{J}^T_{U_{1_{\text{Re}}}}\mathcal{J}^T_{\gamma_{j_{\text{re}}}} \\ +\mathcal{J}_{\gamma_{j_{\text{re}}}}\mathcal{J}_{U_{1_{\text{Re}}}}\mathcal{J}_{\tilde{R}(s),\tilde{A}_c,\tilde{C}_C}\Sigma_{\tilde{A}_c,\tilde{C}_c}(\mathcal{J}_{\tilde{R}(s),\tilde{A}_c,\tilde{C}_C})^T\mathcal{J}^T_{U_{1_{\text{Re}}}}\mathcal{J}^T_{\gamma_{j_{\text{re}}}},\end{aligned} \tag{6.67}$$

since the system matrices are obtained on different statistically independent measurements data from healthy and damaged states.

Statistical evaluation of χ_j^2-test for γ_j^c:

After stacking the real and imaginary parts of γ_j^c in (6.56) for a chosen s-value, it follows as

$$\bar{\gamma}_j^c = \left[\ \gamma_j^c(s)_{\text{re}}\ \right]. \tag{6.68}$$

Then, all components in $\bar{\gamma}_j^c$ corresponding to an element j are being tested for a hypothesis test where all computed values depends on their covariance. For each element j, a scaler χ_j^2 test is derived.
Let $\bar{\gamma}_j \in \mathbb{R}^{2n_j}$ be the selection matrix that identifies all entries computed for an element j in the subspace angle $\bar{\gamma}_j^c$ and n_j be the number of the internal stresses for an element that depends on kind of the structure. For an element j, the covariance of the vector $\bar{\gamma}_j$ is taken from $\Sigma_{\gamma_j^c(s)}$ as

$$\Sigma_j = \bar{\gamma}_j\Sigma_{\gamma_j^c(s)}\bar{\gamma}_j^T \tag{6.69}$$

Since an estimate of the stress vector $\bar{\gamma}_j$ is asymptotically Gaussian distributed, it is tested in the statistical evaluation of the $\chi^2_{\gamma_j^c}$-test. Finally, if tested element is being 0 then it's potentially damaged

$$\chi^2_{\gamma_j^c} = \bar{\gamma}_j^T\Sigma_j^{-1}\bar{\gamma}_j. \tag{6.70}$$

6.6 Comparison between SDDLV and ILDL approach

- Both methods (SDDLV and ILDL) are a vibration-based damage localization approach that is based on a finite element (FE) model of the structure and modal parameters estimated from output-only measurements in the damaged and reference states of the system.

- In ILDL approach, a vector is obtained in the image U_1 of the changes in the transfer matrix between healthy and damaged states. Damage is located at elements where the subspace angle between the image and the influence line computed from the FE model is zero. The ILDL approach is complementary to the SDDLV approach, where loads in the kernel V_2 of δG are applied to a FE model to compute the stress field. Therefore, damage localization is related to this stress where it is zero or close to zero in practice.

- In the implementation of the SDDLV, usually only one vector in the null space is considered, namely the vector associated to the smallest singular value, which does not require a decision on the rank of δG. In the ILDL, all vectors in the image need to be considered, which requires a decision on the rank. Thus, in the implementation, both methods are not equivalent, since usually not all null space vectors are considered in the SDDLV, but all image vectors in the ILDL. A detailed investigation of this effect should be part of future works.

- While the SDDLV does not demand the effective dimension of the null space, this dimension is required in its statistical evaluation. Specific guidelines for the rank appear in [Ber10]. In the ILDL, the statistical tests for the arbitrary rank case are equivalent to the SDDLV when considering all null space vectors.

- Finally, the results of both methods could be combined as they are built upon the same principles but in two different ways. Hence, uncertainties may have a different impact on the evaluation in both methods. This issue should be analyzed in more detail in future work, where it could be indeed beneficial to combine both evaluations.

6.7 Conclusions

In this chapter, the ILDL approach has been extended with a statistical framework with considering uncertainties. In previous works, evaluation was done for $s = 0$, where the uncertainty quantification was tempted. Here, the damage indicator of the ILDL is reconsidered to allow an uncertainty quantification, before deriving its statistical evaluation of damage localization. For such an evaluation, the modal parameter covariance is propagated to the obtained subspace in a sensitivity-based approach. Finally, all computed values corresponding to an element are being tested for damage in a hypothesis test where the computed subspace is evaluated with their individual covariance. The proposed approach has been demonstrated on a numerical application in Chapter 10.

Chapter 7

Transfer matrix-based output-only statistical damage localization and quantification

7.1 Introduction

This chapter deals with vibration-based damage localization and quantification from output-only measurements. Based on the SDDLV and ILDL methods only the localization is possible using output-only data, but not quantification. The problems of damage localization and quantification are divided into two separate problems. First, the damaged elements are detected in statistical tests, and then, the damage is quantified only for the damaged elements. To achieve both localization and quantification, a Gaussian framework has been described in Chapter 4, where localization is performed by statistical tests on a data-driven residual with respect to different parameters from a FE model, and finally quantification is performed by estimating the parameter change corresponding to the damaged element(s). So far, this framework has only been applied to a subspace-based residual [DMZ16]. In the current work, we want to benefit from the strong theoretical properties of the transfer-matrix difference based SDDLV and ILDL methods, with the goal to combine them with the exisiting Gaussian framework to perform also damage quantification. Therefore, a new transfer matrix-based residual is proposed that is based on the SDDLV approach. The challenges are first to show the adequacy of this residual for the existing Gaussian framework, namely its asymptotic Gaussian distributions in undamaged and damaged states. Second, it needs to be linked with parameters from the FE model and respective sensitivities need to be computed analytically. Third, its covariance needs to be evaluated, which is based in part on Chapter 5. The statistical tests for fault isolation and estimation for fault quantification are then used to perform damage localization and quantification in the so-called sensitivity and minmax

approaches.

This chapter is proposed as follows. In Section 7.3, the parametrized Gaussian residual vector is defined for each mode sets and the sensitivities of the residual ζ is derived. In Section 7.4 and 7.5, the damage localization and quantification framework is detailed, respectively, and then applied on both numerical and real case applications in Chapter 11 and 13, respectively.

7.2 Framework of damage localization and quantification

In Chapter 4, the details are given for statistical damage localization and quantification. Let $\theta \in \mathbb{R}^p$ be a parameter vector that describes the monitored system in the current state, and $\theta_0 \in \mathbb{R}^p$ its value in the reference system. For damage localization and quantification we assume that damage is linked to stiffness changes. In this case, assume that θ is the collection of p stiffness parameters of the elements of the structure, where θ_0 is obtained from a finite element model. For example, the components of θ can be the stiffnesses of a mass-spring chain system, Young modulus of beam elements or it can be basically any quantity linked to damage-sensitive properties of the system.

In Chapter 4, a statistical framework has been set up for Gaussian residual vectors parametrized by θ with the purpose to decide which parts of θ have changed (for damage localization) and then to estimate this change (for damage quantification). The Gaussian residual vector $\zeta \in \mathbb{R}^h$ is computed from the measurements of the system and needs to satisfy

$$\zeta \sim \begin{cases} \mathcal{N}(0, \Sigma) & \text{in reference state} \\ \mathcal{N}(\mathcal{J}\delta, \Sigma) & \text{in damaged state,} \end{cases} \tag{7.1}$$

with $\delta = \sqrt{N}(\theta - \theta_0) \in \mathbb{R}^l$ is the unknown change in parameter vector, N is the data length used for the computation of ζ, the sensitivity matrix $\mathcal{J} \in \mathbb{R}^{h \times l}$ has full column rank and the residual covariance matrix $\Sigma \in \mathbb{R}^{h \times h}$ is positive definite.

Before introducing the statistical tests and estimators for damage localization and quantification, the damage residual functions are recalled from Section 2.2.

7.3 Transfer matrix Gaussian-residual vector

The parametrized Gaussian-residual needs to fulfill the properties of $\zeta \sim \mathcal{N}(\mathcal{J}\delta, \Sigma)$ with mean $\mathcal{J}\delta$ and covariance Σ of the residual under H_1 for a faulty system. Inspired by the SDDLV approach in Section 2.2, where the null space of the transfer matrix difference between reference and damaged states is evaluated based on mechanical properties. Here a similar residual is defined and evaluated it in the statistical framework above.

The transfer matrix of the model is recalled from (2.20) as

$$G(s) = R(s)D_c,$$

where

$$R(s) = C_c(sI - A_c)^{-1} \begin{bmatrix} C_c A_c \\ C_c \end{bmatrix}^{\dagger} \begin{bmatrix} I \\ 0 \end{bmatrix}, \tag{7.2}$$

In (7.2), I is the identity matrix of size $r \times r$, 0 is the zero matrix of size $r \times r$, and † denotes the Moore-Penrose pseudoinverse. Matrix $R(s)$ can be estimated from output-only measurements. Denote matrices in the damaged state with tilde, and matrices in the reference state without tilde. Assume that damage is due to changes in stiffness and mass is constant. Then $D_c = \tilde{D}_c$, and the matrix differences $\tilde{G}(s) - G(s)$ and $\tilde{R}(s)^T - R(s)^T$ are identical up to the multiplication by an invertible matrix.

Considering the transfer matrix for a mode set j, assume that $R(\theta) = \tilde{R}^j(s)$ and $R(\theta_0) = R^j(s)$ for a particular mode set j and Laplace-variable s can be any arbitrary value. Then, the transfer matrix differences can be defined as

$$\delta R^j(s) = \mathrm{vec}(R(\theta) - R(\theta_0))_{\mathrm{re}}, \tag{7.3}$$

which contains estimate parameter changes of the system and strictly related to θ_0. Recall that $\mathrm{vec}(\cdot)$ defines the column stacking vectorization operator. Now, consider the Taylor expansion of $\mathrm{vec}(\tilde{R}^j(s)^T)_{\mathrm{re}}$ corresponding to θ and $\mathrm{vec}(R^j(s)^T)_{\mathrm{re}}$ corresponding to θ_0 can be defined as

$$\mathrm{vec}(R(\theta))_{\mathrm{re}} \approx \mathrm{vec}(R(\theta_0))_{\mathrm{re}} + \mathcal{J}_{R,\theta}(\theta - \theta_0), \tag{7.4}$$

where $\mathcal{J}_{R,\theta} = \left.\frac{\partial \mathrm{vec}(R(s)^T)_{\mathrm{re}}}{\partial \mathrm{vec}(\theta)}\right|_{\theta=\theta_0}$ is the sensitivity matrix. Then, it follows

$$\sqrt{N}\mathrm{vec}(R(\theta) - R(\theta_0))_{\mathrm{re}} \approx \mathcal{J}_{R,\theta}\sqrt{N}(\theta - \theta_0), \tag{7.5}$$

and thus

$$\sqrt{N}\mathrm{vec}(R(\theta) - R(\theta_0))_{\mathrm{re}} \approx \mathcal{J}_{R,\theta}\,\delta. \tag{7.6}$$

Therefore, the Gaussian-residual vector can be defined as

$$\zeta \overset{\mathrm{def}}{=} \sqrt{N}\mathrm{vec}(\tilde{R}^j(s)^T - R^j(s)^T)_{\mathrm{re}}, \tag{7.7}$$

which satisfies the distribution properties of (7.1) with constant mean $\mathcal{J}_{R(s),\theta}\delta$ and covariance Σ. Note that asymptotic normality follows from the estimation of the modal parameters from subspace identification that are used in the computation of $R(s)$ and $\tilde{R}(s)$, as detailed in Section 3.2.

In the following, the sensitivity of the residuals are derived for each mode set $\mathcal{M}_j$, $j = 1, \ldots, n_s$ with respect to the physical parameter of the system subsequently the covariance expression are also derived based on the residuals.

7.3.1 Sensitivity of the residual

The sensitivity of the residual $\mathrm{vec}(R^j(s))$ with respect to the modal parameters is derived in Section 4.2.2.2. To obtain the required sensitivity matrix $\mathcal{J}^j_{R(s),\theta}$, the derivative of the modal parameters $(\lambda^j_{(c,l)}, \varphi^j_l)$ with respect to the structural parameters is computed for each mode

set $\mathcal{M}_j$, starting from the eigenvalues $\lambda_{c,l}^j$ and mode shapes φ_l^j, $l = 1, \ldots, m_j$, for each mode set j.

Denote $\lambda_c^j = [\lambda_{c,1}^j ... \lambda_{c,m_j}^j]$ and $\varphi^j = [\varphi_1^j ... \varphi_{m_j}^j]$ the collection of eigenvalues and mode shapes of mode set j. This yields

$$\mathcal{J}_{R(s),\theta}^j = \mathcal{J}_{R(s),(\lambda_c,\varphi)}^j \mathcal{J}_{(\lambda_c,\varphi),\theta}^j \tag{7.8}$$

Considering the first derivative, it holds

$$\mathcal{J}_{R(s),(\lambda_c,\varphi)}^j = \left[\frac{\partial \mathrm{vec}(R^j(s))}{\partial (\lambda_c)_{\mathrm{re}}} \;\middle|\; \frac{\partial \mathrm{vec}(R^j(s))}{\partial \mathrm{vec}(\varphi)_{\mathrm{re}}} \right],$$

where both parts are directly obtained from (3.7).

The eigenvalues and mode shapes $(\lambda_{(c,l)}, \varphi_l^j)$ are linked to the changes of the physical parametrization of the system due to stiffness loss. For the sensitivity analysis, the partial derivative of the modal parameters can be derived with respect to the system parameter θ. Following [HLS98], the partial derivatives of the eigenvalues λ_l and mode shapes φ_l with respect to a parameter θ change are derived through,

$$\frac{\partial \lambda_l}{\partial \theta_k} = -\frac{1}{a_l} \phi_l^T \frac{\partial K(\theta)}{\partial \theta_k} \phi_l, \tag{7.9}$$

$$\text{and} \quad \frac{\partial \varphi_l}{\partial \theta_k} = \sum_{i=1, i \neq l}^{m_j} \frac{1}{a_i} \frac{1}{\lambda_i - \lambda_l} \phi_i^T \frac{\partial K(\theta)}{\partial \theta_k} \phi_l \varphi_i + \sum_{i=1}^{m_j} \frac{1}{a_i^*} \frac{1}{\lambda_l^* - \lambda_l} \phi_i^H \frac{\partial K(\theta)}{\partial \theta_k} \phi_l \varphi_i^* \tag{7.10}$$

where

$$a_i = 2\lambda_i \phi_i^T M \phi_i + \phi_i^T C \phi_i$$

"$*$" denotes the complex conjugate and "H" the conjugate transpose, and ϕ_i are the eigenvectors of system (2.1) at all DOFs. Note that φ_i is equal to the components of ϕ_i at the sensor DOFs. Assembling the real and imaginary parts of (7.9) and (7.10) for $l = 1, \ldots, m_j$ in the rows and for $k = 1, \ldots, p$ in the columns leads to the Jacobian matrix. Plugging this derivative into (7.8) yields the desired derivative of the transfer matrix resultant to the structural parameters,

$$\mathcal{J}_{(\lambda,\phi),\theta}^j = \begin{bmatrix} \frac{\partial (\lambda_c)_{\mathrm{re}}}{\partial \theta} \\ \frac{\partial \mathrm{vec}(\phi)_{\mathrm{re}}}{\partial \theta} \end{bmatrix}. \tag{7.11}$$

7.3.2 Covariance of the residual

The covariance of the residual vectors ζ in (7.7) is obtained in both reference and damaged states of the structure for a chosen s-value. The uncertainty of the residual is related to the uncertainty of the Hankel matrix in both states. Hence, the covariance propagation to the

residuals ζ in both states is computed based on the following relation together with (7.6) and (7.7), similar to Section 5.4.3

$$\begin{aligned}(\mathrm{vec}\triangle\zeta^j(s))_{\mathrm{re}} &= \mathcal{J}^j_{\tilde{R}(s)^T,(\tilde{A}_c,\tilde{C}_c)}\begin{bmatrix}\mathrm{vec}(\triangle\tilde{A}^j_c)\\ \mathrm{vec}(\triangle\tilde{C}^j_c)\end{bmatrix} - \mathcal{J}^j_{R(s)^T,(A_c,C_c)}\begin{bmatrix}\mathrm{vec}(\triangle A^j_c)\\ \mathrm{vec}(\triangle C^j_c)\end{bmatrix}\\ &= \tilde{\mathcal{J}}^j_{\tilde{R}(s)^T,(\tilde{A}_c,\tilde{C}_c)}\tilde{\mathcal{J}}^j_{(\tilde{A}_c,\tilde{C}_c),\tilde{\mathcal{H}}}\mathrm{vec}(\triangle\tilde{\mathcal{H}}) - \mathcal{J}^j_{R(s)^T,(A_c,C_c)}\mathcal{J}^j_{(A_c,C_c),\mathcal{H}}\mathrm{vec}(\triangle\mathcal{H})\\ &= \tilde{\mathcal{J}}^j_{\tilde{R}(s),\tilde{\mathcal{H}}}\mathrm{vec}(\triangle\tilde{\mathcal{H}}) - \mathcal{J}^j_{R(s),\mathcal{H}}\mathrm{vec}(\triangle\mathcal{H}),\end{aligned} \tag{7.12}$$

where $\tilde{\mathcal{J}}^j_{\tilde{R}(s),\tilde{\mathcal{H}}} = \tilde{\mathcal{J}}^j_{\tilde{R}(s)^T,(\tilde{A}_c,\tilde{C}_c)}\tilde{\mathcal{J}}^j_{(\tilde{A}_c,\tilde{C}_c),\tilde{\mathcal{H}}}$ with $\tilde{\mathcal{J}}^j_{(\tilde{A}_c,\tilde{C}_c),\tilde{\mathcal{H}}} \overset{\mathrm{def}}{=} \begin{bmatrix}\mathcal{J}_{\tilde{A}^j_c,\tilde{\mathcal{H}}}\\ \mathcal{J}_{\tilde{C}^j_c,\tilde{\mathcal{H}}}\end{bmatrix}$ and $\mathcal{J}^j_{R(s),\mathcal{H}} = \mathcal{J}^j_{R(s)^T,(A_c,C_c)}\mathcal{J}^j_{(A_c,C_c),\mathcal{H}}$ with $\mathcal{J}^j_{(A_c,C_c),\mathcal{H}} \overset{\mathrm{def}}{=} \begin{bmatrix}\mathcal{J}_{A^j_c,\mathcal{H}}\\ \mathcal{J}_{C^j_c,\mathcal{H}}\end{bmatrix}$ have been derived in Section 5.4.2, and the respective sensitivity matrices are detailed in Section 5.4.3. Following (7.12), the covariance expression of the residuals are defined, $\Sigma^j_\zeta(s) = \mathrm{cov}(\zeta^j(s))$ as follows

$$\begin{aligned}\Sigma^j_\zeta(s) &= \mathcal{J}^j_{\tilde{R}(s)^T,(\tilde{A}_c,\tilde{C}_c)}\begin{bmatrix}\mathrm{vec}(\triangle\tilde{A}^j_c)\\ \mathrm{vec}(\triangle\tilde{C}^j_c)\end{bmatrix}\mathcal{J}^j_{\tilde{R}(s)^T,(\tilde{A}_c,\tilde{C}_c)}{}^T + \mathcal{J}^j_{R(s)^T,(A_c,C_c)}\begin{bmatrix}\mathrm{vec}(\triangle A^j_c)\\ \mathrm{vec}(\triangle C^j_c)\end{bmatrix}\mathcal{J}^j_{R(s)^T,(A_c,C_c)}{}^T\\ &= \tilde{\mathcal{J}}^j_{\tilde{R}(s),\tilde{\mathcal{H}}}\Sigma_{\tilde{\mathcal{H}}}\mathcal{J}^j_{\tilde{R}(s),\tilde{\mathcal{H}}}{}^T + \mathcal{J}^j_{R(s),\mathcal{H}}\Sigma_{\mathcal{H}}\mathcal{J}^j_{R(s),\mathcal{H}}{}^T.\end{aligned} \tag{7.13}$$

7.3.3 Joint evaluation of the residuals

Assume that the residual vector $\zeta^j(s)$ is evaluated at a possibly different s-value $s = s^j$ from (7.7) for each mode set $\mathcal{M}_j$, $j = 1,\ldots,n_s$. After stacking the real and imaginary parts of the residual vectors, the total residual vector is derived as

$$\zeta \overset{\mathrm{def}}{=} \begin{bmatrix}\mathrm{vec}(\tilde{R}^1(s^1)^T - R^1(s^1)^T)_{\mathrm{re}}\\ \vdots\\ \mathrm{vec}(\tilde{R}^{n_s}(s^{n_s})^T - R^{n_s}(s^{n_s})^T)_{\mathrm{re}}\end{bmatrix}, \tag{7.14}$$

and its uncertainty follows from (7.12) as

$$\triangle\zeta = \begin{bmatrix}\tilde{\mathcal{J}}^1_{\tilde{R}(s^1),\tilde{\mathcal{H}}}\\ \vdots\\ \tilde{\mathcal{J}}^{n_s}_{\tilde{R}(s^{n_s}),\tilde{\mathcal{H}}}\end{bmatrix}\mathrm{vec}(\triangle\tilde{\mathcal{H}}) - \begin{bmatrix}\mathcal{J}^1_{R(s^1),\mathcal{H}}\\ \vdots\\ \mathcal{J}^{n_s}_{R(s^{n_s}),\mathcal{H}}\end{bmatrix}\mathrm{vec}(\triangle\mathcal{H}) \tag{7.15}$$

Note that vector ζ contains the information for all mode sets at all elements of the structure. Together with (5.8) and (7.13), the covariance $\Sigma \overset{\text{def}}{=} \text{cov}(\zeta)$ of the total residual ζ yields

$$\Sigma = \begin{bmatrix} \tilde{\mathcal{J}}^1_{\tilde{R}(s^1),\tilde{\mathcal{H}}} \\ \vdots \\ \tilde{\mathcal{J}}^{n_s}_{\tilde{R}(s^{n_s}),\tilde{\mathcal{H}}} \end{bmatrix} \Sigma_{\tilde{\mathcal{H}}} \begin{bmatrix} \tilde{\mathcal{J}}^1_{\tilde{R}(s^1),\tilde{\mathcal{H}}} \\ \vdots \\ \tilde{\mathcal{J}}^{n_s}_{\tilde{R}(s^{n_s}),\tilde{\mathcal{H}}} \end{bmatrix}^T + \begin{bmatrix} \mathcal{J}^1_{R(s^1),\mathcal{H}} \\ \vdots \\ \mathcal{J}^{n_s}_{R(s^{n_s}),\mathcal{H}} \end{bmatrix} \Sigma_{\mathcal{H}} \begin{bmatrix} \mathcal{J}^1_{R(s^1),\mathcal{H}} \\ \vdots \\ \mathcal{J}^{n_s}_{R(s^{n_s}),\mathcal{H}} \end{bmatrix}^T \tag{7.16}$$

since the datasets from healthy and damaged states can be regarded as statistically independent. This covariance expression is derived based on the parameterized Gaussian residual vector ζ. Similarly, for the multiple mode sets, the sensitivity of the residuals (7.8) with respect to the parameter θ are stacked together as

$$\mathcal{J} = \begin{bmatrix} \mathcal{J}^1_{R(s^1),\theta} \\ \vdots \\ \mathcal{J}^{n_s}_{R(s^{n_s}),\theta} \end{bmatrix}. \tag{7.17}$$

From the above derivation, the sensitivity $\mathcal{J}$ and covariance expression Σ are known that are estimated based on the parametric Gaussian residual vector containing the faulty components of the system. In the Gaussian framework, the properties of $\zeta \sim \mathcal{N}(\begin{bmatrix} \mathcal{J}^1_{R(s^1),\theta} \\ \vdots \\ \mathcal{J}^{n_s}_{R(s^{n_s}),\theta} \end{bmatrix} \delta, \Sigma)$ are satisfied with constant mean $(\begin{bmatrix} \mathcal{J}^1_{R(s^1),\theta} \\ \vdots \\ \mathcal{J}^{n_s}_{R(s^{n_s}),\theta} \end{bmatrix} \delta)$ and covariance Σ. Based on this residual distribution, the damage localization corresponds to which components of the δ are non-zero and the damage quantification corresponds to estimate the changes δ of the damaged elements can be performed in the framework of the statistical tests with the sensitivity and minmax approaches described in the Section (7.4) .

7.3.4 Joint evaluation of the residuals using Multiple mode sets for different s-values

In the previous section, the residuals (7.14) was derived using only one Laplace variable for each mode set, while there is a possibility to use several Laplace variables. Therefore, the computation of the residuals in (7.7) can be easily generalized for several Laplace variables (s-values) such as

$$\zeta^t = \text{vec}(\tilde{R}^j(s^j_w)^T - R^j(s^j_w)^T)_{\text{re}}$$

for each mode set $\mathcal{M}_j$ denoted by s^j_w, where $w = 1, ..., \kappa^j$ and κ^j is the number of s-values used for mode set $\mathcal{M}_j$. After stacking the real and imaginary parts of the residuals vectors

for multiple s-values and mode sets, the joint evaluation of the residuals vector is written as analogously

$$\zeta^t = \begin{bmatrix} \mathrm{vec}(\tilde{R}^1(s_1^1)^T - R^1(s_1^1)^T)_{\mathrm{re}} \\ \vdots \\ \mathrm{vec}(\tilde{R}^1(s_{\kappa^1}^1)^T - R^1(s_{\kappa^1}^1)^T)_{\mathrm{re}} \\ \vdots \\ \mathrm{vec}(\tilde{R}^{n_s}(s_1^{n_s})^T - R^{n_s}(s_1^{n_s})^T)_{\mathrm{re}} \\ \vdots \\ \mathrm{vec}(\tilde{R}^{n_s}(s_{\kappa^{n_s}}^{n_s})^T - R^{n_s}(s_{\kappa^{n_s}}^{n_s})^T)_{\mathrm{re}} \end{bmatrix}. \tag{7.18}$$

Then covariance of the residuals (7.18) with respect to different s-values can be derived together with (7.16) for mode sets $\mathcal{M}_j$, $j = 1, \ldots, n_s$, as

$$\Sigma = \tilde{\mathcal{J}}_{\tilde{R}(s),\tilde{\mathcal{H}}} \Sigma_{\tilde{\mathcal{H}}} \tilde{\mathcal{J}}^T_{\tilde{R}(s),\tilde{\mathcal{H}}} + \mathcal{J}_{R(s),\mathcal{H}} \Sigma_{\mathcal{H}} {\mathcal{J}_{R(s),\mathcal{H}}}^T \tag{7.19}$$

where

$$\tilde{\mathcal{J}}_{\tilde{R}(s),\tilde{\mathcal{H}}} = \begin{bmatrix} \tilde{\mathcal{J}}^1_{\tilde{R}(s_1^1),\tilde{\mathcal{H}}} \\ \vdots \\ \tilde{\mathcal{J}}^1_{\tilde{R}(s_{\kappa^1}^1),\tilde{\mathcal{H}}} \\ \vdots \\ \tilde{\mathcal{J}}^{n_s}_{\tilde{R}(s_1^{n_s}),\tilde{\mathcal{H}}} \\ \vdots \\ \tilde{\mathcal{J}}^{n_s}_{\tilde{R}(s_{\kappa^{n_s}}^{n_s}),\tilde{\mathcal{H}}} \end{bmatrix}, \quad \mathcal{J}_{R(s),\mathcal{H}} = \begin{bmatrix} \mathcal{J}^1_{R(s_1^1),\mathcal{H}} \\ \vdots \\ \mathcal{J}^1_{R(s_{\kappa^1}^1),\mathcal{H}} \\ \vdots \\ \mathcal{J}^{n_s}_{R(s_1^{n_s}),\mathcal{H}} \\ \vdots \\ \mathcal{J}^{n_s}_{R(s_{\kappa^{n_s}}^{n_s}),\mathcal{H}} \end{bmatrix}.$$

Analogously to the previous section, the covariance expression (7.19) is derived based on the residuals vector in a statistical aggregation scheme for multiple mode sets using several s-values. Then, Gaussian distribution of the residual as follows

$$\zeta \sim \mathcal{N}\left(\begin{bmatrix} \mathcal{J}^1_{R(s_1^1),\theta} \\ \vdots \\ \mathcal{J}^1_{R(s_{\kappa^1}^1),\theta} \\ \vdots \\ \mathcal{J}^{n_s}_{R((s_1^{n_s}),\theta} \\ \vdots \\ \mathcal{J}^{n_s}_{R((s_{\kappa^{n_s}}^{n_s}),\theta} \end{bmatrix} \delta, \Sigma \right)$$

with mean ($\begin{bmatrix} \mathcal{J}^1_{R(s^1_1),\theta} \\ \vdots \\ \mathcal{J}^1_{R(s^1_{\kappa^1}),\theta} \\ \vdots \\ \mathcal{J}^{n_s}_{R((s^{n_s}_1),\theta} \\ \vdots \\ \mathcal{J}^{n_s}_{R((s^{n_s}_{\kappa^{n_s}}),\theta} \end{bmatrix}$ δ) of the non-centrality parameter and covariance Σ of the residual.

In the following section, the statistical tests and estimators for damage localization and quantification are presented, it is recalled here shortly from Section 4.3.3 and 4.3.4 in Chapter 4.

7.4 Damage localization

From the previous section, the sensitivity $\mathcal{J}$ and covariance expression Σ are known that are estimated based on the parametric Gaussian residual vector containing the faulty components of the system. Recall that θ be the parameters of the structure. In the statistical tests, the damage localization corresponds to which components of the $\delta = \theta - \theta_0$ are non-zero (i.e. $\delta \neq 0$) and the damage quantification corresponds to estimate the changes of δ in the damaged elements.

For making decision about damage localization, it has to be known which components of δ are non-zero by testing each components of δ separately. Assuming that different partitions of the vector δ into 2 subvectors,

$$\delta = \begin{bmatrix} \delta_a \\ \delta_b \end{bmatrix}, \tag{7.20}$$

where one of the sub-vectors are tested. For damage localization, $\delta_a = 0$ is tested against $\delta_a \neq 0$. Following (7.20), the sensitivity $\mathcal{J}$ and the Fisher information matrix $F = \mathcal{J}^T \Sigma^{-1} \mathcal{J}$ are analogously derived as follows

$$\mathcal{J} = \begin{bmatrix} \mathcal{J}_a & \mathcal{J}_b \end{bmatrix}, F = \begin{bmatrix} F_{aa} & F_{ab} \\ F_{ba} & F_{bb} \end{bmatrix} = \begin{bmatrix} \mathcal{J}_a^T \Sigma^{-1} \mathcal{J}_a & \mathcal{J}_a^T \Sigma^{-1} \mathcal{J}_b \\ \mathcal{J}_b^T \Sigma^{-1} \mathcal{J}_a & \mathcal{J}_b^T \Sigma^{-1} \mathcal{J}_b \end{bmatrix}, \tag{7.21}$$

details are given in Section 4.3.3. In the following section, the sensitivity and minmax tests have taken into account for damage localization and quantification.

7.4.1 Senstivity test

Assuming that $\delta_b = 0$ for testing $\delta_a = 0$ against $\delta_a \neq 0$, where $\zeta \sim \mathcal{N}(\mathcal{J}_a \delta_a, \Sigma)$. The generalized likelihood ratio(GLR) tests are follows as

$$t_{sens} = \zeta^T \Sigma^{-1} \mathcal{J}_a^T (\mathcal{J}_a^T \Sigma^{-1} \mathcal{J}_a)^{-1} \mathcal{J}_a^T \Sigma^{-1} \zeta, \tag{7.22}$$

which is called sensitivity test. The test statistic t_{sens} is χ^2 distributed with non-centrality parameter $\delta_a^T F_{aa} \delta_a$. For making decision about the damage location, the test variable is compared to a threshold. Generally, the threshold is chosen for a given probability of false alarms according to the $\chi 2$ distribution of the nominal system.

7.4.2 Minmax test

Instead of assuming the components of $\delta_b = 0$, the variable δ_b is substituted by its least favorable value for making a decision about δ_a, which leads to the minmax test as follows. Define the partial residuals

$$\zeta_a = \mathcal{J}_a^T \Sigma^{-1} \zeta \tag{7.23a}$$

$$\zeta_b = \mathcal{J}_b^T \Sigma^{-1} \zeta, \tag{7.23b}$$

and the robust residual

$$\zeta_a^* = \zeta_a - F_{aa} F_{bb}^{-1} \zeta,$$

whose mean is sensitive to changes δ_a but not to δ_b. Testing $\delta_a = 0$ against $\delta_a \neq 0$ with the GLR test yields

$$t_{mm} = \zeta_a^* F_a^{*-1} \zeta_a^*, \tag{7.24}$$

where $F_a^* = F_{aa} - F_{ab} F_{bb}^{-1} F_{ba}$. The test statistic t_{mm} is χ^2 distributed with non-centrality parameter $\delta_a^T F_a^* \delta_a$.

7.5 Damage quantification

In the previous sections, a decision is made for the faulty system between $\delta_a = 0$ and $\delta_a \neq 0$ in the components of δ based on the sensitivity and the minmax tests. In both tests, the test variables is compared to a threshold level to make a decision about faulty components when $\delta_a \neq 0$. In the following section, estimates of the change $\delta = \theta - \theta_0$ are derived based on the properties of the sensitivity and minmax approaches, respectively.

7.5.1 Quantification based on senstivity test

In the sensitivity approach, an estimate of the δ_a can be derived from the residual vector ζ for the damage quantification. Together with (7.21) and (7.22), the following expression can be derived

$$\hat{\delta}_a^{sens} = \left(\mathcal{J}_a^T \Sigma^{-1} \mathcal{J}_a \right)^{-1} \mathcal{J}_a^T \Sigma^{-1} \zeta, \tag{7.25}$$

where $\hat{\delta}_a^{sens} \sim \mathcal{N}(\delta_a, F_{aa}^{-1})$ for the assumption $\delta_b = 0$.

7.5.2 Quantification based on minmax test

Similarly, an estimate of the δ_a can be derived based on minmax approach in the previous section follows

$$\hat{\delta}_a^{mm} = F_a^{*-1} \zeta_a^*, \tag{7.26}$$

with $\hat{\delta}_a^{mm} \sim \mathcal{N}(\delta_a, F_a^{*-1})$, where details are given in Section 4.3.4.

7.6 Comparison to SDDLV

- In SDDLV, recall that both a Finite Element (FE) model of the structure and modal parameters estimated from output-only measurements in the damage and reference states of the system is required for vibration-based damage localization. A vector is obtained in the null space of the changes in the transfer matrix from both states and then applied as a load vector to the model. Damage localization is related to this stress field where the computed stress is zero or close to zero in practice. On the other hand, the sensitivity approach based on a data-driven residual vector that is statistically evaluated using information from a FE model. In this approach, the parameterized Gaussian residual vector is generated in both states from the measurements data in the context of SDDLV.

- The SDDLV approach is derived only to damage localization while both localization and quantification is possible in the sensitivity and minmax approaches.

- The SDDLV performs good for large damage extents because of the significant changes of the transfer matrix differences between healthy and damaged states with compared to small damage extents, while the sensitivity and minmax approaches are not good for large damage extents due to increasing error of the system parameter changes.

- In the SDDLV, the Laplace variable s has a strong influence with compared to the sensitivity and minmax approach. This is due to the fact that the SDDLV approach is based on the physical properties of the transfer matrix difference, and the choice of s is directly related to bias of the transfer matrix. With this bias, the null space of the transfer matrix difference may not be the "true" null space anymore that leads to zero stress at damaged elements, even if the modal parameters are correctly estimated. On the other hand, the sensitivity-based approaches require only the derivative of the transfer matrix, which is accurate when the modal parameters are correctly estimated (and when damage is small), independently of s.

- The statistical evaluation of the SDDLV approach and the Gaussian framework for damage localization and quantification in this chapter both rely on an asymptotical Gaussian vector, which are the stress vector for the SDDLV and the residual vector based on the transfer matrix difference, respectively. In both cases it is therefore assumed that these quantities can be approximated reasonably by a Gaussian vector when computed on finite data, which means that enough data should be available.

7.7 Conclusions

In this chapter, the transfer matrix-based residual was presented in a statistical output-only damage localization and quantification approach in a Gaussian framework based on the sensitivity and minmax tests. The residual is obtained in the context of SDDLV that is based on the transfer matrix difference between the reference and damaged states. It has an interesting property and relations to the SDDLV damage localization approach. Furthermore, it

has been extended considering a joint statistical evaluation of multiple mode sets for same or different Laplace variables. The robustness of the damage localization and quantification has been obtained by taking into account the information from all identified modes of the structure. The computation of the test values using multiple mode sets increases the information contents of the damaged or non-damaged elements of the structure. Finally, the method is applied on both numerical and real case applications in Chapters 11, 12, and 13, respectively.

7.8 Dissemination

Parts of this chapter have been published or are submitted to:

[BVD+ny] M.D.H. Bhuyan, E. Viefhues, M. Döhler, Y. Lecieux, L. Mevel, F. Hille, and F. Schoefs. Output-only subspace and transfer matrix-based damage localization and quantification. In *7th International Operational Modal Analysis Conference (IOMAC'2017)*, May 10-12, 2017, Ingolstadt, Germany.

[BAD+SA] M.D.H. Bhuyan, S. Allahdadian, M. Döhler, Y. Lecieux, L. Mevel, F. Schoefs, and C. Ventura. Transfer matrices-based output-only statistical damage localization and quantification. In *11th International Workshop on Structural Health Monitoring (IWSHM)*, September 12-14, 2017, Stanford, CA, USA.

Part III

Numerical applications

Chapter 8

Methodology for numerical applications

8.1 Introduction

This Chapter describes the methodology for damage localization based on the contribution chapters for the application of the methods in numerical case studies in the following chapters. In the contribution of thesis, three statistical damage localization methods have been proposed such as i) statistical damage localization with stochastic load vectors using multiple mode sets (SDDLV), ii) the statistical damage localization of influence lines damage localization (ILDL), and iii) the transfer-matrix based residuals for both localization and quantification using multiple mode sets. Note that details of these methods are stated in the contribution Chapters 5, 6 and 7.

In this Chapter, the presentation of the performance indicators for the developed methods and the presentation of the numerical models used for the application chapters 9, 10 and 11 is described. Based on the numerical models presented in this chapter, several case studies have been carried-out to analyze the performance of the methods, such as dependence of s-value and sensitivity to the mesh sizes for different applications. Furthermore, in Chapters 9 and 10, the methods are validated with respect to the distributions before going to apply statistical damage localization approach.

In the applications, the proposed damage localization methods have been applied on several numerical simulations depending on the complexity of the structures. There are five case studies for numerical applications, though not all of them are studied for each method.

First, the proposed method using multiple mode sets from Chapter 5 is validated on numerical simulations. A simple mass-spring chain and a more complex 3D cube beam model have been considered as numerical applications. Then, the damage localization with the SDDLV approach has been applied on a 2D beam model with different size of cracks.

Finally, the SDDLV has been investigated on a 2D beam model assuming large and small damaged zone, depending on different mesh size. To obtain these results from simulated or measured data, the modes of the system are estimated using a stabilization diagram procedure with SSI [DM12] in both reference and damaged states. They are estimated together with their covariance [DM13]. Then, the system matrices and their covariance are assembled from the modes.

Secondly, the statistical damage localization of the ILDL approach from Chapter 6 has been validated by a numerical simulation of a mass-spring chain system.

Thirdly, the transfer-matrix based approach (see Chapter 7) has been applied on two numerical simulations of a mass-spring chain and 2D beam model for damage localization and quantification.

Finally, the numerical implementation of these methods has been presented in Chapter 12 by using Abaqus software for the application of realistic FE models for more complex structures.

This chapter is formulated as follows. In Section 8.2, the presentation of the performance indicators are defined for the damage localization methods. Then different numerical models are presented in details in Section 8.3, and an overview of the different methods are stated in Section 8.4.

8.2 Performance evaluation criteria

8.2.1 Performance evaluation of damage localization

To analyze the performance of the proposed damage localization method, the success rate (or probability) of correct damage localization is evaluated for several sets of simulated measurement data. Each dataset is an independent realization and defines a Monte-Carlo experiment. In order to indicate if an element is potentially damaged or not, the χ_t^2 value has to be computed for each structural element. For each Monte-Carlo realization, damage localization is seen as successful when the lowest χ_t^2 value among all elements is indeed at the damaged element. This only holds for the SDDLV and ILDL, not for the sensitivity-based method where the maximum χ_t^2 value is important. For damage localization with single damage, there is no need to use threshold because we can simply look the minimum or maximum value depending on the methods. Here, we want to validate the methods for single damage and want to get the performance evaluation in that way. This success rate of correct damage localization is analogous to the probability of detection or power of the test in the context of hypothesis testing. Here, it is numerically evaluated as the percentage of datasets, among all Monte Carlo experiments for which the χ_t^2 value at the damaged element is the smallest χ_t^2 value for SDDLV and ILDL, and maximum χ_t^2 value for sensitivity-based method. The success rate depends on the chosen s-value(s) and the damage element, and serves as the performance indicator of the method not only - this is a general performance indicator of the method for a given structural discretization.

Note that the generation of several datasets allows the evaluation of the success rate, while in reality usually only one dataset is available.

In order to evaluate the influence of the s-values on the success rate of damage localization, each dataset in the Monte-Carlo simulations is evaluated for a set of s-values with different real and imaginary parts in order to obtain the success rate in dependence of s. The range of s-values has been chosen in the vicinity of the identified poles to reduce the effects of modal truncation in the transfer matrix [Ber10]. The resulting success rate as a function of s is presented in 3D bar diagrams, where it is plotted on the z-axis in dependence of the real and imaginary parts of s on the x and y-axis, respectively.

For simplicity, an example is shown in Figure 8.1 for each element of the structure, where the performance evaluation of the proposed method is illustrated. First, the statistical evaluation with the χ_t^2-test is obtained at one s-value using one experiment from the estimated modal parameters in both healthy and damaged states. Recall that the damage localization is inferred by the stress value closest to zero. In the statistical evaluation of the χ_t^2-test, the damage localization is found correctly at the smallest χ_t^2 values at damage element 8. Second, the success rate of correct damage localization is evaluated for Monte-Carlo experiments, where it is numerically obtained as the percentage of the simulated datasets, among all Monte-Carlo experiments for which the χ_t^2 value at the damaged element is the smallest one. The success rate (z-axis) depends on the chosen s-values (x and y-axis) and serves as the performance indicator of the method. The range of the performance indicator is between 0 to 100%. Note that 0 and 100 indicates the bad and best performance of the method, respectively.

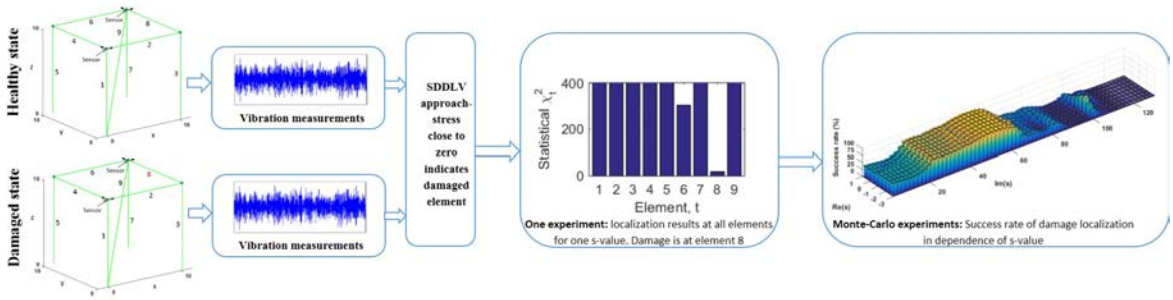

Figure 8.1 – Performance evaluation (or success rate) of damage localization in dependence of s-values (x and y-axis) with $\mathrm{Re}(s)$, $\mathrm{Im}(s)$.

Besides the presentation of the success rate of the statistical damage localization using several datasets from Monte-Carlo simulations, the statistical localization approach is compared to the underlying stress computation based on modal parameters from the model (theoretical stress) or from estimated (without statistical evaluation). The theoretical stress evaluation allows to assess the achievable localization accuracy under modal truncation, which is always present in practice. Comparing the localization results from stress estimation and its statistical evaluation allows to evaluate the importance of taking into account the statistical estimation errors in the new method.

8.2.2 Probability of Good and Wrong Localization (PGL and PWL)

For the performance evaluation in the previous section, damage localization was seen as successful when the lowest χ_t^2 value among all elements is indeed at the damaged element for the SDDLV and ILDL, or a highest χ_t^2 value for the transfer matrix sensitivty-based approach, respectively.

However, in practice damage can locate at the neighbour elements from the damaged zone. We introduced here a detection threshold in terms of distance from the true damage. Therefore, for the evaluation of the damage localization with the SDDLV approach, we proposed the Probability of Good or Wrong Localization (PGL and PWL) as a function of the detection threshold, defect size and Laplace variables [RS03, DBAPS17]. The evaluation of PGL or PWL depends on the threshold (th), defect size (x) and Laplace variable (LV). Mathematically, it can be defined as follows,

$$PGL(th, x, LV) = P(0 \leq d(x) \leq th | x, th, LV) \tag{8.1a}$$

$$\text{and } PWL(th, x, LV) = P(d(x) > th | x, th, LV), \tag{8.1b}$$

where the value of th can be considered as the required detection threshold for the localization of the damaged element. In this study, the PGL or PWL is evaluated for several sets of simulated measurement data in order to evaluate the performance of the localization method. Each dataset is an independent realization and defines a Monte-Carlo experiment.

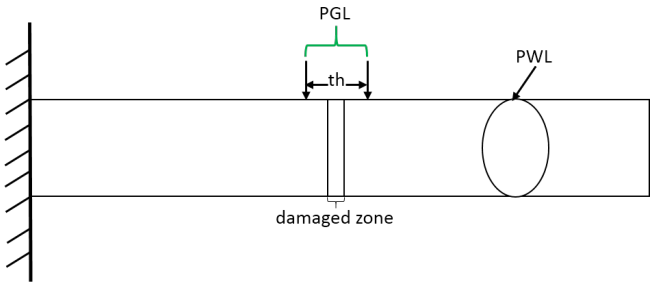

Figure 8.2 – Probability of Good or Wrong Localization (PGL or PWL) in terms of distance.

To evaluate the PGL or PWL, the following criteria can be considered for each Monte-Carlo realization:

- First, recognized the element with the smallest χ_t^2-value. If this element is one of the actually damaged ones, assume $distance, d = 0$. If not, then compute the distance from the damaged zone, where $distance, d = | \, middle \; of \; the \; recognized \; damaged \; element - middle \; of \; the \; damaged \; zone \, | - \frac{1}{2} \times width \; of \; the \; damaged \; zone$.
- Set a threshold from the damaged zone: 0, 1 cm, 2 cm, 3 cm, 4 cm,...etc. For example, in Section 8.3.3 in Figure 8.8(a), damage is located at element 13 for a damaged zone of 4 cm. In order to evaluate PGL or PWL, we set a detection threshold in terms of distance from the true damaged zone.

- If the damaged element within the range of threshold, evaluate PGL.

For each Monte-Carlo realization, damage localization is seen as successful when the lowest χ_t^2 value is located within the range of threshold level. The success rate corresponds to the probability of good localization (PGL) and it is possible to determine zones where the PGL is larger for several sets of simulated measurement data. Numerically, it is obtained as the percentage of datasets. The PGL depends on the chosen s-value(s) and serves as the performance indicator of the method in terms of distance.

General estimate for a given range of predicted defect size

Consider a damage model or the performance model of the structure which indicates certain damage distribution of the service life. There is a probability distribution of the damage. For discretization of the damage, this probability distribution is continuous in terms of defect size where the probability distribution is given by performance model or damaged model. Then, for each of those damage sizes using model, we can evaluate the probability of good damage localization. From both information, we can give an assessment of the probability of good damage localization and the distribution of damage in the service life.

Therefore, the general estimate of a given range of predicted defect size is derived from a given structure. It is obtained based on the probability of damage distribution of a predicted defect size with mean and standard deviation, and the performance evaluation of the PGL (8.1) from simulated datasets. Mathematically, the probability of the damage distribution density (PDD) can be obtained as follows

$$PDD(th, LV) = \int_x P(0 \leq d(X) \leq th|x, th, LV)\, f_x(x)\, \mathrm{d}x, \tag{8.2}$$

where $f_x(x)$ is the probability of damage distribution of a defect size (x), and note that th is threshold from the damaged zone and LV is the Laplace variable. This expression gives the density of the damage distribution for a predicted defect size.

8.3 Numerical models

In this section, different numerical models are presented for the proposed methods of damage localization and quantification. A simple mass-spring chain, beam model, crack beam, and a more complex 3D cube beam model have been considered as numerical applications. These numerical applications are idealized test cases for the validation of the new developments of the proposed methods.

For example, the behavior of a mechanical structure is described for a linear time-invariant (LTI) dynamic system in (2.1). We can formulate the derivation for an eigenvalue problem. In the absence of excitation, the expression (2.1) rewrittes and reduces to

$$M\ddot{u}(t) + C\ddot{u}(t) + Ku(t) = 0 \tag{8.3}$$

where u, $\dot{u}$ and $\ddot{u}$ are the displacement, velocity and accelerations, respectively. A general solution of this system is as follows where ω_0^2 is a simple root of the equation,

$$u = \phi e^{(\mathrm{i}\omega_0 t)}. \tag{8.4}$$

Where $\omega_0 = 2\pi f$ and $f = \omega_0/2\pi$ represents the natural frequency of the harmonic response of the system and ϕ eigenmode associated vibration. Replacing the expression of u in the equation (8.3), we can get that the natural frequency f from the following equation:

$$\left(-\omega_0^2 M + i\omega_0 C + K\right)\phi = 0 \tag{8.5}$$

If there is no damping, the above equation can be rewritten as follows,

$$K\phi = \omega_0^2 M\phi. \tag{8.6}$$

This is the characteristic equation of a generalized eigenvalue problem.

In the following, first, the numerical model of the structure is presented in details. Second, the stiffness and mass matrix of the healthy and damaged states of the structure are described. Finally, the modes of the system are estimated from simulated data using a stabilization diagram procedure with SSI [DM12, DM13], together with their covariance. Then, the system matrices and their covariance are assembled from the modes. Notice that damage is assumed to be related to stiffness loss, either stiffness reduction or crack. Note that there is uncertainty on measurements from sensors simulated by a white noise.

8.3.1 Mass-spring chain system

In a first numerical application, the damage localization method has been applied on a mass-spring chain system with six DOFs as shown in Figure 8.3. This system is a good candidate for a first application since the mechanical properties are feasible and no numerical approximations are required. The stiffness parameters are defined by the terms k_i, and the mass of all elements is 1 in suitable units. Damping is defined such that each mode has a damping ratio of 2%. Damage is simulated by decreasing the stiffness of spring 4 by 10% of its original value. For damaged and undamaged states, the acceleration data length for each set is $N = 50{,}000$. Data were generated from collocated white noise excitation using three sensors at elements 2, 4 and 6 with a sampling frequency of 50 Hz, and in addition, white measurement noise with 5% magnitude of the outputs was added.

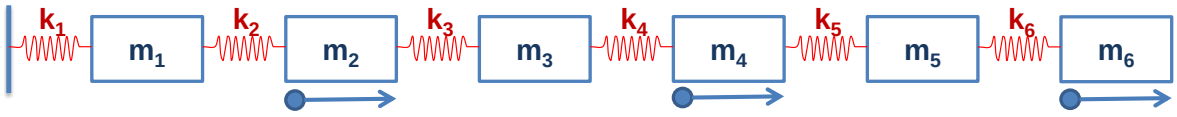

Figure 8.3 – Mass-spring chain (with modal damping) -using three sensors at elements 2, 4 and 6.

In the following, the physical stiffness and mass matrix of an element in both healthy and damaged states are described. The damage is assumed to be stiffness loss, while the mass is unchanged in both states.

For 1D element of a Mass-spring chain system, the displacement vectors can be written as follows

$$U^e = [\bar{u}_i \ \bar{u}_j]$$

where $\bar{u}_i$ and $\bar{u}_j$ are translational displacements at node i and j respectively, details are given in the literature of structural mechanics [Kri95, Bat, JNJ04]. The bar means that the displacement forces are written in the local axis. The stiffness matrix K^h for one finite element can be derived as follows

$$K^h = \frac{ES}{L}\begin{bmatrix} k_i & -k_i \\ -k_i & k_i \end{bmatrix}, \tag{8.7}$$

where E, S, L are 1 in suitable units. Considering the damage model of Mazars [MPC89, MBR90], the stiffness matrix of the damaged structure can be obtained as $K^d = (1-D)K^h$, where D is the damage parameter of the Mazars model $D \in [0, 1]$ in which 0 indicates the safe structure and 1 indicates fully damaged structure.

In the following, the global stiffness matrix of the model in Figure 8.3 for 6 DoFs can be obtained after assembling the stiffness matrix (8.7) for each of the element in the global axis.

Total stiffness and mass matrix of healthy structure

The stiffness parameters are defined as $k_1 = k_3 = k_5 = 4000$, $k_2 = k_4 = k_6 = 2000$, and the mass of all elements is 1 in suitable units in Figure 8.3. Then, the stiffness matrix of the healthy structure can be obtained as follows,

$$K^h = \begin{bmatrix} k_1+k_2 & -k_2 & 0 & 0 & 0 & 0 \\ -k_2 & k_2+k_3 & -k_3 & 0 & 0 & 0 \\ 0 & -k_3 & k_3+k_4 & -k_4 & 0 & 0 \\ 0 & 0 & -k_4 & k_4+k_5 & -k_5 & 0 \\ 0 & 0 & 0 & -k_5 & k_5+k_6 & -k_6 \\ 0 & 0 & 0 & 0 & -k_6 & k_6 \end{bmatrix}. \tag{8.8}$$

The mass matrix M^h is written as

$$M^h = \begin{bmatrix} m_1 & 0 & 0 & 0 & 0 & 0 \\ 0 & m_2 & 0 & 0 & 0 & 0 \\ 0 & 0 & m_3 & 0 & 0 & 0 \\ 0 & 0 & 0 & m_4 & 0 & 0 \\ 0 & 0 & 0 & 0 & m_5 & 0 \\ 0 & 0 & 0 & 0 & 0 & m_6 \end{bmatrix}, \tag{8.9}$$

where the mass of all elements is 1 in suitable units.

Total stiffness matrix of damaged structure

Considering the damage model of Mazars [MPC89, MBR90], the stiffness matrix of the damaged structure can be obtained as $K^d = (1-D)K^h$, where D is the damage parameter of the Mazars model $D \in [0, 1]$ in which 0 indicates the safe structure and 1 indicates fully damaged

structure. In this model, damage is simulated by decreasing the stiffness of spring 4 by 10% of its original value, with factor $D = 0.1$. Hence, damage is assumed to be related to stiffness loss in spring 4. In the following, the stiffness matrix K^d of the damaged structure can be obtained as follows,

$$K^d = \begin{bmatrix} k_1 + k_2 & -k_2 & 0 & 0 & 0 & 0 \\ -k_2 & k_2 + k_3 & -k_3 & 0 & 0 & 0 \\ 0 & -k_3 & k_3 + k_4 - D * k_4 & D * k_4 - k_4 & 0 & 0 \\ 0 & 0 & D * k_4 - k_4 & k_4 - D * k_4 + k_5 & -k_5 & 0 \\ 0 & 0 & 0 & -k_5 & k_5 + k_6 & -k_6 \\ 0 & 0 & 0 & 0 & -k_6 & k_6 \end{bmatrix}. \tag{8.10}$$

Modal analysis and uncertainties

All six modes of the structure (see Table 8.1) can be identified using stabilization diagram from the simulated measurements of the structure with subspace-based system identification as described in details in Chapter 3. Then, the system matrices A_c and C_c in both healthy and damaged states (3.2.3) are filled and their uncertainties are obtained from the same dataset as described in Section 3.3.

Using three sensors in this example, only a limited set of three modes could be used for localization in previous works [Ber10, DMBM13, MDBM15] as the number of modes cannot be bigger than the number of sensors. For the proposed method in chapter 5 and 7, all modes can be considered by using two mode sets $\mathcal{M}_1$ and $\mathcal{M}_2$ of three modes each.

Table 8.1 – Eigenfrequencies f_c and Eigenvalues λ_c of mass-spring chain model.

	Healthy state		Damaged state		
Mode	Modal freq.	Eigenvalues	Modal freq.	Eigenvalues	Mode set
1	2.0324	$-0.255 + 12.76$i	2.0106	$-0.253 + 12.63$i	$\mathcal{M}_1$
2	5.9472	$-0.747 + 37.36$i	5.8563	$-0.736 + 36.78$i	
3	9.2755	$-1.16 + 58.26$i	9.1583	$-1.15 + 57.53$i	
4	12.3762	$-1.55 + 77.74$i	12.3281	$-1.54 + 77.44$i	$\mathcal{M}_2$
5	15.6246	$-1.96 + 98.15$i	15.6224	$-1.96 + 98.13$i	
6	16.9628	$-2.13 + 106.6$i	16.7983	$-2.11 + 105.5$i	

8.3.2 Beam model with 5 elements

In this application, the proposed damage localization method from chapter 7 has been applied to a 2D Beam model as shown in Figure 8.4 for both damage localization and quantification. The structure is modeled with 5 beam elements of total length 1 m. The beam elements in the model are circular with the external diameter of 0.02 m. The mass density, Young modulus (E) and Poisson ratio (ν) are 7800 kg.m^{-3}, 207 GPa and 0.3, respectively. The

total number of Degrees Of Freedom (DOFs) of the structure are 15. For the damaged and undamaged states, the acceleration data length of each set is $N = 25{,}000$ is generated from collocated white noise excitation using three sensors in the y-direction at node 1, 4 and 5 with a sampling frequency of 3125 Hz, 1% damping ratio and 5% white noise was added to the output data.

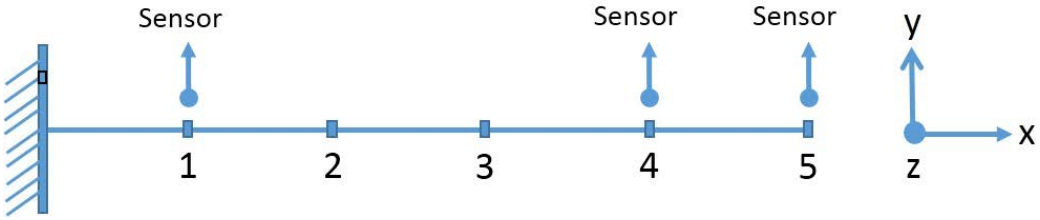

Figure 8.4 – 2D Beam model with 5 elements (15 DOFs) -using three sensors at nodes 1, 4, and 5 in y-direction

For the damage localization method, an FE model of the healthy structure and estimated modal parameters needed from simulated data in both healthy and damaged states. In the following, the physical stiffness and mass matrix of an element in both healthy and damaged states are described. The damage is assumed to be stiffness loss, while the mass is unchanged in both states.

Stiffness and mass matrix of healthy element

In a 2D beam element, each node has three degrees of freedom such as two translational displacements in the x and y-axis, and one rotational displacement along the z-axis. Figure 8.5 shows a beam element in the x-y plane, oriented along its local x-axis called $\bar{x}$. The bar means that the displacement and nodal forces are written in the local axis.

The element in Figure 8.5 has six degrees of freedom which corresponds to the following displacement vector,

$$U^e = [\bar{u}_{xi}\ \bar{u}_{yi}\ \bar{\theta}_{zi}\ \bar{u}_{xj}\ \bar{u}_{yj}\ \bar{\theta}_{zj}]^t,$$

where $\bar{u}_{xi}$, $\bar{u}_{yi}$ and $\bar{u}_{xj}$, $\bar{u}_{yj}$ are translational, and $\bar{\theta}_{zi}$ and $\bar{\theta}_{zj}$ are rotational displacements at node i and j respectively, details are given in the literature of structural mechanics [Kri95, Bat, JNJ04]. Taking into account both flexural and traction-compression stiffness K^h for one beam finite element can be derived as follows,

$$K^h = \begin{bmatrix} \frac{EA}{L} & 0 & 0 & -\frac{EA}{L} & 0 & 0 \\ 0 & \frac{12EI_z}{L^3} & \frac{6EI_z}{L^2} & 0 & -\frac{12EI_z}{L^3} & \frac{6EI_z}{L^2} \\ 0 & \frac{6EI_z}{L^2} & \frac{4EI_z}{L} & 0 & -\frac{6EI_z}{L^2} & \frac{2EI_z}{L} \\ -\frac{EA}{L} & 0 & 0 & \frac{EA}{L} & 0 & 0 \\ 0 & -\frac{12EI_z}{L^3} & -\frac{6EI_z}{L^2} & 0 & \frac{12EI_z}{L^3} & -\frac{6EI_z}{L^2} \\ 0 & \frac{6EI_z}{L^2} & \frac{2EI_z}{L} & 0 & -\frac{6EI_z}{L^2} & \frac{4EI_z}{L^2} \end{bmatrix}. \tag{8.11}$$

The mass matrix M^h is written as

$$M^h = \frac{\rho AL}{420}\begin{bmatrix} 140 & 0 & 0 & 70 & 0 & 0 \\ 0 & 156 & 22L & 0 & 54 & -13L \\ 0 & 22L & 4L^2 & 0 & 13L & -3L^2 \\ 70 & 0 & 0 & 140 & 0 & 0 \\ 0 & 54 & 13L & 0 & 156 & -22L \\ 0 & -13L & -3L^2 & 0 & -22L & 4L^2 \end{bmatrix}, \tag{8.12}$$

where E is the Young modulus, A is the cross-section area, L is the length of the element with $L_{ij} = \sqrt{(x_j - x_i) + (y_j - y_i)}$, I_z is the moment of inertia along the z-axis, and ρ is the mass density. Therefore, the global stiffness and mass matrix of the 2D beam model in Figure 8.4 can be obtained after assembling the stiffness and mass matrix (8.11)-(8.12) in the global axis for each of the element.

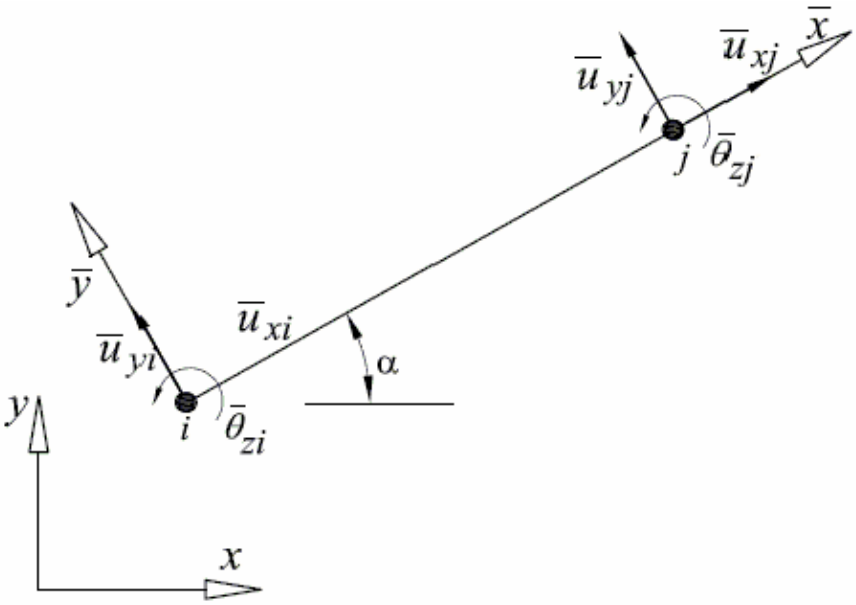

Figure 8.5 – Beam element in the x-y plane (6 DOFs)

Stiffness matrix of the damaged element

For damaged case, considering the damage model of Mazars [MPC89, MBR90], the stiffness matrix of the damaged structure is obtained as $K^d = (1 - D)K^h$, where D is the damaged parameter of the Mazars model $D \in [0, 1]$. Recall that 0 for the safe structure and 1 for fully damaged structure. In this model, damage is simulated by decreasing the stiffness at element 3 by 10% of its original value, with factor $D = 0.1$ (see Table 8.2).

Modal analysis and uncertainties

As similar to the previous example, 6 modes (see Table 8.2) can be identified using stabilization diagram from the simulated measurements of the structure with subspace-based system identification as described in details in Chapter 3. Then, the system matrices A_c and C_c in both healthy and damaged states (3.2.3) are filled and their uncertainties are obtained from the same dataset as described in Section 3.3.

In this example using three sensors, only a limited set of three modes could be used for localization in previous works [Ber10, DMBM13, MDBM15] as the number of modes cannot be bigger than the number of sensors. For the proposed method in chapter 7 for both localization and quantification, we consider the first 6 modes (see Table 8.2), split into two mode sets $\mathcal{M}_1$ and $\mathcal{M}_2$ of three modes each.

Table 8.2 – Eigenfrequencies f_c and Eigenvalues λ_c of beam model.

	Healthy state		Damaged state		
Mode	Modal freq.	Eigenvalues	Modal freq.	Eigenvalues	Mode set
1	14.4140	$-1.81131 + 90.5477\text{i}$	13.7573	$-1.80163 + 90.0637\text{i}$	$\mathcal{M}_1$
2	90.3750	$-11.3568 + 567.728\text{i}$	77.8136	$-11.1269 + 556.234\text{i}$	
3	253.834	$-31.8977 + 1594.57\text{i}$	244.832	$-31.7679 + 1588.08\text{i}$	
4	501.446	$-63.0132 + 3150.04\text{i}$	494.534	$-62.1450 + 3106.62\text{i}$	$\mathcal{M}_2$
5	832.276	$-104.586 + 5228.29\text{i}$	823.621	$-103.499 + 5173.92\text{i}$	
6	1382.64	$-173.747 + 8685.64\text{i}$	1369.44	$-172.089 + 8602.74\text{i}$	

8.3.3 Beam model for different mesh size

In this study, we present the same structure with various mesh sizes with compared to previous example in Section 8.3.2. This case is important because it governs the accuracy of the numerical solutions and the accuracy of the localization. Note that the material properties and dimensions of the beam are also similar to previous example. The damaged element in the model is simulated by multiplying all the rigidity by a factor $(1 - D)$.

To analyze the performance of the method, the following things are considered for the same dimension and material properties of the beam.

- **Case 1:** For a large damage zone of 20 cm, the damage localization method has been applied on a rough and fine mesh of 25 and 100 beam elements in Figure 8.7(a) and 8.7(b), respectively. It implies that in the first case 5 elements are damaged while in the second one 20 elements are damaged.

- **Case 2:** For a small damage zone of 4 cm, the damage localization method has been applied on a rough and fine mesh of 25 and 100 beam elements in Figure 8.7 and 8.8, respectively. It implies that in the first one 1 element is damaged while in the second one 4 elements are damaged.

- **Case 3:** For a small damage zone of 4 cm, the load vectors computed from estimated data of 100 beam elements (fine mesh) and then applied to the L_{model} of 25 elements (rough mesh). In this case, 1 element is damaged.

The aim of this study to assess the influences of the mesh size because we supposed that it influences on the modal truncation.

For both damaged and undamaged states, the acceleration data length for each set is taken $N = 200{,}000$ in order to obtain good estimated modal parameters. Data were generated from collocated white noise excitation using 5 sensors in the y-direction at 0.2 m, 0.4 m, 0.6 m, 0.8 m and 1.0 m from the fixed end with a sampling frequency of 20 kHz which is sufficient to estimate the modal parameters, 1% damping ratio, and 5% white noise were also added to the output data. Then output datasets were decimated into lower sampling rate for the accuracy of subspace identification.

As similar to the previous example in Section 8.3.2, the global mass and stiffness matrix for both healthy and damaged states are obtained after assembling the mass and stiffness matrix for each finite element beam.

In order to analyze the stiffness matrix for rough and fine mesh of beam model, for simplicity, here a simple truss element has been considered in both healthy and damaged states.

Example 1:

A truss element of length 2L is shown in Figure 8.6(a).

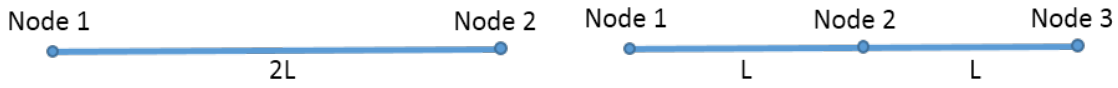

(a) Truss model with one element, 2L (b) Truss model with two elements, 2L

Figure 8.6 – Truss model of same length

The stiffness matrix of the healthy structure in Figure 8.6(a) is made of one finite element,

$$K^h_{1,2} = \frac{ES}{2L}\begin{bmatrix} 1 & -1 \\ -1 & 1 \end{bmatrix}, \tag{8.13}$$

where E, S, L are 1 in suitable units. Considering the damage model of Mazars, the stiffness matrix of the damaged structure is obtained as $K^d = (1 - D)K^h$ with factor $D = 0.5$, where D is the damage parameter of the Mazars model $D \in [0, 1]$. This follows as,

$$K^d_{1,2} = \frac{ES}{2L}(1 - D)\begin{bmatrix} 1 & -1 \\ -1 & 1 \end{bmatrix} = \frac{ES}{4L}\begin{bmatrix} 1 & -1 \\ -1 & 1 \end{bmatrix}. \tag{8.14}$$

Example 2:

The same structure, discretized into 2 elements for each length of L is shown in Figure 8.6(b). Similar to previous example, the stiffness matrix for each of the healthy element can be derived as follows,

$$K^h_{1,2} = K^h_{2,3} = \frac{ES}{L}\begin{bmatrix} 1 & -1 \\ -1 & 1 \end{bmatrix}. \tag{8.15}$$

Considering the damage model of Mazars, the stiffness matrix, $K^d = (1-D)K^h$ of the damaged structure is obtained with factor $D = 0.5$. Total stiffness is written as follows by assembling the stiffness matrix for each finite element beam,

$$K^h_{1,3} = \frac{ES}{L}\begin{bmatrix} 1 & -1 & 0 \\ -1 & 2 & -1 \\ 0 & -1 & 1 \end{bmatrix}. \tag{8.16}$$

and the associated super finite element of the healthy model is obtained considering only the external nodes of the model

$$K^h_{1,3} = \frac{ES}{2L}\begin{bmatrix} 1 & -1 \\ -1 & 1 \end{bmatrix}. \tag{8.17}$$

The stiffness matrix for each of the damaged element can be derived as follows,

$$K^d_{1,2} = K^d_{2,3} = \frac{ES}{L}(1-D)\begin{bmatrix} 1 & -1 \\ -1 & 1 \end{bmatrix}. \tag{8.18}$$

Therefore, in the following, the total stiffness matrix is obtained by assembling the stiffness matrix for each finite element beam,

$$K^d_{1,3} = \frac{ES}{L}(1-D)\begin{bmatrix} 1 & -1 & 0 \\ -1 & 2 & -1 \\ 0 & -1 & 1 \end{bmatrix}, \tag{8.19}$$

and the associated super finite element of the damaged model can be written as

$$K^d_{1,3} = \frac{ES}{2L}(1-D)\begin{bmatrix} 1 & -1 \\ -1 & 1 \end{bmatrix}. \tag{8.20}$$

From the above discussion, it is seen that the equivalent stiffness matrix are same. Between the same structure discretized with 25 or 100 elements - for case study 2 and 3 - the only change is the number of elements. Since the stiffness is unchanged, the interpretation of the results in numerical experiments performed on the rough and fine mesh will allow to discuss the sensitivity of the method to mesh size.

Modal analysis and uncertainties

As similar to the previous example, 5 well estimated modes (see Table 8.3) are identified using stabilization diagram from the simulated measurements of the structure with subspace-based system identification as described in details in Chapter 3 where the computation of the analytical beam frequency is stated in Section 13.2.2. Then, the system matrices A_c and C_c (3.2.3) are filled in both healthy and damaged states and their uncertainties are obtained from the same dataset as described in Section 3.3.

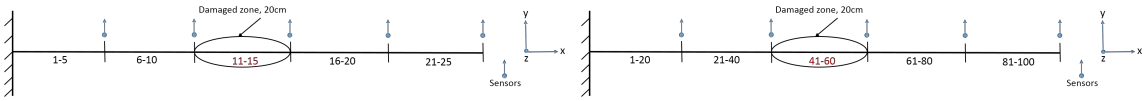

(a) 25 elements (rough mesh) (b) 100 elements (fine mesh)

Figure 8.7 – 2D Beam model on x-y plane, damaged is located between 0.41-0.60 m (large damaged zone) from the fixed end -using 5 sesnsors

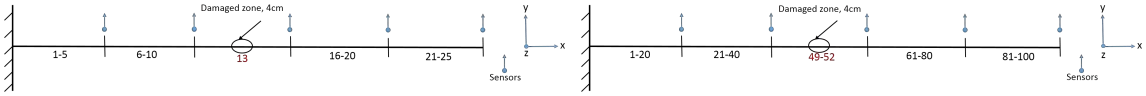

(a) 25 elements (rough mesh) (b) 100 elements (fine mesh)

Figure 8.8 – 2D Beam model on x-y plane, damaged is located between 0.49-0.52 m (small damaged zone) from the fixed end -using 5 sesnsors

Table 8.3 – Eigenfrequencies, f_c and eigenvalues, λ_c of beam model for 25 elements.

			Healthy state		Damaged state
Mode	Ana. freq	Model freq.	Eigenvalues	Model freq.	Eigenvalues
1	14.41	14.41	$-1.8113 + 90.5477$i	13.75	$-1.8016 + 90.0637$i
2	90.32	90.32	$-11.356 + 567.728$i	77.78	$-11.126 + 556.234$i
3	252.87	252.93	$-31.897 + 1594.570$i	244.02	$-31.767 + 1588.081$i
4	495.63	495.65	$-63.013 + 3150.049$i	454.25	$-62.145 + 3106.629$i
5	819.31	819.38	$-104.586 + 5228.298$i	755.41	$-103.499 + 5173.929$i

8.3.4 Beam model with crack

In the recent years, the formulation of crack beam finite element has gained an increasing attention of many researchers. To study of a cracked beam, several methods e.g. analytical and numerical methods are developed in the literature [Sek83, PD87, SP92, SR99, ZF01, ZK04]. For a cracked beam element, the main problem in using the finite element method is how to get the stiffness matrix approximately. In [ZK04] described a method to obtain the

stiffness matrix of a cracked beam element, considering same matrix size and no additonal DOFs. The formulation we choose is theoretically tracable, and validated through numerical study. Additionally, this work has been cited and used in many other works. It allow to consider a physical damage related to the size of a crack and not only a global decreasing of a stiffness matrix.

In this application, the damage localization approach with SDDLV has been applied to a 2D circular beam for crack localization as shown in Figure 8.9. Note that material properties of the beam, length and mesh size of the model are similar to previous example in Section 8.3.2. Here the diameter of the beam is 0.03 m and increasing the damage with respect to crack depth. For damaged and undamaged states, the acceleration data length for each set is $N = 100{,}000$. Data were generated from collocated white noise excitation using 5 sensors at y-direction of the beam model with a sampling frequency of 20 kHz, 2% damping ratio and 5% white noise were also added to the output data.

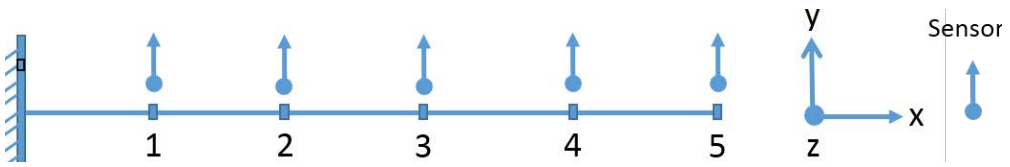

Figure 8.9 – 2D Circular beam model with 5 elements (15 DOFs) -using five sensors at nodes 1, 2, 3, 4, and 5 in y-direction

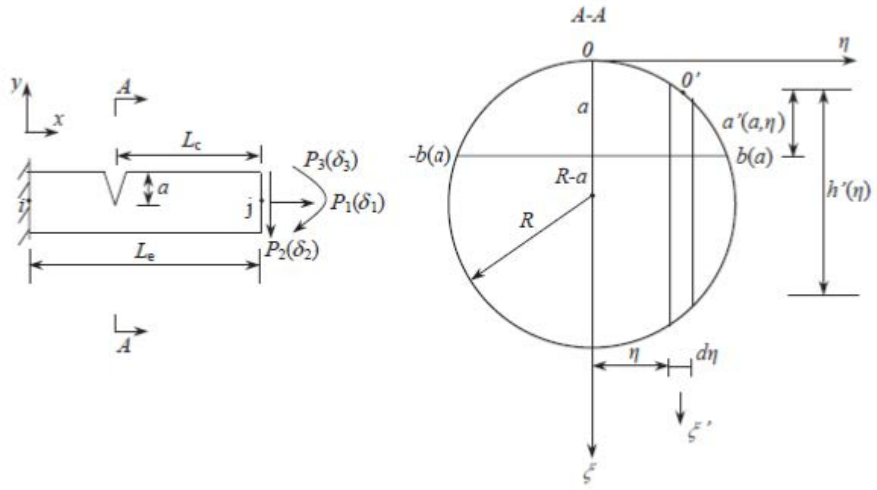

Figure 8.10 – A circular cross-sectional crack beam element [ZK04]

In the proposed method, an FE model of the healthy structure and estimated modal parameters are needed from simulated data in both healthy and damaged states. In Section 8.3.2, the stiffness and mass matrix of a healthy beam element are described. For damaged

case, the stiffness matrix of a cracked beam element can be obtained in the following.

Stiffness matrix of a cracked beam element

A typical cracked beam element with a circular cross-section is illustrated in Figure 8.10. In the figure, the node i is assumed fixed, while the node j is subjected to axial force P_1, shearing force P_2 and bending moment P_3 and the respective generalized displacements are defined as δ_1, δ_2, and δ_2. In Figure 8.10, a presents the crack depth and L_c denotes the distance between the crack location and the end node j. The beam element has length L_e, cross-sectional area A and bending rigidity I. The geometrical dimensions are as follows,

$$\xi^{'} = \xi + \sqrt{\frac{D^2}{4} - \eta^2} - \frac{D}{2}, \tag{8.21}$$

$$b(a) = \sqrt{Da - a^2}, \tag{8.22}$$

$$h^{'}(\eta) = \sqrt{D^2 - 4\eta^2}, \tag{8.23}$$

$$a^{'}(a,\eta) = \sqrt{\frac{D^2}{4} - \eta^2} - (\frac{D}{2} - a), \tag{8.24}$$

where D is diameter of the beam and ξ is the crack depth. The additional strain energy subject to the existance of the crack can be expressed as follows,

$$\pi_c = \int GdA = \int_{A_c} [\int_0^{a^{'}(a,\eta)} Gd\xi^{'}]d\eta, \tag{8.25}$$

where A_c is the effective cracked area and G is the strain energy release rate function. It can be expressed as [TPI00]

$$G = [(K_{I1} + K_{I2} + K_{I3})^2 + K_{II2}^2], \tag{8.26}$$

where $E^{'} = E/(1-\mu^2)$ is related for plane strain problem and $E^{'} = E$ for plane stress problem. K_{I1}, K_{I2}, K_{I3}, and K_{II2}^2 are the stress intensity factors due to loads P_1, P_2, and P_3 as follows

$$K_{I1} = \frac{4P_1}{\pi D^2}\sqrt{\pi\xi^{'}}F_1(\frac{\xi^{'}}{h^{'}}),\ K_{I2} = \frac{32P_2L_ch^{'}}{\pi D^4}\sqrt{\pi\xi^{'}}F_2(\frac{\xi^{'}}{h^{'}}), \tag{8.27}$$

$$K_{I3} = \frac{32P_3h^{'}}{\pi D^4}\sqrt{\pi\xi^{'}}F_2(\frac{\xi^{'}}{h^{'}}),\ K_{II2} = \frac{4P_2}{\pi D^2}\sqrt{\pi\xi^{'}}F_{II}(\frac{\xi^{'}}{h^{'}}), \tag{8.28}$$

where ξ is the crack depth and F_1, F_2, and F_{II} are the correction factors for stress intensity factors with

$$F_1(s) = \sqrt{\frac{tg(\pi s/2)}{(\pi s/2)}}\frac{0.752 + 2.02s + 0.199(1 - sin(\pi s/2))^4}{cos(\pi s/2)}(s = \xi/h), \tag{8.29}$$

$$F_2(s) = \sqrt{\frac{tg(\pi s/2)}{(\pi s/2)}}\frac{0.923 + 0.199(1 - sin(\pi s/2))^4}{cos(\pi s/2)}(s = \xi/h), \tag{8.30}$$

$$F_{II}(s) = \frac{1.122 - 0.561s + 0.085s^2 + 0.180s^3}{1-s}(s = \xi/h), \tag{8.31}$$

where ξ is the crack depth during the process of penetrating from 0 to a/D. Note that a is the final crack depth. Following Paris equation,

$$\delta_i = \frac{\partial \pi_c}{\partial P_i} \quad (i = 1, 2, 3). \tag{8.32}$$

Then, the elements of the overall additional flexibility matrix c_{ij} can be obtained as

$$c_{ij} = \frac{\partial \delta_i}{\partial P_j} = \frac{\partial^2 \pi_c}{\partial P_i \partial P_j} \quad (i = 1, 2, 3). \tag{8.33}$$

Following the expressions (8.27)-(8.31), the strain release energy can be obtained from (8.26). Now, with the combination (8.25) and (8.33), and assuming that all K are independent of η, then c_{ij} can be obtained as

$$c_{ij} = \frac{b}{E'}\frac{\partial^2}{\partial P_i \partial P_j}\int_{-\sqrt{(Da-a^2)}}^{\sqrt{(Da-a^2)}}\int_0^{\sqrt{(D^2/4-\eta^2)}-(D/2-a)} \{[\frac{4P_1}{\pi D^2}\sqrt{\pi\xi'}F_1(\frac{\xi'}{h'}) + \frac{32P_2L_ch'}{\pi D^4}\sqrt{\pi\xi'}F_2(\frac{\xi'}{h'}) + \frac{32P_3h'}{\pi D^4}\sqrt{\pi\xi'}F_2(\frac{\xi'}{h'})]^2 + \frac{16P_2}{\pi D^4}\pi\xi' F_{II}^2(\xi' h')\}d\xi' d\eta. \quad (i,j = 1,2,3) \tag{8.34}$$

From (8.34), the elements of the overall additional flexibility matrix c_{ij} can be obtained. In order to get the stiffness matrix of the crack beam element, first the total flexibilty matrix C_{tot} is obtained with (8.34) and then taking inverse of it. Following [ZK04, SP92, Sek83], the stiffness matrix K_c of a cracked beam element can be obtained through the equilibrium conditions,

$$K_c = LC_{tot}^{-1}L^T, \tag{8.35}$$

where

$$L = \begin{bmatrix} -1 & 0 & 0 \\ 0 & -1 & 0 \\ 0 & -L_e & -1 \\ 1 & 0 & 0 \\ 0 & 1 & 0 \\ 0 & 0 & 1 \end{bmatrix}, C_{tot} = \begin{bmatrix} \frac{L_e}{EA} + c_{11} & -c_{12} & -c_{13} \\ -c_{21} & \frac{L_e^3}{3EI} + c_{22} & \frac{L_e^2}{2EI} + c_{23} \\ -c_{31} & \frac{L_e^2}{2EI} + c_{32} & \frac{L_e}{EI} + c_{33} \end{bmatrix}. \tag{8.36}$$

Modal analysis and uncertainties

Similar to the previous example, all estimated modes were chosen using a stabilization diagram procedure [DM12] from the simulated measurements of the structure with subspace-based system identification as described in details in Chapter 3. Then, the system matrices A_c and C_c (3.2.3) in both healthy and damaged states, together with their uncertainties are obtained from the same dataset as described in Section 3.3. We here consider the first 5

modes for localization with SDDLV, see Table 8.4. For damaged case, assuming that 0.01 m is the crack depth.

Table 8.4 – Eigenfrequencies f_c and eigenvalues λ_c of a crack beam model.

	Healthy state		Damaged state	
Mode	Modal freq.	Eigenvalues	Modal freq.	Eigenvalues
1	21.56	$-2.71 + 135.49i$	21.48	$-2.574 + 128.12i$
2	135.23	$-16.994 + 849.53i$	130.97	$-16.45 + 822.78i$
3	379.83	$-47.73 + 2386.10i$	372.35	$-46.79 + 2339.11i$
4	750.35	$-94.29 + 4713.64i$	741.78	$-93.21 + 4659.84i$
5	1245.39	$-156.50 + 7823.48i$	1236.49	$-155.38 + 7767.54i$

8.3.5 3D Cube beam model

In this application, the damage localization approach has been tested on a 3D cube beam model as shown in Figure 8.11, considering a more complex structure than in the previous example. The structure is modeled with 9 beam elements of length 10.2 m (except for the diagonal one). The elements are modeled as pipes with an internal and external diameter of 1.08 m and 1.12 m, respectively. The Young modulus (E), Poisson ratio and mass density of the beam are 210 GPa, 0.3 and 7800 kg.m^{-3}, respectively. The bottom of the elements 1, 3, 5 and 7 is fixed to the support. The total number of DOFs of the structure is 24. Damage is introduced in element 8 by multiplying all the rigidity by a factor $(1 - D)$.

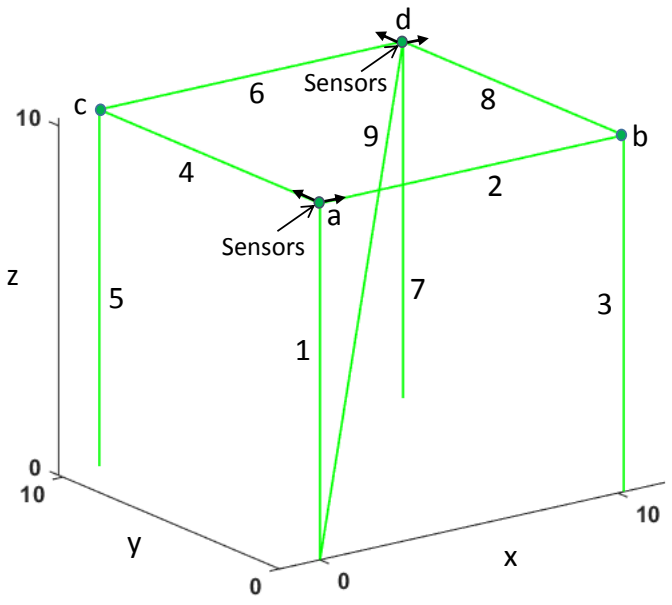

Figure 8.11 – 3D Cube model with beam elements (24 DOFs)

For both healthy and damaged states, acceleration datasets of length $N = 200{,}000$ are simulated from collocated white noise excitation at four accelerometers in the $x-y$-direction at nodes a and d, at a sampling frequency of 350 Hz which is sufficient to estimate the modal parameters. White measurement noise with 5% magnitude of the simulated outputs was added.

To get the damage localization results, an FE model of the healthy structure and estimated modal parameters are needed from simulated data in both healthy and damaged states. Therefore, the stiffness and mass matrix of a healthy and damaged beam element are stated in the following.

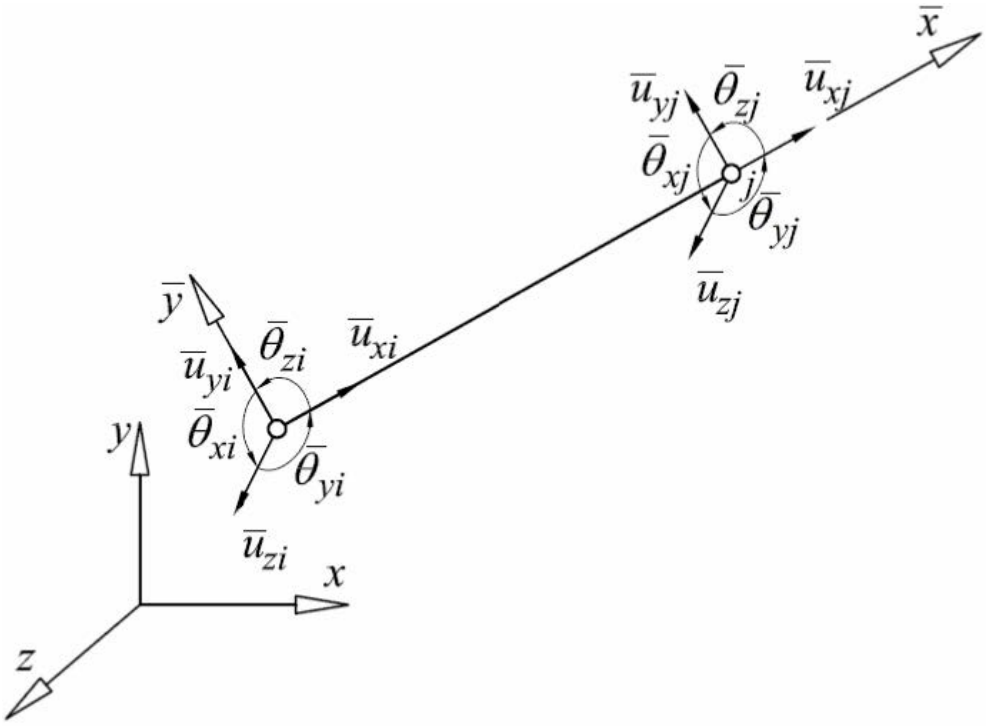

Figure 8.12 – 3D Beam element

Stiffness and mass matrix of a healthy element

In 3D beam element, each node has six degrees of freedom such as three translational and three rotational displacements in the x, y, and z-axis. Figure 8.12 shows a beam element in the x-y-z plane. This element has twelve degrees of freedom corresponds to the following displacement vector,

$$U^e = [\bar{u}_{xi}\ \bar{u}_{yi}\ \bar{u}_{zi}\ \bar{\theta}_{xi}\ \bar{\theta}_{yi}\ \bar{\theta}_{zi}\ \bar{u}_{xj}\ \bar{u}_{yj}\ \bar{u}_{zj}\ \bar{\theta}_{xj}\ \bar{\theta}_{yj}\ \bar{\theta}_{zj}]^t,$$

where $\bar{u}_{xi}$, $\bar{u}_{yi}$, $\bar{u}_{zi}$ and $\bar{\theta}_{xi}$, $\bar{\theta}_{yi}$, $\bar{\theta}_{zi}$ are translational and rotational displacements at node i respectively. Similalry, for node j, $\bar{u}_{xj}$, $\bar{u}_{yj}$, $\bar{u}_{zj}$ and $\bar{\theta}_{xj}$, $\bar{\theta}_{yj}$, $\bar{\theta}_{zj}$ are the respectives transla-

tional and rotational displacements. Details are given in the literature of structural mechanics [Bat, Kri95, JNJ04].

Taking into account both flexural and traction-compression stiffness K^h for one beam finite element can be derived as follows,

$$K^h = \begin{bmatrix}
\frac{EA}{L} & 0 & 0 & 0 & 0 & 0 & -\frac{EA}{L} & 0 & 0 & 0 & 0 & 0 \\
0 & \frac{12EI_z}{L^3} & 0 & 0 & 0 & \frac{6EI_z}{L^2} & 0 & -\frac{12EI_z}{L^3} & 0 & 0 & 0 & \frac{6EI_z}{L^2} \\
0 & 0 & \frac{12EI_y}{L^3} & 0 & -\frac{6EI_y}{L^2} & 0 & 0 & 0 & -\frac{12EI_y}{L^3} & 0 & -\frac{6EI_y}{L^2} & 0 \\
0 & 0 & 0 & \frac{GI_x}{L} & 0 & 0 & 0 & 0 & 0 & -\frac{GI_x}{L} & 0 & 0 \\
0 & 0 & -\frac{6EI_y}{L^2} & 0 & \frac{4EI_y}{L} & 0 & 0 & 0 & \frac{6EI_y}{L^2} & 0 & \frac{2EI_y}{L} & 0 \\
0 & \frac{6EI_z}{L^2} & 0 & 0 & 0 & \frac{4EI_z}{L} & 0 & -\frac{6EI_z}{L^2} & 0 & 0 & 0 & \frac{2EI_z}{L} \\
-\frac{EA}{L} & 0 & 0 & 0 & 0 & 0 & \frac{EA}{L} & 0 & 0 & 0 & 0 & 0 \\
0 & -\frac{12EI_z}{L^3} & 0 & 0 & 0 & -\frac{6EI_z}{L^2} & 0 & \frac{12EI_z}{L^3} & 0 & 0 & 0 & -\frac{6EI_z}{L^2} \\
0 & 0 & -\frac{12EI_y}{L^3} & 0 & \frac{6EI_y}{L^2} & 0 & 0 & 0 & \frac{12EI_y}{L^3} & 0 & \frac{6EI_y}{L^2} & 0 \\
0 & 0 & 0 & -\frac{GI_x}{L} & 0 & 0 & 0 & 0 & 0 & \frac{GI_x}{L} & 0 & 0 \\
0 & 0 & -\frac{6EI_y}{L^3} & 0 & \frac{2EI_y}{L} & 0 & 0 & 0 & \frac{6EI_y}{L^2} & 0 & \frac{4EI_y}{L} & 0 \\
0 & \frac{6EI_z}{L^2} & 0 & 0 & 0 & \frac{2EI_z}{L} & 0 & -\frac{6EI_z}{L^2} & 0 & 0 & 0 & \frac{4EI_z}{L}
\end{bmatrix}. \tag{8.37}$$

The mass matrix M^h is written as

$$M^h = \frac{\rho AL}{420}\begin{bmatrix}
140 & 0 & 0 & 0 & 0 & 0 & 70 & 0 & 0 & 0 & 0 & 0 \\
0 & 156 & 0 & 0 & 0 & 22L & 0 & 54 & 0 & 0 & 0 & -13L \\
0 & 0 & 156 & 0 & -22L & 0 & 0 & 0 & -54 & 0 & -13L & 0 \\
0 & 0 & 0 & 140It/A & 0 & 0 & 0 & 0 & 0 & 70It/A & 0 & 0 \\
0 & 0 & -22L & 0 & 4L^2 & 0 & 0 & 0 & -13L & 0 & -3L^2 & 0 \\
0 & 22L & 0 & 0 & 0 & 4L^2 & 0 & 13L & 0 & 0 & 0 & -3L^2 \\
70 & 0 & 0 & 0 & 0 & 0 & 140L & 0 & 0 & 0 & 0 & 0 \\
0 & 54 & 0 & 0 & 0 & 13L & 0 & 156 & 0 & 0 & 0 & -22L \\
0 & 0 & 54 & 0 & -13L & 0 & 0 & 0 & 156 & 0 & 22L & 0 \\
0 & 0 & 0 & 70It/A & 0 & 0 & 0 & 0 & 0 & 140It/A & 0 & 0 \\
0 & 0 & 13L & 0 & -3L^2 & 0 & 0 & 0 & 22L & 0 & 4L^2 & 0 \\
0 & -13L & 0 & 0 & 0 & -3L^2 & 0 & -22L & 0 & 0 & 0 & 4L^2
\end{bmatrix}, \tag{8.38}$$

where ρ is the mass density, A is the cross-section area, L is the length of the element, E is the Young modulus, I_x, I_y, and I_z are the moment of inertia in the x, y, and z-axis, and It is the torsional moment of inertia. Finally, the global mass and stiffness matrix of the 3D beam model in Figure 8.11 can be obtained after assembling the mass and stiffness matrix for each of the element.

Stiffness matrix of damaged element

For damaged case, considering the damage model of Mazars, the stiffness matrix of the damaged structure is obtained as $K^d = (1 - D)K^h$, where D is the damage parameter of the Mazars model $D \in [0, 1]$. In this application, damage is introduced in element 8 by multiplying all the rigidity by a factor with $D = 0.5$.

Modal analysis and uncertainties

In this example, 13 modes can be well identified using stabilization diagram from the simulated measurements of the structure with subspace-based system identification as described in details in Chapter 3. Then, the system matrices A_c and C_c (3.2.3) in both healthy and damaged states, together with their uncertainties are obtained from the same dataset as described in Section 3.3. Using four sensors in this example, only a limited set of four modes could be used for localization in previous works [Ber10, DMBM13, MDBM15] as the number of modes cannot be bigger than the number of sensors. For localization we consider the first 12 modes (see Table 8.5), split into three mode sets $\mathcal{M}_1$, $\mathcal{M}_2$ and $\mathcal{M}_3$ of four modes each for the proposed method in chapter 5. In Figure 8.13, the first four mode shapes of the cube structure are illustrated.

Table 8.5 – Eigenvalues λ_c of cube.

Mode	Healthy state	Damaged state	Mode set
1	$-0.938 + 46.90\text{i}$	$-0.910 + 45.46\text{i}$	$\mathcal{M}_1$
2	$-1.13 + 56.70\text{i}$	$-1.12 + 56.20\text{i}$	
3	$-1.52 + 76.03\text{i}$	$-1.44 + 71.99\text{i}$	
4	$-3.45 + 172.5\text{i}$	$-3.37 + 169.0\text{i}$	
5	$-7.49 + 374.7\text{i}$	$-6.80 + 340.4\text{i}$	$\mathcal{M}_2$
6	$-8.18 + 409.3\text{i}$	$-7.47 + 373.6\text{i}$	
7	$-9.41 + 470.8\text{i}$	$-8.69 + 435.9\text{i}$	
8	$-9.91 + 495.4\text{i}$	$-9.54 + 477.2\text{i}$	
9	$-11.0 + 552.6\text{i}$	$-10.5 + 527.4\text{i}$	$\mathcal{M}_3$
10	$-11.3 + 566.7\text{i}$	$-11.3 + 564.2\text{i}$	
11	$-11.8 + 591.4\text{i}$	$-11.7 + 586.2\text{i}$	
12	$-12.3 + 615.1\text{i}$	$-12.1 + 606.0\text{i}$	

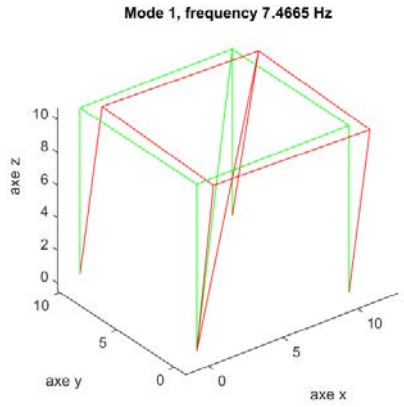

(a) Mode 1 for frequency 7.4665 Hz

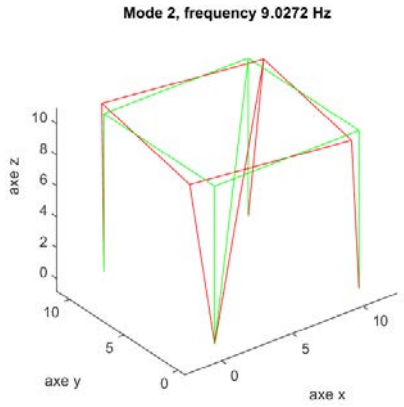

(b) Mode 2 for frequency 9.0272 Hz

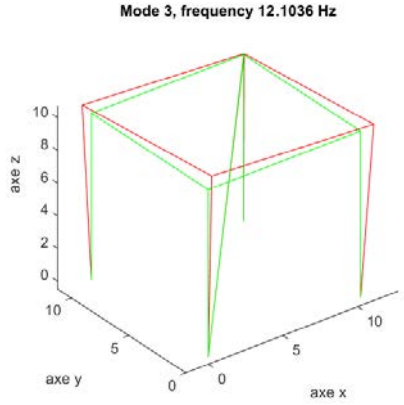

(c) Mode 3 for frequency 12.1036 Hz

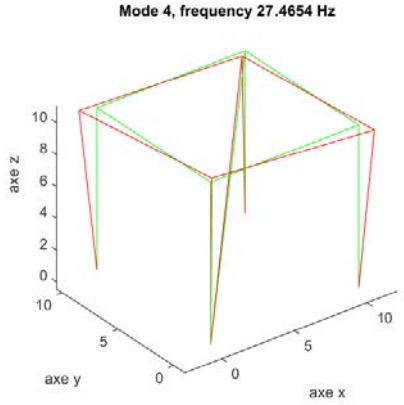

(d) Mode 4 for frequency 27.4654 Hz

Figure 8.13 – First four mode shapes of the cube structure (healthy state).

8.4 Overview for different methods

Based on the contribution Chapters (5, 6 and 7), different damage localization methods have been applied on both numerical and real applications. In Chapter 9, 10, and 11, the following numerical applications has been considered:

In chapter 9, first the damage localization method has been applied on numerical simulations based on contribution chapter 5. A simple mass-spring chain and a more complex 3D cube beam model has been cosidered as numerical applications. These numerical applications are idealized test cases for the validation of the new developments of this chapter using Multiple mode sets approach, allowing in particular a statistical performance evaluation based on Monte-Carlo simulations. For each application, the outcome of the damage localization results using multiple mode sets are compared with the ones using only one of the single mode sets separately. Secondly, the damage localization wih SDDLV has been applied on a

2D beam model with crack. Finally, the SDDLV has been investigated on a 2D beam model assuming large and small damaged zone depending on different mesh size i.e. rough and fine mesh.

In chapter 10, the damage localization method has been validated on a numerical application of Mass-spring chain based on the contribution chaper 6 that deals with the statistical evaluation of ILDL. Monte-Carlo simulations have been demonstrated for evaluating the success rate of correct damage localization at different s-values.

In chapter 11, the damage localization method has been applied on two different numerical simulations such as mass-spring chain and 2D beam model based on contribution chapter 7 that presents the transfer-matrix based residuals for damage localization and quantification using Multiple mode sets in the context of SDDLV. Monte-Carlo simulations have been carried-out for evaluating the performance of the damage localization and quantification for single and multiple mode sets at different s-values.

Then in chapter 12 the numerical implementation of the damage localization methods is presented by using Abaqus software. In Chapters 9, 10, and 11, the localization methods are applied on different numerical simulations where the FE model are generated using Matlab code more challenging to make an accurate FE model for bigger structure. Therefore, the purpose of this chapter is to compute the FE model of a structure in practice, generally for any kind of structure using Abaqus-Python script for the feasibility of the damage localization and quantification methods described in this thesis. Finally, both methods from chapter 5 and 7 are tested for localization and quantification on a 2D cantilever beam model.

The overview of the different methods is shown shortly in Table 8.6.

Table 8.6 – Overview for different methods (numerical applications)

Contribution chapter	Methods	Numerical applications
5	SDDLV using Multiple mode sets	Mass-spring chain and 3D cube model
	SDDLV	Beam model with crack
	SDDLV	Beam model for different mesh size
6	ILDL	Mass-spring chain
7	Transfer-matrix based residual	Mass-spring chain and beam model

8.5 Discussion

In this Chapter, the performance evaluation criteria of the damage localization methods are presented based on the probability of successful damage localization and the probability of good or wrong localization (PGL or PWL) in terms of the detection threshold, defect size and Laplace variables. The descriptions of the numerical models are illustrated for different damage localization methods. Finally, an overview of different methods and applications has been presented.

Chapter 9

SDDLV with single and multiple mode sets

9.1 Introduction

In this Chapter, the damage localization algorithm from Chapter 5 is applied on numerical simulations. A simple mass-spring chain, a 3D cube model, a crack beam and a beam model depending on mesh size have been considered as numerical applications, which allow Monte-Carlo simulations for the validation of the method.

For mass-spring chain and 3D cube model, the outcome of the damage localization results using multiple mode sets are compared with the ones using only one of the single mode sets separately. To obtain these results from simulated or measured data, the modes of the system are estimated using a stabilization diagram procedure with SSI [DM12] in both reference and damaged states. They are estimated together with their covariance [DM13]. Then, the system matrices and their covariance are assembled from the modes. For each single mode set, the stress vector and its uncertainty are computed. Finally, the estimated stress at the multiple (or single) mode sets and at multiple (or single) s-values is evaluated and statistically aggregated for each structural element with the new method using multiple approach. Comparisons to the deterministic aggregation are based on (5.5). Recall that stress values close to zero indicate potentially damaged elements.

Assessing the performance of the method is a requirement for showing the benefits of this approach. A proper criterion for the evaluation of the success rate is proposed based on Monte Carlo simulations. The SDDLV approach is strongly dependent on the choice of the Laplace variable s where the transfer function is evaluated. Performance can be highly different in the classical SDDLV approach depending on the choice of the Laplace variable. Accommodating multiple s variables has been treated in [MDBM15]. Still, the choice of the Laplace variable is a complicated part of the procedure, even if past guidelines push for

choosing this variable around the identified modes in the complex plane. That is why, in this section, Monte Carlo simulations have been done for many s variables in the complex plane and results are evaluated on 2D grids. Performance of the proposed approach is tested against the requirement that such choice should not be critical.

This Chapter is formulated as follows. In Section 9.2, the distribution of the load vector and stress field is validated before going to apply statistical damage localization approach. In Section 9.3, the new approach using Multiple mode sets has been applied on two different numerical applications, a mass-spring chain, and a 3D cube model. In Section 9.4, the damage localization with the SDDLV approach has been applied on a beam model for crack propagation. In Section 9.5, it has been applied on beam model influence of mesh size and in Section 9.6, the performance evaluation of the method has been investigated based on the PGL interms of distance. Finally, the conclusion of the work is presented in Section 9.7.

9.2 Distribution of load vectors and stresses

In SDDLV, a vector is obtained in the null space of the changes in the transfer matrix from both states and then applied as a load vector to the model that yields stress field. Recall that the damage localization is related to this stress where it is close to zero. Due to random input noise, the estimated load vectors are random values for each simulated datasets. Therefore, it is important to analysis the distribution of the random variables in Monte-Carlo experiments.

The load vector v in the null space of $\delta R(s)^T$ can be chosen as any linear combination of the vectors in V_2. Particularly, the vector corresponding to the smallest singular value is taken as the desired load vector. Hence, the last singular vector $v_s = v(:, r)$ has considered as the desired load vector v which is obtained from a model or from an estimated data. From a simulated data sets, one gets the estimated $\widehat{V}_2$ of the null space. First, the theoretical load vector $v_s = v(:, r)$ from model has projected to the estimated null space vectors $\widehat{V}_2$. To find an estimate vector $\widehat{v}_s$ within all null space vectors in $\widehat{V}_2$, it is essential to calculate the linear combination of the vectors in $\widehat{V}_2$. Note that the theoretical load vector v_s is expected approximately equal to the estimated load vector $\widehat{v}_s$ from simulated data. The estimated load vector $\widehat{v}_s$ is written as

$$\widehat{v}_s = \sum_{i=1}^{r-t} \alpha_i v_i, \tag{9.1}$$

where $r - t$ is the dimension of the null space vectors, $v_i = \widehat{V}_2(:, i)$ is the null space vectors of $\delta R(s)^T$, and α_i is the scaler coefficient of the vector. The scaler coefficient α_i is calculated using orthogonal projection of v_s vector into $v_i = \widehat{V}_2(:, i)$ of the null space vectors. The scaler coefficient α_i can be obtained as

$$\alpha_i = \frac{v_s v_i}{||v_i||} \tag{9.2}$$

In Monte-carlo experiments, the following things are considered to analyze the probability distribution of load vectors and stresses,

- The distribution of the estimated load vectors are observed for each of the element, and a comparison is made between the probability density of the estimated load vectors and

the theoretical load vector that computed from a model. Then an analysis has been performed to see the difference between the mean of the estimated load vectors and theoretical load vectors.

- For the validation of stress covariance computation, the probability distribution of the stress values is computed for damaged and undamaged elements from Monte Carlo simulations with compared to theoretical stress values. Then, the difference between the mean of the estimated stress and theoretical stress vectors are illustrated. It is seen that the estimated stress is asymptotically Gaussian distributed.

- Validation of covariance computation: to compare Monte-Carlo standard deviation, $\hat{\sigma}$ of the estimated stress with the mean of the computed standard deviation, σ.

- Finally, a continuous Monte Carlo experiments have been performed to observe the convergence of the estimated ones to theoretical parameters. That's why the mean of the estimated load vectors and stress values have been considered in a progressive Monte-Carlo Simulations. Therefore, we observed that after some experiments the estimated value has converged to the theoretical value.

For an example, a mass-spring chain of six DOF as shown in Figure 9.1. The stiffness parameters are $k_1 = k_3 = k_5 = 4000$, $k_2 = k_4 = k_6 = 2000$, and the mass of all elements is 1 in suitable units. Damping is defined such that each mode has a damping ratio of 2%. Damage is simulated by decreasing the stiffness of spring 3 by 10% of its original value. For damaged and undamaged states, the acceleration data length for each set is $N = 50{,}000$. Data were generated from collocated white noise excitation using six sensors at each element with a sampling frequency of 50 Hz, and white measurement noise with 5% magnitude of the outputs was added. All six modes of the structure can be identified from the simulated measurements when using SSI. In the simulation results, a comparison between theoretical and estimated modal parameters has explained for Monte-Carlo experiments of 1000 datasets.

Figure 9.1 – Mass-spring chain (with modal damping), six sensors.

9.2.1 Validation of load vectors and stresses

Since the number of damaged element is one, the rank of $\delta R(s)^T$ is 1. The null space vectors $\widehat{V}_2$ are spanned by the last 5 column vectors and the null space of $\delta R(s)^T$ is equal to zero. Each column vector of $\widehat{V}_2$ can be used as the desired load vector but the last column vector has chosen for better accuracy because it gives the lowest singular value. For each experiment, the estimated load vectors are random variables. The theoretical load vector v_s is projected to the estimated null space vectors $\widehat{V}_2$ and the estimated load vector $\widehat{v}(s)$ is the linear combination of the vectors $\widehat{V}_2$ where estimated load vectors $\widehat{v}(s)$ are close to $v(s)$.

In Figure 9.2, a comparison is shown between the probability distribution of the estimated load vectors and theoretical load vectors that obtained from the model. Note that the most density of the estimated load vectors is closest to the theoretical value. In Figure 9.3, the

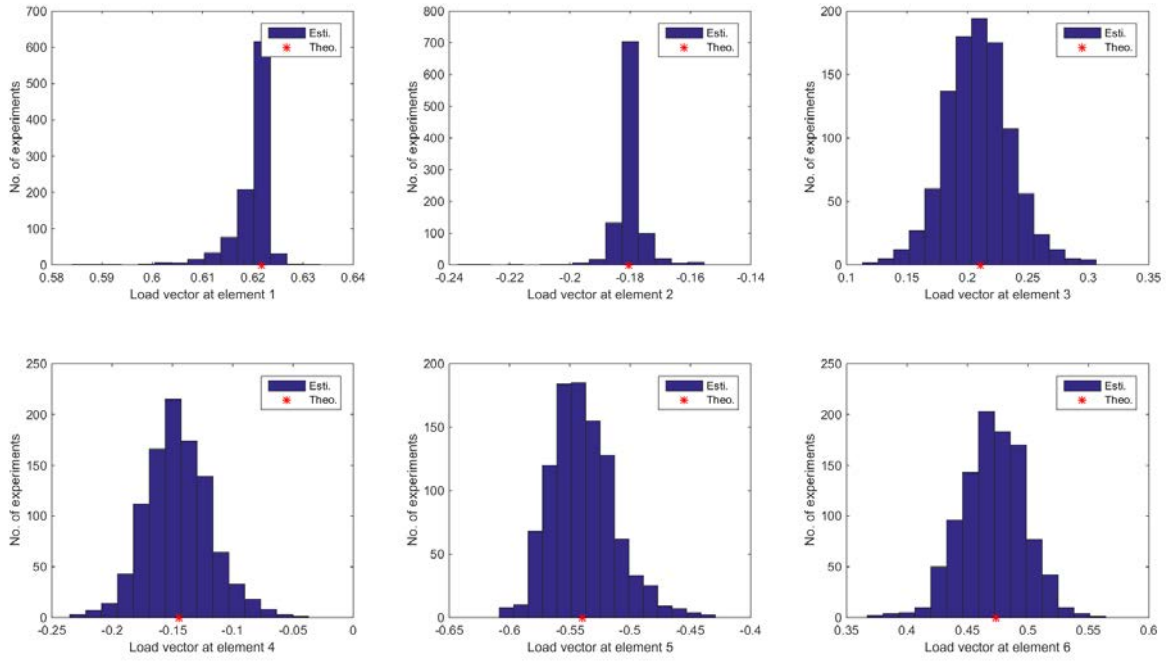

Figure 9.2 – Load vector at each of the element between estimated and theoretical value ['bar' indicates the distribution of estimated value and '$*$' for theoretical value].

mean of the estimated load vector for Monte-Carlo experiments and its standard deviation as shown and compoared to the theoretical value. Note that the standard deviation indicates how far away the estimated random variables can lie from the mean values.

Now, the estimated load vectors $\widehat{v}(s)$ are applied to the model in order to get the stress field. In Figure 9.4, the distribution of the stress value at each of the elements from Monte-Carlo experiments and the theoretical stress values are illustrated. The stresses close to zero correspond to potentially damaged elements. Here, most of the distribution of stresses at 3rd element are close to zero but some of them are not close to zero. Therefore, it is difficult to make a decision about damaged element of the structure. Then, the mean of the estimated stress in Monte-Carlo experiments and its standard deviation is computed for each experiment. In Figure 9.5, a comparison between the mean of the computed standard deviation of the stress (estimated) for all experiment and the std. deviation of the estimate stress value (true) is shown. It is seen that the difference between these parameters is not so small due to white noise and uncertainties in the datasets.

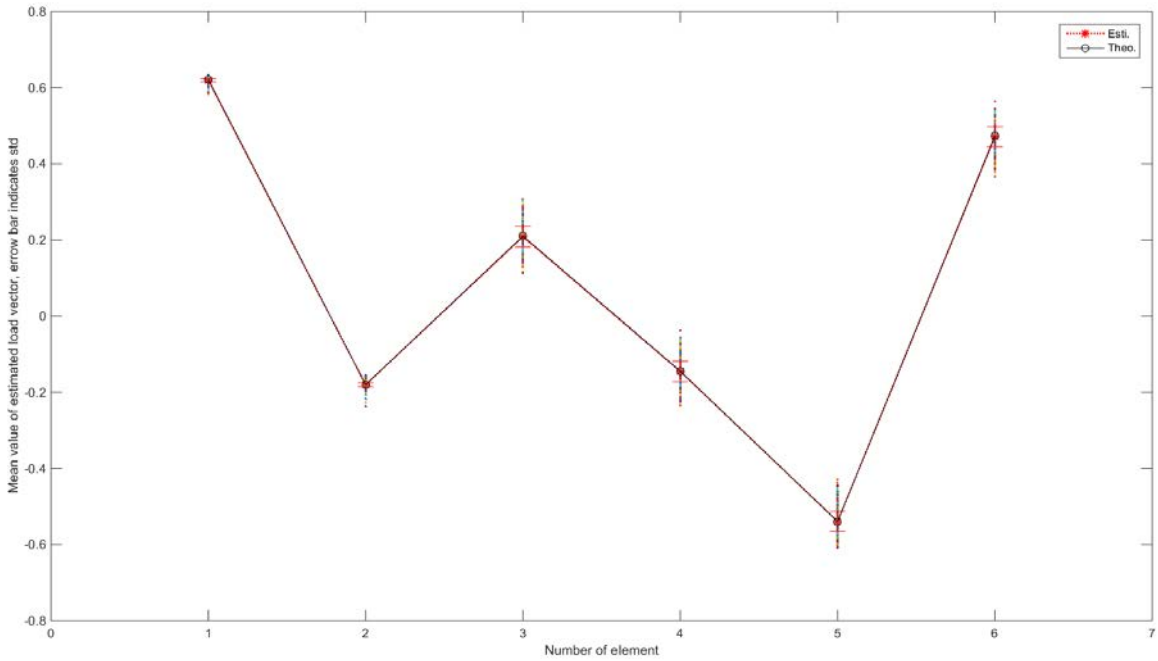

Figure 9.3 – Mean of the estimated load vectors at each of the element between estimated and theoretical values ['$redline$' -estimated value and '$blackline$' -theoretical value].

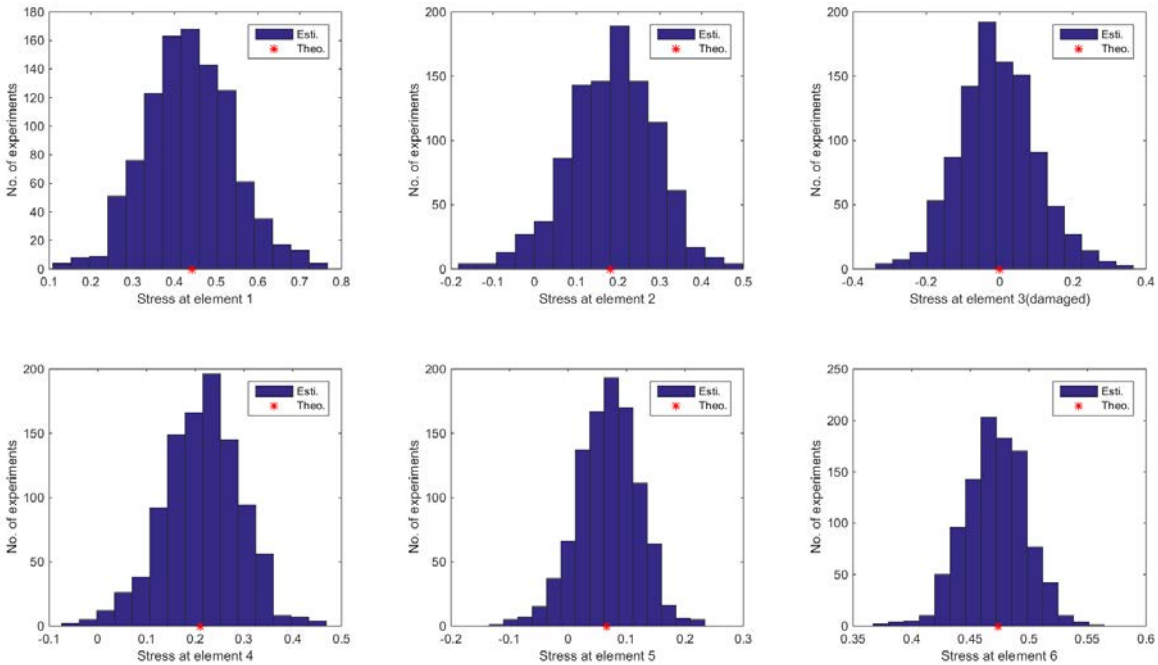

Figure 9.4 – Stress at each of the element between estimated and theoretical values ['bar' -estimated value and '$*$' -theoretical value].

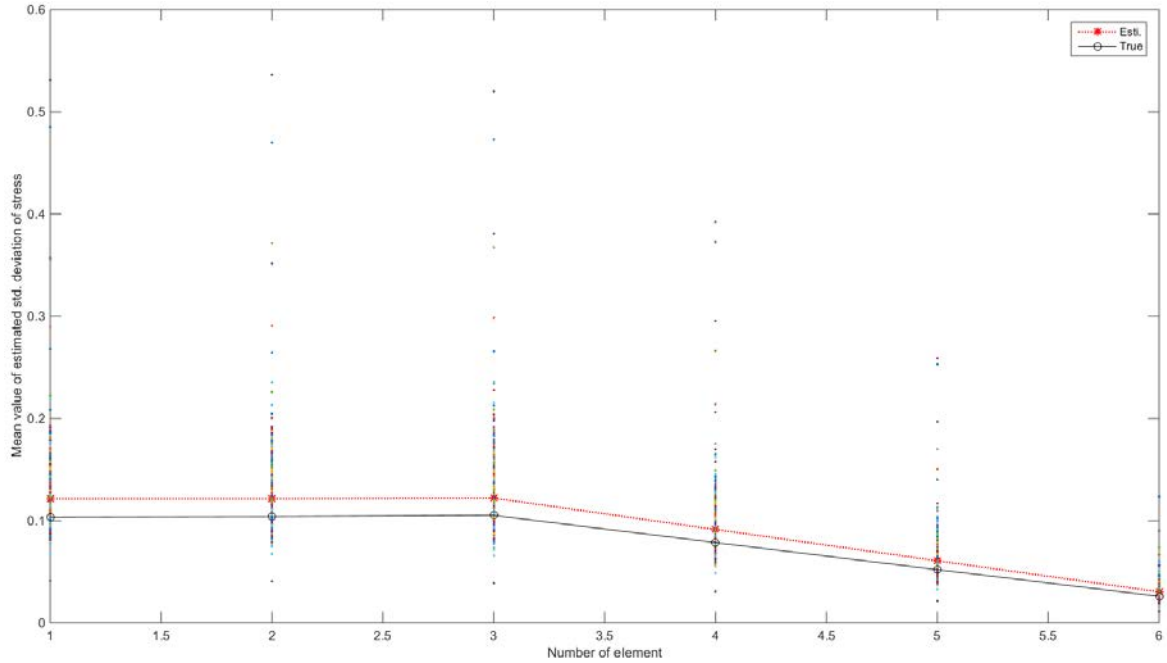

Figure 9.5 – Comparison between mean of the computed std. deviation of stress (estimated) and the std. deviation of stress value (true) for all experiment ['$redline$' -estimated value and '$blackline$' -true value].

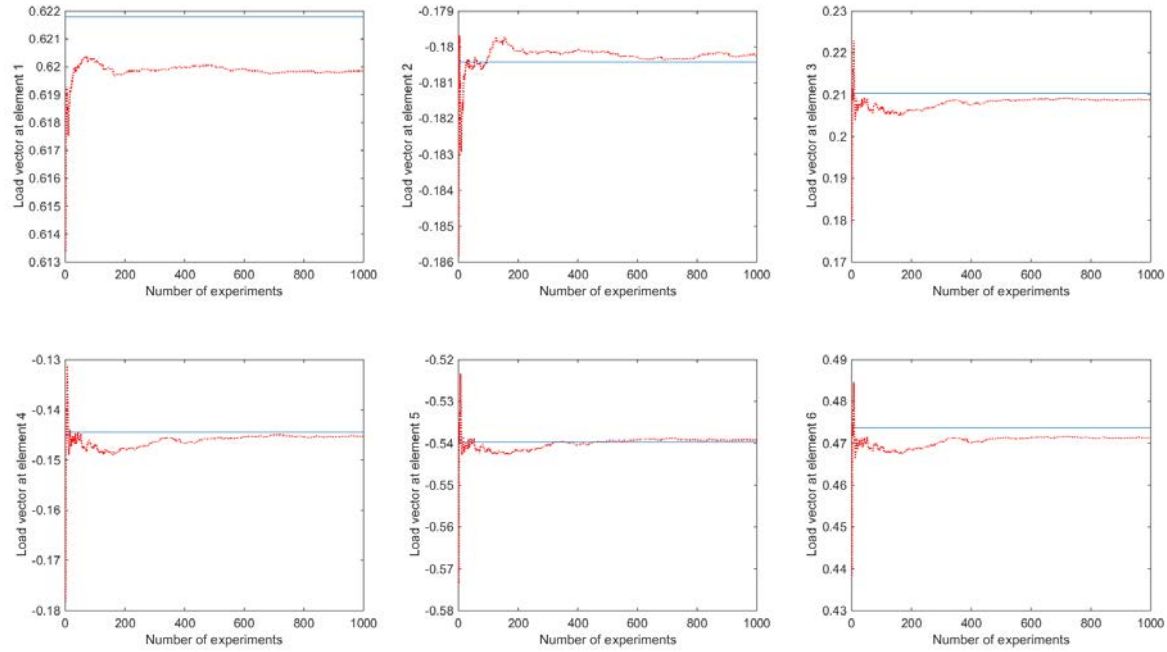

Figure 9.6 – Progressive Monte Carlo simulations for mean of the estimated load vectors at each of the elements 1, .., 6 from top-left to bottom-right ['$redline$' -mean quantity of the estimated value and '$blueline$' -theoretical value].

Finally, a progressive Monte-Carlo experiment has performed to analyze the convergence of the estimated value to theoretical value. The mean of the estimated load vectors and stress values has considered for continuous Monte experiments where the mean is taken from the results of the experiments $i = 1, .., 1000$. The mean of the quantity of the estimated load vectors and stress values are shown in Figure 9.6 and Figure 9.7, respectively. We observed that after some experiments the estimated value has converged to the theoretical value.

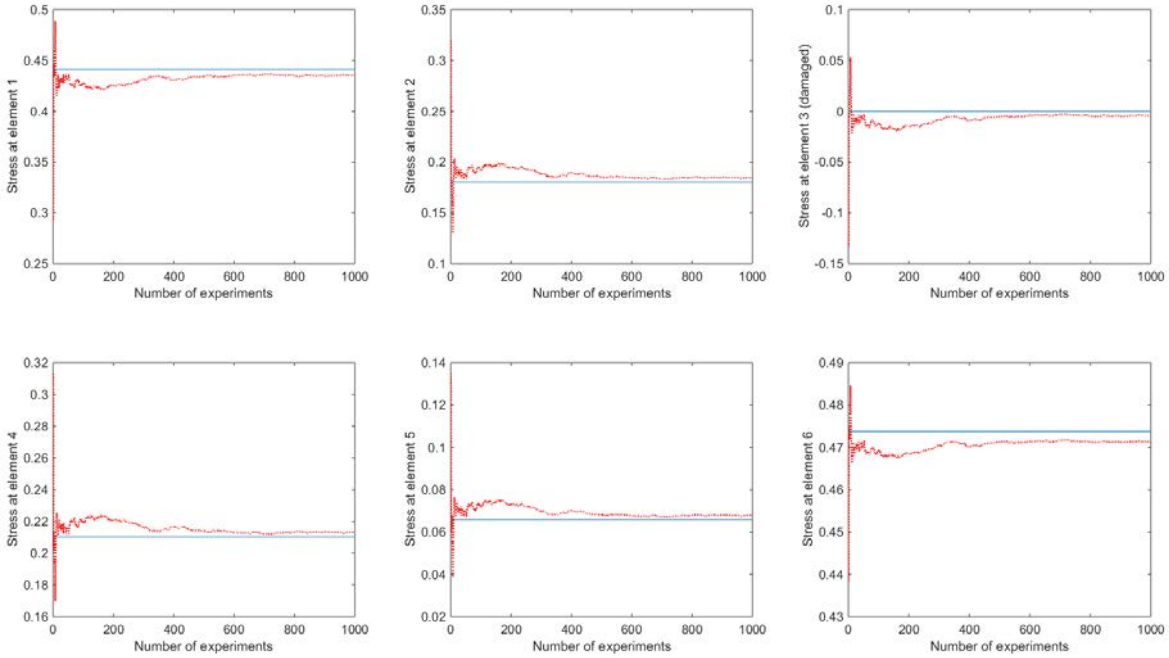

Figure 9.7 – Progressive Monte Carlo simulations for mean of the estimated stress values at each of the elements 1, .., 6 from top-left to bottom-right [$'redline'$ -mean quantity of the estimated value and $'blueline'$ -theoretical value].

From this section, it can be summarized that estimated stress is asymptotically Gaussian distributed as shown in Figure 9.4. There are false positives (i.e. stress of some healthy elements around 0) and false negatives (i.e. stress correctly centered at 0 at damaged element 3), but with values possibly far away from 0. In Figure 9.7, we also observed that after some experiments the estimated value has nearly converged to the theoretical value. In reality the whole distribution is not available, just one value. Therefore, statistical evaluation χ_t^2 test is essential based on stress and its covariance to avoid false detection.

9.3 Validation of SDDLV for single and multiple mode sets

9.3.1 Numerical application 1: mass-spring chain system

In a first numerical application, the damage localization method has been applied on a mass-spring chain system with six DOFs using three sensors as shown in Figure 8.3 in Section

8.3.1.

In the following, the localization results at all structural elements are presented for single mode set $\mathcal{M}_1$ and multiple mode set $\mathcal{M}_j$ at one s-value, before evaluating the success rate of correct damage localization for single and multiple mode sets at different s-values.

9.3.1.1 Localization of results in all elements at one s-value

In this section, the stress computation and its statistical evaluation for damage localization results for each element of the mass-spring chain are shown in Figure 9.8 for mode set $\mathcal{M}_1$ and Figure 9.9 for multiple mode set $\mathcal{M}_j$ at one s-value. Note that 5% measurements noise is added in the simulated datasets. The s-value was chosen in the vicinity of mode set $\mathcal{M}_1$ as $s = -2 + 51\mathrm{i}$ and $\mathcal{M}_2$ as $s = -2 + 90\mathrm{i}$. Recall that the damage localization is inferred by the stress value closest to zero.

In Figure 9.8(a), the theoretical stress values are computed from the modal parameters corresponding to $\mathcal{M}_1$ in the healthy and damaged states. The effect of modal truncation leads to stress that is not exactly zero in damaged element 4, but that is close to zero and the smallest compared to the stress at the other elements. When computing the stress from modal parameter estimated from simulated datasets in Figure 9.8(b), the damage localization cannot be correctly indicated anymore, which is probably due to variance errors in the estimation from noisy data. Considering the variance of the modal parameters in the method, the damage localization is correctly found since the smallest χ_t^2 value is at element 4 in Figure 9.8(c). It can be seen that χ_t^2 in Figure 9.8(c) shows similar results as the theoretical result in Figure 9.8(a).

In Figure 9.9, all stress values are computed using joint evaluation of multiple mode sets from the single mode sets $\mathcal{M}_1$ and $\mathcal{M}_2$ in the healthy and damaged states. In this case, the estimated modal parameters can identify the damage localization in Figure 9.9(b) compared to Figure 9.8(b). However, when taking into account the uncertainties in the statistical evaluation of the χ_t^2-test, the damage localization is found at the smallest χ_t^2 values at damage element 4 in both of Figure 9.8(c) and Figure 9.9(c).

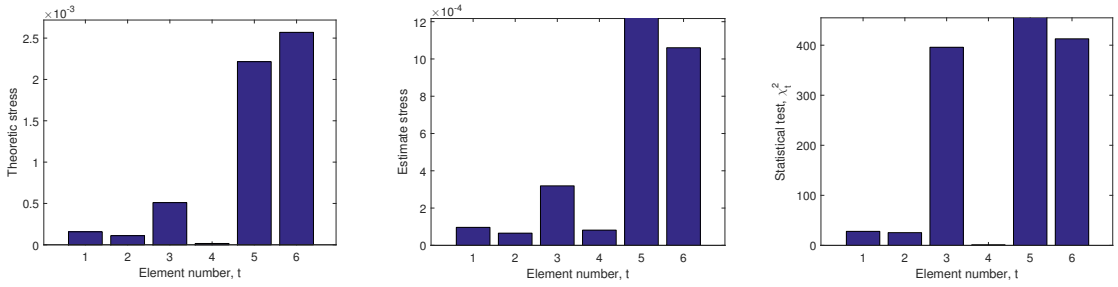

(a) SDDLV for theoretical stress (b) SDDLV for estimated stress (c) S-SDDLV (statistical test)

Figure 9.8 – Localization results at all elements of mass-spring chain using single mode set $\mathcal{M}_1$ using stress computation and statistical evaluation at $s^1 = -2 + 51\mathrm{i}$. Damage is at element 4.

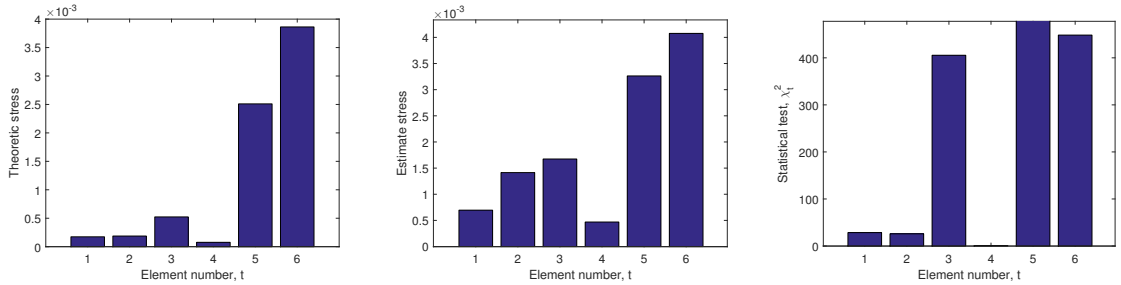

(a) SDDLV for theoretical stress (b) SDDLV for estimated stress (c) S-SDDLV (statistical test)

Figure 9.9 – Localization results with new statistical method using multiple mode sets: stress computation and statistical evaluation at $s^1 = -2 + 51\mathrm{i}, s^2 = -2 + 90\mathrm{i}$ *-using three sensor. Damage is at element 4.*

In this section, the localization of results has been demonstrated for one data set at one s-value only. In the next section, the success rate of the damage localization has been investigated using single mode set. Recall that success rate of the damage localization is defined as the number of occurrences of the smallest stress values in the damage element, while all s-values are evaluated for each of the 500 datasets.

9.3.1.2 Success rate of the damage localization using single mode set

In the last section, the damage localization results was illustrated only for one dataset and one s-value, now we are going to evaluate the performance of the damage localization for theoretical, estimated and statistical test based either on single mode set $\mathcal{M}_1$ or $\mathcal{M}_2$ in dependence of the chosen s-value, before going to the joint evaluation of the multiple mode sets in the next section.

For the evaluation of the success rate of correct damage localization at element 4, using either mode set $\mathcal{M}_1$ or $\mathcal{M}_2$, 500 datasets of vibration data were generated for the Monte Carlo evaluation. Then, the modes of these datasets and their uncertainties were identified using SSI, both in reference and damaged states. Finally, the success rate was determined based on the computation of the stress estimated in (5.5) and χ_t^2 test values in (5.14), using either the modes from $\mathcal{M}_1$ or $\mathcal{M}_2$, for different s-values. The s-values were chosen in the vicinity of the modes (see Table 8.1) on a global grid with $\mathrm{Re}(s) \in [-3, 1]$ and $\mathrm{Im}(s) \in [0, 130]$.

In Figures 9.10, 9.12, 9.14 and 9.11, 9.13, 9.15, the success rates of the damage localization (z-axis) are shown in dependence of the real and imaginary part of the chosen s-values (x and y-axis) for mode sets $\mathcal{M}_1$ and $\mathcal{M}_2$, respectively. Indeed it can be seen that damage localization for both mode sets is satisfactory only for s-values in the vicinity of the modes of the respective mode sets.

For mode set $\mathcal{M}_1$, corresponding to the first three modes, it can be seen in Figure 9.11 that success of damage localization from the exact modal parameters is obtained only in the interval $[1, 63]$ on the imaginary line. The same happens for the estimated stress from the simulated datasets as shown in Figure 9.13, where the success rate of the damage localization is around 60% only due to modal truncation and estimation errors. Figure 9.14 shows that the success rate is satisfactory only in the interval of the Laplace variables with $\mathrm{Im}(s) \in [20, 64]$,

where it reaches up to 90% and much higher than estimated in Figure 9.12. Beyond this interval, it is almost close to zero and the damage localization cannot be indicated due to the modal truncation error, which is significant outside the interval containing the identified modes (see Table 8.1). Note that the considered modes in this example are in the interval $[1, 62]$ on the imaginary line (see Table 8.1).

Similarly, for mode set $\mathcal{M}_2$ corresponding to the last three modes of the structure, it can be seen in Figure 9.11 that success of damage localization from the exact modal parameters is obtained only in the interval $[77, 117]$ on the imaginary line. The same happens for the estimated stress from the simulated datasets as shown in Figure 9.13, where the success rate of the damage localization is around 60% only due to modal truncation and estimation errors. It can be seen in Figure 9.15 that the success rate of damage localization is satisfying with up to 85% when $\mathrm{Im}(s)$ belongs to the interval $[102, 128]$. This area corresponds only to the last two identified modes in $\mathcal{M}_2$. While lower performance at s-values around the modes of $\mathcal{M}_1$ can be expected due to significant modal truncation errors, the success rate at s-values near the fourth mode of the structure is also very low. Hence, choosing the s-value in the vicinity of the identified poles does not necessarily give perfect results.

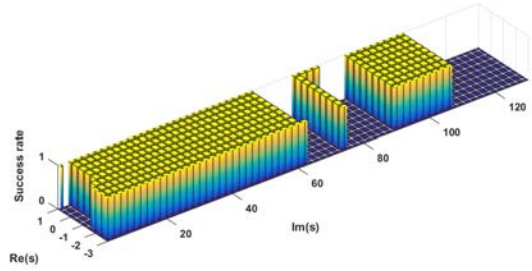

Figure 9.10 – Success of the SDDLV from theoretical modal parameters using single mode set $\mathcal{M}_1$ in dependence of s.

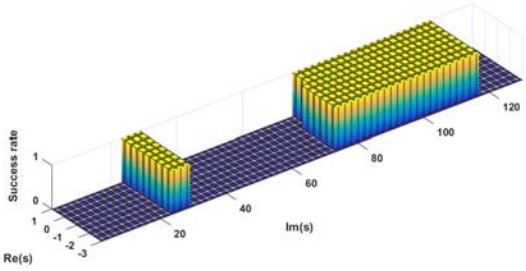

Figure 9.11 – Success rate of the SDDLV from theoretical modal parameters using single mode set $\mathcal{M}_2$ in dependence of s.

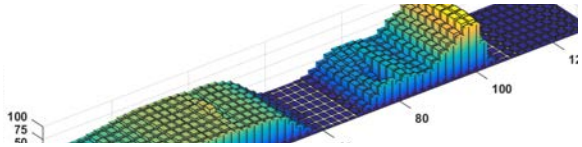

Figure 9.12 – Success rates of the SDDLV from estimated modal parameters using single mode set $\mathcal{M}_1$ in dependence of s.

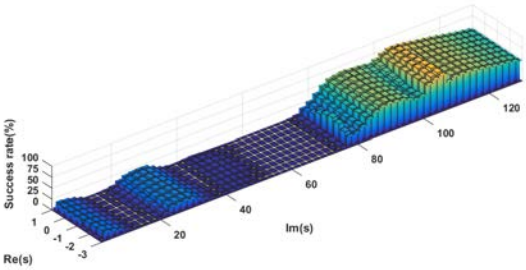

Figure 9.13 – Success rates of the SDDLV from estimated modal parameters using single mode set $\mathcal{M}_2$ in dependence of s.

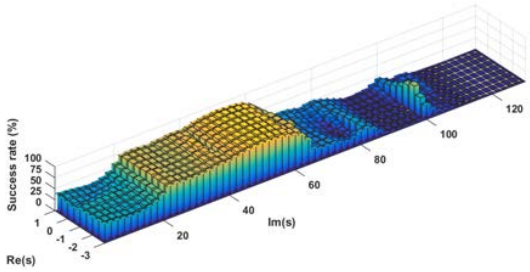

Figure 9.14 – Success rates of the S-SDDLV using single mode set $\mathcal{M}_1$ in dependence of s

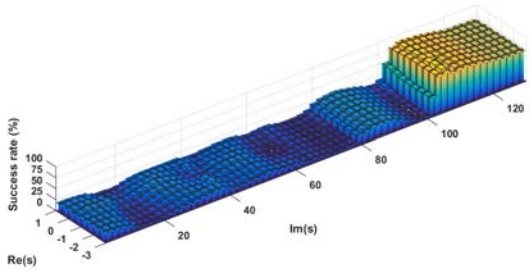

Figure 9.15 – Success rates of the S-SDDLV using single mode set $\mathcal{M}_2$ in dependence of s

9.3.1.3 Success rate of the damage localization using multiple mode sets

In the previous section, the success rate of the damage localization using a single mode set was not successful everywhere in the s-plane mainly because of modal truncation errors. Even considering the s-value in the vicinity of the identified modes, where modal truncation errors should be low, was not sufficient to achieve a reasonable success rate (e.g. $> 85\%$) for all choices of s, especially for $\mathcal{M}_2$ in Figure 9.15. It cannot be known beforehand which s-values lead to good results in real experiments, however, the only reasonable assumption is to choose them in the vicinity of the identified modes. This motivates the use of the additional information in multiple mode sets instead of using a single mode set alone, expecting better results for the entire s-plane. Therefore, the computation of stress for damage localization has been obtained by taking into account the information using multiple mode sets instead of using single mode set. Considering the statistical uncertainties of the modal parameters using multiple mode sets for the subsequent stress evaluation can improve the situation significantly. In the meanwhile, the theoretical stress from modal parameters and estimated stress from data sets are also weighted by taking norm of all stress.

For the new approach using multiple mode sets, first the s-values are chosen similarly for mode set $\mathcal{M}_1$ and $\mathcal{M}_2$ with $\mathrm{Re}(s^1), \mathrm{Re}(s^2) = 1$, $\mathrm{Im}(s^1), \mathrm{Im}(s^2) \in [0, 130]$ and then, the s-values are chosen separately for each mode set $\mathcal{M}_1$ and $\mathcal{M}_2$, such that they are in the vicinity of the identified modes of the respective mode set. This means that the s-value s^1 for mode set $\mathcal{M}_1$ is chosen with $\mathrm{Im}(s^1) \in [0, 64]$, and s^2 for mode set $\mathcal{M}_2$ with $\mathrm{Im}(s) \in [66, 128]$, while the real parts are both in the interval $\mathrm{Re}(s^1), \mathrm{Re}(s^2) \in [-3, 1]$.

The impact of the choice of s-values s, s^1 and s^2 when treating the multiple mode sets has been investigated same or differently for the respective mode sets. The following three cases are now considered:

Case 1: combination of $\mathcal{M}_1$ and $\mathcal{M}_2$ with the same s-values from the entire range in the vicinity of modes.

In this case, the damage localization results are obtained using multiple mode sets in the combination of single mode set $\mathcal{M}_1$ and $\mathcal{M}_2$ for the chosen s-value with $\mathrm{Re}(s^1), \mathrm{Re}(s^2) = 1$ and $\mathrm{Im}(s^1), \mathrm{Im}(s^2) \in [0, 130]$. In Figure 9.16, it is shown that the performance of the damage localization from the theoretical modal parameters are significant with compared to the single mode sets in Figure 9.10 and 9.11 in the interval of $\mathrm{Im}(s^1) \in [0, 62], \mathrm{Im}(s^2) \in [77, 130]$.

On other hands, it is seen in Figure 9.17 that the success rates of the damage localization from the estimated stress are also improved but not satisfactory at all (i.e. $< 85\%$) due to modal truncation and estimation errors. Then, it can be seen in Figure 9.18 that the statistical combination of the results from the single mode sets significantly improves the damage localization performance nearly everywhere in the s-plane. Figure 9.18 shows that overall success rates are satisfactory in the range of the s-values compared to the respective single mode sets, even though the performance for the chosen s^1 and s^2 was not satisfied at everywhere in the s-plane for mode set $\mathcal{M}_1$ and $\mathcal{M}_2$, respectively.

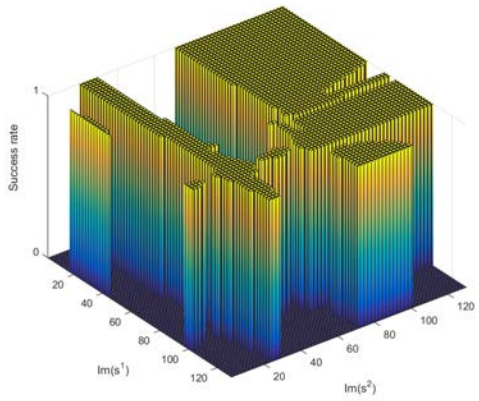

Figure 9.16 – Case 1: success of the SDDLV from theoretical modal parameters using multiple mode sets $\mathcal{M}_1$ and $\mathcal{M}_2$, in dependence of s with $\mathrm{Im}(s^1), \mathrm{Im}(s^2) \in [0, 130]$.

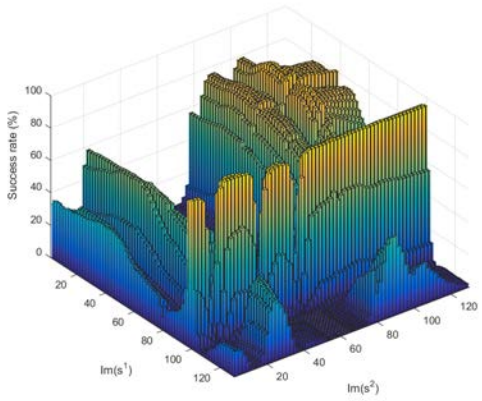

Figure 9.17 – Case 1: success rates of the SDDLV from estimated modal parameters using multiple mode sets $\mathcal{M}_1$ and $\mathcal{M}_2$, in dependence of s with $\mathrm{Im}(s^1), \mathrm{Im}(s^2) \in [0, 130]$.

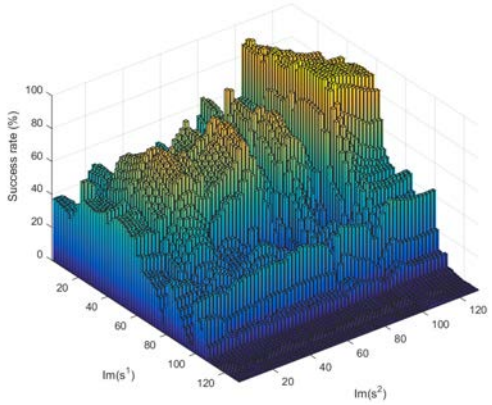

Figure 9.18 – Case 1: success rates of the S-SDDLV using multiple mode sets $\mathcal{M}_1$ and $\mathcal{M}_2$, in dependence of s with $\mathrm{Im}(s^1), \mathrm{Im}(s^2) \in [0, 130]$.

In the interval $\mathrm{Im}(s^1) \in [0, 60], \mathrm{Im}(s^2) \in [90, 120]$ the maximum success rate is achieved, which is slightly lower than 80% for single mode set $\mathcal{M}_1$ in Figure 9.14, but significantly higher than for single set $\mathcal{M}_2$ at the respective s-value in Figure 9.15.

Notice that combining the information from multiple mode sets strongly mitigates the risk of accidentally choosing s-values with poor performance in the single mode sets. The overall results with the multiple mode sets are as good or better than the ones in both single mode set cases.

Case 2: combination of $\mathcal{M}_1$ and $\mathcal{M}_2$ with different s-values

- s^1 from the entire range in the vicinity of $\mathcal{M}_1$, and
- s^2 with $\mathrm{Im}(s^2) = 83$, where it gave a poor performance using $\mathcal{M}_2$ only (see Figure 9.15).

In this case, Figure 9.19 shows that the performance of the damage localization from the theoretic modal parameters are good with compared to the single mode sets in Figure 9.10 and 9.11, while the performance of the damage localization from estimated stress is average in Figure 9.20 with compared to Figures 9.12 and 9.13 due to modal truncation and estimation errors. Then, Figure 9.21 shows that reasonable success rates ($> 85\%$) are achieved in a large range of s-values compared to the respective single mode sets, even though the performance for the chosen s^2 was poor in mode set $\mathcal{M}_2$. In the interval $\mathrm{Im}(s^1) \in [20, 62]$, the maximum success rate is achieved, which is slightly lower than 80% for single mode set $\mathcal{M}_1$ in Figure 9.14, but significantly higher than for single set $\mathcal{M}_2$ at the respective s-value in Figure 9.15. In the less optimal region with $\mathrm{Im}(s^1) \in [0, 20]$, the success rate using the multiple mode sets is much higher than in the respective regions using the single mode sets.

Case 3: combination of $\mathcal{M}_1$ and $\mathcal{M}_2$ with selected s-values

- s^1 from the entire range in the vicinity of $\mathcal{M}_1$, and
- s^2 with $\mathrm{Im}(s^2) = 106$, where it gave a good performance using $\mathcal{M}_2$ only (see Figure 9.15).

In this case, the performance of the damage localization in Figure 9.22 and 9.23 from the theoretical and estimated stress is satisfactory with compared to single mode sets. Then, it can be seen in Figure 9.24 that the success rate of the damage localization with the new method has significantly improved the situation everywhere in the s-plane, compared to all previous results, with success rates between 85% and 99%.

From cases 1, 2 and 3, it can be concluded that the treatment of all available modes with the statistical multiple mode set strategy of this paper improves the damage localization performance, compared to the consideration of using a limited number of modes in a single mode set in the previous approach [Ber10, DMBM13, MDBM15]. Choices of the respective s-values should be within the vicinity of the respective mode sets. The effect of s-values with poor performance are mitigated, and a significant improvement on the localization success rate is made through the statistical combination of results in the approach.

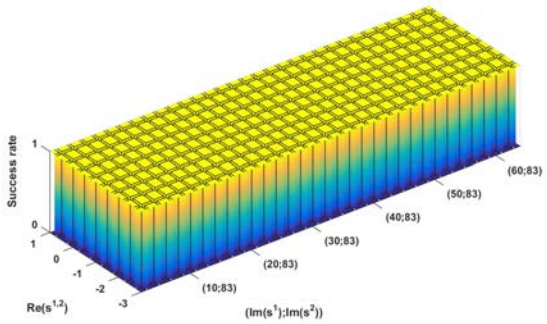

Figure 9.19 – Case 2: success of the SDDLV from theoretical modal parameters using multiple mode sets $\mathcal{M}_1$ and $\mathcal{M}_2$, in dependence of s^1 and s^2 with $\mathrm{Im}(s^1) \in [0, 64], \mathrm{Im}(s^2) = 83$.

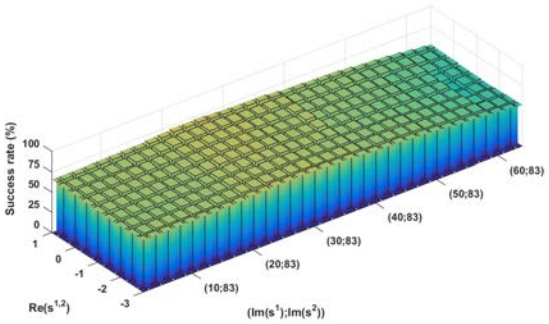

Figure 9.20 – Case 2: success rates of the SDDLV from estimated modal parameters using multiple mode sets $\mathcal{M}_1$ and $\mathcal{M}_2$, in dependence of s^1 and s^2 with $\mathrm{Im}(s^1) \in [0, 64], \mathrm{Im}(s^2) = 83$.

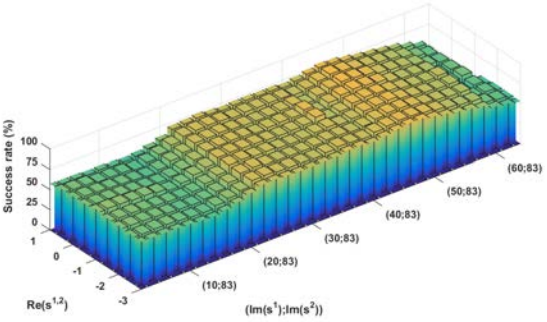

Figure 9.21 – Case 2: success rates of the S-SDDLV using multiple mode sets $\mathcal{M}_1$ and $\mathcal{M}_2$, in dependence of s^1 and s^2 with $\mathrm{Im}(s^1) \in [0, 64], \mathrm{Im}(s^2) = 83$.

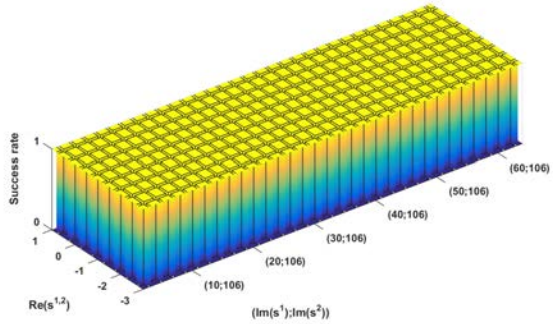

Figure 9.22 – Case 3: success of the SDDLV from theoretical modal parameters using multiple mode sets $\mathcal{M}_1$ and $\mathcal{M}_2$, in dependence of s^1 and s^2 with $\mathrm{Im}(s^1) \in [0, 64], \mathrm{Im}(s^2) = 106$.

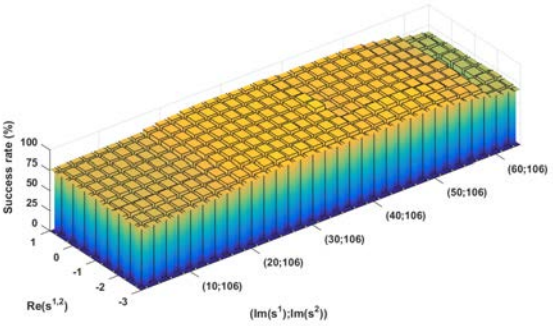

Figure 9.23 – Case 3: success rates of the SDDLV from estimated modal parameters using multiple mode sets $\mathcal{M}_1$ and $\mathcal{M}_2$, in dependence of s^1 and s^2 with $\mathrm{Im}(s^1) \in [0, 64], \mathrm{Im}(s^2) = 106$.

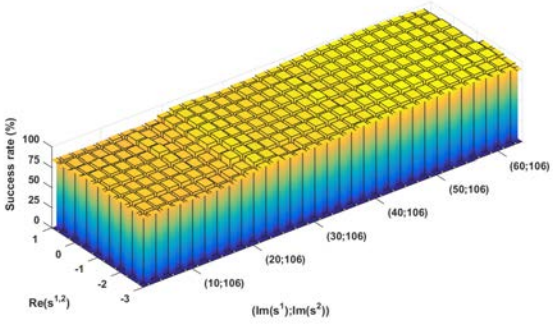

Figure 9.24 – Case 3: success rates of the S-SDDLV using multiple mode sets $\mathcal{M}_1$ and $\mathcal{M}_2$, in dependence of s^1 and s^2 with $\mathrm{Im}(s^1) \in [0, 64], \mathrm{Im}(s^2) = 106$.

9.3.2 Damage localization subject to different noise level

In this section, Monte-Carlo experiments of 100 datasets have been demonstrated in order to see the influence of the damage localization results at different noise level, starting from 5% to 200%. In Figures 9.25 and 9.26, the results are shown for estimated stress and statistical χ_t^2-tests, respectively. Note that the s-values, $\mathrm{Re}(s) = -[0.5, 3]$ and $\mathrm{Im}(s) \in [1, 61]$ are chosen in the vicinity of the first mode sets $\mathcal{M}_1$, corresponding to first three modes.

Summarizing the results, it is found that the success of the damage localization seems to decrease linearly with respect to increasing noise level for both estimated stress (see Figure 9.25) and statistical evaluation of χ_t^2-test (see Figure 9.26). Note that when taking into account the uncertainties from the measurements, the statistical tests improves the results in comparison to estimates.

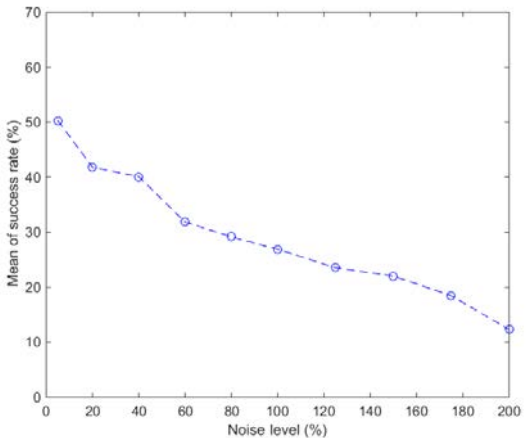

Figure 9.25 – Success rates of damage localization from estimated stress at different noise level for s-values, $\mathrm{Re}(s) = -[0.5, 3]$ *and* $\mathrm{Im}(s) \in [1, 61]$

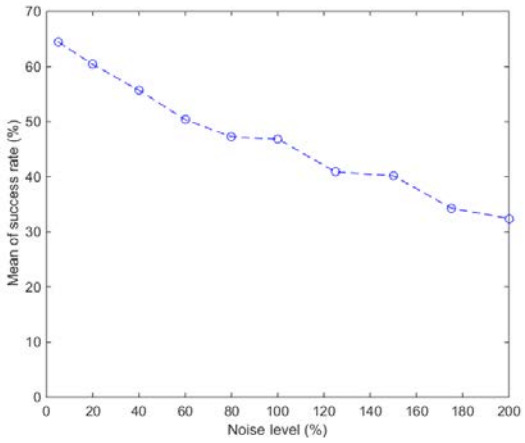

Figure 9.26 – Success rates of damage localization from statistical χ_t^2*-tests at different noise level for s-values,* $\mathrm{Re}(s) = -[0.5, 3]$ *and* $\mathrm{Im}(s) \in [1, 61]$

9.3.3 Numerical application 2: 3D cube beam model

In a second numerical application, the damage localization approach has been demonstrated on a 3D cube beam model as shown in Figure 8.11 in Section 8.3.5, considering a more complex structure than in the previous example.

9.3.3.1 Localization of results in all elements at one s-value

The localization results at all elements are computed using one dataset in both damaged and healthy states. For a single mode set, the computation of all stresses is done at $s_1 = -1 + 26\mathrm{i}$. In Figure 9.27(a)-9.27(c), all stress values corresponding to all elements are presented, while the smallest stress value is correctly located in the damaged element at bar 8. Considering uncertainties, the damage localization is correctly found at the smallest χ_t^2 values at element 8 in Figure 9.27(c).

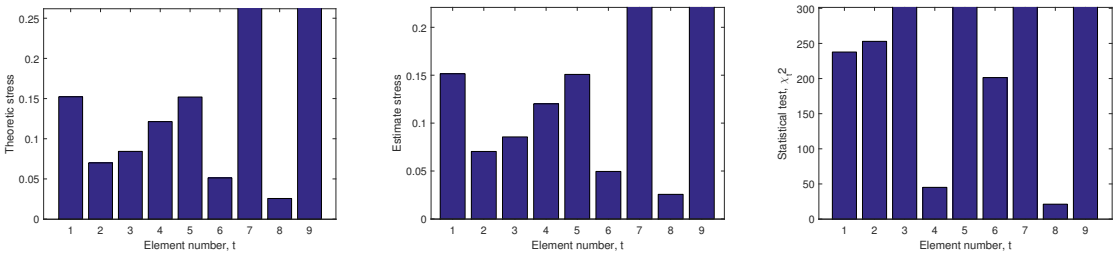

(a) SDDLV for theoretic stress (b) SDDLV for estimated stress (c) S-SDDLV (statistical test)

Figure 9.27 – Localization using a single mode set: stress computation and statistical evaluation at $s_1 = -1 + 26\mathrm{i}$ *-four sensors, 5% output noise, 50% stiffness reduction at bar 8.*

Recall that there is always a possibility to use the same or different s-values for the computation of stress with the proposed method. As in the previous example, we analyze the success rate for localization with the mode sets separately in dependence of the chosen s-value, before jointly evaluating it based on all three mode sets with the new method from this paper. Monte Carlo simulations are carried out using 100 simulated datasets in healthy and reference states to determine the success rate, where for each dataset the modes and their uncertainties are identified using SSI. The entire s-value range in the vicinity of the modes (see Table 8.5) is $\mathrm{Re}(s) \in [-12, -7] \cup [-4, -1]$ and $\mathrm{Im}(s) \in [0, 650]$.

In the next section, the success rate of the damage localization results has been computed using the single mode sets separately in Monte-Carlo simulation for 100 datasets. Then, the success rate of the damage localization is illustrated with the new proposed method for the joint statistical evaluation of the multiple mode sets.

9.3.3.2 Success rate of the damage localization using a single mode set

We evaluate the success rates of the statistical damage localization for based either on single mode set $\mathcal{M}_1$, $\mathcal{M}_2$ or $\mathcal{M}_3$ in dependence of the chosen s-value, before going to the joint evaluation of the multiple mode sets in the next section.

The s-values were chosen within the global range described above to see the influence of the different s-values also beyond the range of each individual mode set. In Figures 9.30, 9.33 and 9.36, the success rates of correct damage localization (z-axis) are shown in dependence of the real and imaginary part of the chosen s-values (x and y-axis) for mode sets $\mathcal{M}_1$, $\mathcal{M}_2$ and $\mathcal{M}_3$, respectively. Indeed it can be seen that damage localization for both mode sets is satisfactory only for s-values in the vicinity of the modes of the respective mode sets.

For mode set $\mathcal{M}_1$, corresponding to the first four modes in the region $\mathrm{Im}(s) \in [0, 175]$, the success rate of the damage localization results are shown in Figure 9.28-9.30 from the theoretical stress, estimated stress and statistical evaluation of χ_t^2-test. Figure 9.30 shows that the success rate is satisfactory only in the interval of the Laplace variables with $\mathrm{Im}(s) \in [0, 81] \cup [120, 201]$, where it reaches up to 100%. Beyond this interval, it is close to zero and the damage localization cannot be indicated due to the modal truncation error, which is significant outside the interval containing the identified modes (see Table 8.5). However, there is also a region within the vicinity of the modes of $\mathcal{M}_1$, where the success rate is close

to zero. Notice that the considered modes in this example are in the interval $[1, 175]$ on the imaginary line.

For mode set $\mathcal{M}_2$, the success rate of the damage localization results from theoretical stress, estimated stress and statistical evaluation of χ^2_t-test are shown in Figure 9.31-9.33. The four modes in mode set $\mathcal{M}_2$ are within the region $\mathrm{Im}(s) \in [300, 475]$, and it can be seen in Figure 9.33 that the success rate of damage localization is satisfying ($> 85\%$) in the interval $\mathrm{Im}(s) \in [300, 445]$, covering nearly the entire region. Possibly, the success rate in the last part of the region is low due to the proximity of mode set $\mathcal{M}_3$ and the resulting truncation errors.

Finally, for mode set $\mathcal{M}_3$, the results are shown in Figure 9.34-9.36 for the theoretical stress, estimated stress and statistical evaluation of χ^2_t-test. It can be seen in Figure 9.36 that the success rate of damage localization for the statistical χ^2_t-test is satisfactory in comparison to Figure 9.35, where the modes are in the interval $\mathrm{Im}(s) \in [450, 625]$. The success rate is good ($> 70\%$) for $\mathrm{Im}(s) \in [500, 580]$, covering only a part of the region corresponding to $\mathcal{M}_3$.

Similarly as in the previous example, this shows that choosing the s-value in the vicinity of the identified poles does not necessarily give perfect results. This motivates the combination of results of different mode sets for more robustness and less dependence on the particular choice of s.

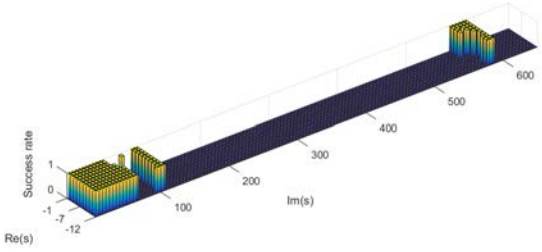

Figure 9.28 – Success of the SDDLV from theoretical modal parameters using single mode set $\mathcal{M}_1$, in dependence of s.

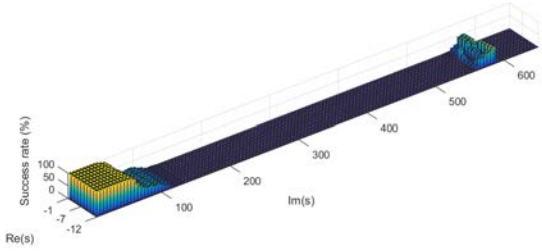

Figure 9.29 – Success rates of the SDDLV from estimated modal parameters using single mode set $\mathcal{M}_1$, in dependence of s.

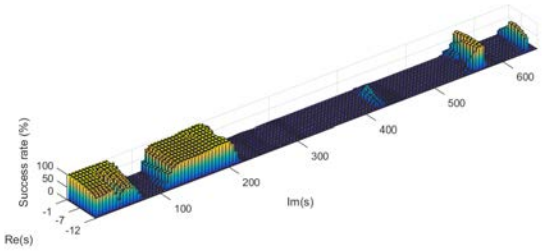

Figure 9.30 – Success rates of the S-SDDLV using single mode set $\mathcal{M}_1$, in dependence of s.

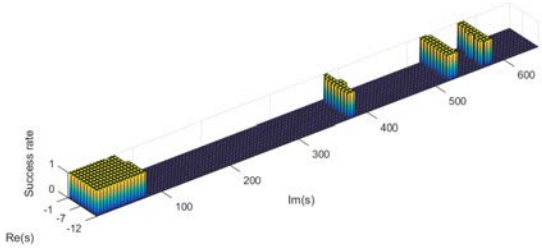

Figure 9.31 – Success of the SDDLV from theoretical modal parameters using single mode set $\mathcal{M}_2$, in dependence of s.

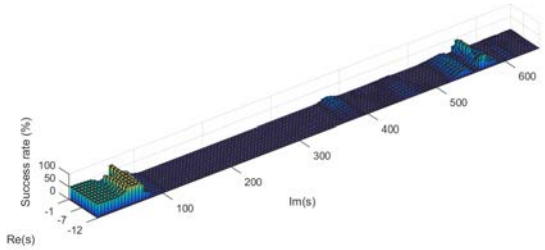

Figure 9.32 – Success rates of the SDDLV from estimated modal parameters using single mode set $\mathcal{M}_2$, in dependence of s.

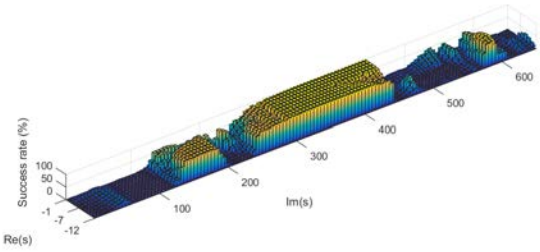

Figure 9.33 – Success rates of the S-SDDLV using single mode set $\mathcal{M}_2$, in dependence of s.

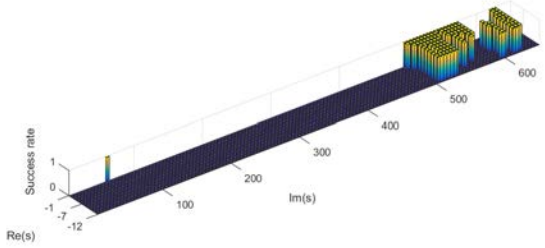

Figure 9.34 – Success of the SDDLV from theoretical modal parameters using single mode set $\mathcal{M}_3$, in dependence of s.

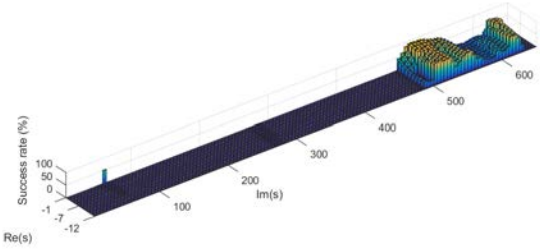

Figure 9.35 – Success rates of the SDDLV from estimated modal parameters using single mode set $\mathcal{M}_3$, in dependence of s.

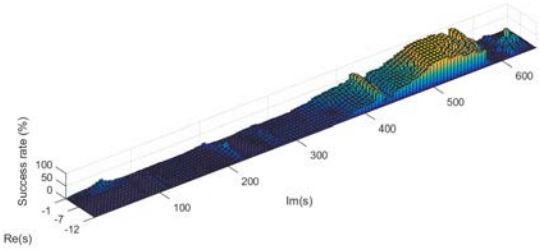

Figure 9.36 – Success rates of the S-SDDLV using single mode set $\mathcal{M}_3$, in dependence of s.

9.3.3.3 Success rate of the damage localization using multiple mode sets

For the new statistical approach using multiple mode sets, the s-values are chosen separately for each mode set $\mathcal{M}_1$, $\mathcal{M}_2$ and $\mathcal{M}_3$, such that they are in the vicinity of the identified modes of the respective mode set. Therefore, the range of the respective s-values s^1, s^2 and s^3 is

chosen with $\mathrm{Re}(s^1) \in [-4,-1]$, $\mathrm{Im}(s^1) \in [0,175]$, $\mathrm{Re}(s^2) \in [-10,-7]$, $\mathrm{Im}(s^2) \in [300,475]$, $\mathrm{Re}(s^3) \in [-12,-9]$, $\mathrm{Im}(s^3) \in [450,625]$.

The impact of the choice of s-values s^1, s^2 and s^3 in the respective mode sets has been investigated for the joint evaluation of the stress, where the evaluation for each triplet (s^1, s^2, s^3) is carried out with s^1, s^2 and s^3 covering the above range of s-values used in the respective mode sets.

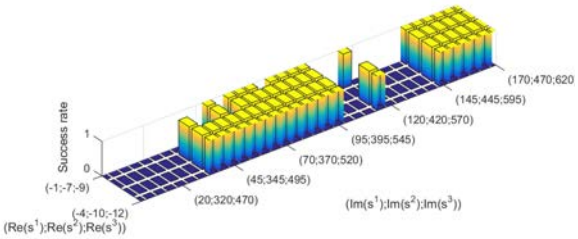

Figure 9.37 – Success of the SDDLV from theoretical modal parameters using multiple mode sets $\mathcal{M}_1$, $\mathcal{M}_2$ and $\mathcal{M}_3$, in dependence of s^1, s^2 and s^3.

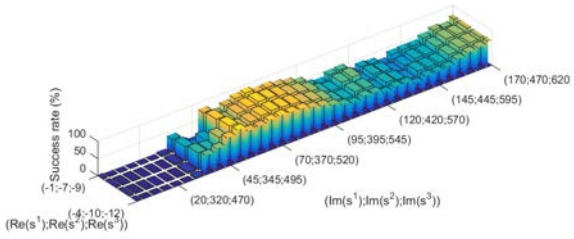

Figure 9.38 – Success rates of the SDDLV from estimated modal parameters using multiple mode sets $\mathcal{M}_1$, $\mathcal{M}_2$ and $\mathcal{M}_3$, in dependence of s^1, s^2 and s^3.

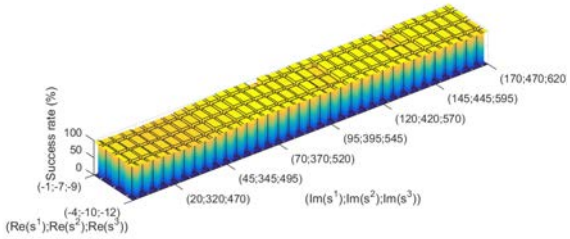

Figure 9.39 – Success rates of the S-SDDLV using multiple mode sets $\mathcal{M}_1$, $\mathcal{M}_2$ and $\mathcal{M}_3$, in dependence of s^1, s^2 and s^3.

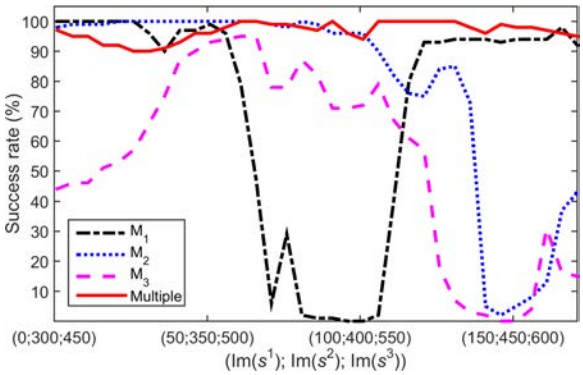

Figure 9.40 – Success rates of the S-SDDLV in the single mode sets $\mathcal{M}_1$, $\mathcal{M}_2$ and $\mathcal{M}_3$ with s in the vicinity of the respective modes, compared to the success rate using jointly the multiple mode sets.

The results are shown in Figure 9.37-9.39 for the theoretical stress, estimated stress and statistical evaluation of χ^2_t-test using multiple mode sets. The resulting success rate of the joint evaluation is shown in Figure 9.39, where it can be seen that the success rate is nearly at 100% everywhere in the s-plane and significantly improves the results with compared to estimated in Figure 9.38. A comparison to the success rates from the single mode sets in the respective range of s-values is made in Figure 9.40 for fixed real parts $\mathrm{Re}(s^1) = -3$, $\mathrm{Re}(s^2) = -9$ and $\mathrm{Re}(s^3) = -11$, where it can be clearly seen that the statistical combination of the results from the single mode sets significantly improves the damage localization performance

nearly everywhere in the s-plane. In particular, the choice of s-values in the vicinity of the identified modes always yields very good success rates in the joint evaluation of the multiple mode sets, while this was not always the case using the single mode sets separately.

9.3.4 Result analysis

Summarizing the results, it is found that that the statistical evaluation in general improves the damage localization performance. For example, the statistical evaluation with the χ_t^2-test in Figure 9.39 gives good performance with respect to Figures 9.37 and 9.38, where the success of the damage localization is poor in some part of the s-plane in both theoretical and estimated stress. Only in one example the chi2-test showed a slightly decreased performance, namely in Figure 9.18 with respect to theoretical and estimated stress in Figures 9.16 and 9.17, but only for few s-values in the complex plane. Notice that in both theoretical and estimated stress, the damage localization criteria (5.5) is strictly followed by taking into account the norm of all stress values/element (including the real and imaginary part of stress). In the statistical evaluation of χ_t^2-test (5.14) the covariance is propagated to the estimated stress, and this covariance depends on the limited sampled data containing the measurements noise.

In general, taking into account the statistical uncertainties of damage indicators in their evaluation should increase the performance of damage assessment. They provide an additional information and quantify the confidence we can have in the estimation of a damage indicator. Thus, they provide a natural weighting of a damage indicator in order to evaluate significance.

When aggregating damage indicators corresponding to the same element, e.g. for different s-values, different mode sets, or different kinds of stress, their uncertainties provide a natural weighting to combine them. It can be assumed that badly estimated damage indicators have a higher uncertainty than well estimated ones, and e.g. s-values with a low damage localization performance in a mode set lead are linked to a badly estimated damage indicator with relatively high uncertainty. When combining them from different mode sets or different s-values, those badly estimated indicators with high uncertainty will have a low weight, while well-estimated indicators having low uncertainty will have a strong weight. When aggregating several indicators based on different s-value and/or mode sets, those with a low uncertainty will have a strong weight. Since these are the ones which are a priori well estimated and have a good performance in the respective mode set for the respective s-value, the aggregation benefits particularly from the indicators with a good performance, while indicators with a bad performance are mitigated. This statistical aggregation hence should in general lead to better results than a deterministic aggregation, where just the norm is taken of the indicators for the same element, providing them with the same weight. Even the deterministic aggregation in the theoretical case where no variance errors are present may then show less performance than the statistical aggregation, due to the same weighting of different values in the theoretical case vs. a different more adapted weighting when taking into account the uncertainties.

9.4 Beam model with crack

In this numerical application, the damage localization with SDDLV has been applied on a 2D circular beam of 15 DOFs for crack localization using five sensors as shown in Figure 8.9 in Section 8.3.4.

As in the previous example, the localization results are demonstrated in all elements at one s-value for one dataset and then we analyze the success rate for localization with the 5 modes in dependence of the chosen s-value. Monte Carlo simulations are carried out using 100 simulated datasets in healthy and damaged states to determine the success rate, where in each dataset the modes and their uncertainties are identified using SSI. The entire s-value range in the vicinity of the modes is $\mathrm{Re}(s) \in [-260, -2]$ and $\mathrm{Im}(s) \in [0, 10000]$.

9.4.1 Localization of results in all elements at one s-value

The localization results at all elements are computed using one of the Monte-Carlo datasets in both healthy and damaged states. Recall that the damage localization is inferred by the stress value closest to zero. Using these 5 modes, the computation of all stresses is done at $s_1 = -1 + 510\mathrm{i}$. In Figure 9.41(a), all stress values corresponding to healthy and damaged elements are presented, while the smallest stress value is correctly located in the damaged element at bar 1. Considering uncertainties, the crack localization is correctly found at the smallest χ_t^2 values at element 1 in Figure 9.41(c). It can be seen that χ_t^2 in Figure 9.41(c) shows similar results as the theoretical result in Figure 9.41(a).

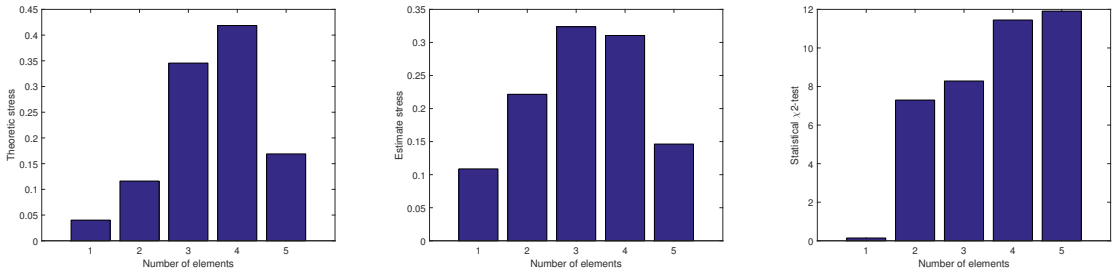

(a) SDDLV for theoretic stress (b) SDDLV for estimated stress (c) S-SDDLV (statistical test)

Figure 9.41 – Localization results: stress computation and statistical evaluation at $s_1 = -1 + 510\mathrm{i}$ -using five sensors [Y-direction at each node], 5% output noise, 0.01m crack depth at bar 1.

In Figure 9.42, the crack localization results are shown from the true modal parameters in dependence of the real and imaginary part of the chosen s-values (x and y-axis). However, there is also a region within the vicinity of the modes, where the success rate is zero due to the modal truncation error and may be the close choice of s-value. Figure 9.43 shows that the success rates of the crack localization are poor from estimated modal parameters and the crack localization cannot be indicated because of modal truncation and variation errors.

However, when considering the uncertainties in the statistical evaluation, the performance of the crack localization good in Figure 9.44 compared to Figure 9.43. Possibly, the success

rate in the last part of the s-plane region is low where the s-value is far away from the modes and the resulting truncation errors.

9.4.2 Success rate of the crack localization at element 1

In this section, the success rates of the crack localization are evaluated using the first 5 identified modes in dependence of the real and imaginary part of the chosen s-values (x and y-axes). The s-values were chosen within the global range described above to see the influence of the different s-values also beyond the range of each mode. In Figure 9.42, 9.43, 9.44, the crack localization results are illustrated from theoretical, estimated and statistical χ_t^2-test respectively. All these computations are done at Laplace variables, $\mathrm{Re}(s) \in [-260, -2]$ and $\mathrm{Im}(s) \in [0, 10000]$ which are located in the vicinity of the identified poles (see Table 8.4).

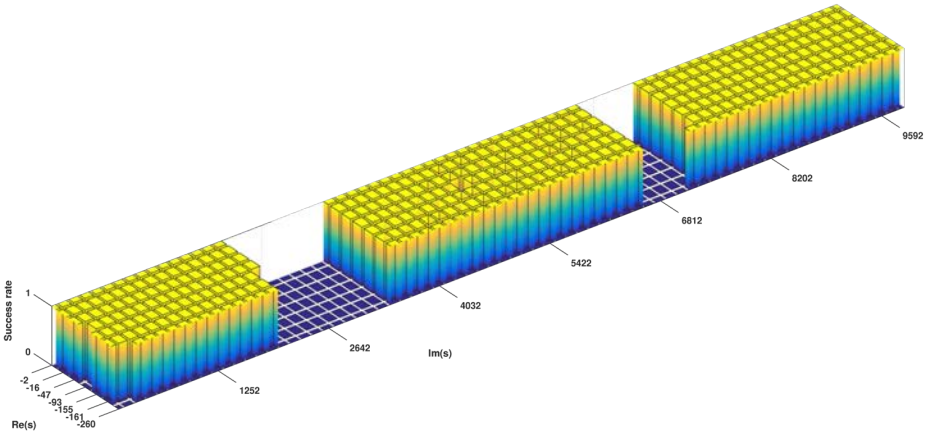

Figure 9.42 – Success of the SDDLV from theoretical modal parameters in dependence of s (crack depth 0.01m)

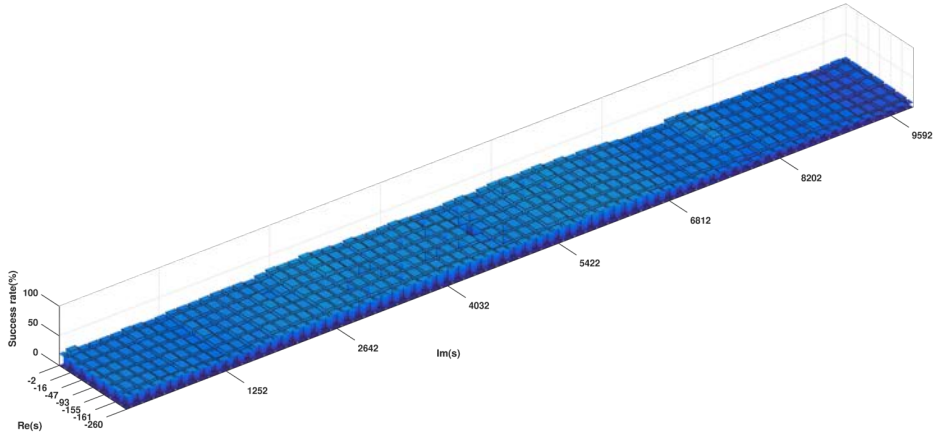

Figure 9.43 – Success rates of the SDDLV from estimated modal parameters in dependence of s (crack depth 0.01m)

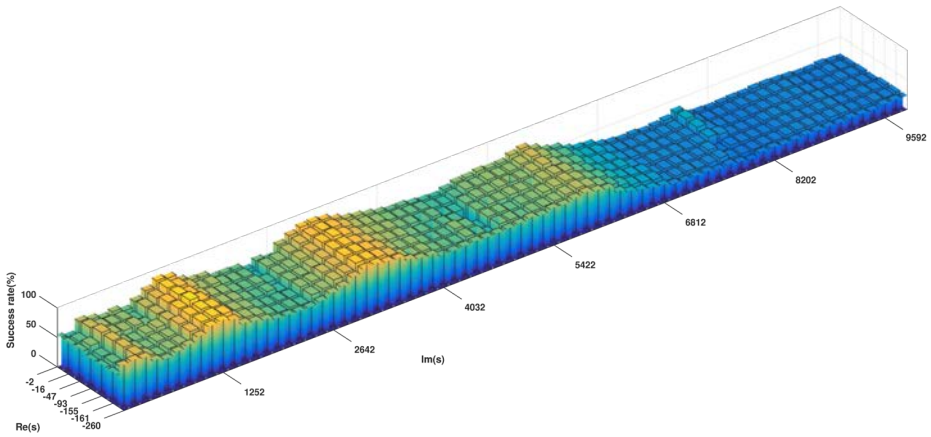

Figure 9.44 – Success rates of the S-SDDLV in dependence of s for crack at element 1 (crack depth 0.01m)

In the following, the success rates of the crack localization are obtained at element 1 with respect to different crack depth.

9.4.3 Success rate Vs. crack depth

In the previous section, the outcome of the crack localization results is investigated at element 1 for a fixed crack depth of 0.01 m in dependence of the real and imaginary part of the chosen s-values (x and y-axes) for the identified modes.

In this section, the success rate of the crack localization is obtained by increasing the depth of crack from starting 0.0001 m to 0.012 m with a step size of 0.0005 m. For each crack level, a Monte-Carlo experiments of 100 datasets has been demonstrated in order to see the success rate of the crack localization. In Figure 9.45(a) assuming crack at element 1, the success rate of the crack localization is obtained for a fixed s-value, $s_1 = -16 + 1252\mathrm{i}$ by increasing the crack depth. In Figure 9.45(b), the mean of the success rate (%) of the crack localization has also shown for the choice of s-values, $\mathrm{Re}(s) = -16$ and $\mathrm{Im}(s) \in [100, 3437]$ with respect to increasing the crack level.

From Figures 9.45, it is seen that the success rate of the crack localization has increased, while the depth of crack level increases. For very low damage, since we have 5 elements, the success rates for damage should be 1/5 or 20% at beginning. Therefore, Figure 9.45(a) shows that the minimum success rate starts around 20% while in the beginning the success rates around 30%, possibly it is caused due to the small crack size, noise, or lack of accuracy of the identification problems in the Monte-Carlo experiments.

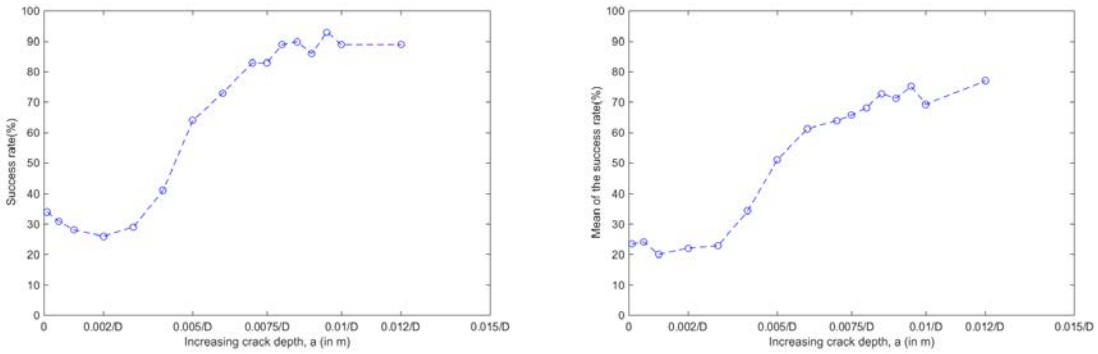

(a) Success rate for a fixed s-value

(b) Success rate for s-values

Figure 9.45 – Crack at element 1: success rate Vs. crack level (increasing) with a/D -using five sensors [Y-direction at each node], 5% output noise, note that a is the crack depth and D is the diameter of the beam.

9.5 2D Beam model: Influence of mesh size

In this section, the damage localization method has been applied on a 2D beam model in the influence of different mesh size as detailed in Section 8.3.3. To analyze the performance of the method, the following cases are considered for the same configuration of sensors

- **Case 1:** For a large damage zone of 20 cm, the damage localization method has been applied on a rough and fine mesh of 25 and 100 beam elements respectively.
- **Case 2:** For a small damage zone of 4 cm, the damage localization method has been applied on a rough and fine mesh of 25 and 100 beam elements respectively.
- **Case 3:** For a small damage zone of 4 cm, the load vectors computed from estimated data of 100 beam elements (fine mesh) and then applied to the L_{model} of 25 elements (rough mesh).

In all cases, the success rates of the damage localizations are evaluated only with the identified modes in dependence of the chosen s-value. Monte Carlo simulations are carried out using 100 simulated datasets in healthy and damaged states to determine the success rate, where in each dataset the modes and their uncertainties are identified using SSI.

9.5.1 Case 1: Beam model with 25 elements (rough mesh), large damaged zone of 20 cm

In this case, the damage localization method has been applied to a 2D beam model of 25 elements (rough mesh) as shown in Figure 8.7(a). The total number of Degrees Of Freedom (DOFs) of the structure is 75. The damage elements are considered as 11-15. The damaged element in the model is simulated by decreasing Young and Shear modulus by 50 % of their original value.

In the application, the outcome of the damage localization results is investigated in dependence of the real and imaginary part of the chosen s-values (x and y-axis) for the identified modes (see Table 8.3). Recall that stress values close to zero indicate potentially damaged elements. Then, real and imaginary parts of the stress vector and their joint covariance are computed. For each element t, the stress values are aggregated statistically in the χ_t^2-test. The entire s-value range in the vicinity of the modes (see Table 8.3) is $\mathrm{Re}(s) \in [-50, -1]$ and $\mathrm{Im}(s) \in [0, 5500]$. We remind that the performance of the method is illustrated in a 3D-bar diagram where x-y axes indicate real-imaginary parts of s-value and z-axis corresponds to the success rate of damage localization.

In the next section, the success rate of the damage localization results has been evaluated using these 5 identified modes only. Monte-Carlo simulations are carried out using 100 simulated datasets in both healthy and damaged states to determine the success rate, where in each dataset the modes and their uncertainties are identified using SSI.

9.5.1.1 Success rate of the damage localization at elements 11-15

The success rates of the damage localization are evaluated based on identified modes in dependence of the chosen s-value. The s-values were chosen within the global range described above to see the influence of the different s-values. In Figures 9.46, 9.47 and 9.48 the success rates of the damage localization are shown from theoretical, estimated and statistical χ_t^2-test respectively, in dependence of the real and imaginary part of the chosen s-values (x and y-axis) for the identified modes (see Table 8.3).

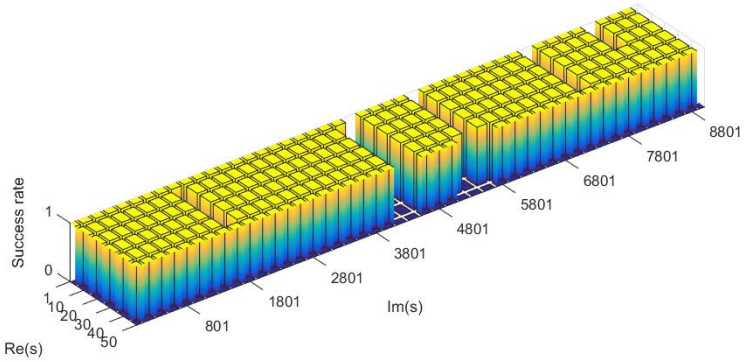

Figure 9.46 – Success of the SDDLV from theoretical modal parameters in dependence of s - using five sensors, 5% output noise, 50% stiffness reduction at elements 11-15 for large damaged zone 20 cm.

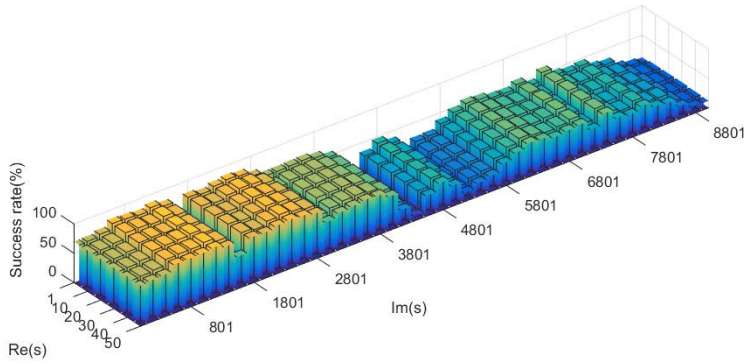

Figure 9.47 – Success rates of the SDDLV from estimated modal parameters in dependence of s - using five sensors, 5% output noise, 50% stiffness reduction at elements 11-15 for large damaged zone 20 cm.

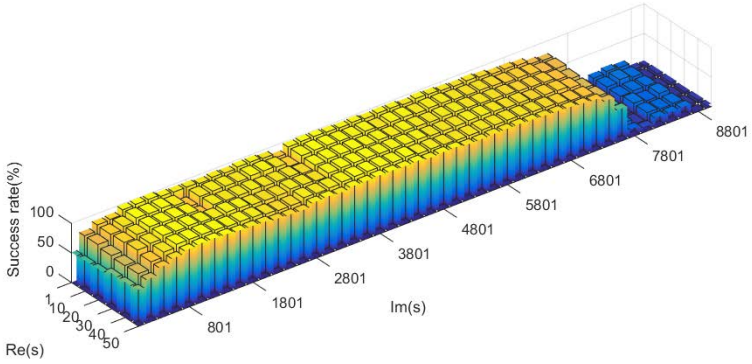

Figure 9.48 – Success rates of the S-SDDLV in dependence of s - using five sensors, 5% output noise, 50% stiffness reduction at elements 11-15 for large damaged zone 20 cm.

From results, it can be summarized that there are some differences in Figures 9.46, 9.47 and 9.48 for the theoretical stress, estimated stress and the statistical χ_t^2-test, respectively. In Figure 9.46, the theoretical stress is unable to indicate the damage localization in some part of the s-values, particularly due to the modal truncation errors and choice of s-value in the close of the mode. Same happens in Figure 9.47, where the success rates of the damage localization from estimated modal parameters are not satisfactory at all because of modal truncation and estimation errors. When considering the uncertainties in the statistical evaluation, the success rates of the damage localization are improved significantly in Figure 9.48 in comparison with Figure 9.47.

9.5.2 Case 1: Beam model with 100 elements (fine mesh), large damaged zone 20 cm

In this case, 2D Beam model with 25 elements (rough mesh) in Figure 8.7(a) has been discretized into 100 elements (fine mesh) as shown in Figure 8.7(b). The total number of

Degrees Of Freedom (DOF) of the structure is 300. Note that the area of damaged zone is same as previously (section 9.5.1) and the damage elements are located here at elements 41-60 (same position).

Similar to previous example, the success rate of the damage localization is analyzed here with the identified modes in dependence of the chosen s-value, $\mathrm{Re}(s) \in [-50, -1]$ and $\mathrm{Im}(s) \in [0, 9000]$. Monte Carlo simulations are carried out using 100 simulated datasets to determine the success rate, where in each dataset the modes and their uncertainties are identified using SSI.

9.5.2.1 Success rate of the damage localization at elements 41-60

In this section, the damage localization results are illustrated using fine mesh of 100 beam elements in Figure 9.49 from statistical χ^2_t-test. All the computations are done in dependence of s-values which are located in the vicinity of the identified poles. It is seen that the success rates of the damage localization in the statistical χ^2_t-test in Figure 9.49 are less in comparison to Figure 9.48 due to large modal truncation error.

Note that for the same configuration of sensors and damaged zone, the performance of the localization results is good using rough mesh with compared to fine mesh, because of large modal truncation error.

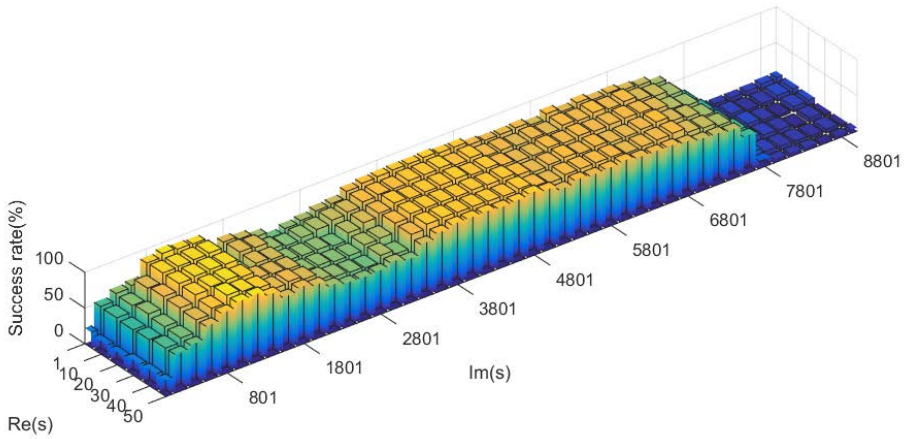

Figure 9.49 – Success rates of the S-SDDLV in dependence of s - using five sensors, 5% output noise, 50% stiffness reduction at elements 41-60 for large damaged zone 20 cm.

In the next Section, the success rates of the damage localization are evaluated by considering a small damaged zone (i.e. 4 cm) instead of large damaged zone (i.e. 20 cm) on both 25 (rough mesh) and 100 elements (fine mesh) respectively.

9.5.3 Case 2: Beam model with 100 elements (fine mesh), damaged elements 49-52 and damaged zone 4 cm

In the previous example, it was seen that the performance evaluation of the damage localization method was satisfied for a large damaged zone on both rough and fine mesh of 2D beam model.

In this section, the localization method has been demonstrated on a 2D beam model of 100 elements (fine mesh) as shown in Figure 8.8(b), assuming a small damaged zone of 4 cm which is located between 0.49-0.52 m from the fixed support. Note that the damaged elements in the model are simulated by decreasing Young and Shear modulus by 50 % of its original value. The total number of Degrees Of Freedom (DOF) of the structure is 300. In order to compute stress field for the damage localization, the load vectors v(s) are computed from the datasets of fine mesh with 100 beam elements and then applied to the L_{model} of 100 beam elements. As previous example, the success rate for localization is analyzed within the identified modes in dependence of the chosen s-value, $\mathrm{Re}(s) \in [-50, -1]$ and $\mathrm{Im}(s) \in [0, 9000]$. In the next Section, Monte Carlo simulations are carried out using 100 simulated datasets to determine the success rate of the statistical evaluation of χ_t^2-test, where in each dataset the modes and their uncertainties are identified using SSI.

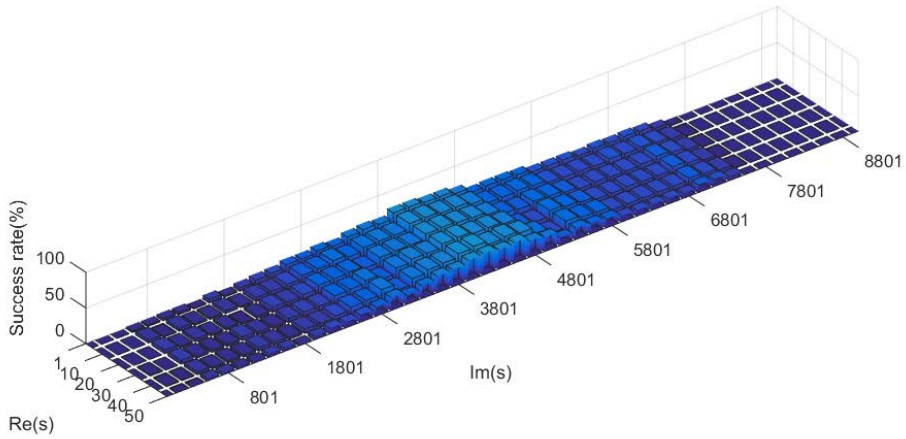

Figure 9.50 – Success rates of the S-SDDLV in dependence of s - using five sensors, 5% output noise, 50% stiffness reduction at elements 49-52 for small damaged zone 4 cm.

9.5.3.1 Success rate of the damage localization at elements 49-52

In Figure 9.50, the success rates of the damage localization are shown from statistical χ_t^2-test in dependence of the real and imaginary part of the chosen s-values (x and y-axis) for the identified modes. From the results, it is seen that the performance of the localization results are not satistfied for small damaged area of 4 cm and the resulting large modal truncation errors.

In the following, the success rates of the localization results are evaluated using a rough mesh of 25 beam elements.

9.5.4 Case 3: Beam model from fine to rough mesh, damaged zone 4 cm

In this case, the localization method has been demonstrated on a 2D beam model of 25 elements (rough mesh) as shown in Figure 8.8(a). Similar to the previous example, assuming that the damaged zone is small and the sensor configurations are also same. Therefore, the load vectors are computed from datasets of fine mesh with 100 beam elements, and then applied to L_{model} of 25 beam elements (rough mesh) as shown in Figure 8.8(a). The damaged is located at element 13. As the previous example, the success rates of the damage localization in the χ_t^2-test are evaluated for Monte-Carlo experiments of 100 datasets.

9.5.4.1 Success rate of the damage localization at element 13

In the previous example, it is seen that the performances of the damage localization results are not satisfied. Hence, the load vectors are computed from the estimated data of 100 beam elements and then it is applied to L_{model} of 25 beam elements (rough mesh) in order to get the stress field. Recall that stress values close to zero indicate potentially damaged elements.

The damage localization results are illustrated in Figure 9.51 from statistical χ_t^2-test in dependence of the real and imaginary part of the chosen s-values (x and y-axes). From the results, it is seen that the performance of the localization results are improved slightly by using the L_{model} of 25 elements in Figure 9.51 instead of fine mesh in Figure 9.50. For a small damaged zone, note that the performance of the method is not satisfied on both rough and fine mesh, possibly due to small damage residuals in the transfer matrix differences between healthy and damaged states in (6.3).

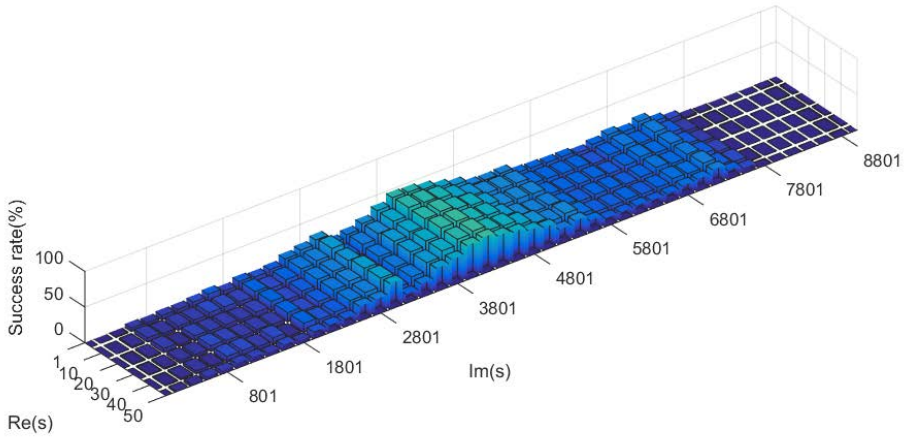

Figure 9.51 – Success rates of the S-SDDLV in dependence of s - using five sensors, 5% output noise, 50% stiffness reduction at element 13 for small damaged zone 4 cm.

Summarizing the results to all cases, it is found that the rough mesh gives better results compared to fine mesh in this example. Recall that in this method, the transfer matrix (5.2) is computed from the estimated modal parameters, satisfying the condition that number of modes could not be higher than number sensors. Therefore, the modal truncation error is very large in the fine mesh model compared to rough mesh, though fine mesh improves the accuracy of the modes. Hence, the performance of the method is poor in this example.

9.5.5 Performance evaluation depending on the mesh

In this section, the localization results are computed depending on the influence of mesh. For the performance evaluation, the load vectors are computed using 100 simulated datasets of a 2D beam model with 100 elements (see Figure 8.8(b)) in both healthy and damaged states, and then it is applied to the L_{model} of different mesh (e.g. 5, 10, 20, 30, 40, 50, and 100) in order to get the stress field. The damaged zone is located in the elements between 47-54 (8 cm) in the fine model, and they are generated by decreasing 50% stiffness of its original value. Note that the estimated load vectors and the damaged zone are same in this study, only the L_{model} is different that is computed depending on the mesh of the FE models. The the Laplace variables $\mathrm{Re}(s) = -[1, 50]$ and $\mathrm{Im}(s) \in [4000, 5000]$ are chosen in the vicinity of modes. Therefore, the evaluation of the performance depends on the threshold (th), defect size (x), mesh, and Laplace variables (s-values).

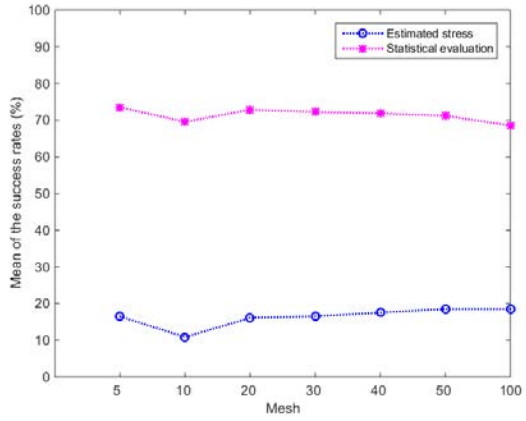

Figure 9.52 – Mean of the success rates with respect to mesh with a threshold (th) 6 cm, defect size (47-54 cm), s-values $\mathrm{Re}(s) = -[1, 50]$, $\mathrm{Im}(s) \in [4000, 5000]$.

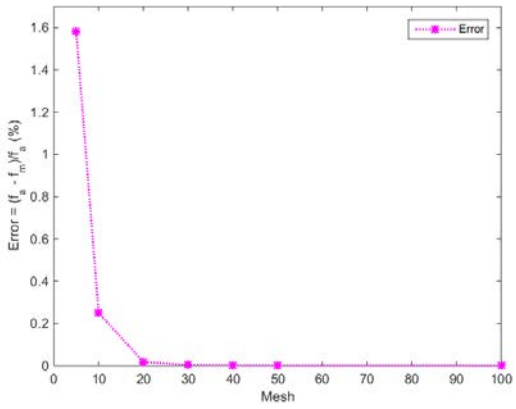

Figure 9.53 – Error in the fifth mode between the analytical (f_a) and model frequency (f_m).

A detection threshold (th) of 6 cm (8.1) has been considered within the vicinity of the damaged zone for the localization of the damaged element since the L_{model} is different and damaged zone is located in the same place. It means that the successful damage localization are guaranteed within 41-60 cm to accommodate the highest mesh size for 5 beam elements. In Figure 9.52, the mean of the success rates (y-axis) are illustrated in Monte-Carlo experiments with respect to different mesh (x-axis) for the respective estimated and the statistical evaluation with the χ^2_t-tests, where in each experiment the modes and their uncertainties

are identified using SSI. From the results, it is seen that the success rates of the damage localization remain in the interval between 68% and 75% for a detection threshold of 6 cm from the damaged zone of 8 cm. It seems that there is hardly any influence of the mesh size in the results. On the other hand, Figure 9.53 shows that error is decreasing with respect to increasing the mesh size.

9.6 Probability of Good Localization (PGL) in terms of distance

In the previous examples, for a rough and fine model of a 2D beam, it has been seen that the performances of the damage localization are not satisfied everywhere in the s-plane mainly because of modal truncation errors and small damaged zone i.e. defect size. Even considering the s-value in the vicinity of the identified modes where modal truncation errors should be low, was not sufficient to achieve a reasonable success rate ($> 85\%$) for all choices of s. Notice that in the 25 beam elements, the accuracy of the localization is reasonable ($> 85\%$) for defect size of 0.2 m in the statistical evaluation in comparison with estimated results, and the total computation time takes only 11.110874 seconds for each experiment.

In practice damage can locate at the neighbour elements from the damaged zone. This motivates the use of the Probability of Good Localization (PGL) in terms of the detection threshold (th) (8.1) within the vicinity of the damaged zone. The value of th can be considered as the required detection threshold for the localization of the damaged element. The evaluation of PGL depends on the threshold (th), defect size (x), mesh, and Laplace variable (LV). In this study, the PGL is evaluated for several sets of simulated measurement data in order to evaluate the performance of the localization method. Each dataset is an independent realization and defines a Monte-Carlo experiment.

In the following two cases are investigated, where PGLs are evaluated on both fine and rough model of a 2D beam in Monte-Carlo experiments. Monte Carlo experiments are carried out using 100 simulated datasets to determine the PGL from estimated stress and statistical evaluation of χ^2_t-test, where in each dataset the modes and their uncertainties are identified using SSI.

Case-1: In order to compute the stress field for the damage localization, the load vectors are computed from estimated datasets of the fine model, and then applied to L_{model} of the structure where the L_{model} is obtained from 2D beam model with 100 elements (fine mesh) as shown in Figure 8.8(b). The computation of PGL (8.1) is obtained depending on the detection threshold (th), Laplace variable (LV), and different defect size (x).

Figures 9.54(a) and 9.54(b) presents the PGL from the estimated and statistical evaluation of χ^2_t-test respectively for a particular choice of Laplace variable (LV), $s = -1 + 4000\mathrm{i}$. Note that defect sizes are assumed starting from 4 to 20 cm with a step size of 2 cm and the detection threshold is defined from 0-8 cm from the damaged zone. For each defect size, the PGLs are evaluated in Monte-Carlo experiments of 100 simulated datasets.

The results indicate that it is possible to determine zones where the PGL is larger for several sets of simulated measurement data. The PGL remains around 85 % in the statistical tests when the defect sizes are considered more than 14 cm. The worse detections are located

between the defect sizes of 4-10 cm and the PGL is less than 35%. However, it is observed that the PGL is larger in Figure 9.54(b) to compare to Figure 9.54(a) for the larger defect size and improves highly except 0 to 2 cm when the threshold is increased.

Case-2: As similiar to previous case 1, the damage localization algorithm has been applied on a 2D beam model of 25 elements (rough mesh) as shown in Figure 8.8(b), while the load vectors are computed from estimated datasets of the fine model. To get the stress field, these load vectors are applied to L_{model} of rough model.

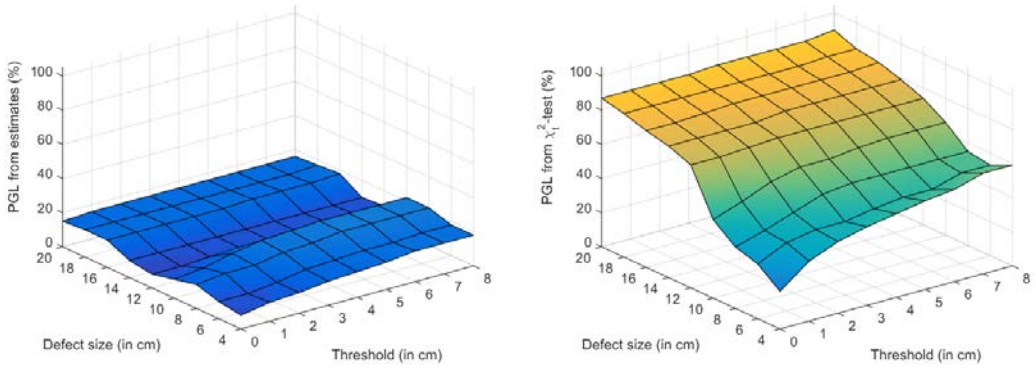

(a) PGL from estimated stress (b) PGL from χ_t^2-test

Figure 9.54 – Case-1: PGL from fine model of 100 beam elements -using five sensors, threshold (0-8 cm), defect size (4-20 cm), Laplace variable $s = -1 + 4000\mathrm{i}$, 5% output noise.

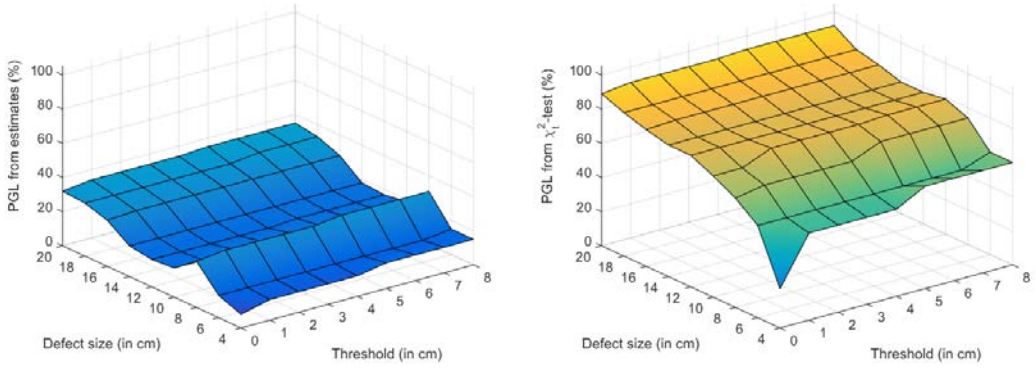

(a) PGL from estimated stress (b) PGL from χ_t^2-test

Figure 9.55 – Case-2: PGL from rough model of 25 beam elements -using five sensors, threshold (0-8 cm), defect size (4-20 cm), Laplace variable $s = -1 + 4000\mathrm{i}$, 5% output noise.

In Figures 9.55(a) and 9.55(b), the PGLs are shown for the respective estimated stress and statistical evaluation of χ_t^2-test. Note that the choice of s-value, defect size, datasets and threshold are similar to the previous example. For each defect size, the success rates of the PGL are evaluated in Monte-Carlo experiments of 100 simulated datasets.

From the results, it is possible to determine zones where the PGL is larger for simulated measurements data. The results indicate that the PGLs are slightly increased to around 90 % in the statistical tests with compared to fine model when the defect sizes are considered more than 12 cm. Similar to the previous example, the worse detections are located for the defect sizes of 4 to 10 cm. Notice that when considering the uncertainties in the statistical tests, the PGL gives better performance in Figure 9.55(b) than compare to 9.55(a) due to modal truncation and the variance errors.

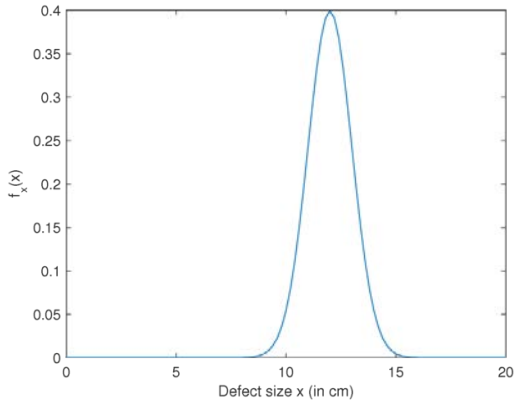

(a) Damage distribution for a defect size (x) with $\mu = 12$ and $\sigma = 1$

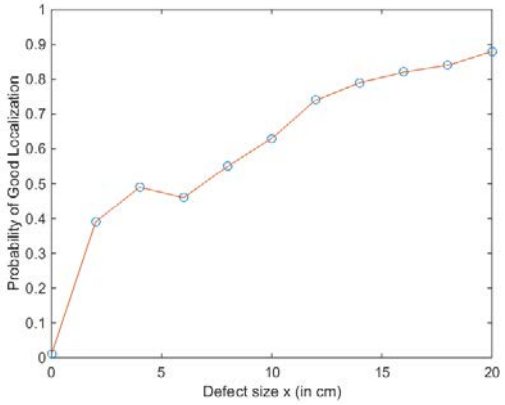

(b) PGL from simulated datasets with threshold (th) 4 cm, defect sizes (0-20 cm), Laplace variable $s = -1 + 4000\text{i}$, 5% output noise.

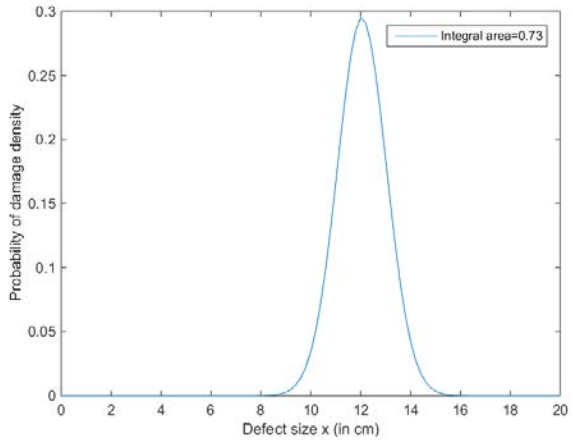

(c) Probability of damage density for a given defect size

Figure 9.56 – General estimate of a given range of a predicted defect size ($i.e. \mu = 12$ and $\sigma = 1$) with threshold (th) 4 cm, defect size (0-20 cm), Laplace variable $s = -1 + 4000\text{i}$, 5% output noise.

It can be concluded that in the statistical tests (see Figures 9.54(b) and 9.55(b)) there is an improvement of the PGL for small defect sizes with respect to increasing threshold, while

there is no significant improvement for larger defect sizes (14-20 cm), though the performance of the PGL is greater than 80% in both cases. The localization is lower due to the large modal truncation errors.

9.6.1 General estimate for a given range of predicted defect size:

In this study, the density of the damage distribution for a predicted defect size is estimated. From (8.2), the general estimate for a given range of predicted defect size is derived for a given structure. It is obtained based on the probability of damage distribution of a predicted defect size with mean (μ), standard deviation (σ), and the PGL (8.1) from simulated datasets with mesh size of 100 beam elements (see Figure 8.8(b)).

Figure 9.56(a) presents the probability of damage distribution for a defect size of 12 cm with mean (μ) and standard devaiation (σ) of 12 and 1 respectively. In Figure 9.56(b), the PGLs are evaluated from simulated datasets of defect size from 0 to 20 cm with a threshold of 4 cm from the damaged area. Then the density of the damage distribution for a predicted defect size is shown in Figure 9.56(c).

9.7 Discussion

In this chapter, first, the proposed damage localization algorithm using Multiple mode sets has been tested on a simple mass-spring chain and a more complex 3D cube model. Using multiple mode sets approach, the robustness of damage localization has been obtained by a joint statistical evaluation taking into account the information from all modes of the structure. The stress computation using multiple mode sets increases the information content of the damaged or non-damaged elements of the structure. In the applications, several experiments have been carried out to evaluate the success of the damage localization in dependence of the s-value, where all stress values corresponding to an element are being tested for damage in a hypothesis test. From results, it is seen that the proposed method has increased the success rate of the correct damage localization significantly almost everywhere in the complex s-plane compared to using a single mode set.

Second, the SDDLV method has been applied on a 2D beam model for crack propagation. From results, it is seen that the performance of the method is not satisfied at all due to the effect of modal truncation error and the resulting variance errors. Notice that the success rates of the damage localization in the statistical test are good to compare to estimated stress. Furthermore, the success rates of the crack localization have increased, while the depth of the crack level increases. For a small level of crack depth, the performance of the method is poor. Possibly it happens due to the small transfer matrix differences between the healthy and damaged states due to small crack. Third, the SDDLV approach has been applied on a 2D beam model depending on the influence of mesh size. For a large damaged zone, the method has been applied on a rough and fine model. From results, it is seen that the performance of the method in the statistical tests is satisfactory for rough mesh in comparison to fine mesh model due to large damaged area and less modal truncation error in the rough model. On the other hand, the success rates of the damage localization are not satisfactory at all for a small damage zone of fine mesh model due to the effect of large modal truncation and the

small damaged residuals in the transfer matrix differences between the healthy and damaged states. Further investigation has been carried-out, where the load vectors are computed from the datasets of fine model for a small damaged zone and then, applied to the L_{model} of rough model. In this case, from the simualtion results, it is seen that the performance of the damage localization method is slightly improved to compare to fine mesh model.

Finally, the performance of the method has been evaluated based on the probability of good localization (PGL) from the damaged zone, since the performances of the correct damage localization are not satisfied with both fine and rough model of a 2D beam for a small damage zone. The PGL depends on Laplace variable, the defect size and the threshold in terms of distance from the damaged area. The results indicate that it is possible to determine zones where the PGL is larger for several sets of simulated measurement data. It is observed that the PGL gives good performance in the statistical tests with compared to estimated for a large defect size and increases when the threshold level is increased.

Chapter 10

Statistical damage localization with the ILDL approach

10.1 Introduction

In this Chapter, the contribution of the statistical damage localization of the ILDL approach (see chapter 6) is validated on a numerical application. Recall that the ILDL approach is an output-only damage localization method based on an FE model of the reference structure and modal parameters estimated from output-only measurements in the damaged and healthy states. A vector is obtained in the image of the changes in the transfer matrix between healthy and damaged states. Then, the damage is located at elements where the subspace angle between the image and the influence line computed from the FE model is zero. This localization approach is complementary to the SDDLV approach [MDBM13].

In previous works [MDBM13], the deterministic aggregation of the damage indicator in ILDL was done for $s = 0$, where the uncertainty quantification was tempted. In Section 6, we reconsider the damage indicator of the ILDL to allow an approximate uncertainty quantification, before deriving its statistical evaluation of damage localization.

This chapter is formulated as follows. In Section 10.2, the distribution of the image vectors and damage localization indicators are validated before going to apply statistical damage localization approach. In Section 10.3, the new approach is applied to a numerical application of a mass-spring chain system, and finally, the conclusion of the work is presented in Section 10.4.

10.2 Distribution of images and damage indicators for ILDL

In ILDL, the estimated image vectors are random values due to random input noise from each simulated datasets. Therefore, it is important to analysis the distribution of the random

variables in Monte-Carlo experiments. For Monte Carlo simulations, the estimated U_1 vectors are random variables due to random input noise and hence difficulties are arises in the element of influence line's due to both positive and negative direction of U_1 vectors. To analyze of the influence line (IL), it is important to ensure that one chosen non-zero element of the singular vector is always positive in different simulations. That's why the negative sign at the non-zero element of the singular vectors U_1 are multiplied with -1 factor to make it same direction. First, the distribution of singular vectors U_1 are observed where the probability density of the image vectors are closest to the theoretical value. Then, the mean values of the U_1 vectors are considered for influence lines. Second, the distribution of the subspace angles is analyzed in Monte-Carlo experiments. Finally, a progressive Monte Carlo simulations have taken into consideration to see the performance of the experiment for the convergence of the estimated to theoretical modal parameters.

In Monte-Carlo experiments, the following things are considered to analyze the probability distribution of image vectors and the damage localization indicators (i.e. subspace angles),

- The distribution of the estimated image vectors are observed for each of the element of the model, and a comparison is made between the probability density of the estimated image vectors and the theoretical image vector that computed from model. Then an analysis has been performed to see the difference between the mean of the estimated image and theoretical image vectors.

- Validation of subspace angles and covariance computation: the probability distribution of the generalized damage localization indicators (i.e. subspace angles) are computed for all healthy and damaged elements from Monte Carlo simulations in comparison to theoretical damage indicators.

- Finally, subsequent Monte Carlo experiments have been performed to analyze the convergence of the estimated ones to theoretic ones. In such way, the mean of the estimated image and damage localization residuals have been considered in a progressive Monte-Carlo Simulations. Therefore, we observed that after some experiments the estimated value has converged to the theoretical value.

For an example, a mass-spring chain of six DOF as shown in Figure 10.1. The stiffness parameters are $k_1 = k_3 = k_5 = 4000$, $k_2 = k_4 = k_6 = 2000$, and the mass of all elements is 1 in suitable units. Damping is defined such that each mode has a damping ratio of 2%. Damage is simulated by decreasing the stiffness of spring 3 by 10% of its original value. For damaged and undamaged states, the acceleration data length for each set is $N = 50{,}000$. Data were generated from collocated white noise excitation using six sensors at each element with a sampling frequency of 50 Hz, and white measurement noise with 5% magnitude of the outputs was added. All six modes of the structure can be identified from the simulated measurements when using SSI. In the simulation results, a comparison between theoretical and estimated modal parameters has explained for 1000 experiments.

Figure 10.1 – Mass-spring chain (with modal damping) -using six sensors.

10.2.1 Distribution of images and damage residuals

For the computation of generalized damage residuals γ_j, the vectors (U_1) has been applied to all theoretical Influence lines (IL) which are obtained from FE model. In ILDL, the left singular vector U_1 is the image of $\delta R(s)$. Since the number of damaged element is one in Figure 10.1, the rank of $\delta R(s)^T$ is 1 and the image U_1 is a single column vector due to one damaged element in the mass-spring system. For Monte Carlo simulation, the singular vector U_1 is estimated for each experiment and the direction of these vectors are not unique. For the analysis of influence lines and to make uniqueness, the negative value of the non-zero element of the singular vectors U_1 are multiplied with -1 factor to make it same direction.

In Figure 10.2, a comparison is shown between the probability distribution of the estimated image vectors and theoretical image vectors that obtained from the model. It is seen that most densities of the estimated image vectors are approximately equal to the theoretic value.

In Figure 10.3, the mean of the estimated image vectors from Monte-Carlo experiments and its standard deviation are shown and then, compared to the theoretical value.

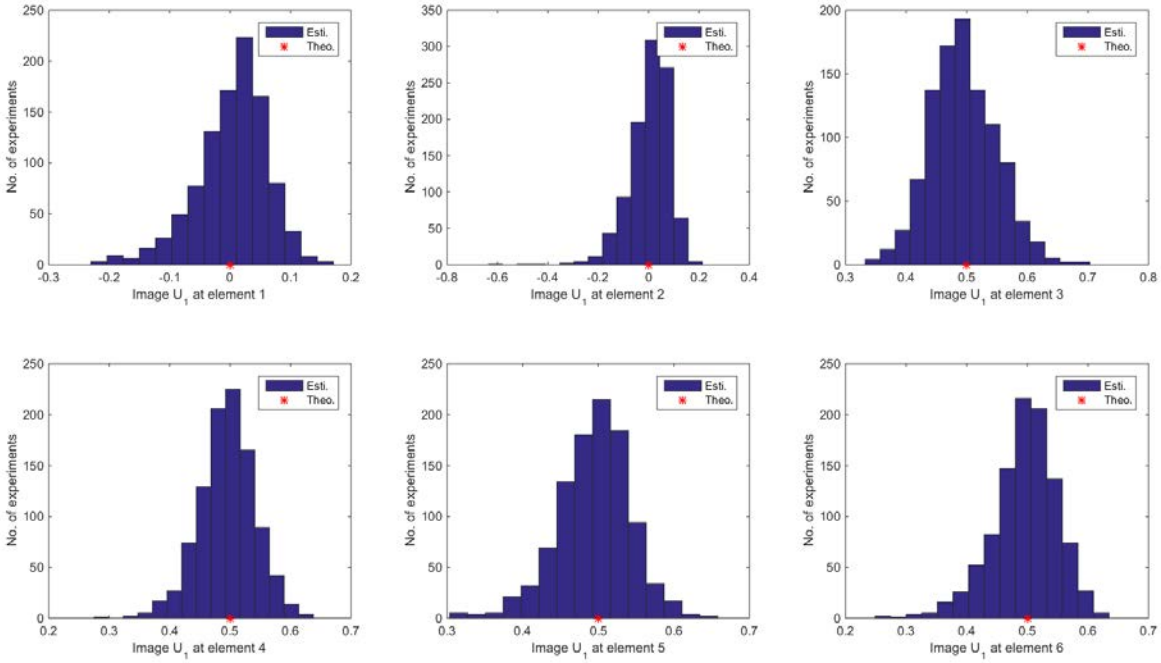

Figure 10.2 – Image of U_1 at each of the element between estimated and theoretical values.

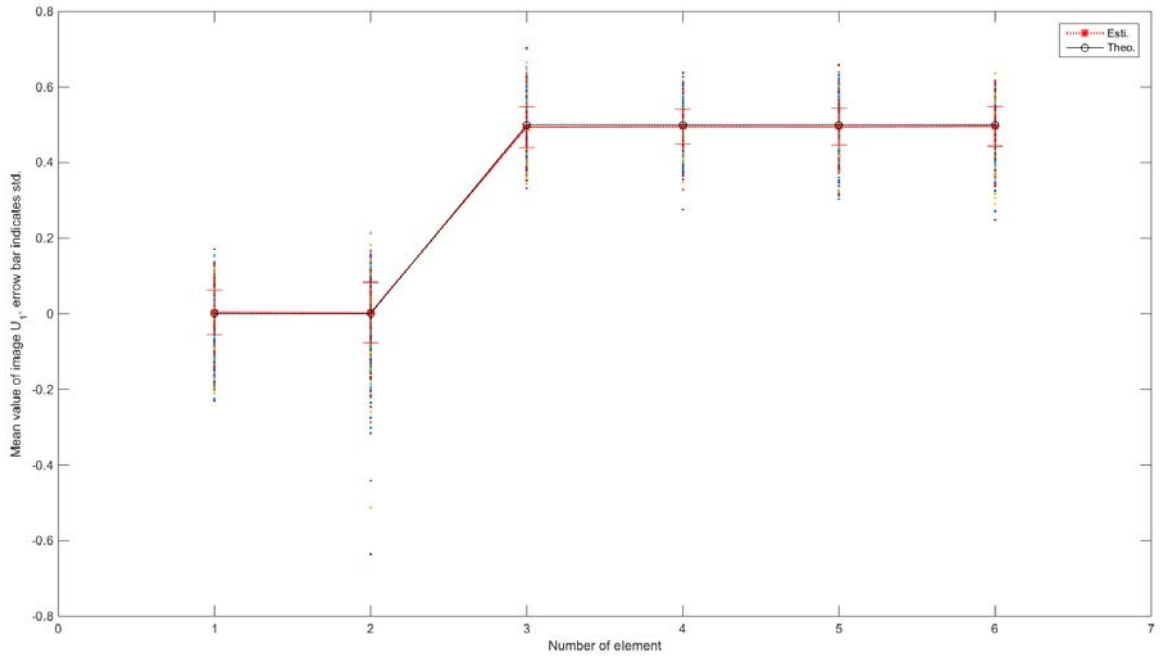

Figure 10.3 – Mean values of U_1 for estimated and theoretical values [$'redline'$ -estimated value and $'blackline'$ -theoretical value].

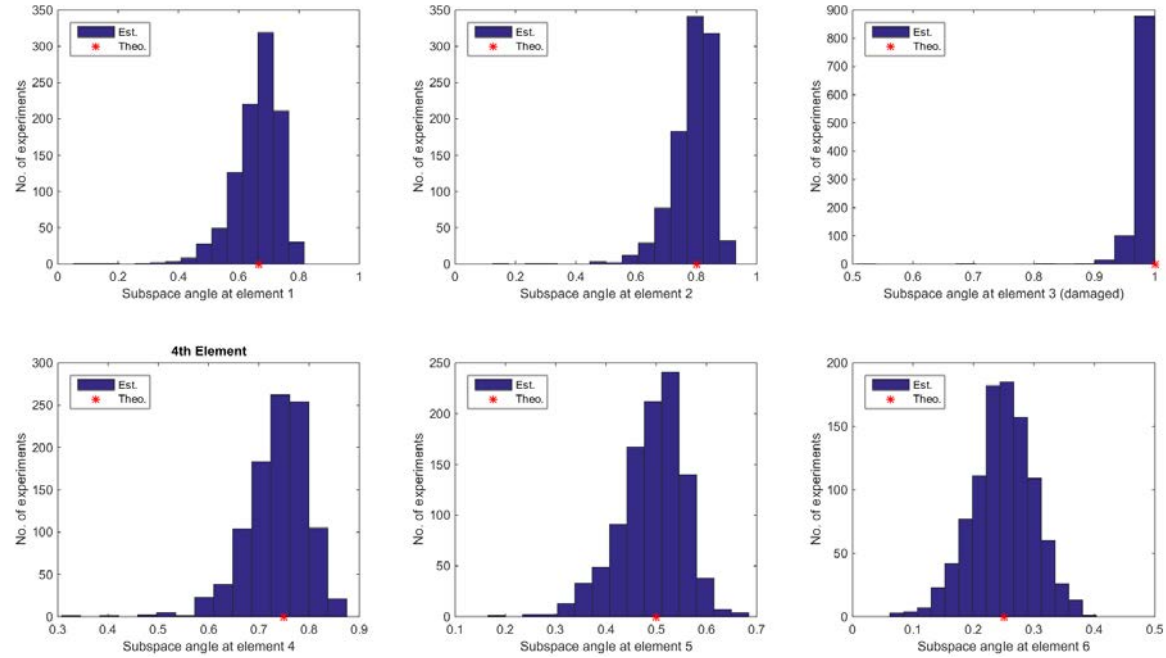

Figure 10.4 – Damage indicator at each of the element between estimated and theoretical values [$'bar'$ indicates the distribution of estimated value and $'*'$ for theoretical value].

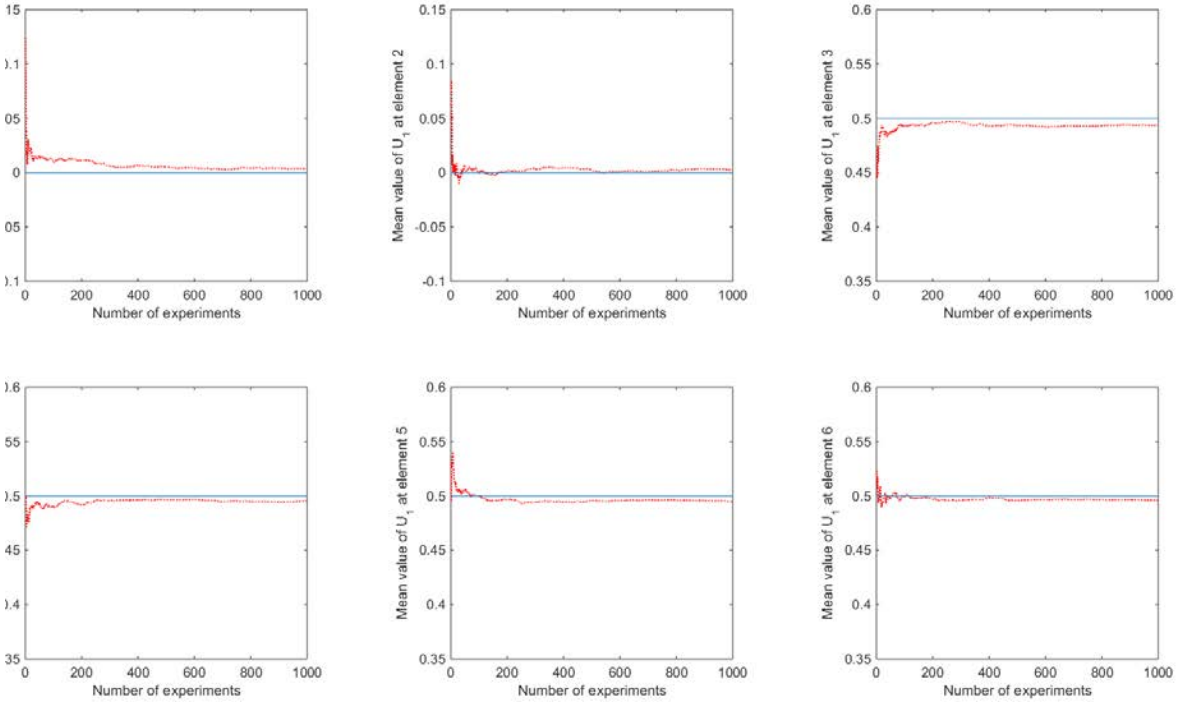

Figure 10.5 – Progressive Monte Carlo simulations for mean of the estimated U_1 vectors at each of the elements 1, .., 6 from top-left to bottom-right [$'redline'$ -mean quantity of the estimated value and $'blueline'$ -theoretical value].

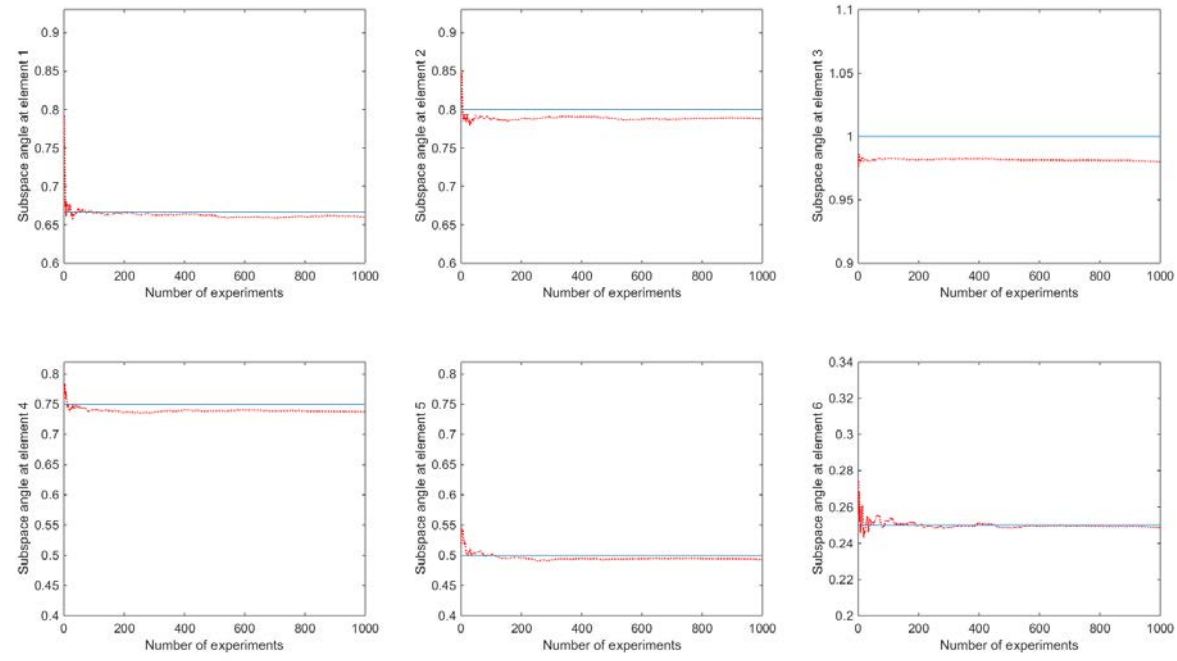

Figure 10.6 – Progressive Monte Carlo simulations for mean of the generalized subspace angles at each of the elements 1, .., 6 from top-left to bottom-right [$'redline'$ -mean quantity of the estimated value and $'blueline'$ -theoretical value].

In Figure 10.4, the distribution of the damage indicators at each of the elements from Monte-Carlo experiments and the theoretical stress values are illustrated. Note that the damage indicators close to 1 correspond to potentially damaged elements. Here, most of the distribution of damage indicators in the healthy elements are closest to theoretical value while the distribution in the damaged element are confined to border 1, means that clearly non-Gaussian distribution.

Finally, progressive Monte-Carlo experiments have been performed to analyze the convergence of the estimated value to theoretical value. The mean of the estimated image vectors and the corresponding damage indicators has considered for continuous Monte experiments where the mean is taken from the results of the experiments $i = 1, .., 1000$. The mean of the quantity of the estimated image vectors and subspace angles are shown in Figure 10.5 and Figure 10.6, respectively. We observed that after some experiments the estimated value has converged to the theoretical value.

10.3 Numerical application: Mass-spring chain system

In a numerical application, the statistical damage localization method of ILDL has been applied on a mass-spring chain system with six DOFs as shown in Figure 10.1. The stiffness parameters are $k_1 = k_3 = k_5 = 4000$, $k_2 = k_4 = k_6 = 2000$, and the mass of all elements is 1 in suitable units. Damping is defined such that each mode has a damping ratio of 2%. Damage is simulated by decreasing the stiffness of spring 4 by 10% of its original value. For damaged and undamaged states, the acceleration data length for each set is $N = 50{,}000$. Data were generated from collocated white noise excitation using three sensors at elements 2, 4, 6 with a sampling frequency of 50 Hz, and white measurement noise with 5% magnitude of the outputs was added.

All six modes of the structure (see Table 10.1) can be identified by SSI from the simulated measurements using threee sensors. Hence, the identified modes split into two mode sets such as $\mathcal{M}_1$ and $\mathcal{M}_2$ of three modes each.

Table 10.1 – Eigenvalues λ_c of mass-spring chain.

Mode	Healthy state	Damaged state	Mode set
1	$-0.255 + 12.76\text{i}$	$-0.253 + 12.63\text{i}$	$\mathcal{M}_1$
2	$-0.747 + 37.36\text{i}$	$-0.736 + 36.78\text{i}$	
3	$-1.16 + 58.26\text{i}$	$-1.15 + 57.53\text{i}$	
4	$-1.55 + 77.74\text{i}$	$-1.54 + 77.44\text{i}$	$\mathcal{M}_2$
5	$-1.96 + 98.15\text{i}$	$-1.96 + 98.13\text{i}$	
6	$-2.13 + 106.6\text{i}$	$-2.11 + 105.5\text{i}$	

The performance evaluation criteria of the damage localization method have already detailed in Section 8.2.1. In order to evaluate the influence of the s-values on the success rate of damage localization, each dataset in the Monte-Carlo simulations is evaluated for a set of

s-values with different real and imaginary parts in order to obtain the success rate in dependence of s. The range of s-values has been chosen in the vicinity of the identified poles to reduce the effects of modal truncation in the transfer matrix estimates [Ber10]. The resulting success rate as a function of s is presented in 3D bar diagrams, where it is plotted on the z-axis in dependence of the real and imaginary parts of s on the x and y-axis.

10.3.1 Complex case for rank 1

For complex case rank 1, two versions are tested based on the theory development in Section 6.4.2.2 and 6.4.2.3. In the following, first, the degenerate distribution is directly taken into account in evaluating (6.47), and second, the degenerate distribution of these vectors is circumvented based on (6.52) by comparing their elements separately.

In the following, the localization results at all structural elements are presented for single mode set $\mathcal{M}_1$ at one s-value for both version 1 and 2, before evaluating the success rate of correct damage localization for single mode sets at different s-values. Monte-Carlo simulations are carried out using 500 simulated datasets in healthy and damaged states to determine the success rate, where in each dataset the modes and their uncertainties are identified using SSI. The entire s-value range in the vicinity of the modes is $\mathrm{Re}(s) \in [-3, -1]$ and $\mathrm{Im}(s) \in [1, 130]$.

Localization of results in all elements at one s-value for version 1 (R1v-S-ILDL) and 2 (R1e-S-ILDL)

In this section, to illustrate the stress computation and its statistical evaluation for damage localization results for each element of the mass-spring chain are shown in Figure 10.7 for version 1 and Figure 10.8 for version 2 using single mode set $\mathcal{M}_1$ at one s-value. The s-value was chosen in the vicinity of mode set $\mathcal{M}_1$ as $s = -1 + 41\mathrm{i}$. Recall that the damage localization is inferred by the stress value closest to zero.

In Figure 10.7(a) for version 1 (see Section 6.4.2.2), the theoretical stress values are computed from the exact modal parameters corresponding to $\mathcal{M}_1$ in the healthy and damaged states. The effect of modal truncation leads to stress that is not exactly zero in damaged element 4, but that is close to zero and the smallest compared to the stress at the other elements. When computing the stress from modal parameter estimated from simulated datasets in Figure 10.7(b), the damage localization is indicated at element 4 but not similar to theoretic results, which is probably due to variance errors in the estimation from noisy data. Considering the variance of the modal parameters in the method, the damage localization is correctly found since the smallest χ_j^2 value is at element 4 in Figure 10.7(c). Note that χ_j^2 in Figure 10.7(c) shows almost similar results as the theoretical result in Figure 10.7(a).

Similarly, in Figure 10.8, all stress values are computed for version 2 (Section 6.4.2.3) from the single mode sets $\mathcal{M}_1$ in the healthy and damaged states. In this case, the theoretical, estimated and the statistical tests can identify the damage localization in Figure 10.8(a), 10.8(b) and 10.8(c), respectivley.

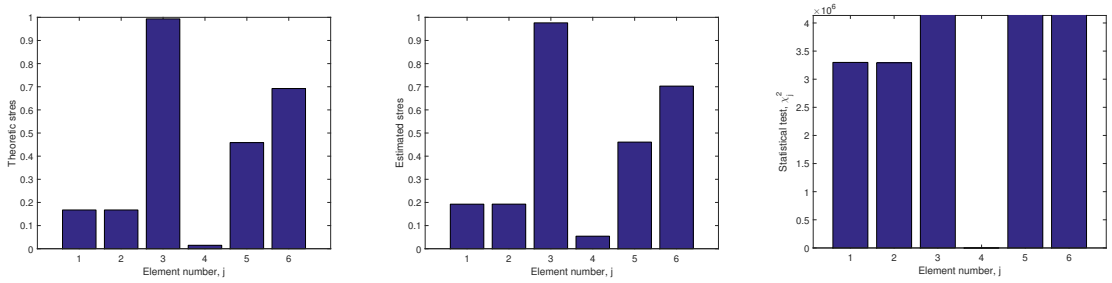

(a) R1v-ILDL for theoretic stress (b) R1v-ILDL for estimated stress (c) R1v-S-ILDL (statistical test)

Figure 10.7 – Version 1: R1v-ILDL (residual vectors with degenerate normal distribution) - Localization results at all elements of mass-spring chain using single mode set $\mathcal{M}_1$ using stress computation and statistical evaluation at $s = -1 + 41\mathrm{i}$. Damage is at element 4.

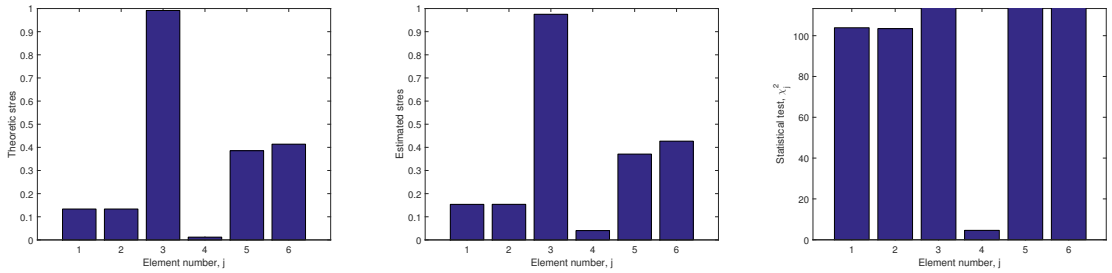

(a) R1e-ILDL for theoretic stress (b) R1e-ILDL for estimated stress (c) R1e-S-ILDL (statistical test)

Figure 10.8 – Version 2: R1e-ILDL (element-wise tests of residual vector) - Localization results at all elements of mass-spring chain using single mode set $\mathcal{M}_1$ using stress computation and statistical evaluation at $s = -1 + 41\mathrm{i}$. Damage is at element 4.

10.3.1.1 Version 1: R1v-S-ILDL (residual vectors with degenerate normal distribution for S-ILDL)

In the last section, the damage localization results was illustrated only for one dataset and one s-value, now we are going to evaluate the performance of the damage localization for theoretical, estimated and statistical test based either on single mode set $\mathcal{M}_1$ or $\mathcal{M}_2$ in dependence of the chosen s-value.

Success rate of the damage localization using single mode set

For the performance evaluation of correct damage localization at element 4, using either mode set $\mathcal{M}_1$ or $\mathcal{M}_2$, 500 datasets of vibration data of accelerometers were generated for the Monte Carlo evaluation. Then, the modes of these datasets and their uncertainties were identified using SSI, both in reference and damaged states. Finally, the success rate was determined based on the computation of the stress estimated in (6.47) and χ_t^2 test values in (6.50), using either the modes from $\mathcal{M}_1$ or $\mathcal{M}_2$, for different s-values. The s-values were

chosen in the vicinity of the modes (see Table 8.1) on a global grid with $\mathrm{Re}(s) \in [-3, 1]$ and $\mathrm{Im}(s) \in [1, 130]$.

In Figures 10.9, 10.11, 10.13 and Figures 10.10, 10.12, 10.14, the success rates of the damage localization (z-axis) are shown in dependence of the real and imaginary part of the chosen s-values (x and y-axis) for mode sets $\mathcal{M}_1$ and $\mathcal{M}_2$, respectively. Indeed it can be seen that damage localization for both mode sets is satisfactory only for s-values in the vicinity of the modes of the respective mode sets.

For mode set $\mathcal{M}_1$, corresponding to the first three modes, it can be seen in Figure 10.9 that success of damage localization from the exact modal parameters is obtained only in the interval $[1, 64]$ on the imaginary line. Same happens for the estimated stress from the simulated datasets as shown in Figure 10.11 where the success rate of the damage localization is around 100% only in the interval $[26, 64]$ on the imaginary line, and the remaining part of the s-plane the success rates are not satisfied due to modal truncation and estimation errors. Figure 10.13 shows that the success rate is satisfactory only in the interval of the Laplace variables with $\mathrm{Im}(s) \in [24, 48]$, where it reaches up to 100% and not similar to estimated in Figure 10.17. Beyond this interval, it is almost close to zero and the damage localization cannot be indicated due to the modal truncation error, which is significant outside the interval containing the identified modes (see Table 8.1). Note that the considered modes in this example are in the interval $[1, 62]$ on the imaginary line (see Table1).

Similarly, for mode set $\mathcal{M}_2$ corresponding to the last three modes of the structure, it can be seen in Figure 10.10 that success of damage localization from the exact modal parameters is obtained only in the interval $[102, 120]$ on the imaginary line. As similar to the estimated stress from the simulated datasets as shown in Figure 10.12, the success rate of damage localization is satisfying with up to 90% in Figure 10.14, when $\mathrm{Im}(s)$ belongs to the interval $[104, 128]$. This area corresponds only to the last two identified modes in $\mathcal{M}_2$. While the lower performance at s-values around first mode of $\mathcal{M}_1$, the success rate at s-values near the fourth mode of the structure is also very low due to significant modal truncation errors. Hence, choosing the s-value in the vicinity of the identified poles does not necessarily give satisfactory results.

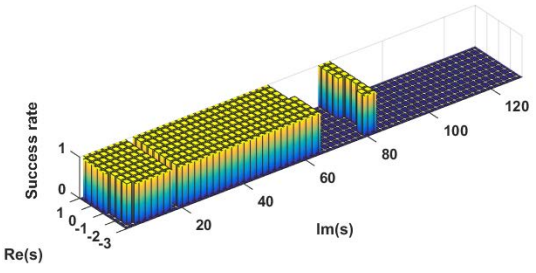

Figure 10.9 – Version 1: Success of the R1v-ILDL from theoretical modal parameters using single mode set $\mathcal{M}_1$ in dependence of s.

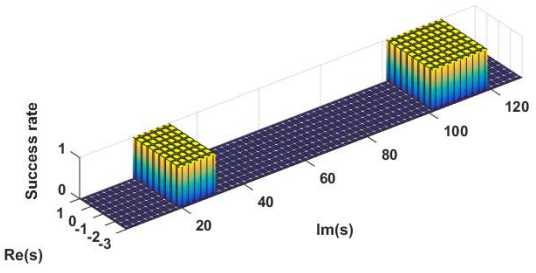

Figure 10.10 – Version 1: Success of the R1v-ILDL from theoretical modal parameters using single mode set $\mathcal{M}_2$ in dependence of s.

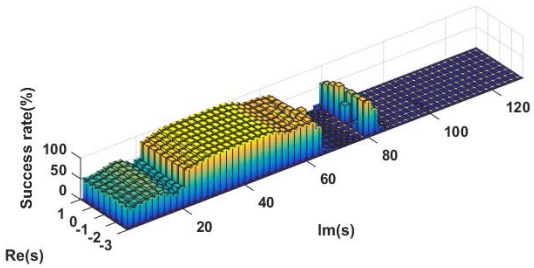

Figure 10.11 – Version 1: Success rates of the R1v-ILDL from estimated modal parameters using single mode set $\mathcal{M}_1$ in dependence of s.

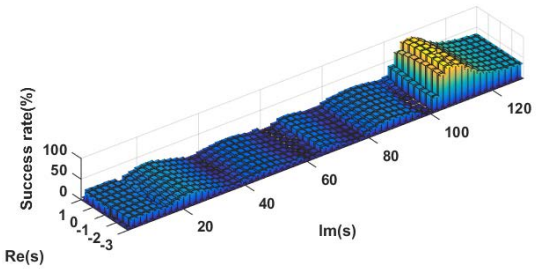

Figure 10.12 – Version 1: Success rates of the R1v-ILDL from estimated modal parameters using single mode set $\mathcal{M}_2$ in dependence of s.

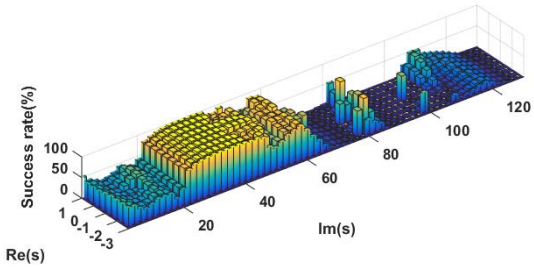

Figure 10.13 – Version 1: Success rates of the R1v-S-ILDL using single mode set $\mathcal{M}_1$ in dependence of s

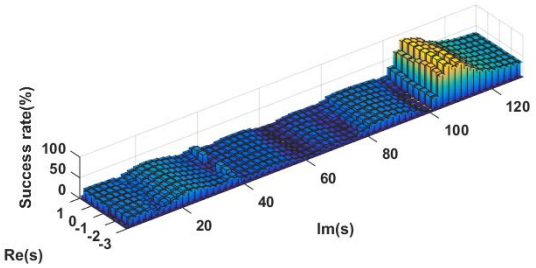

Figure 10.14 – Version 1: Success rates of the R1v-S-ILDL using single mode set $\mathcal{M}_2$ in dependence of s

10.3.1.2 Version 2: R1e-S-ILDL (element-wise tests of residual vector for S-ILDL)

In the last section, the damage localization results was illustrated for theoretical, estimated and statistical test where the degenerate distribution is directly taken into account in evaluating (6.47) in dependence of the chosen s-value. In the following, the success rates of damage localization results was obtained by element-wise tests of residual vector (6.52) using single modeset.

Success rate of the damage localization using single modeset

As similar to previous section (i.e. Version 1), the success rates of the damage localization (z-axis) are shown in Figures 10.15, 10.17, 10.19 and Figures 10.16, 10.18, 10.20 for the theoretic, estimates and statistical tests in dependence of the real and imaginary part of the chosen s-values (x and y-axis) for mode sets $\mathcal{M}_1$ and $\mathcal{M}_2$, respectively.

For mode set $\mathcal{M}_1$, it can be seen that the results are almost similar compared to Version 1 for the theoretical, estimates and statistical test in Figures 10.15, 10.17, and 10.19, respectively. Note that the results are slighlty improved in the statistical evaluation in Figure 10.19 with compared to Figure 10.13.

Similarly, for mode set $\mathcal{M}_2$, it can be seen in Figures 10.16, 10.18, and 10.20 that success of damage localization from the exact modal parameters, the simulated datasets and the statistical tests are also nearly similar with compared to Version 1 for mode sets $\mathcal{M}_2$.

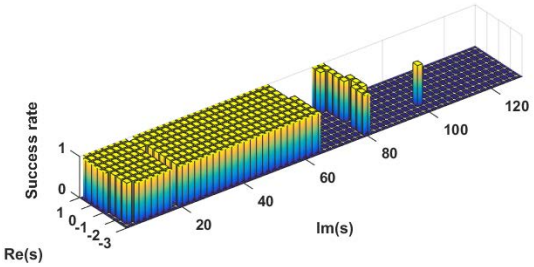

Figure 10.15 – Version 2: Success of the R1e-ILDL from theoretical modal parameters using single mode set $\mathcal{M}_1$ in dependence of s.

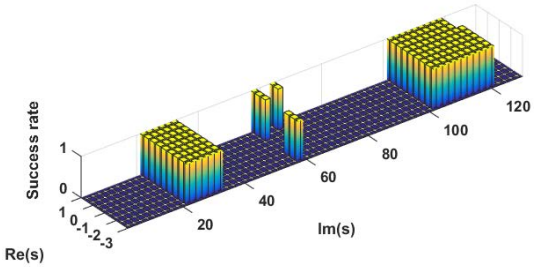

Figure 10.16 – Version 2: Success of the R1e-ILDL from theoretical modal parameters using single mode set $\mathcal{M}_2$ in dependence of s.

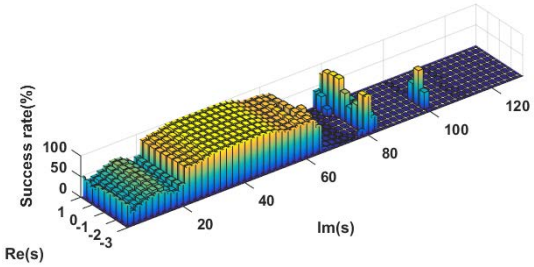

Figure 10.17 – Version 2: Success rates of the R1e-ILDL from estimated modal parameters using single mode set $\mathcal{M}_1$ in dependence of s.

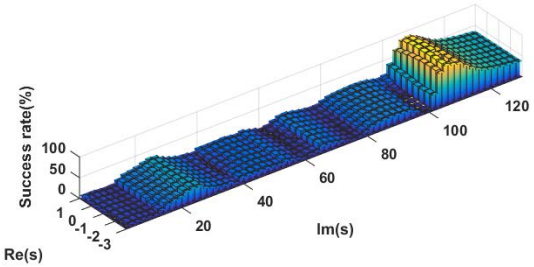

Figure 10.18 – Version 2: Success rates of the R1e-ILDL from estimated modal parameters using single mode set $\mathcal{M}_2$ in dependence of s.

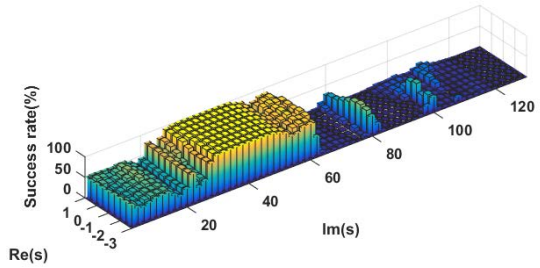

Figure 10.19 – Version 2: Success rates of the R1e-S-ILDL using single mode set $\mathcal{M}_1$ in dependence of s

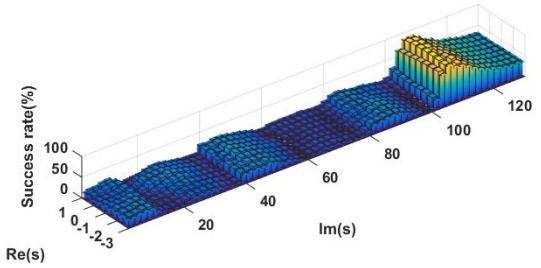

Figure 10.20 – Version 2: Success rates of the R1e-S-ILDL using single mode set $\mathcal{M}_2$ in dependence of s

Summarizing the results, for version 1 and 2, it can be concluded that the success rates of damage localization for both mode sets $\mathcal{M}_1$ and $\mathcal{M}_2$ is satisfactory only for s-values in the vicinity of the modes of the respective mode sets. Beyond this range, it is almost close to zero and the damage localization cannot be indicated due to the modal truncation error, which is significant outside the interval containing the identified modes.

10.3.1.3 Considering all modes for Version 1 (R1v-S-ILDL) and 2 (R1e-S-ILDL)

In this case, the success rates of the damage localization are evaluated considering all modes i.e. without modal truncation error, and vibration datasets 0f 100 were generated using all sensors for the Monte Carlo evaluation. Then, the modes of these datasets and their uncertainties were identified using SSI, both in reference and damaged states. Finally, for version 1 and 2, the success rate was determined based on the computation of the stress estimated in (6.47) and (6.52), and the χ_t^2 test values in (6.50) and (6.54), using all modes, for different s-values. The s-values were chosen in the vicinity of the modes (see Table 8.1) on a global grid with $\mathrm{Re}(s) \in [-3, 1]$ and $\mathrm{Im}(s) \in [1, 130]$.

In this case, consiering all modes, it can be seen that the success of the damage localization (z-axis) are shown satisfactory results in Figures 10.21, 10.23, 10.25 and Figures 10.22, 10.24, 10.26 in dependence of the real and imaginary part of the chosen s-values (x and y-axis) for version 1 and 2, respectively.

For both version 1 and 2, it can be summarized that the success of damage localization from the exact modal parameters is same in Figures 10.21 and 10.26, respectively since there is no modal truncation error. While the estimated stress from the simulated datasets in Figures 10.23 and 10.24, the success rates of the damage localization are satisfied but not perfectly similar to theoretical results, perhaps due to the estimation errors. However, the statistical evaluation in Figures 10.25 and 10.26 shows that the success rate is not satisfactory only in the interval of the Laplace variables with $\mathrm{Im}(s) \in [94, 100]$, which looks similar to estimated in Figures 10.23 and 10.24, respectively.

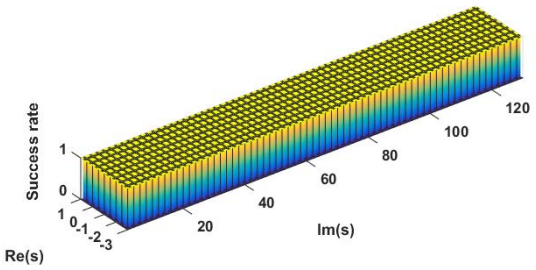

Figure 10.21 – Version 1: Success of the R1v-ILDL from theoretical modal parameters using all modes in dependence of s.

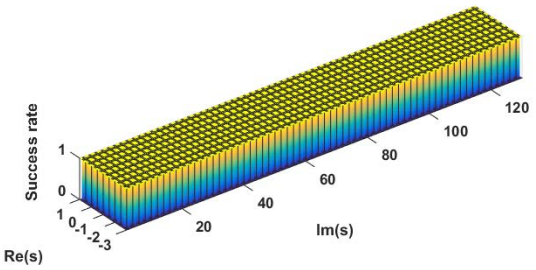

Figure 10.22 – Version 2: Success of the R1e-ILDL from theoretical modal parameters using all modes in dependence of s.

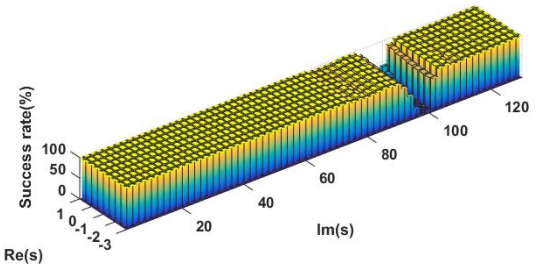

Figure 10.23 – Version 1: Success rates of the R1v-ILDL from estimated modal parameters using all modes in dependence of s.

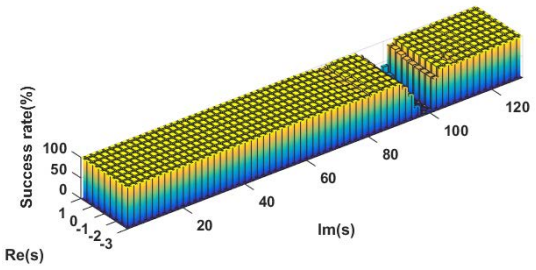

Figure 10.24 – Version 2: Success rates of the R1e-ILDL from estimated modal parameters using all modes in dependence of s.

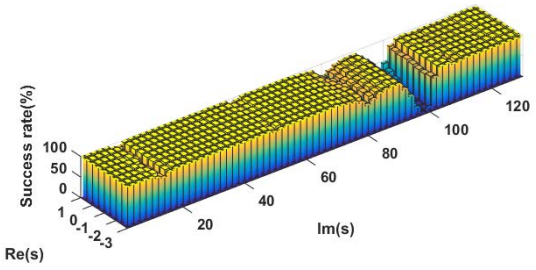

Figure 10.25 – Version 1: Success rates of the R1v-S-ILDL using all modes in dependence of s

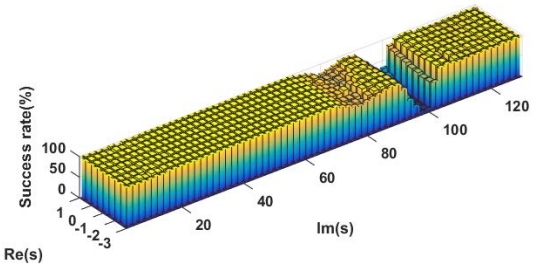

Figure 10.26 – Version 2: Success rates of the R1e-S-ILDL using all modes in dependence of s

10.3.1.4 Comparison to SDDLV

In this section, a comparison is made for the performance evaluation between SDDLV and ILDL methods based on the application of a mass-spring chain system in Section 9.3.1.2 and 10.3.1.1, respectively. Note that for performance evaluation of the methods, Monte-Carlo experiments are carried-out using 500 simulated datasets in both healthy and damaged states to determine the success rate, where in each dataset the modes and their uncertainties are identified using SSI. Recall that success rate of the damage localization is defined as the number of occurrences of the smallest stress values in the damage element, while all s-values are evaluated for each of the 500 datasets. Then both methods can be summarized as follows,

- For modal truncation, using single mode set $\mathcal{M}_1$, corresponding to the first 3 modes, it is seen that the success rates of the damage localization in the statistical test reaches up to 90% and much higher than estimated for the SDDLV approach for a particular choice of s-values (see section 9.3.1.2). While in the ILDL approach the success rates of the damage localization for both statistical and estimated stress are around 100% for version 1 and 2 (see section 10.3.1.1 and 10.3.1.2), respectively.
- For single mode set $\mathcal{M}_2$, corresponding to the last 3 modes, the result shows that the success of the damage localization in the statistical test reaches up to 80% in the vicinity of the last two modes which is slightly higher compared to estimated for both SDDLV and ILDL.
- Compared to single mode sets between $\mathcal{M}_1$ and $\mathcal{M}_2$, it can be concluded that the performance of the methods (i.e. SDDLV and ILDL) is much stronger for $\mathcal{M}_1$ than $\mathcal{M}_2$. While the success rate of the damage localization using a single mode set was not successful everywhere in the s-plane mainly because of modal truncation errors. Even considering the s-value in the vicinity of the identified modes, where modal truncation errors should be low, was not sufficient to achieve a reasonable success rate for all choices of s, especially for $\mathcal{M}_2$ in Figure 9.15 for SDDLV, and in Figure 10.14 and 10.20 for ILDL, respectively.
- While lower performance at s-values around the modes of $\mathcal{M}_1$ can be expected due to significant modal truncation errors, the success rate at s-values near the fourth mode of the structure is also very low. Hence, choosing the s-value in the vicinity of the identified poles does not necessarily give perfect results.
- In overall, the result shows that for modal truncation the statistical evaluation of the ILDL approach gives better performance than SDDLV approach.

10.4 Discussion

In this chapter, the statistical evaluation of the ILDL approach is validated on a numerical application. In previous works, this deterministic aggregation was done for $s = 0$, where the uncertainty quantification was tempted. Here, the damage indicator of the ILDL is considered to allow an uncertainty quantification for its statistical evaluation of damage localization. For

such an evaluation, the modal parameter covariance is propagated to the obtained damage indicators in a sensitivity-based approach. Finally, all computed values corresponding to an element are being tested for damage in a hypothesis test where the computed subspace angles are evaluated with their individual covariance. From the results, it is seen that the success rates of the damage localization in the statistical tests are satisfactory with respect to theoretical or estimated value for rank 1.

Chapter 11

Transfer matrix-based output-only statistical damage localization and quantification

11.1 Introduction

In this chapter, the transfer-matrix based residuals for damage localization and quantification method from Chapter 7 have been applied on numerical simulations. A mass-spring chain and a 2D beam model have been considered as numerical applications. In Section 11.2, the performance evaluation criteria of the new method is defined, and then it has been applied on two different numerical applications to evaluate the performance of the proposed method using Multiple mode sets, where the results are compared with a single mode set experiment. Finally, the conclusion of the work is presented in Section 11.6.

11.2 Performance evaluation for both damage localization and quantification

To analyze the performance of the proposed method (see Chapter 7) using multiple mode sets, the results are compared with a single mode set experiment. Let $\theta = [\theta^1 \cdots \theta^p]$ is the parameters of an FE model of the structure.

For the damage localization, each of the components θ^i, $i = 1 \cdots p$ are tested with the sensitivity and minmax approaches. For the faulty system, the component of $\delta_a = 0$ is tested against $\delta_a \neq 0$ based on the sensitivity and the minmax tests. Then the test variables are compared to a threshold level to make a decision about faulty components when $\delta_a \neq 0$. Estimates of the changes δ are computed with the respective approaches described in

Section (7.5). Successful damage localization means that the highest t_{sens} and t_{mm} value at the damaged element. In the numerical applications, several datasets are generated by Monte-Carlo simulations to evaluate the success rate of the fault isolation. The success rate corresponds to the probability of detection for damage localization and it is defined as the number of occurrences of the highest values of t_{sens} and t_{mm} at damaged elements. For the damage quantification, the results are shown for several damage cases and extents, while each quantified value is estimated by taking a mean of the Monte-Carlo simulations with their standard deviations.

In order to see the influence of all s-values s, a grid map in the complex s-plane has been proposed.The range of s-values has been chosen in the vicinity of the identified poles. For each of the Monte-Carlo datasets, the highest values of t_{sens} and t_{mm} at damaged elements are evaluated for all s-values in order to see the influence of different s-values. Then performance evaluation of the method is illustrated with a 3D-bar diagram where x-y axes indicate real-imaginary parts of s-value and z-axis corresponds to the success rate of the damage localization.

In the following, the transfer matrix based residual for damage localization and quantification have been applied on two numerical applications, first a mass-spring chain and second, a 2D beam model with 5 elements. The damaged element in the model is simulated by decreasing stiffness of its original value. In both approaches, the acceleration data length was generated from collocated white noise excitation for damaged and undamaged states and white measurement noise with 5% magnitude of the standard deviation of each output was added.

For testing, all parameters such as sensitivity $\mathcal{J}$, residual ζ and covariance Σ are estimated from the reference datasets and the information from reference model of the structure. For damage localization, if the test value of t_{sens} and t_{mm} for a parameter θ exceeds a threshold, the respective structural element is damaged. Note that maximum values at the damaged element indicate potentially faulty components. For the quantification of the damage extent, estimated value of the changes parameter δ are derived from $\hat{\delta}_a^{sens}$ (7.25) and $\hat{\delta}_a^{mm}$ (7.26), respectively.

11.3 Numerical application 1: Mass-spring chain

In the first numerical application, a damped mass-spring chain system is considered for the damage localization and quantification as shown in Figure 8.3 (see Section 8.3.1). In this example, all 6 modes (see Table 8.1) can be identified from the model of the structure using SSI. For the proposed method using multiple mode sets in Chapter 7, the identified modes are split into two mode sets namely $\mathcal{M}_1$ and $\mathcal{M}_2$ of 3 modes each.

In the following, the localization results at all structural elements are presented for different mode set at one s-value, before evaluating the success rate of the correct damage localization in Monte-Carlo experiments for single and multiple mode sets at different s-values.

11.3.1 Localization results at all elements for one dataset

For the localization test statistics (i.e. sensitivity and minmax tests) at all elements are computed using one of the Monte-Carlo datasets in both damaged and healthy states, where the damaged element is simulated by decreasing stiffness by 10% of its original value. Recall that the highest value indicates the success of damage localization. For the mode set $\mathcal{M}_1$, the localization results are shown in Figure 11.1 at $s_1 = -1+45\mathrm{i}$ and it is seen that damaged element is located at bar 4, while the sensitivity test reacts more strongly in the healthy elements for $\delta_b = 0$ than minmax tests. In Figure 11.2 for the mode set $\mathcal{M}_2$, both tests are identified the damage element. Considering multiple mode sets, the damage localization is correctly found at element 4 in Figure 11.3. From the results, it is seen that the minmax test behave perfectly while the healthy elements at 1 and 2 in the sensitivity test react for the violation of $\delta_b = 0$. Note that the localization results using multiple mode sets $\mathcal{M}_j$ in Figure 11.3 is more accurate compared to Figure 11.1 and 11.2.

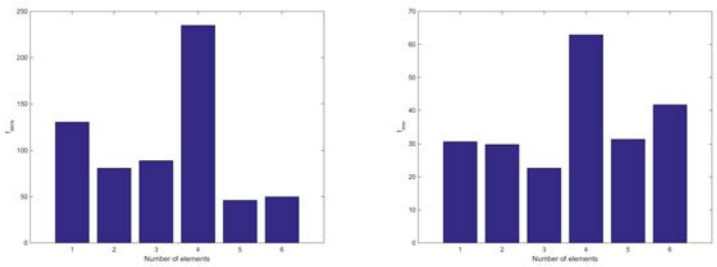

(a) Sensitivity tests (b) Minmax tests

Figure 11.1 – Localization using a single mode set, $\mathcal{M}_1$: Sensitivity tests (left) and minmax tests (right) at $s_1 = -1 + 25\mathrm{i}$ - three sensors, 5% output noise, 10% stiffness reduction at bar 4.

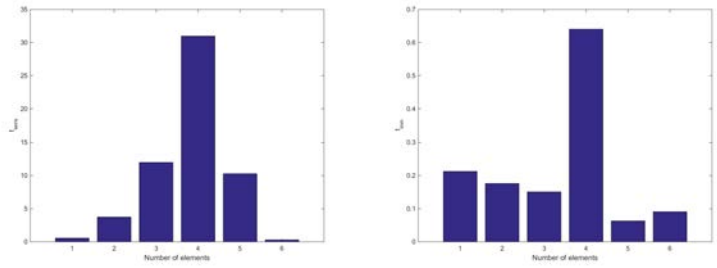

(a) Sensitivity tests (b) Minmax tests

Figure 11.2 – Localization using a single mode set, $\mathcal{M}_2$: Sensitivity tests (left) and minmax tests (right) at $s_2 = -1 + 101\mathrm{i}$ - three sensors, 5% output noise, 10% stiffness reduction at bar 4.

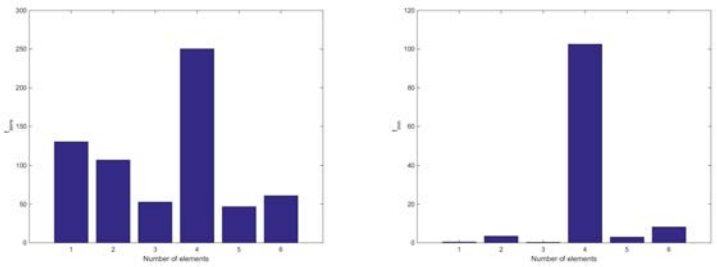

(a) Sensitivity tests (b) Minmax tests

Figure 11.3 – Localization using multiple mode set: Sensitivity tests (left) and minmax tests (right) at $s = [-1 + 25\mathrm{i}; -1 + 101\mathrm{i}]$ *- three sensors, 5% output noise, 10% stiffness reduction at bar 4.*

11.3.2 Success rate of the damage localization using single mode set

In the previous section, based on the sensitivity and minmax tests, the localization results have been demonstrated at all elements of the structure using one datasets. In this section, the damage localization results are only illustrated in dependence of the chosen s-value for both single mode sets $\mathcal{M}_1$ and $\mathcal{M}_2$, comprising the first and last three modes respectively, before going to illustrate the joint evaluation of the multiple mode sets in the next section.

For the mode set $\mathcal{M}_1$ and $\mathcal{M}_2$, the success rate of the damage localization is evaluated at element 4. Note that 100 datasets were generated for the Monte-Carlo simulations and estimate modes of these datasets with their uncertainties were identified using SSI for both in the reference and damaged states. Therefore, the success rate was determined based on the computation of the t_{sens} and t_{mm}-tests in (7.22) and (7.24) at different s-values for the respective modes $\mathcal{M}_1$ or $\mathcal{M}_2$. The s-values was chosen in the vicinity of the modes (see Table 8.1) on a global grid with $\mathrm{Re}(s) \in [-3, 1]$ and $\mathrm{Im}(s) \in [0, 130]$. In Figures 11.4 and 11.5, the success rates of the damage localization are shown in the z-axis in dependence of the chosen s-values where x and y-axis corresponds to real and imaginary part of the s-values in the vicinity of an identified poles.

For the first 3 modes, the results are shown in Figure 11.4 for the sensitivity and minmax tests. It is seen in Figure 11.4(a) that the success rate of the damage localization is better only in the interval of the Laplace variables with $\mathrm{Im}(s) \in [0, 34]$ than $\mathrm{Im}(s) \in [35, 130]$, while the damage localization results from minmax tests in Figure 11.4(b) gives better performance compared to the sensitivity tests in Figure 11.4(a).

For the last 3 modes, it can be seen in Figure 11.5 that the performance of damage localization is almost similar at everywhere in the Laplace variables. Note that the success rates of the damage localization using the mode set $\mathcal{M}_2$ in Figure 11.5(a) is around 65%, which is good enough compare to Figure 11.4(a). So, choosing the s-value in the vicinity of the identified poles is not necessary for both sensitivity and minmax tests.

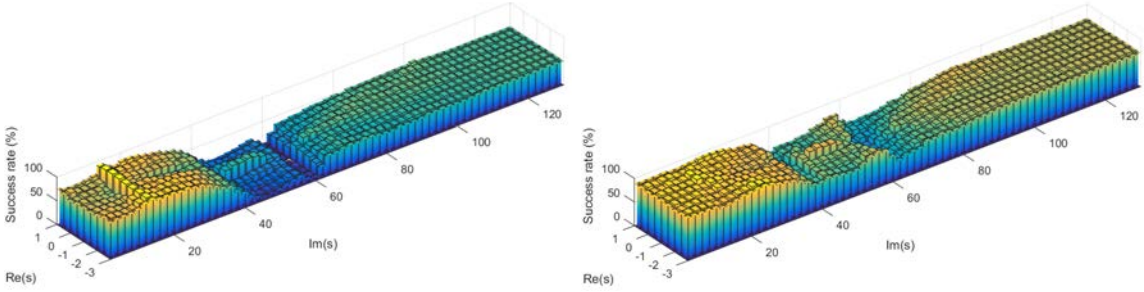

(a) Sensitivity tests (b) Minmax tests

Figure 11.4 – Success rate of statistical damage localization using single mode set $\mathcal{M}_1$, in dependence of s. - three sensors, 5% output noise, 10% stiffness reduction at bar 4.

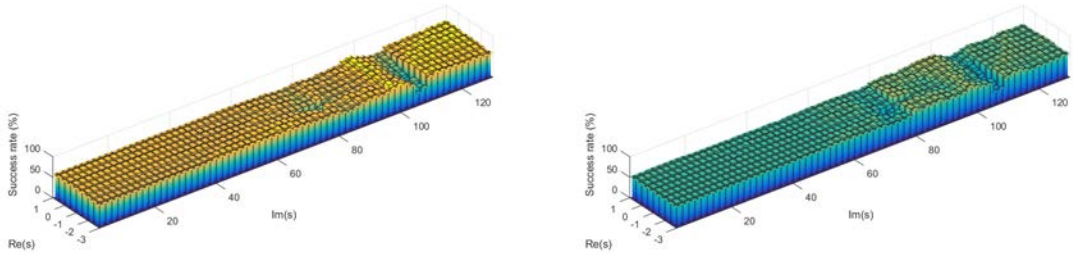

(a) Sensitivity tests (b) Minmax tests

Figure 11.5 – Success rate of statistical damage localization using single mode set $\mathcal{M}_2$, in dependence of s. - three sensors, 5% output noise, 10% stiffness reduction at bar 4.

So, in the next section, we propose the new statistical approach using multiple mode sets to increase the success rate of the damage localization at almost everywhere in the s-plane.

11.3.3 Success rate of the damage localization using multiple mode sets

In the previous section, the results was presented in the s-plane in dependence of s-values and the success rate of the damage localization was not satisfactory in the s-plane because of modal the truncation and estimation errors. In the tests, it has seen that the success rate of the damage localization is not sufficient in Figure 11.4(a) and 11.5(a), and Figure 11.4(b) and 11.5(b) for the respective mode sets $\mathcal{M}_1$ and $\mathcal{M}_2$. This motivates the use of multiple mode sets instead of using a single mode set alone.

Therefore, the localization results are computed by taking into account the information using multiple mode sets instead of using a single mode set. The joint evaluation of the residual is obtained from (7.14) and its joint covariance is derived in (7.16) for the multiple mode sets.

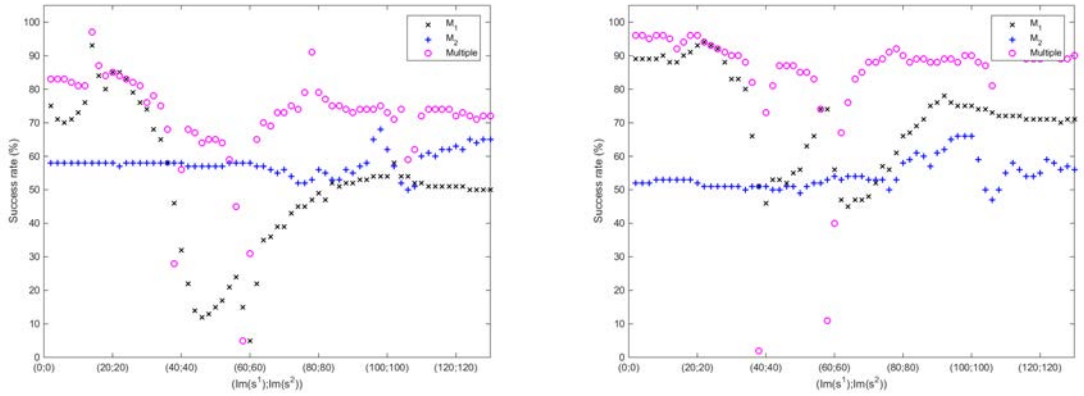

(a) Sensitivity tests (b) Minmax tests

Figure 11.6 – Success rates of statistical damage localization of single mode sets $\mathcal{M}_1$ and $\mathcal{M}_2$ with s in the vicinity of the modes, compared to the success rate using jointly the multiple mode sets. - using three sensors, 5% output noise, 2% damping, 10% stiffness reduction at bar 4.

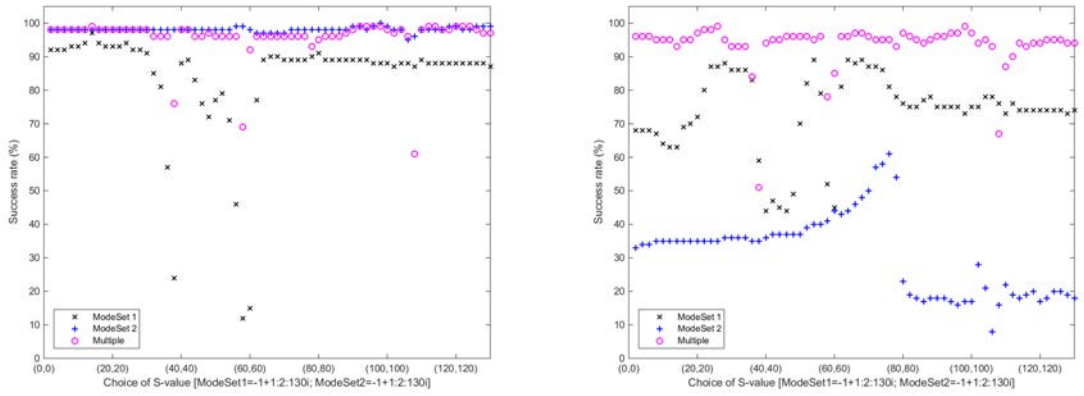

(a) Sensitivity tests (b) Minmax tests

Figure 11.7 – Success rates of statistical damage localization of single mode sets $\mathcal{M}_1$ and $\mathcal{M}_2$ with s in the vicinity of the modes, compared to the success rate using jointly the multiple mode sets. - using three sensors, 5% output noise, 0.2% damping, 10% stiffness reduction at bar 4.

For the joint statistical approach using multiple mode sets, the s-values is chosen in the vicinity of the modes. The s-value s^1 is chosen for the mode set $\mathcal{M}_1$ with $\mathrm{Im}(s^1) \in$

$[0, 130]$, and s^2 with $\mathrm{Im}(s^2) \in [0, 130]$ for mode set $\mathcal{M}_2$, while the real parts are defined as $\mathrm{Re}(s^1), \mathrm{Re}(s^2) \in [-3, 1]$.

A comparison is made in Figure 11.6(a) and 11.6(b) with sensitivity and minmax tests in order to see the improvement of the proposed method, where the success rates of the damage localization using multiple mode sets are obtained from the single mode sets. From the sensitivity tests, it can be seen in Figure 11.6(a) that the statistical combination of the result improves the damage localization performance from the single mode set $\mathcal{M}_1$ and $\mathcal{M}_2$ at almost everywhere in the s-plane. While the statistical combination of the results in Figure 11.6(b) from the minmax test significantly improves the performance compare to $\mathcal{M}_1$ and $\mathcal{M}_2$. Notice that the joint evaluation of the multiple mode sets from minmax tests gives good results compared to sensitivity test.

11.3.4 Damage quantification results at all elements using one dataset

In the previews section, the test values of the sensitivity and minmax test corresponding only to the decision if the respective element is damaged or not by comparing them to a threshold value. They are not linked to the quantification of the damage extent, which is estimated separately in this section.

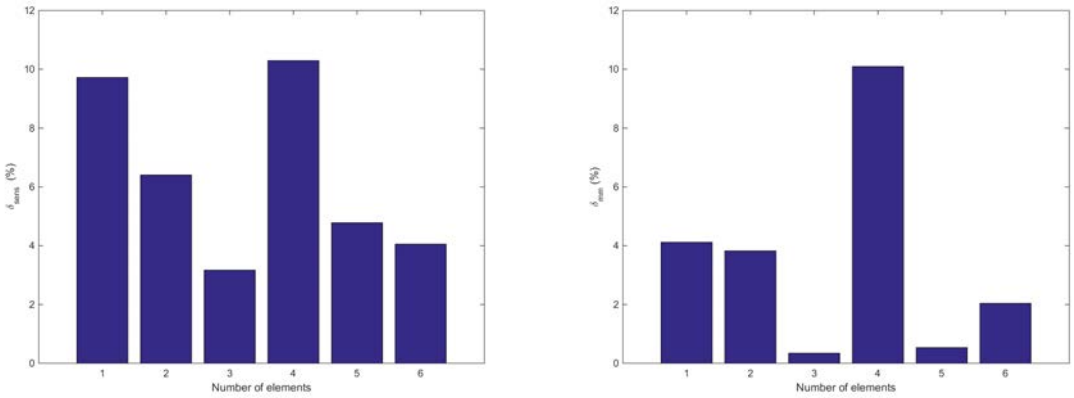

(a) Sensitivity tests (b) Minmax tests

Figure 11.8 – Damage extents using multiple mode set: Sensitivity tests (left) and minmax tests (right) at $s = [-1 + 25\mathrm{i}; -1 + 101\mathrm{i}]$ *- three sensors, 5% output noise, 2% damping ratio, 10% stiffness reduction at bar 4.*

The damage extent at all elements is computed using one of the Monte-Carlo datasets in both damaged and healthy states. Using multiple mode sets $\mathcal{M}_j$, the results of the damage extent are shown in Figure 11.8 for the sensitivity and minmax approaches. For the quantification of the damage extent, the values of $\hat{\delta}_{sens}$ and $\hat{\delta}_{mm}$ were estimated, leading to the parameter change of 10.3% and 10.1% for the respective sensitivity and minmax approaches with the transfer matrix-based method. In the sensitivity test of Figure 11.8(a), the quantified value of the damage extent is well estimated at only damaged element 4 while the healthy element at 1 is overestimated due to the violation of $\delta_b = 0$. For the minmax test

in Figure 11.8(b), the quantified value of the damage extent is slightly underestimated at damaged element 4 but the healthy elements have lower values than the sensitivity tests.

11.3.5 Quantification of damage extents using multiple mode sets

In this section, the quantification results are shown for different damage cases and extents, where each quantified value of the damage extent is evaluated by taking mean from the 100 estimates together with their standard deviations.

Recall that the damage extents is estimated from the derivation of $\hat{\delta}_a^{sens}$ (7.25) and $\hat{\delta}_a^{mm}$ (7.26) for the respective sensitivity and minmax tests in dependence of the choice of s-values. For the mode set $\mathcal{M}_1$, the s-value s^1 is chosen with $\mathrm{Im}(s^1) \in [0, 130]$ and for mode set $\mathcal{M}_2$, s^2 is chosen with $\mathrm{Im}(s^2) \in [0, 130]$ while the real part is fixed with $\mathrm{Re}(s^1) = \mathrm{Re}(s^2) = -1$. The results of the damage extent using multiple mode sets are evaluated from the single mode sets.

In the sensitivity tests, it can be seen in Figure 11.9(a) that the quantified stiffness decrease using multiple mode sets has slightly improved the performance of damage extents from the single mode set $\mathcal{M}_1$ but underestimated from $\mathcal{M}_2$ at almost everywhere in the s-plane. While in Figure 11.9(b) from the minmax tests, the quantified damage extent of multiple mode sets is well-estimated and significantly improves the performance compared to $\mathcal{M}_1$(overestimated) and $\mathcal{M}_2$(largely overestimated). Notice that the joint evaluation of the multiple mode sets from minmax tests gives good result compare to sensitivity tests.

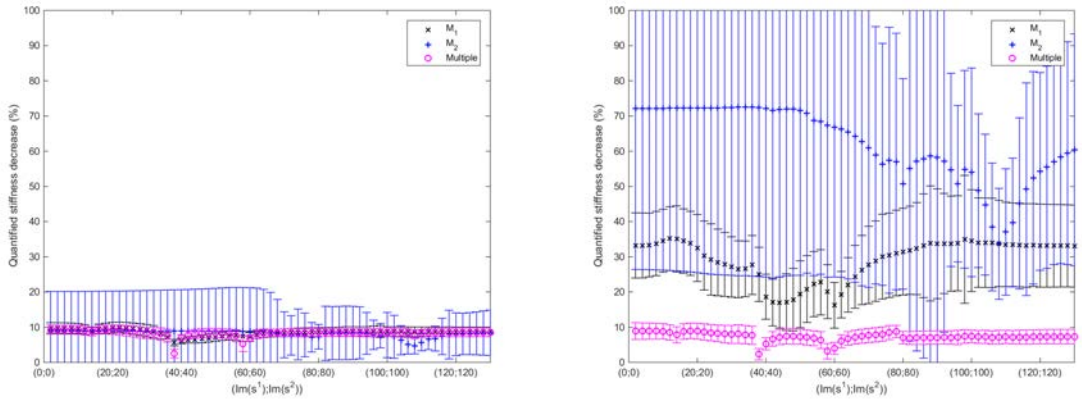

(a) Sensitivity tests

(b) Minmax tests

Figure 11.9 – Quantification of damage extents from single mode sets $\mathcal{M}_1$ and $\mathcal{M}_2$ in dependence of s in the vicinity of the modes, compared to the multiple mode sets. - using three sensors, 5% output noise, 2% damping, 10% stiffness reduction at element 4.

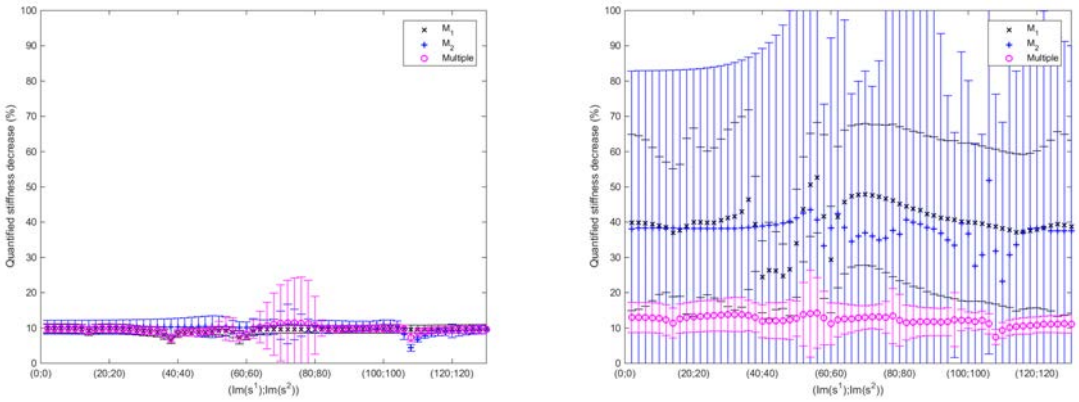

(a) Sensitivity tests

(b) Minmax tests

Figure 11.10 – Quantification of damage extents from single mode sets $\mathcal{M}_1$ and $\mathcal{M}_2$ in dependence of s in the vicinity of the modes, compared to the multiple mode sets. - using three sensors, 5% output noise, 0.2% damping, 10% stiffness reduction at element 4.

11.3.6 Damage quantification for several damage extents and datasets

Based on 100 simulated datasets, respectively for different damage extents between 5% and 30% damage in element 4, the mean and standard deviation of the estimated damage extent have been calculated. The results are shown in Figure 11.11(a) and 11.11(b) for several damage cases in both the sensitivity and the minmax approaches for the transfer matrix-based approach using all modes and multiple mode sets, respectively.

In Figure 11.11(a), the quantification results are obtained without modal truncation error but containing estimation errors, and it can be seen that the damage extents are always underestimated in both approaches and the error increases for large damage extent compared to true value. In Figure 11.11(b), the joint statistical results of the multiple mode sets are obtained from the single mode sets $\mathcal{M}_1$ and $\mathcal{M}_2$ using three sensors only, and it can be seen that the damage extents are slightly underestimated for both approaches. Finally, it can be summarized that the results are not satisfactory without modal truncation error in Figure 11.11(a), while the multiple mode sets give significantly good results in Figure 11.11(b).

Summarizing the results, it is seen that considering all modes, the quantification of the damage extents is not satisfactory, though it only contains estimation error but no truncation errors. On the other hand, using multiple mode sets, it can be seen that the damage is sometimes underestimated and sometimes overestimated, but always – at least roughly – in the order of the expected values. This approach shows large uncertainties, while the mean values seem to be more accurate using multiple mode sets. It is seen that results with the sensitivity approach are slightly more accurate than with the minmax approach. Therefore, further investigation of the reasons behind this phenomenon are part of the future research.

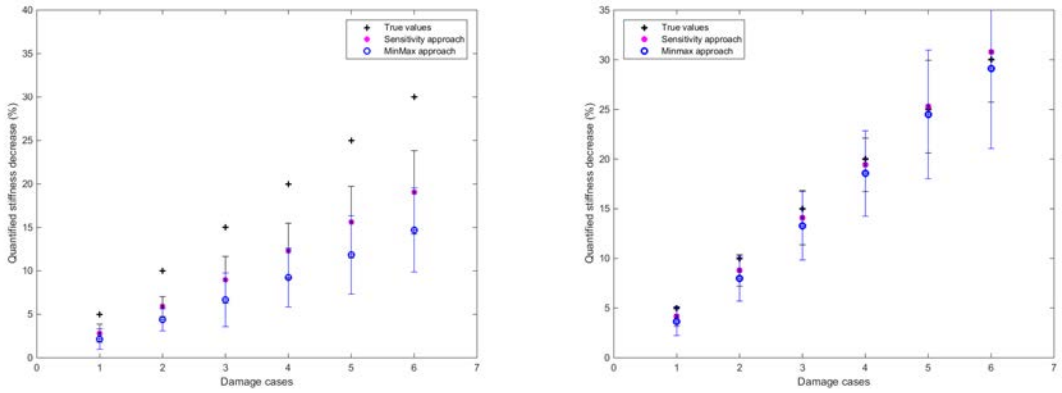

(a) All modes using all sensors

(b) Multiple mode sets using three sensors

Figure 11.11 – Quantification of different damage extents from (a) all modes using all sensors for the chosen $s = -1 + 25\mathrm{i}$ *(left) and (b) multiple mode sets using three sensors for the chosen* $s = [-1 + 25\mathrm{i}; -1 + 101\mathrm{i}]$ *(right) - 5% output noise, 2% damping ratio, damaged at element 4.*

11.4 Numerical application 2: Cantilever beam model

In a second study, a 2D Beam model has been demonstrated (see Section 8.3.2 in Figure 8.2) for the damage localization and quantification. In this example, 6 modes can be identified from the model of the structure using SSI (see Table 8.2), split into two mode sets $\mathcal{M}_1$ and $\mathcal{M}_2$ of three modes each for the proposed method using Multiple mode sets in Chapter 7. Recall that a subset of 3 modes could be used in the previous works [Ber10, DMBM13, MDBM15] as the number of modes could not be bigger than the number of output sensors.

Similar to the previous example, first the damage localization and quantification results are shown in the next section using the first 5 identified modes from table 8.2. Then, the success rate of the damage localization results has been computed using the single mode sets separately in Monte-Carlo simulation for 100 datasets and the success rate of the damage localization is illustrated with the proposed method of transfer matrix based residuals for the joint statistical evaluation of the multiple mode sets.

11.4.1 Damage localization and quantification for one dataset

Analogously as in the previous application, damage localization results are shown for one test case at all elements. The damaged element is simulated by decreasing 20% stiffness of its original value. From the sensitivity and minmax tests in Figure 11.12, it is seen that the damaged element is correctly located at element 3. In comparison to the mass-spring chain, the reaction of the sensitivity test is much stronger now at the undamaged elements, while the minmax test performs very well. From the results, it can be concluded that the healthy elements of the sensitivity tests react for the violation of $\delta_b = 0$ while the minmax approach gives good results.

For the damage quantification, the values $\hat{\delta}_{sens}$, $\hat{\delta}_{mm}$ and $\hat{\delta}_{esti}$ were estimated, leading to an estimated parameter change of 22.8%, 18.6% and 11.2651% in the damaged element. For the sensitivity-based evaluation of the residual $\zeta \sim \mathcal{N}(\mathcal{J}\delta, \Sigma)$, it is essential to take its uncertainty into account, which ensures an adequate weighting of its components. Note that the dimension of the residual is much larger than the dimension of δ, especially when aggregating different mode sets and/or s-values. In the statistical tests in Figures 11.12(a) and 11.12(b), the damaged element is correctly located. However, when solving the inverse problem directly as $\delta = \mathcal{J}^{\dagger}\zeta$ the uncertainty of the residual is not taken into account and the resulting solution in Figure 11.12(c) is obviously wrong, since not only the third component of δ is non-zero. This again underlines the necessity of taking the uncertainties into account in the evaluation of the damage indicators.

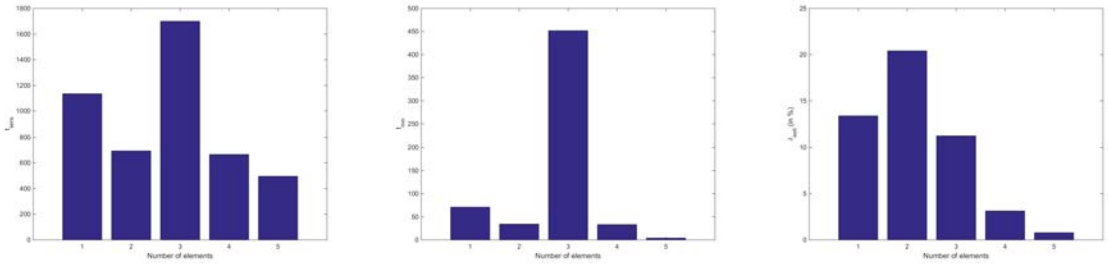

(a) Sensitivity tests (b) Minmax tests (c) Estimates value

Figure 11.12 – Localization results: (a) sensitivity tests and (b) minmax tests and (c) estimates value at $s = -1 + 200\mathrm{i}$ - five sensors and five modes, 5% output noise, 20% stiffness reduction at bar 3.

11.4.2 Success rate of the damage localization using a single mode set

In this section, the damage localization results are illustrated in dependence of the chosen s-value for both single mode sets $\mathcal{M}_1$ and $\mathcal{M}_2$, corresponding the first and last three modes respectively, before going to illustrate the joint evaluation of the multiple mode sets in the next section.

In this example, 100 datasets were generated for the Monte Carlo simulations. The well-estimated modes of these datasets with their uncertainties were identified using SSI in both reference and damaged states. Therefore, the success rate of the damage localization was computed from t_{sens} and t_{mm}-tests for the chosen s-value of the respective modes $\mathcal{M}_1$ or $\mathcal{M}_2$. The s-values was chosen in the vicinity of the entire modes (see Table 8.2) on a global grid in the interval with $\mathrm{Re}(s) \in [-1, 50]$ and $\mathrm{Im}(s) \in [0, 9000]$. In Figures 11.13 and 11.14, the success rates of the damage localization are shown in the z-axis in dependence of the chosen s-values where x and y-axis corresponds to real and imaginary part of the s-values for mode set $\mathcal{M}_1$ and $\mathcal{M}_2$, respectively.

Using a mode set $\mathcal{M}_1$, the results are shown in Figure 11.13 for the sensitivity and minmax tests. In both tests, it is seen that the performance of the damage localization is satisfactory at everywhere in the Laplace variables.

For the mode set $\mathcal{M}_2$, it can be seen in Figure 11.14 that the performance of damage

localization results is not satisfactory in the s-plane. Notice that the success rates of the damage localization using the mode set $\mathcal{M}_2$ in Figure 11.14 are around 50%, which is less enough in comparison to Figure 11.13.

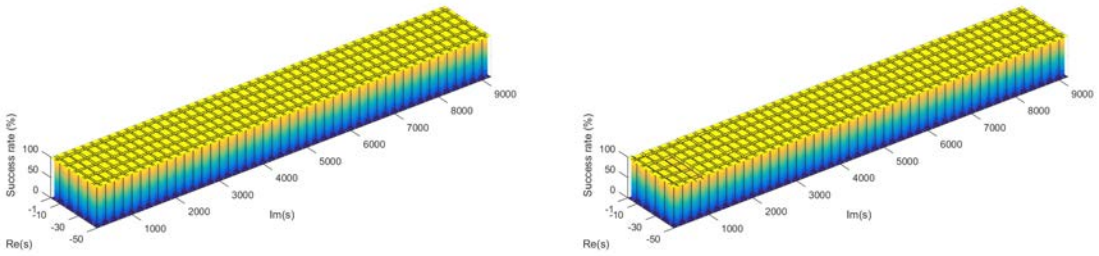

(a) Sensitivity tests (b) Minmax tests

Figure 11.13 – Success rate of statistical damage localization using single mode set $\mathcal{M}_1$, in dependence of s. - three sensors, 5% output noise, 1% damping ratio, 10% stiffness reduction at element 3.

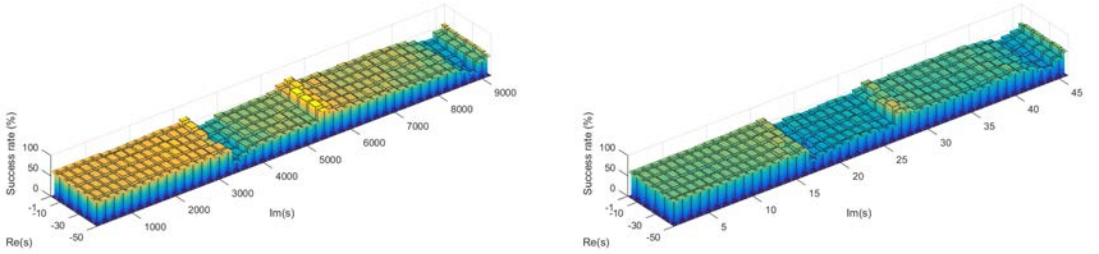

(a) Sensitivity tests (b) Minmax tests

Figure 11.14 – Success rate of statistical damage localization using single mode set $\mathcal{M}_2$, in dependence of s. - three sensors, 5% output noise, 1% damping ratio, 10% stiffness reduction at element 3.

In the next section, the new statistical approach using multiple mode sets has been proposed to increase the success rate of the damage localization at almost everywhere in the s-plane.

11.4.3 Success rate of the damage localization using multiple mode sets

In the previous section based on sensitivity and minmax tests, the success rate of the damage localization was only satisfactory for mode set $\mathcal{M}_1$ but not for $\mathcal{M}_2$ because of modal the truncation and estimation errors. This motivates the use of multiple mode sets instead of using a single mode set alone. The joint evaluation of the residual is obtained from (7.14) and its joint covariance is derived in (7.16) for the multiple mode sets.

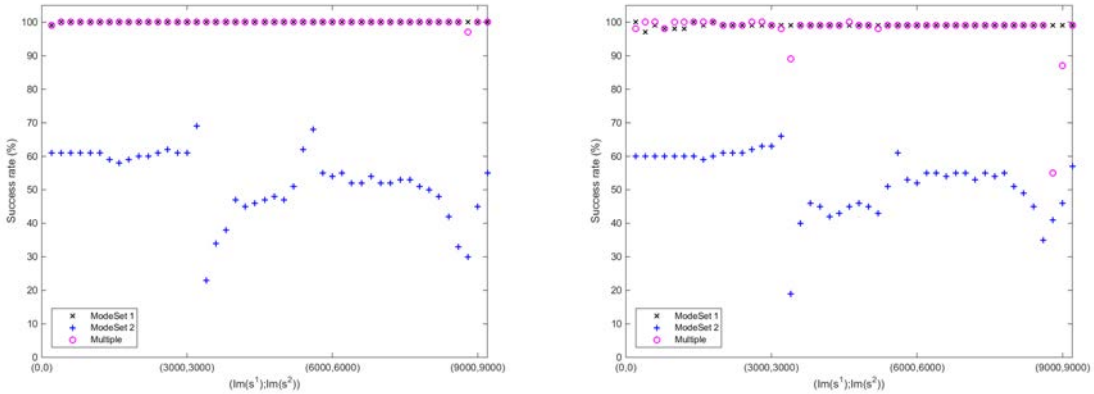

(a) Sensitivity tests (b) Minmax tests

Figure 11.15 – Success rate of statistical damage localization of single mode sets $\mathcal{M}_1$ and $\mathcal{M}_2$ with s in the vicinity of the modes, compared to the success rate using jointly the multiple mode sets. - using three sensors, 5% output noise, 1% damping ratio, 10% stiffness reduction at element 3.

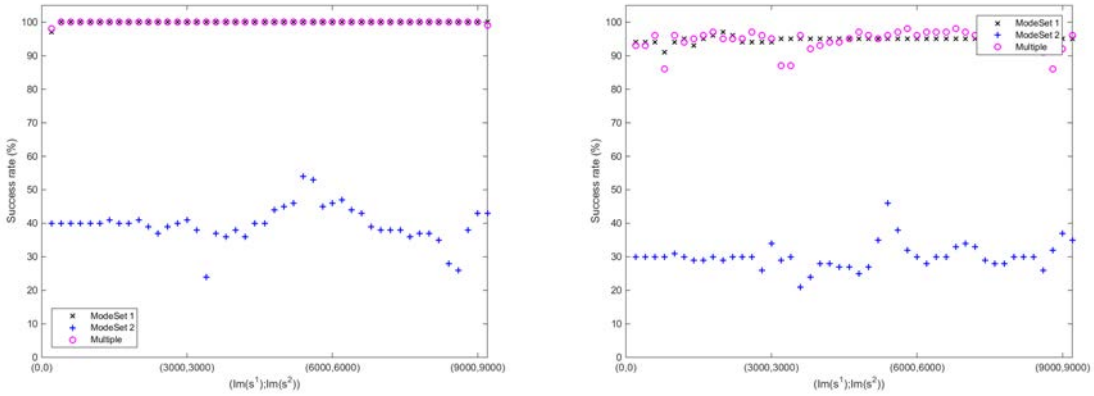

(a) Sensitivity tests (b) Minmax tests

Figure 11.16 – Success rate of statistical damage localization of single mode sets $\mathcal{M}_1$ and $\mathcal{M}_2$ with s in the vicinity of the modes, compared to the success rate using jointly the multiple mode sets. - using three sensors, 5% output noise, 2% damping ratio, 10% stiffness reduction at element 3.

For multiple mode sets, the same s-values are chosen in the vicinity of the modes such as

s^1 for mode set $\mathcal{M}_1$ with $\mathrm{Im}(s^1) \in [0, 9000]$, and s^2 for mode set $\mathcal{M}_2$ with $\mathrm{Im}(s^2) \in [0, 9000]$ while the real part is fixed with $\mathrm{Re}(s^1), \mathrm{Re}(s^2) = -1$.

In Figure 11.15(a) and 11.15(b), the results are shown for the respective sensitivity and minmax tests, where the success rates of the damage localization of multiple mode sets are computed from the single mode sets. For the sensitivity and minmax tests, it can be seen in Figure 11.15 that the joint statistical evaluation using multiple mode sets improves the damage localization performance significantly at almost everywhere in the s-plane to compare to the single mode set $\mathcal{M}_1$ and $\mathcal{M}_2$.

11.4.4 Damage extents using multiple mode sets

In the previous section, the test value in the sensitivity and minmax tests corresponds only for the decision if the respective element is damaged or not by comparing them to a threshold. In this section, the estimate of the changes parameter is computed for the quantification of the damage extents in both tests in dependence of the chosen s-values in the vicinity of the modes. Similar to the previous section, the same settings of the s-value is chosen for mode set $\mathcal{M}_1$ and s^2. The results of the damage extents are shown in Figure 11.17 by taking mean from the 100 estimates together with their standard deviations.

In Figure 11.17(a) with sensitivity tests, it can be seen that the quantified value of the damage extent is well-estimated from the statistical evaluation of multiple as well as single mode sets. While in the minmax tests, it can be seen in Figure 11.17(b) that the quantification results is slightly overestimated for mode set $\mathcal{M}_1$ in comparison to multiple mode sets. From both tests, it has been seen that the damage extents with the sensitivity approach give a better result than minmax tests. Indeed, the damage quantification with multiple mode sets gives satisfactory result in comparison to single mode sets.

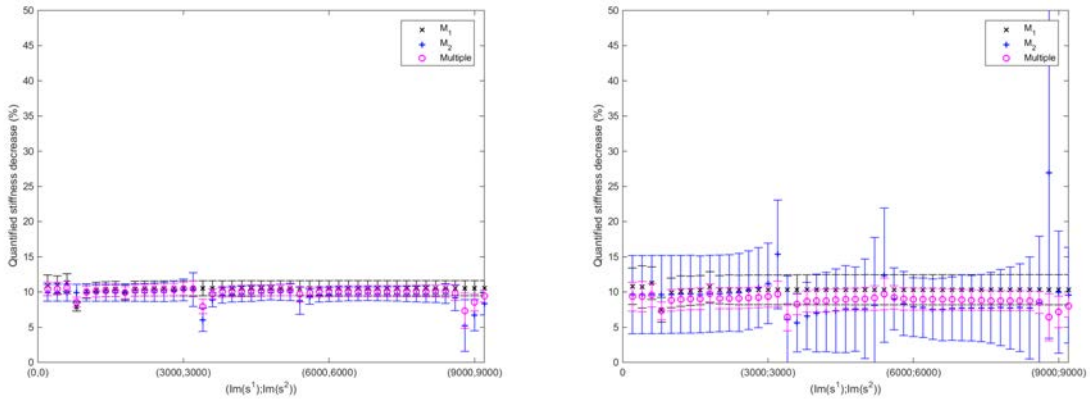

(a) Sensitivity tests

(b) Minmax tests

Figure 11.17 – Quantification of damage extents from single mode sets $\mathcal{M}_1$ and $\mathcal{M}_2$ in dependence of s in the vicinity of the modes, compared to the multiple mode sets. - using three sensors, 5% output noise, Damping 1%, 10% stiffness reduction at element 3.

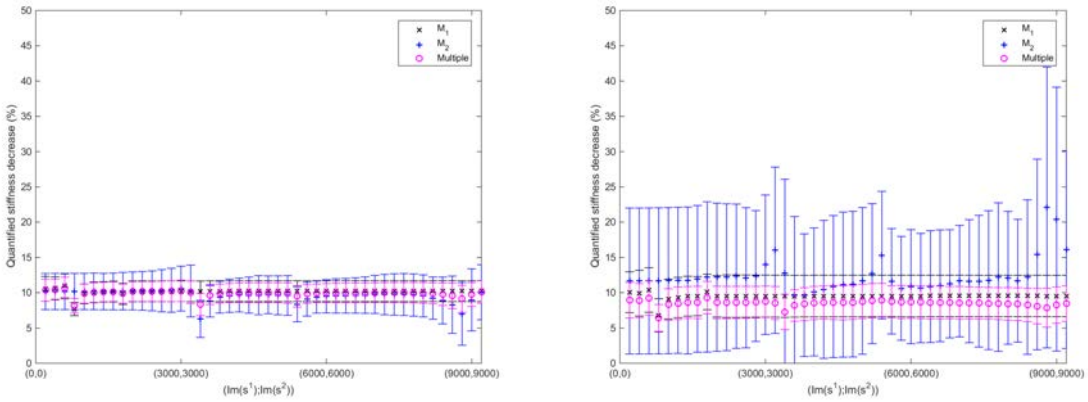

(a) Sensitivity tests

(b) Minmax tests

Figure 11.18 – Quantification of damage extents from single mode sets $\mathcal{M}_1$ and $\mathcal{M}_2$ in dependence of s in the vicinity of the modes, compared to the multiple mode sets. - using three sensors, 5% output noise, Damping 2%, 10% stiffness reduction at element 3.

11.4.5 Damage quantification for several damage extents and datasets

Based again on 100 simulated datasets, respectively for different damage extents between 5% and 30% damage in element 3, the mean and standard deviation of the estimated damage extent have been calculated. The results are shown in Figure 11.19(a) and 11.19(b) for several damage cases in both the sensitivity and the minmax approaches for the transfer matrix-based approach using five modes and multiple mode sets, respectively.

In the transfer matrix-based approach, the sensitivity approach overestimates and the minmax approach underestimates the damage extents. Figures 11.19(a) and 11.19(b) show that the error increases for large damage extents which can be expected since the sensitivity matrix is computed in the reference state and is thus not accurate anymore for large changes. In Figure 11.19(a), further error sources are modal truncation since only five out of 15 modes are taken into account in the sensitivity computation.

In Figure 11.19(b), the joint statistical results of the multiple mode sets are obtained from the single mode sets $\mathcal{M}_1$ and $\mathcal{M}_2$ using three sensors only, and it can be seen that the damage extents are well-estimated for both approaches, only for large damage cases are overestimated. Finally, in comparison to Figure 11.19(a) and 11.19(b), it can be summarized that the multiple approach gives satisfactory results for both sensitivity and minmax approaches.

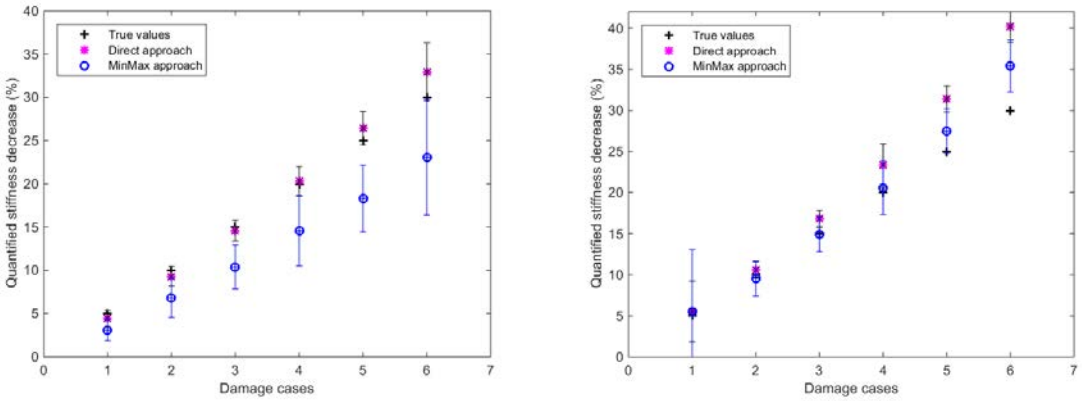

(a) Five modes using five sensors (b) Multiple mode sets using three sensors

Figure 11.19 – Quantification of different damage extents from (a) five modes using five sensors at $s = -1 + 200\mathrm{i}$ *(left) and (b) multiple mode sets using three sensors at* $s = [-1 + 200\mathrm{i}; -1 + 2600\mathrm{i}]$ *(right) - 5% output noise, 1% damping ratio, damaged at element 3.*

11.5 Comparison of the localization results based on the three methods

In this section, the localization results are recalled from the previous experiments in a Mass-spring chain system (see Figure 8.3) in order to make a comparison among the three methods e.g. the statistical evaluation of SDDLV, ILDL, and the transfer matrix sensitivity-based approach. For mode sets $\mathcal{M}_1$, corresponding to the first three modes, the results are illustrated in Figures 11.20, 11.21, and 11.22 for the respective methods. Note that all results are computed using the same simulated datasets (500) in both healthy and damaged states for the Monte-Carlo evaluation, and the s-values were chosen in the vicinity of the modes (see Table 8.1) on a global grid with $\mathrm{Re}(s) \in [-3, 1]$ and $\mathrm{Im}(s) \in [0, 130]$. Similar to previous results, the success rates of the damage localization (z-axis) are shown in dependence of the real and imaginary part of the chosen s-values (x and y-axes).

In the SDDLV approach, Figure 11.20 shows that the success rate in the statistical evaluation is satisfactory only in the interval of the Laplace variables with $\mathrm{Im}(s) \in [20, 64]$, where it reaches up to 90%. Beyond this interval, it is almost close to zero and the damage localization cannot be indicated due to the modal truncation error, which is significant outside the interval containing the identified modes (see Table 8.1).

Using the ILDL approach, the success rates of the damage localization (z-axis) are shown in Figure 11.21 in the element-wise tests of the residual vector for the statistical ILDL (R1e-S-ILDL). Note that the results are slightly improved in Figure 11.21 with compared to Figure 11.20, possibly it may happen because the image U_1 of the flexibility matrix δR in the ILDL approach is differently affected by noise than the null space.

For the transfer matrix sensitivity-based approach, the localization results are illustrated in Figures 11.22(a) and 11.22(b) for the respective sensitivity and minmax tests. It is seen

in Figure 11.22(a) that the success rate of the damage localization is satisfactory only in the interval of the Laplace variables with $\mathrm{Im}(s) \in [0, 34]$ than $\mathrm{Im}(s) \in [35, 130]$, while the localization results from minmax test gives good performance compared to the sensitivity tests.

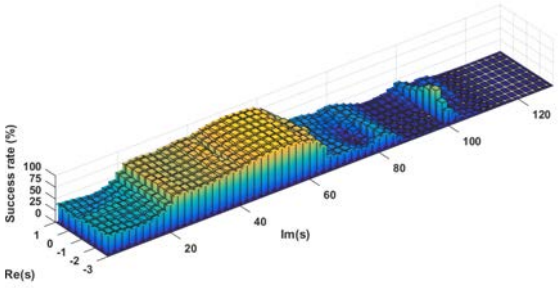

Figure 11.20 – Success rates of the S-SDDLV using single mode set $\mathcal{M}_1$ in dependence of s

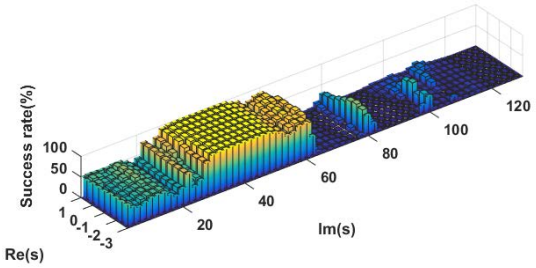

Figure 11.21 – Success rates of the R1e-S-ILDL using single mode set $\mathcal{M}_1$ in dependence of s

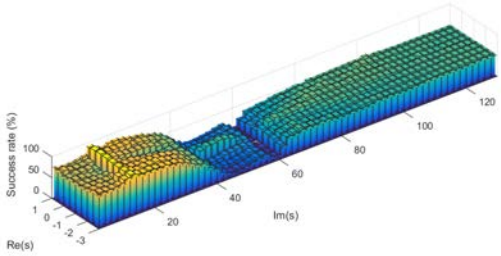

(a) Sensitivity tests

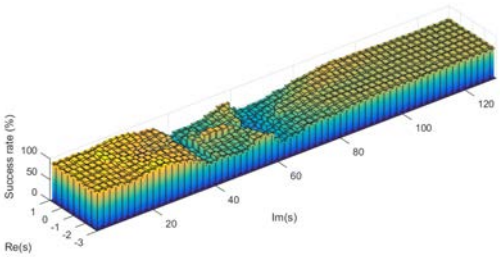

(b) Minmax tests

Figure 11.22 – Success rates of the statistical damage localization using single mode set $\mathcal{M}_1$, in dependence of s.

Summarizing the results, it can be concluded that both SDDLV and ILDL (see Figures 11.20 and 11.21), the Laplace variable s has a strong influence with compared to the sensitivity and minmax approach. This is due to the fact that the SDDLV and ILDL approach is based on the physical properties of the transfer matrix difference, and the choice of s is directly related to the bias of the transfer matrix. On the other hand, the sensitivity-based approaches require only the derivative of the transfer matrix, which is accurate when the modal parameters are correctly estimated (and when damage is small), independently of s.

11.6 Discussion

In this chapter, the transfer-matrix based residual was presented in a statistical output-only damage localization and quantification approach in a Gaussian framework based on the sensitivity and minmax tests. The residual is obtained in the context of SDDLV that is based on the transfer matrix difference between the reference and damaged states. In addition, it has been extended considering a joint statistical evaluation of multiple mode sets for same or different Laplace variables. The robustness of the damage localization and quantification has been obtained by taking into account the information from all modes of the structure.

In the applications, several experiments have been demonstrated in Monte-Carlo simulations to evaluate the success of the damage localization in dependence of the s-value, where each of the parameters corresponding to an element is tested for being non-zero in a Generalized Likelihood Ratio (GLR) test. Damage quantification corresponds to the estimates value of the changes parameter in the damaged elements. From results, it has been seen that the proposed method using multiple mode sets has increased the performance of the damage localization and quantification of the damage extents at almost everywhere in the complex s-plane compared to using a single mode set.

In comparison to SDDLV approach, the sensitivity and minmax tests are not good for large damage extents due to increasing error of the system parameter changes, while the SDDLV performs well for large damage extents because of the significant changes in the transfer matrix differences between the healthy and damaged states. In the SDDLV, the Laplace variable s has a strong influence with compared to the sensitivity and minmax tests. Still, the performance in this framework was not as good without modal truncation. Further investigations of the reasons behind this phenomenon are part of future research.

Chapter 12

Numerical Implementation

12.1 Introduction

In this Chapter, the numerical implementation of the damage localization methods is presented by using Abaqus software. In the previous Chapters 9, 10, and 11, the localization methods are applied on different numerical applications, where the FE model are generated using Matlab code which is more challenging to make an accurate FE model for bigger structure. Therefore, the purpose of this chapter is to compute the FE model of a structure in practice, generally for any kind of structure using Abaqus-Python script for the feasibility of the damage localization and quantification methods described in this thesis.

This chapter is organized as follows. In Section 12.2, an FE model of a healthy structure is described in step by step using Abaqus input file and then, mass and stiffness matrix of the healthy and damaged states are obtained from output database. Using Abaqus-Python script, the L_{model} of the structure is computed by a *for loop* in Section 12.5.1 as well as the sensitivity of modal parameters are derived with respect to the structural parameters to stiffness changes in Section 12.5.2. For instance, a script file is presented for model database as well as output database in Section 13.5 for the computation of L_{model} of the SDDLV approach. Finally, both methods from chapter 5 and 7 are tested for localization and quantification on a 2D cantilever beam model.

12.2 Simulation with Commercial Software@Abaqus

In Abaqus, all models are called input files. The input file is the means of communication between the preprocessor, usually Abaqus/CAE, and the analysis product, Abaqus/Standard or Abaqus/Explicit. It contains a complete description of the numerical model. An input file has two sections; Model and History. The Model section contains all the information about the model and comes before the history section. The History section provides information

about model.

In the following section, the simulation procedure will be discussed step by step. First, a script file has written of a healthy structure using Abaqus input file and then, mass and stiffness matrix of the healthy and damaged structures are obtained from Abaqus output database. Using Abaqus-Python script, the L_{model} of the structure is computed by a *for loop* in Section 12.5.1 as well as the sensitivity of modal parameters are derived with respect to the structural parameters to stiffness changes in Section 12.5.2.

12.3 Writing a script with Abaqus

A script file is written in the following in order to get the FE model of a structure. In Abaqus input file, the following things are considered in step by step.

- First, the node of the FE model of the structure can be defined as follows

```
*NODE,NSET=BEAMS
      1,   0.,    0.
      2,   0.2,   0.
      3,   0.4,   0.
      4,   0.6,   0.
      5,   0.8,   0.
      6,   1.,    0.
```

  The first digit corresponds to the number of the node and the next two correspond to the coordinates of the node, x and y, respectively. The columns are separated by a comma. Numbers must be followed by a period. For decimal numbers, it must be written with a point.

- Second, the number of element of FE model can be written as follows

```
*ELEMENT, TYPE=B23, ELSET=BEAMS
1,1,2
2,2,3
3,3,4
4,4,5
5,5,6
```

  The first digit corresponds to the number of the element, where the next two correspond to the numbers of the nodes that linked to this element. The columns are separated by a comma.

- Third, the parameters of the section is defined as follows. Assume that the beam section is circular cross-section and hence, need to define the diameter of this one.

```
*PARAMETER
R=0.015
```

- Four, the beam section is defined as circular cross-section and the type of the material is defined as steel as follows,

```
*BEAM SECTION,SECTION=CIRC,ELSET=BEAMS, MATERIAL=STEEL
<R>
```

- Five, the material properties of the beam section are defined as follows,

```
*MATERIAL, NAME =STEEL
*ELASTIC
206e9, 0.3
*DENSITY
7800
```

  Since the type of material is steel, the properties of this material are given by Young Modulus, Poisson ratio and its density.

- Six, a node group is created as follows. This command is very useful, when the geometry of the structure is large or complex.

```
*NSET, NSET=CLAMP, GENERATE
1,1,1
```

  This creates a node groups that have the same boundary conditions.

- Finally, the static and dynamic study can be performed.

In such a way, the Abaqus input file is organized and we are able to carry-out a study of any kind of structure using Abaqus software. In this study, we will perform the dynamic studies (modal analysis).

Compiling a script

In order to compile a script, first, open the Abaqus command prompt window, then enter "Abaqus job interactive" and write the name of the script file. By default, the file must be in the "Temp" folder of local disk. This operation will generate several files after compiling the script including a .odb file, which allows visualizing the output result with the CAE interface. The .dat file allows to understand possible error messages during the compilation and displays the different values requested by the user.

Modal analysis

Using the following command, the modal analysis of the structure can be performed

```
*STEP
*FREQUENCY, EIGENSOLVER=LANCZOS
15,0,,
```

Boundary condition

This function is used to prescribe boundary conditions at nodes or to specify the driven nodes in a submodeling analysis. In the following, the first digit corresponds to the number of the node and the next two correspond to the coordinates of the node, DOFs and displacement, respectively.

```
*BOUNDARY
1, 1, 0
1, 2, 0
1, 6, 0
```

Stiffness and mass matrix of the healthy structure

In order to get the stiffness and mass matrix of a structure, the following function is placed at the end of the script. The matrix is generated using the "substructure matrix output" function is written as follows:

```
*SUBSTRUCTURE MATRIX OUTPUT, OUTPUT FILE = USER DEFINED, FILE NAME = K, STIFFNESS = YES
*SUBSTRUCTURE MATRIX OUTPUT, OUTPUT FILE = USER DEFINED, FILE NAME = M, MASS = YES
```

From history output requests, the mass and stiffness matrix of the healthy structure has been imported as a text file. The file name of the matrix will be stored in the defining folder.

12.4 Damaged structure

In order to obtain the FE model of the damaged structure, the following properties of the structure will be reformulated to get the stiffness matrix of the damaged structure. Assume that damage is related to stiffness loss. Let element 3 is damaged, where it is generated by decreasing Young Modulus (E) of its original value which corresponds to the stiffness loss. The following things are reconsidered.

- The number of element is defined as follows, where the healthy and damaged elements of the structure are named as BEAMSAFE and BEAMDAMGE, respectively

  ```
  *ELEMENT, TYPE=B23
  1,1,2
  2,2,3
  3,3,4
  4,4,5
  5,5,6
  *Elset, elset=BEAMSAFE
  1,2,4,5
  *Elset, elset=BEAMDAMAGE
  3
  ```

- The beam section of the model is defined as follows, where the BEAMSAFE corresponds to the healthy elements and BEAMDAMAGE corresponds to the damaged element as well as the material properties are redefined.

```
*BEAM SECTION,SECTION=CIRC,ELSET=BEAMSAFE, MATERIAL=STEEL
<Radius>
*BEAM SECTION,SECTION=CIRC,ELSET=BEAMDAMAGE, MATERIAL=STEEL_DAMAGE
<Radius>
```

- The material properties of the beam section is defined according to healthy and damaged elements of the model. There are two possibilities, such as damage can be generated by decreasing Young modulus of its original value, or stiffness matrix of the damaged model can be imported using Abaqus input file. For the healthy and damaged case, the following properties are given as

```
*MATERIAL, NAME =STEEL
*ELASTIC
2.07e11, 0.3
*DENSITY
7800
*MATERIAL, NAME =STEEL_DAMAGE
*ELASTIC
1.035e11, 0.3
*DENSITY
7800
```

Stiffness and mass matrix of the damaged structure

As similar to the previous section, the same command is used to get the stiffness and mass matrix of the damaged structure,

```
*SUBSTRUCTURE MATRIX OUTPUT, OUTPUT FILE = USER DEFINED, FILE NAME = K_d, STIFFNESS = YE
*SUBSTRUCTURE MATRIX OUTPUT, OUTPUT FILE = USER DEFINED, FILE NAME = M, MASS = YES
```

From the history output file, the mass and stiffness matrix of the damaged structure is obtained as a .text file. The file name of the matrix will be stored in the destination folder. Since the damage is generated by decreasing Young modulus, the stiffness of the structure is only changed, while the mass is unchanged.

Stiffness and mass matrix of the free boundary of the structure

For the modal analysis and computation of the L_{model} of the structure, it is required to export the global mass and stiffness matrices of the structure at all nodes and degrees of freedom.

Therefore, the mass and stiffness matrix are exported for the safe structure where the matrices are stored in the destination folder namely as M.mtx and K.mtx. There, the format

of the matrices are not in the proper order and given only for the lower triangular part of the matrices. Then it is essential to rewrite the matrix (e.g. K.xls or matlab) to get the global mass and stiffness matrix. The following steps are considered

- Export the mass and stiffness matrices as a .text file from the history output file, and then rewrite the format in order to get the global mass and stiffness matrix.
- Finally, delete the entries in the rows and columns for the fixed node (i.e. DoFs per fixed node) from the global mass and stiffness matrices.

Using these information we can perform the modal analysis and compute the L_{model} of the structure from the mass and stiffness matrices of the safe structure. In the following, the L_{model} of the structure is described for the SDDLV and ILDL approaches using Abaqus-Python script.

12.5 FE model with Abaqus-Python script

In the previous section, the FE model of a structure is described using Abaqus input file as well as the mass and stiffness matrix of the structure is shown how to get it. This information is essential in order to design an adequate FE model for a simple or very complex structures. For the damage localization methods in Chapters 5-7, an FE model is required and here it is obtained using Abaqus-Python script, where the mass and stiffness matrix of the structure are obtained from the previous sections. Note that the script is given in the Appendix 13.5.

12.5.1 L_{model} of the structure for SDDLV or ILDL approach

For the damage localization with SDDLV or ILDL approach in Chapters 5-6, the L_{model} of the structure is described in Section 2.2.3. In the previous chapters 9-11, the L_{model} of the structure was obtained using Matlab Code, where it is more challenging to obtain an accurate FE model. Therefore, in this section, the L_{model} (2.2.3) of the structure is computed using Abaqus-Python Script.

- First, an FE model of the healthy structure is made with Abaqus input file or GUI, details are given in Section 12.3. After compiling the script, the mass (M), stiffness (K) and damping (C) matrices of the model are obtained from Abaqus output database.
- Secondly, G_{model} (2.23) is obtained in Matlab from M, C, and K matrices for a selected Laplace variable (s-value), and
- thirdly, the displacement vectors $Z(s)$ (2.24) are computed at all DOFs after applying a unit load to the model at each sensor coordinates.
- Fourthly, in order to get the stress field, the displacement vectors are applied as the Boundary Condition (BC) of the model at all DOFs that yield stress field.

- Finally, a job is created and submitted for analysis in Abaqus-Python using a *for loop*. From Abaqus field-output requests, the output generated stress (i.e. Section Force (SF) and Section Moment (SM)) at all DOFs are saved in a text file for each sensor coordinate. Note that L_{model} be the column of these stress resultants $S(s)_i$. In such a way, L_{model} of the structure is computed using Abaqus-Python script as illustrated in Figure 12.1.

Therefore, the load vector is applied to L_{model} to get the stress resultants, and for each element, these stress values are statistically aggregated in the χ^2_t-test (5.14). Recall that stress value close to zero indicates potentially damaged elements in the SDDLV approach.

For the simplicity, a script file of a 2D beam model of length 1 m with a circular cross-section has been presented in the Appendix for the computation of L_{model}. There, first a script is written for Model Database (.mdb) and then Output Database (.odb) in Section 13.5 and 13.5, respectively.

12.5.2 Sensitivity-based FE model with Abaqus-Python script

In the contribution chapter 7 for the damage localization and quantification, the sensitivity analysis of the modal parameters with respect to structural parameters are required in order to obtain the sensitivity matrix $\mathcal{J}_{R,\theta}$ (7.8). Here, the derivative of the modal parameters with respect to the structural parameters to the stiffness of each element is computed using the finite difference approach. The assumed perturbation factor is 0.1%. The sensitivity analysis was performed using a Python script as follows.

Generally, sensitivity analysis depends on the selection of parameters. For example, the structural parameters can be elements of mass and stiffness matrices. In this study, assume that damage is related to stiffness loss and hence, the beams Young modulus (E) is chosen as an updating parameter. Assume a structural system consists of t elements, then the sensitivity matrix can be obtained as follows.

- First, the FE model of the structure is made and then the eigenfrequencies $f_{(c,l)}$ and modeshapes φ_l, $l = 1, \ldots, m$ are numerically generated for the initial FE model with Abaqus-Python script.

- Second, for each element, the sensitivities of the eigenstructure (frequencies and mode shapes) to the physical parameters (chosen in here as the stiffness of each element) are calculated. A perturbation (rf) 0.1% of stiffness (considering reduction of Young mouduls) change is introduced at j^{th}, $j = 1, \ldots, t$ element of the FE model. Then the corresponding eigenfrequencies $f^*_{(c,l)}$ and modeshapes φ^*_l are numerically computed for the modified FE model.

- Third, using finite difference approach, the difference in eigenfrequencies and modeshapes between the intial and modified FE models, df_l and $d\varphi_l$ is obtained by $df_l = (f^*_l - f_l)$ and $d\varphi_l = (\varphi^*_l - \varphi_l)$, respectively. Then, each component of the j^{th} column of the sensitivity matrix is computed dividing the change in each eigenfrequency and modeshape by the perturbation factor rf.

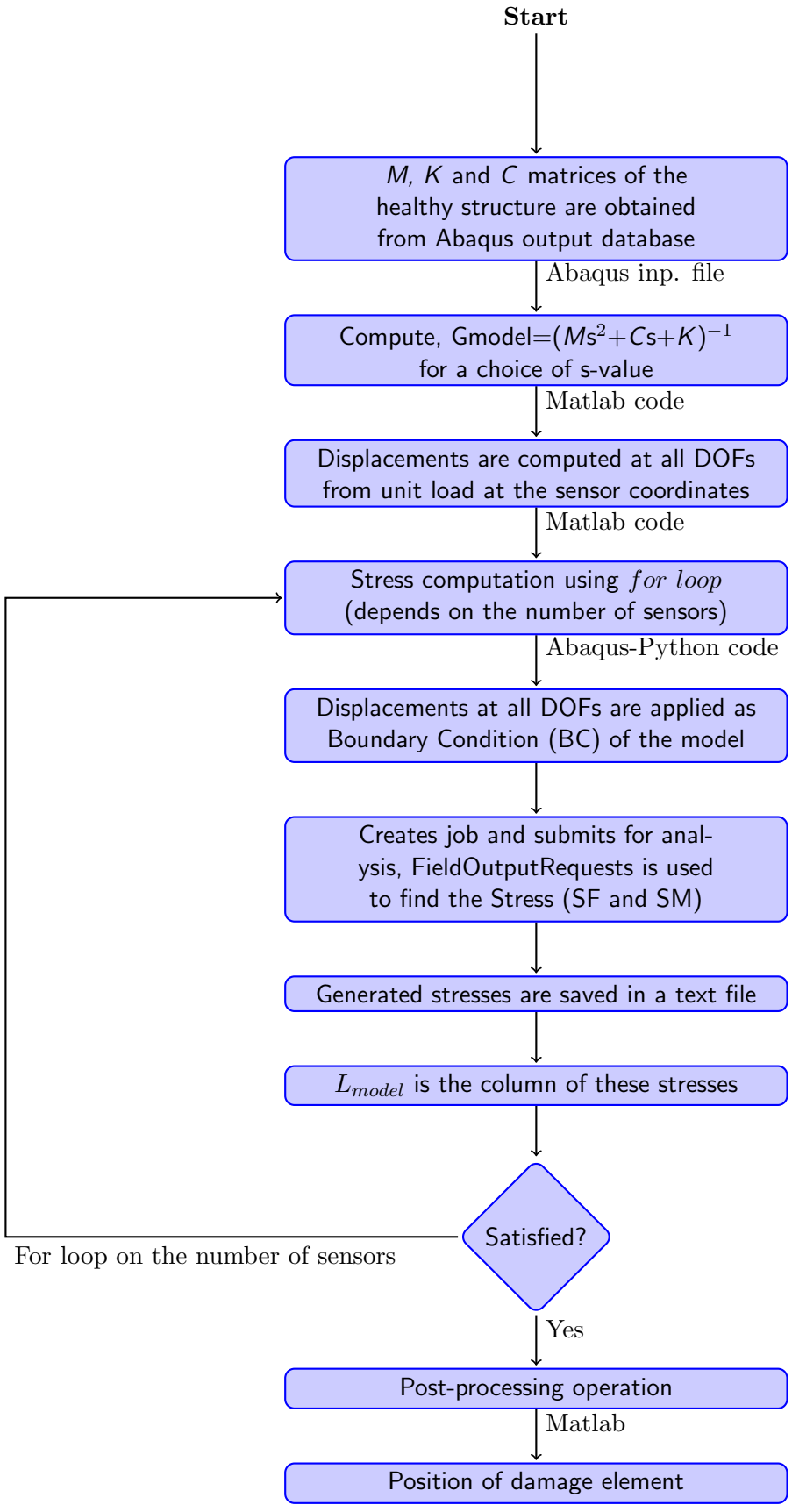

Figure 12.1 – Implementation of the method using commercial software Abaqus

- Finally, the sensitivities of the eigenstructure are obtained by repeating the above procedure for all t elements using a *for loop* and then, the result is saved as a text file.

12.6 Numerical application: 2D Cantilever beam

In this study, a 2D Beam model has been considered (see Figure 12.2) for both damage localization and quantification from chapter 5 and 7. Using Abaqus software, the structure is modeled with 5 beam elements of total length 1 m. The beam elements are circular with an external diameter of 0.02 m. The mass density, Young modulus (E) and Poisson ratio are 7800 kg.m^{-3}, 207 GPa and 0.3, respectively. The total number of degrees of freedom of the structure is 15. Damping is defined such that the damping ratio of all modes is 1%. Damaged is modeled in element 3 by decreasing 20% Young modulus. For the damaged and undamaged states, the acceleration data length is N = 25,000, generated from collocated white noise excitation using five sensors in the Y-direction at each node with a sampling frequency of 2000 Hz, and 5% white noise was added to the output data. For the transfer matrix-based approaches, the first five modes of the structure were identified with subspace identification, as shown in Table 12.1 and the respective modes are illustrated in Figure 12.3.

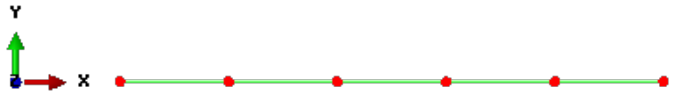

Figure 12.2 – 2D Beam model with 5 elements (15 DOFs) -using Abaqus/CAD Student Edition 6.14-2

Table 12.1 – Eigenvalues λ_c of beam model.

Mode	Healthy state	Damaged state
1	$-0.9057 + 90.5613$i	$-0.8949 + 89.4815$i
2	$-5.6785 + 567.8169$i	$-5.4319 + 543.164$i
3	$-15.950 + 1594.949$i	$-15.805 + 1580.434$i
4	$-31.526 + 3152.450$i	$-30.623 + 3062.156$i
5	$-52.454 + 5245.229$i	$-51.261 + 5125.834$i

12.6.1 FE model with Abaqus-Python script

A finite element model of the structure is required to obtain L_{model} (5.4) for the stress computation in the SDDLV approach, and to obtain the sensitivity of the modal parameters with respect to the structural parameters for the computation of the sensitivity $\mathcal{J}_{R(s),\theta}$ (7.8). Assume that damage is located at element 3. Stress is computed for all elements in the SDDLV approach, and parameter θ is defined as Young modulus of each element in the sensitivity approach. All elements of the FE model are tested.

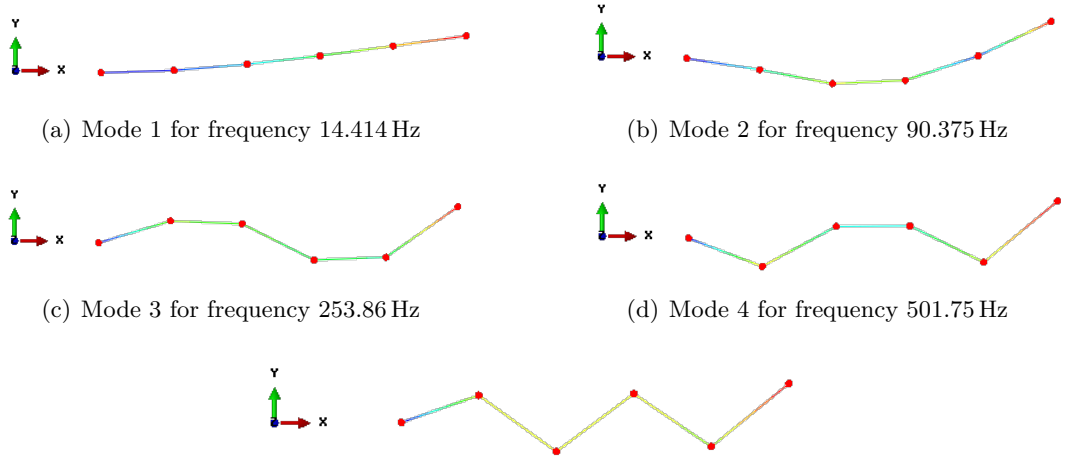

(a) Mode 1 for frequency 14.414 Hz

(b) Mode 2 for frequency 90.375 Hz

(c) Mode 3 for frequency 253.86 Hz

(d) Mode 4 for frequency 501.75 Hz

(e) Mode 5 for frequency 834.85 Hz

Figure 12.3 – First few modes of the 2D Cantilever beam using Abaqus/CAD Student Edition 6.14-2

In the following, the FE model of the structure for the SDDLV and sensitivity approaches is described based on Abaqus-Python script in Section 12.5.

L_{model} for SDDLV approach

Following Section 12.5.1, the $L_{model}(s) \in \mathbb{C}^{l_k \times r}$ of the structure is implemented using Abaqus-Python script for the damage localization with SDDLV approach (see Chapter 5). Where l_k be the number of all stresses that are computed at the elements of the structure and r is the number of outputs. Then, modal parameters estimated from output-only measurements in the reference and damaged states of the system. A vector is obtained in the null space of the changes in the transfer matrix computed in both states and then applied as a load vector to the L_{model} model of the structure. The damage localization is related to this stress where it is close to zero.

Sensitivity analysis based on FE model

In the sensitivity approach for both damage localization and quantification (see Chapter 7), to obtain the required sensitivity matrix $\mathcal{J}_{R(s),\theta}$ (7.8), the derivative of the modal parameters $(f_{(c,l)}, \varphi_l)$, $l = 1, \ldots, m$. with respect to the structural parameters is computed for each mode m, following Section 12.5.2. Let $\theta = [\theta^1 \cdots \theta^p]$ is the parameters of an FE model of the structure. For the damage localization, each of the components θ^i, $i = 1 \cdots p$ are tested with the sensitivity and minmax tests. For the faulty system, the component of $\delta_a = 0$ is tested against $\delta_a \neq 0$ based on the sensitivity and the minmax tests. Then the test variables are compared to a threshold level to make a decision about faulty components when $\delta_a \neq 0$. Estimates of the changes δ are computed with the respective approaches described in Section (7.5). In this approach, the highest t_{sens} and t_{mm} value indicates the damaged elements.

In both approaches, the transfer matrix difference and its covariance are computed based on the identified five modes for a particular choice of Laplace variable s, comprising one variable s in the vicinity of the identified modes. Note that test values close to zero indicate potentially damaged elements in the SDDLV approach, and high values indicate the damaged elements in the sensitivity-based approaches.

12.6.2 SDDLV approach: localization results at all elements

The localization results at all elements are computed using one datasets in both healthy and damaged states. Recall that the damage position is inferred by the stress value closest to zero. The computation of all stresses is done at $s_1 = -1 + 200\mathrm{i}$ for the theoretical, estimated and statistical evaluation of χ_t^2-tests in Figures 12.4(a), 12.4(b) and 12.4(c), respectively. In Figures 12.4(a)-12.4(c), all stress values corresponding to healthy and damaged elements are presented, while the smallest stress value is correctly located in the damaged element at 3.

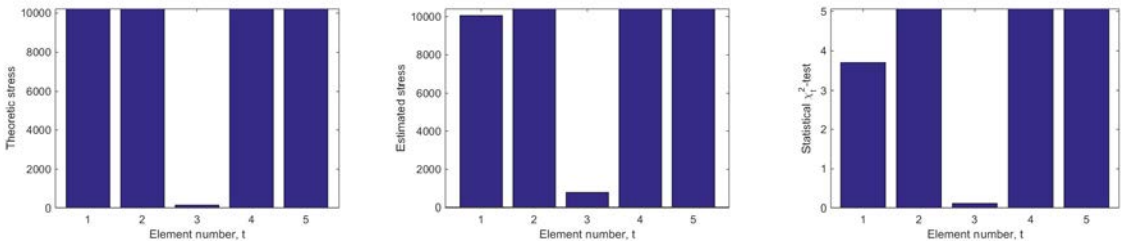

(a) SDDLV for theoretic stress (b) SDDLV for estimated stress (c) S-SDDLV (Statistical χ_t^2-test)

Figure 12.4 – SDDLV-based damage localization: stress computation and statistical evaluation at $s_1 = -1 + 200\mathrm{i}$ -using five sensors, 5% output noise, 20% stiffness reduction at bar 3.

12.6.3 Sensitivity-based approach: damage localization and quantification

Analogously as in the previous application, damage localization results are shown for one test case at all elements. Recall that high value indicates the damaged elements in the sensitivity and minmax approaches. From the sensitivity and minmax tests in Figure 12.5, it is seen that the damaged element is correctly located at element 3. The reaction of the sensitivity test is much stronger at the undamaged elements, while the minmax test performs very well. From the results, it can be concluded that the healthy elements of the sensitivity tests react for the violation of $\delta_b = 0$ while the minmax approach gives good results.

For the damage quantification, the values $\hat{\delta}_{sens}$, $\hat{\delta}_{mm}$ and $\hat{\delta}_{esti}$ were estimated, leading to an estimated parameter change of 23.17%, 20.10% and 13.99% in the damaged element for the transfer matrix-based approach.

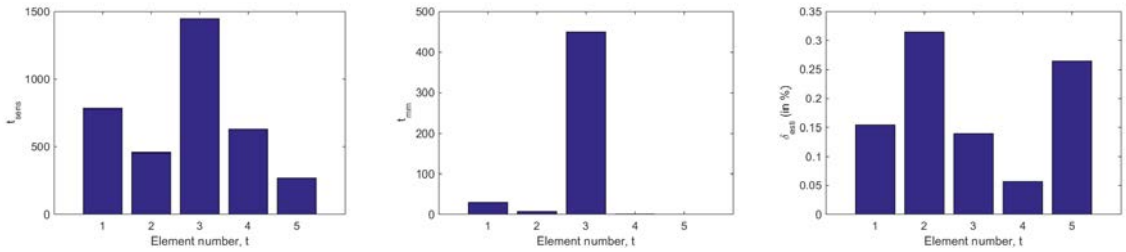

(a) Sensitivity tests (b) Minmax tests (c) Estimates value

Figure 12.5 – Localization results: (a) sensitivity tests, (b) minmax tests and (c) estimates value at $s = -1 + 200\mathrm{i}$ *- five sensors and five modes, 5% output noise, 20% stiffness reduction at bar 3.*

12.7 Discussion

In this Chapter, the damage localization methods are numerically implemented with Abaqus Software. From the localization results, it is seen that two transfer matrix based methods have been successfully identified the damaged element on a numerical application. In addition, the sensitivity-based approach allows the quantification of damage. From the quantification results, it can be concluded that the minmax approach gives almost perfect results with compared to sensitivity test.

Part IV

Real applications

Chapter 13

Real data applications

13.1 Introduction

In this Chapter, the damage localization methods are validated on real applications of structures. This chapter is formulated as follows. In Section 13.2 and 13.3, the new approach using multiple mode sets is validated on two different cantilever beam on a lab experiment. In Section 13.4, the damage localization with SDDLV and the new development of transfer-matrix based damage localization and quantification is applied on a Four-story Yellow Frame structure, and the conclusion of the work is presented in Section 13.5.

13.2 Case study 1: Cantilever beam 1

In a lab experiment, damage tests were conducted on a cantilever beam that is made of plastic, as shown in Figure 13.1. This experiment was performed by Brüel & Kjær in Denmark. Its dimensions are $0.5\,\mathrm{m} \times 0.08\,\mathrm{m} \times 0.01\,\mathrm{m}$ and it is fixed on one side. Damage was introduced by drilling holes, located at $0.08\,\mathrm{m}$ from the fixed end. The beam was excited horizontally by a shaker under white noise excitation and the response was monitored by 18 horizontal and 9 vertical accelerometers. For both the healthy and damaged states, acceleration data of length $N = 295{,}936$ with a sampling frequency of $8192\,\mathrm{Hz}$ were recorded.

This experimental setup has been used previously as a validation case for the SDDLV method [MDBM15]. In this previous work, the localization was performed using all the available horizontal sensors. Consequently, using all the signals it was possible to identify natural frequencies and modes shape in bending and torsion.

The objective of the present study is to localize the damage with a minimum number of sensors to highlight the advantage of using the proposed multiple mode sets method. Furthermore, it is intended to demonstrate the method based on a very simple finite element model of the structure.

Therefore, we consider only three "virtual sensors" located in the center of the structure instead of the full data from the horizontal accelerometers (see Figure 13.1). The measurements of these three sensors at 0.167 m, 0.333 m and 0.5 m from the fixed end are obtained as the mean of the measured accelerations at the top and bottom of the beam. This means that we are voluntarily excluding the torsional modes. We are able to identify five bending modes in the plane $x - z$, which will show to be sufficient for a precise damage localization in the following when considering all five modes in two mode sets with the method from chapter 5.

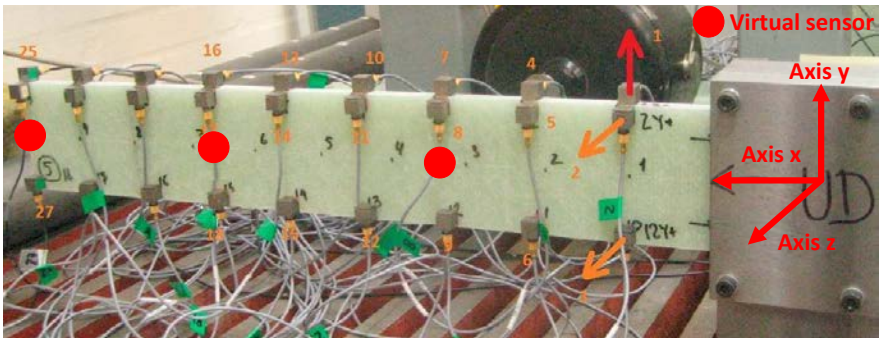

Figure 13.1 – Experimental setup of the beam.

13.2.1 Modal analysis and uncertainties

After downsampling and decimation of the data by factor 4, five well-estimated bending modes were obtained in the healthy and the three damaged states from the measurement data using SSI, together with their uncertainties. The identified frequencies are shown in Table 13.1 for each mode. Since only three sensors are used, the identified modes are split into two mode sets $\mathcal{M}_1$ and $\mathcal{M}_2$ containing two and three modes, respectively.

Table 13.1 – Identified frequencies (in Hz) of beam.

Mode	healthy	1 hole	3 holes	5 holes	Mode set
1	16.53	16.41	16.20	15.83	$\mathcal{M}_1$
2	81.06	81.44	81.52	81.47	
3	326.9	322.9	326.3	327.2	$\mathcal{M}_2$
4	529.4	528.4	527.1	523.9	
5	831.3	831.8	831.5	826.1	

13.2.2 Finite element model

The model needs to be as simple as is practicable but it has to correctly represent the behavior of the structure. The value of the material data (e.g. Young modulus, Poisson ratio and density) are not given in the paper presenting the experimental setup [MDBM15]. We only

know that the beam is made of PVC. Consequently, we have some uncertainties in the model. Therefore, a case study has been carried-out in order to design an approximate FE model. First, a 3D fine mesh beam model (see Figure 13.2) is considered as a reference value and the corresponding modes of the structure are illustrated in Figure 13.4. The Young modulus (E), Poisson ratio and mass density of the beam are chosen as 5 GPa, 0.4 and 1100 $kg.m^{-3}$, respectively.

For further study, a finite element simulation with 72 shell elements (S4R5) has been performed using ABAQUS/CAD Software, the model is illustrated in Figure 13.3. The mesh density of the model is identical to the previous work [MDBM15]. The computed values are given in the Table 13.2. In addition, a simple 2D beam model with 9 elements has been performed using Matlab code as shown in Figure 13.5. In the following, the comparison of the eigenfrequencies among 3D beam, shell model, 2D beam, and the analytical frequencies are mentioned together in Table 13.2 .

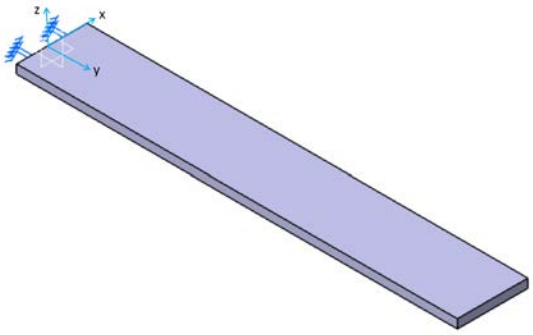

Figure 13.2 – Geometry of the model

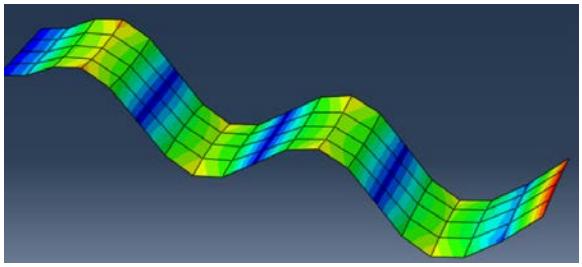

Figure 13.3 – FE shell model with 72 elements

Table 13.2 – Identified frequencies (in Hz) of beam.

Mode no.	3D structure (reference)	Shell Model	Analytical freq (in plane y-z)	2D Beam model (in plane y-z)	Experiment
1	15.048	14.012	13.8	13.77	16.53
2	94.056	88.201	86.3	86.33	81.06
3	108.764	105.08	-		
4	172.764	162.58	-	-	173.3
5	262.938	250.34	241.7	241.8	326.9
6	514.431	501.39	473.7	474.2	529.4
7	525.003	495.0	-	-	-
8	611.989	601.0	-	-	-
9	848.118	852.73	783.1	785.00	831.3

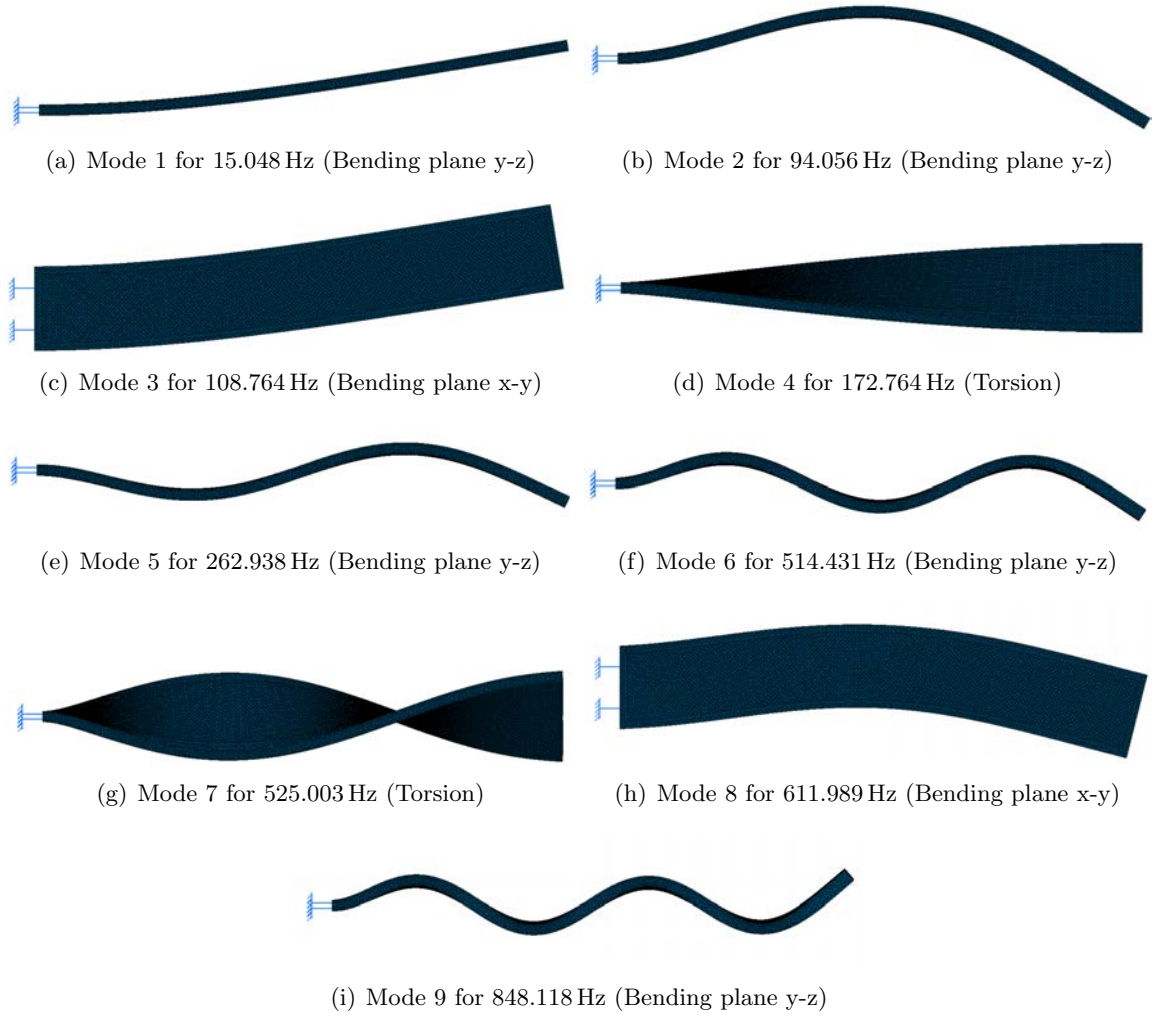

(a) Mode 1 for 15.048 Hz (Bending plane y-z)

(b) Mode 2 for 94.056 Hz (Bending plane y-z)

(c) Mode 3 for 108.764 Hz (Bending plane x-y)

(d) Mode 4 for 172.764 Hz (Torsion)

(e) Mode 5 for 262.938 Hz (Bending plane y-z)

(f) Mode 6 for 514.431 Hz (Bending plane y-z)

(g) Mode 7 for 525.003 Hz (Torsion)

(h) Mode 8 for 611.989 Hz (Bending plane x-y)

(i) Mode 9 for 848.118 Hz (Bending plane y-z)

Figure 13.4 – Mode shapes of 3D beam model

Analytical beam model

For a clamped beam, the eigenfrequencies for bending modes in plane y-z are given by the formula below:

$$\Lambda_1 = 1.875, \quad \Lambda_2 = 4.694 \quad for\ n \geq 3 : \Lambda = (2n-1)\pi/2,$$

$$\omega_1 = \Lambda_1^2 \sqrt{\frac{EI}{\rho S L^4}} = 3.516 \sqrt{\frac{EI}{\rho S L^4}},$$

$$\omega_2 = 4.694^2 \sqrt{\frac{EI}{\rho S L^4}} = 3.516 \sqrt{\frac{EI}{\rho S L^4}} \quad for\ n \geq 3 : \omega = ((2n-1)\pi/2)^2 \sqrt{\frac{EI}{\rho S L^4}}.$$

The corresponding values of the analytical beam model are given in the Table 13.2. The analytical beam model gives the same values as a very fine 2D beam finite element model.

In addition, the bending modes in the plane x-y are not identified here. The bending mode 3 in plan x-y as well as torsional mode 4 in the 3D finite element simulation are missing. So, each mode shape has to be carefully control to allow comparison. However, the shell finite element model gives acceptable results and allows finding the same modes than the 3D one but with some inversions. As you can notice, there is still a gap between the reference value of eigenfrequency (3D model) and the shell model. It suggest that the structure is not really a plate (the ratio width/thickness is equal to 8). Nevertheless, the results obtained with the shell model are better than those obtained using the beam model.

Therefore, in this particular example, a simple 2D beam model gives the correct mode shapes for the bending modes in the plane $x - z$, so it can represent the first five bending modes in the plane $x - z$ of the structure. Considering all the modes, it matches to the modes 1-2-5-6-9 of a 3D model used as reference. Nevertheless the ratio length/width of the structure is equal to 6. It is not strictly speaking a beam (ratio of 10). This leads to a systematic, but acceptable, model error of about 8% considering the gap between the reference values of the eigenfrequencies obtained with a very fine mesh 3D model and the ones obtained with the analytical beam model.

Even the 3D or shell model are better to simulate the structure, they count a large number of elements. Its leads to truncation errors when computes model, and previously, it has been investigated that the performance of method is not satisfactory for large modal truncation errors (see section 9.5.3). So, a simple model could give results for identification. A trade-off between model size, i.e. the number of DOFs, and model precision must be considered for the computation of the stress for damage localization. The stress resultants and their uncertainties are computed for each structural element. Using only three sensors it seems to be reasonable to demand a localization precision within a discretization of nine elements of the beam. Additionally, such a coarse mesh of nine elements is good enough to compute the first five bending modes in the plane $x - z$. It is finally the model that we have chosen in this study, as depicted in Figure 13.5.

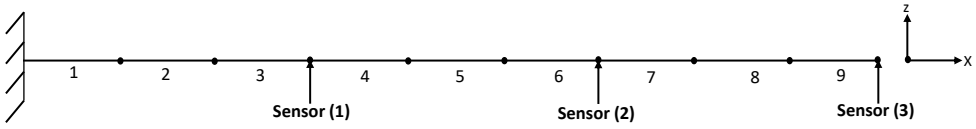

Figure 13.5 – Model of the beam with 3 sensors.

The mass and stiffness matrices are computed using Matlab code according to the formulation presented in Chapter 8 for 2D beam model in Section 8.3.2.

The computed stress resultants for each structural element are the real and imaginary parts of the three internal forces $\tau_t = \left\{ \begin{array}{cc} F_x & 0 \\ 0 & M_y \\ V_z & 0 \end{array} \right\}$. The damage is situated at element 2 in this model, being located at 0.08 m from the fixed end.

13.2.3 Localization results at all elements

The performance of the proposed damage localization method using multiple mode sets is compared to the separate single mode set evaluation for the three different damage scenarios.

The localization results are computed at all elements from the experimental datasets in both damaged and healthy states. The computation of the stress and its uncertainties for the statistical evaluation in the χ_t^2-tests is carried out for two different sets of s-values, each in the vicinity of the respective mode sets. First, one s-value is chosen for each mode set with $s^1 = -10 + 90\mathrm{i}$ for mode set $\mathcal{M}_1$ and $s^2 = -10 + 3200\mathrm{i}$ for mode set $\mathcal{M}_2$. Second, two s-values are chosen for joint evaluation for each mode set as in (5.15)–(5.16): $s_1^1 = -10 + 90\mathrm{i}$, $s_2^1 = -10 + 100\mathrm{i}$ for $\mathcal{M}_1$, and $s_2^2 = -10 + 3200\mathrm{i}$, $s_3^2 = -10 + 3300\mathrm{i}$ for $\mathcal{M}_2$. Third, three s-values are chosen for joint evaluation for each mode set: $s_1^1 = -10 + 90\mathrm{i}$, $s_2^1 = -10 + 100\mathrm{i}$, $s_3^1 = -10 + 200\mathrm{i}$ for $\mathcal{M}_1$, and $s_1^2 = -10 + 2100\mathrm{i}$, $s_2^2 = -10 + 3200\mathrm{i}$, $s_3^2 = -10 + 3300\mathrm{i}$ for $\mathcal{M}_2$. To easily compare the ratios of the stress or associated χ_t^2-values between the undamaged and damaged elements in the different test cases, the computed values are normalized in the figures such that the smallest value of the nine elements is 1.

The estimated stress and its statistical evaluation is shown in detail for the first damage case of 1 hole. In Figures 13.6 and 13.7, the results are shown for considering the single mode sets $\mathcal{M}_1$ and $\mathcal{M}_2$. Neither the estimated stress nor its statistical evaluation can correctly indicate the damage at element 2.

When using the joint statistical evaluation of both mode sets with the method of this paper, the results using one s-value in Figure 13.8(b) indicate the damaged element within the adjacent elements of the damaged one, being close to correct damage localization. By adding information through two and three more s-values in the same setting, the damaged element can be correctly indicated in Figure 13.8(d) and 13.8(f). In this case, notice that the estimated stress can not identify the damage localization correctly due to modal truncation and estimation error.

Then, the localization results with the proposed method of this paper are presented in Figures 13.9 and 13.10 for the further damage severities of three and five holes, showing the estimated stress and statistical evaluation of the multiple mode sets using one, two or three s-values for each mode set. Using one s-value in Figures 13.9(a)–13.9(b) and 13.10(a)–13.10(b), the damage can be localized in the region of the damaged and its adjacent elements for both estimated stress and statistical evaluation, and the χ_t^2-value for the damaged element 2 is slightly lower than for the neighboring elements. Using two or three s-values in Figures 13.9(c)–13.9(d) and 13.10(e)–13.10(f), it can be seen that the damage can be more clearly localized in element 2 with the joint statistical evaluation, while the damage localization based on the estimated stress can be localized in the region of the damaged and its adjacent elements due to modal truncation and variance errors.

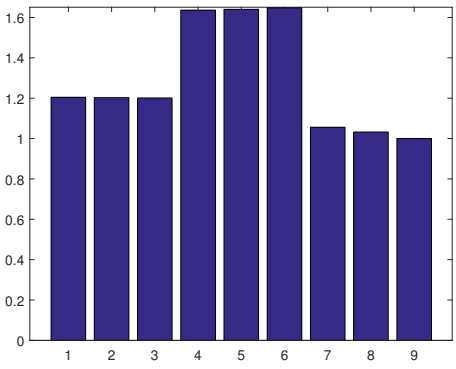

(a) Estimated stress

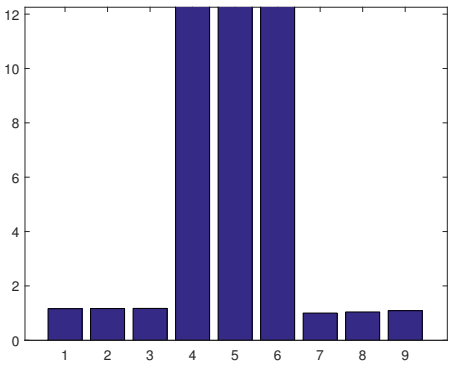

(b) Statistical evaluation in χ^2_t-tests

Figure 13.6 – Localization results for all elements using single mode set $\mathcal{M}_1$ at $s^1 = -10 + 90\mathrm{i}$. Damage case: 1 hole.

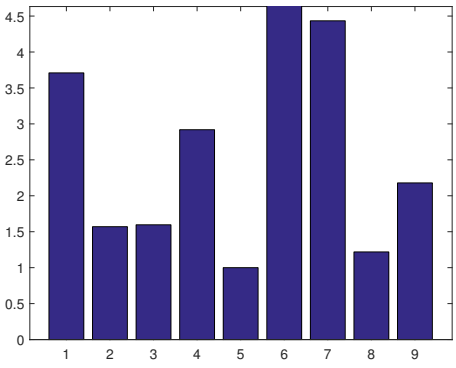

(a) Estimated stress

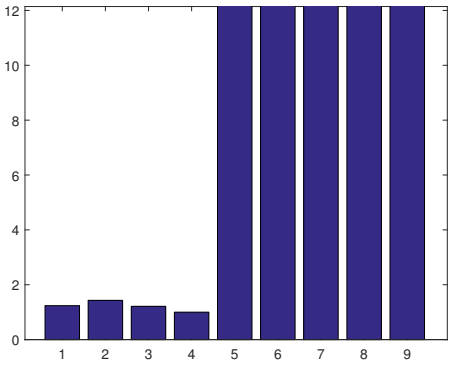

(b) Statistical evaluation in χ^2_t-tests

Figure 13.7 – Localization results for all elements using single mode set $\mathcal{M}_2$ at $s^2 = -10 + 3200\mathrm{i}$. Damage case: 1 hole.

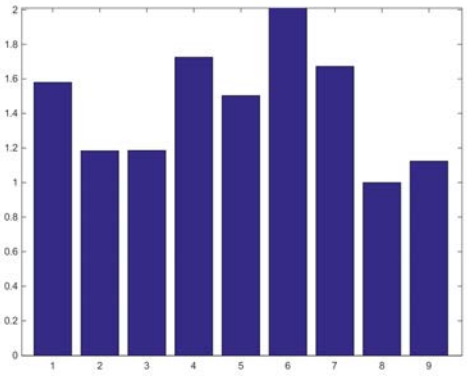

(a) Estimated stress, 1 s-value

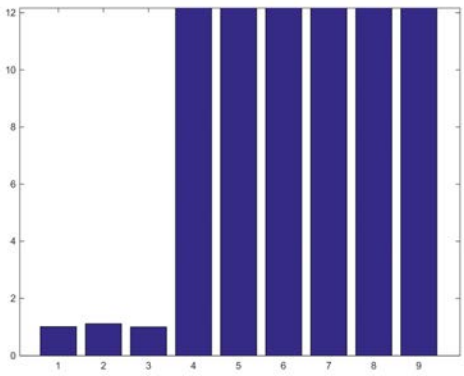

(b) Statistical χ^2_t-tests, 1 s-value

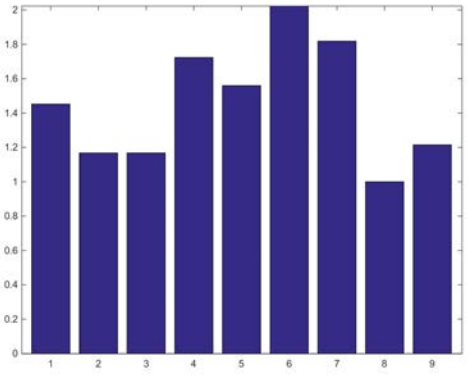

(c) Estimated stress, 2 s-value

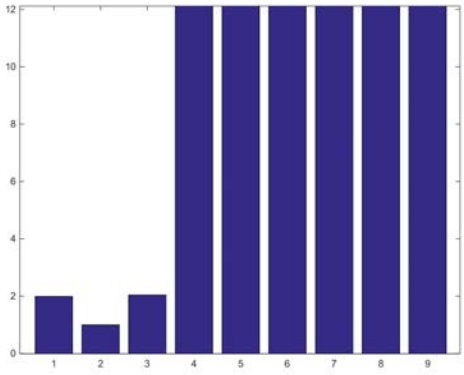

(d) Statistical χ^2_t-tests, 2 s-value

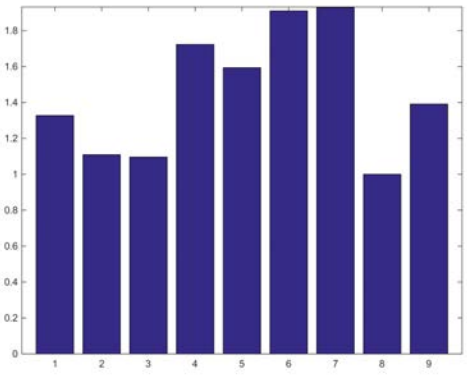

(e) Estimated stress, 3 s-value

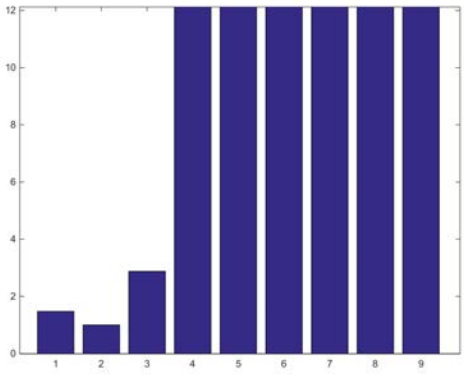

(f) Statistical χ^2_t-tests, 3 s-value

Figure 13.8 – Localization results with new method using both mode sets. Damage case: 1 hole.

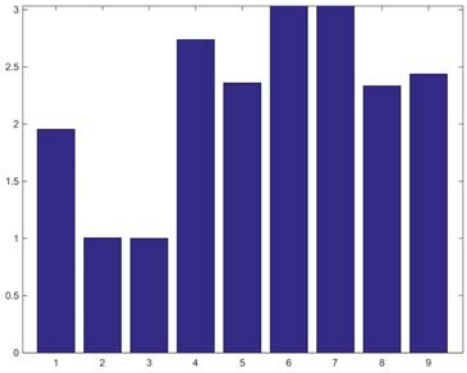

(a) Estimated stress, 1 s-value

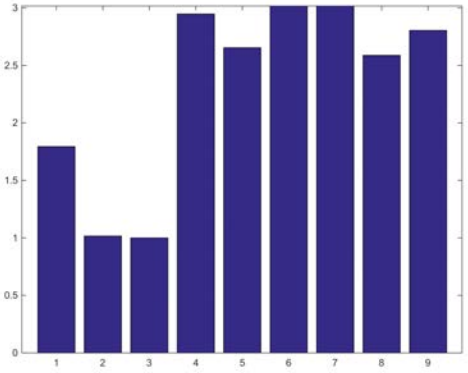

(b) Statistical χ^2_t-tests, 1 s-value

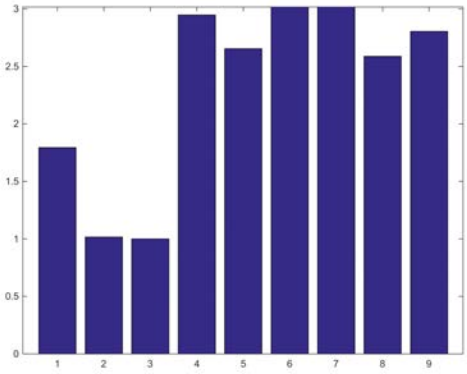

(c) Estimated stress, 2 s-value

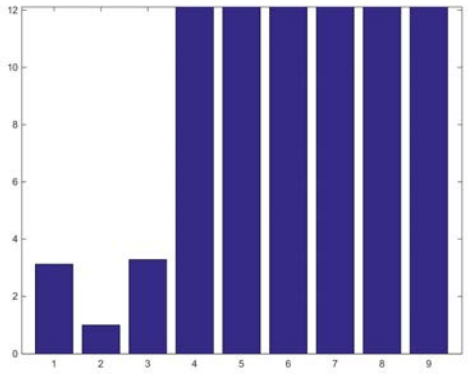

(d) Statistical χ^2_t-tests, 2 s-value

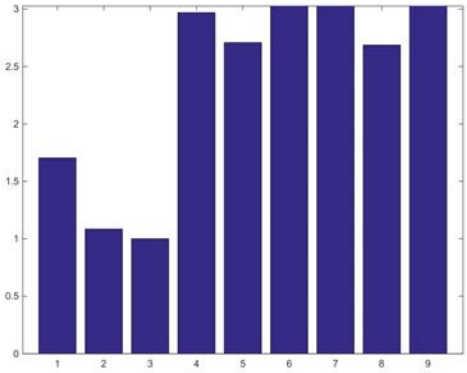

(e) Estimated stress, 3 s-value

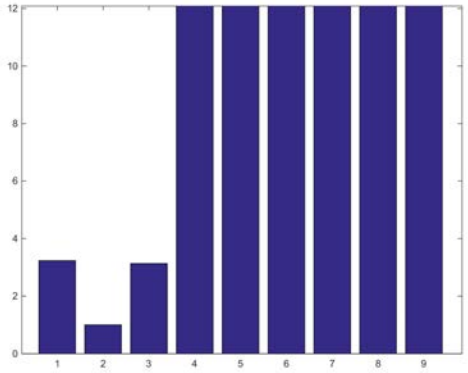

(f) Statistical χ^2_t-tests, 3 s-value

Figure 13.9 – Localization results with new method using both mode sets. Damage case: 3 hole.

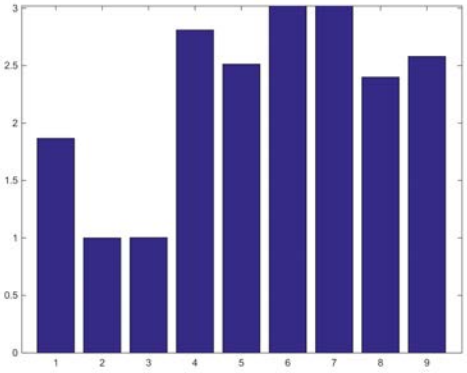

(a) Estimated stress, 1 s-value

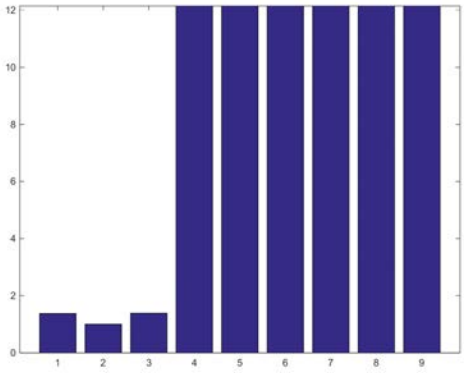

(b) Statistical χ^2_t-tests, 1 s-value

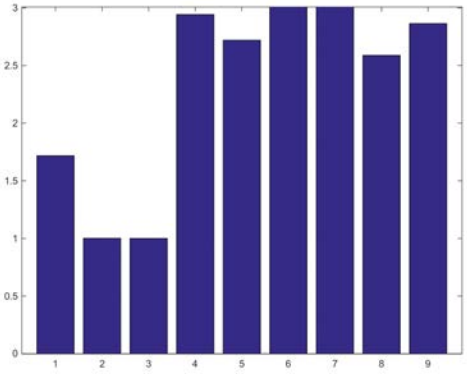

(c) Estimated stress, 2 s-value

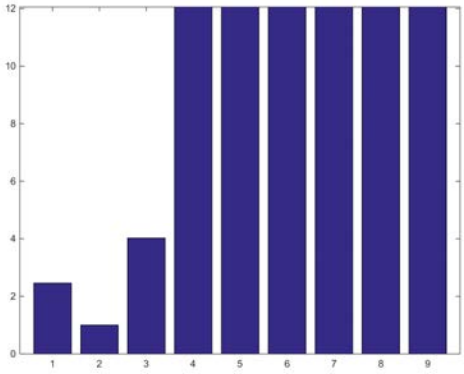

(d) Statistical χ^2_t-tests, 2 s-value

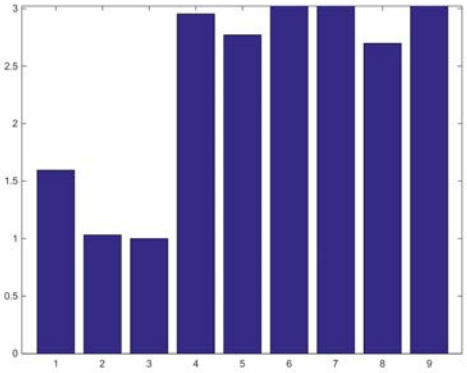

(e) Estimated stress, 3 s-value

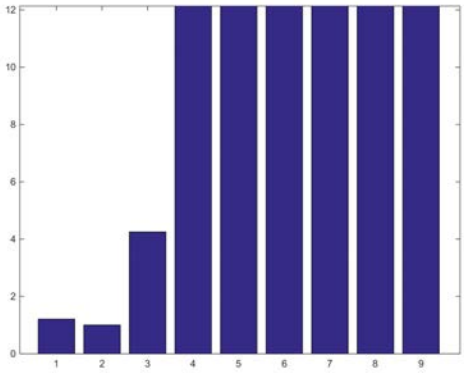

(f) Statistical χ^2_t-tests, 3 s-value

Figure 13.10 – Localization results with new method using both mode sets. Damage case: 5 hole.

Summarizing the results in this experiment, it can be seen that neither the estimated stress from the SDDLV approach nor its statistical evaluation is sufficient for damage localization in the classical formulation using one mode set, which is probably due to significant modal truncation errors when using only limited modal information. The statistical evaluation with the proposed method takes all the modal information into account and correctly indicated the damage locations in this example, based on measurements from only three sensors and five identified modes, together with a coarse FE model of the structure.

13.3 Case study 2: Cantilever beam 2

13.3.1 Experimental setup

The proposed damage localization algorithm using multiple mode sets has been applied on vibrational data of a cantilever beam as shown in Figure 13.11. The beam length is 1 m and is embedded on 5 cm at its lower end.

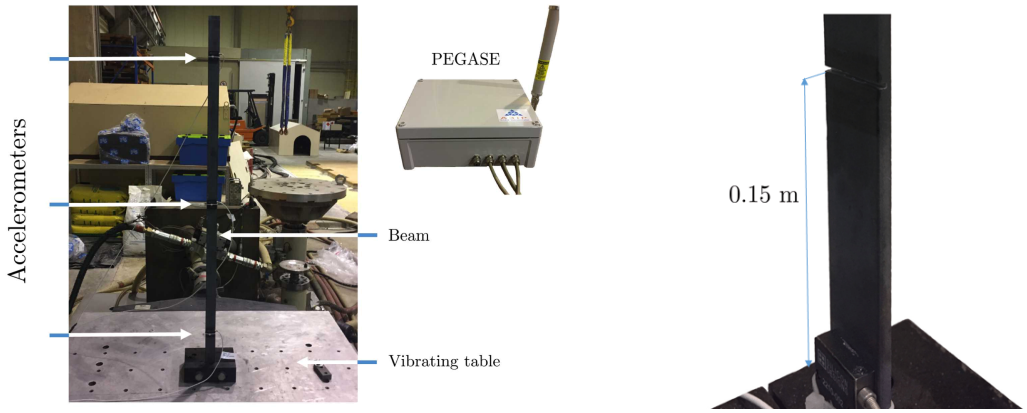

(a) Experimental setup for the beam in healthy state (b) Damaged beam.

Figure 13.11 – Experimental setup of a cantilever beam

The excitation for the tests was provided by an hydraulic shaker. A broadband random acceleration signal was induced via a vibrating table at the bottom of the structure. Response of the beam was measured in the transverse direction with three accelerometer sensors 0.1, 0.5 and 0.9 m of the vibrating table, i.e. 0.05, 0.45 and 0.85 m of the embedding), at a sampling frequency of 2000 Hz and 20,000 samples. Data are recorded and stored with a PEGASE platform, which is a smart wireless sensor systems performing real-time monitoring [LCDLP+16]. With the practical difficulties to access structures, to collect data and then perform off-line and remote computation, this platform offer an advantage compared to classical measurement systems.

A damage was performed by introducing a cut along the length of the beam, at 0.2 m to the vibrating table (i.e. 0.15 m to the embedding), as depicted in Figure 13.11(b). Experimental data for the healthy state were recorded similarly as for the healthy structure.

13.3.2 Finite element model

The underlying healthy finite element model is required for the method and assumed to be known. The structure of 0.95 m length is equally divided into 100 three-dimensional beam elements (6 degrees of freedom per node) as shown in Figure 13.12. The density and elastic modulus of the beam are 7800 kg/m^3 and 2.1×10^{11} Pa, respectively, and the area of cross-section is $(0.03041 \times 0.00514)\,\mathrm{m}^2$. The damage position corresponds to elements 16-17 of the model.

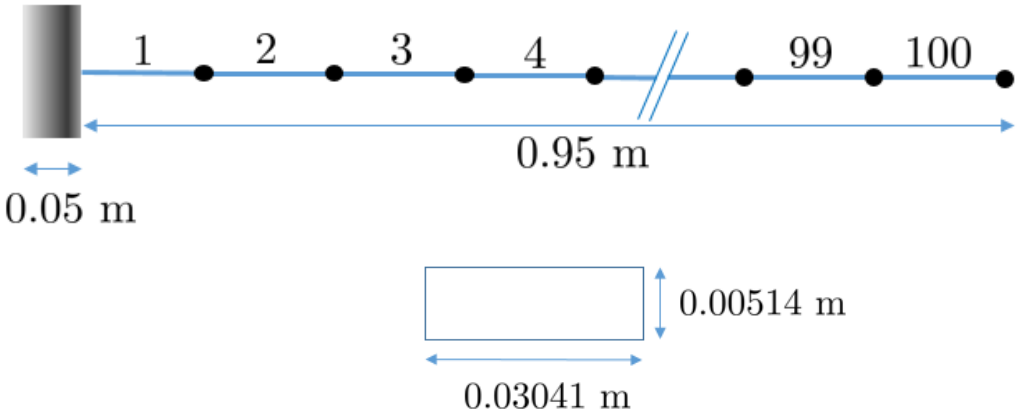

Figure 13.12 – FE model of the beam.

The mass and stiffness matrices are computed using Matlab code according to the formulation presented in Chapter 8 for 3D beam model in Section 8.3.5. The modes of the structure are illustrated in Figure 13.13.

Table 13.3 – Identified frequencies (in Hz) of beam.

Mode no.	Analytical freq	3D Beam model	Experiment
1	4.77	4.77	4.51
2	29.91	29.91	28.46
3	83.76	83.76	80.56
4	164.15	164.15	156.68
5	271.35	271.35	259.56
6	405.35	405.35	384.51

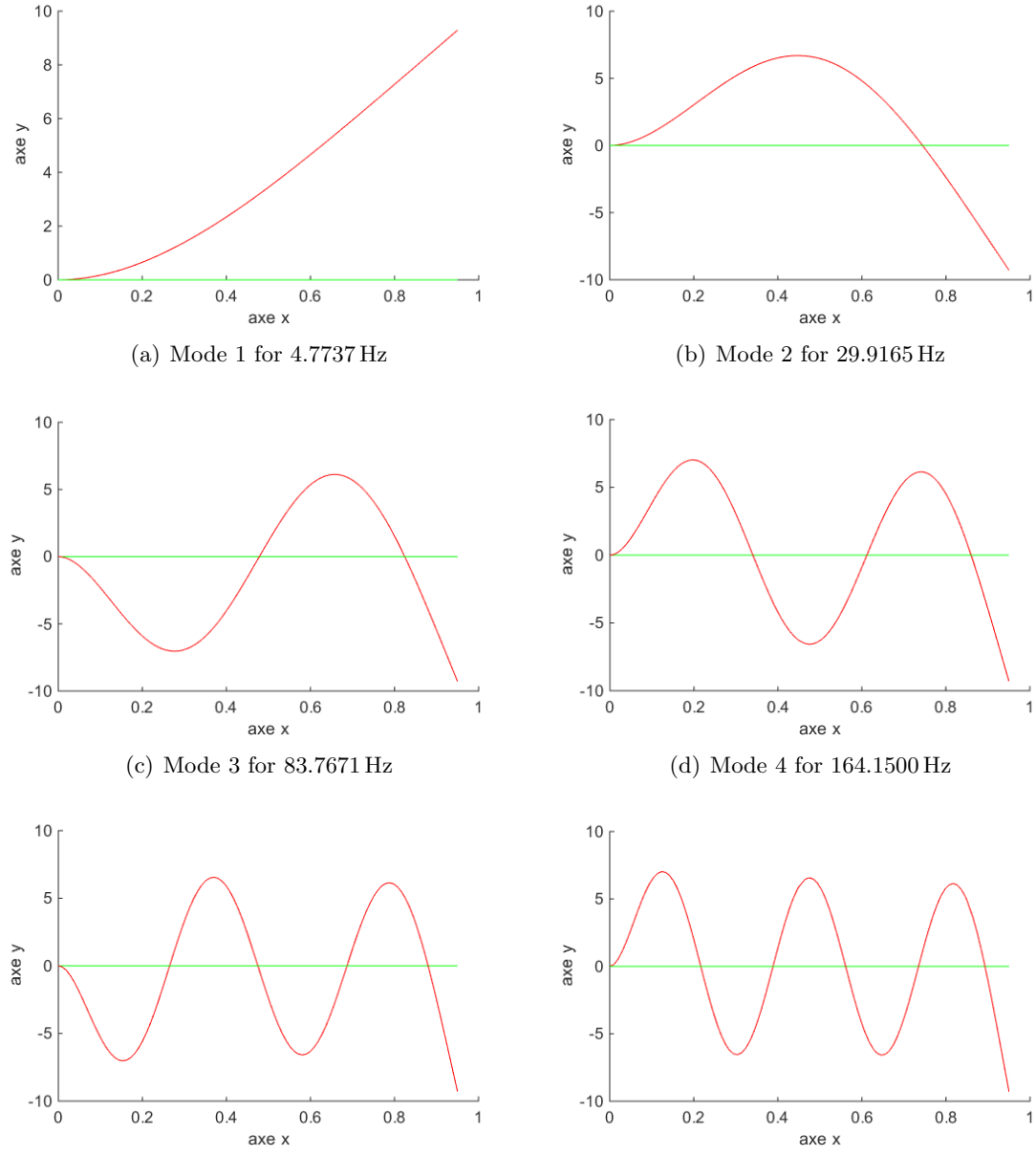

(a) Mode 1 for 4.7737 Hz

(b) Mode 2 for 29.9165 Hz

(c) Mode 3 for 83.7671 Hz

(d) Mode 4 for 164.1500 Hz

(e) Mode 5 for 271.3518 Hz

(f) Mode 6 for 405.3529 Hz

Figure 13.13 – Mode shapes of the beam model (healthy state)

13.3.3 Modal analysis and uncertainties

After downsampling and decimation of the data by factor 2, six well-estimated bending modes were obtained in the healthy and damaged states from the measurement data using subspace identification, together with their covariance. The identified eigenvalues are shown in Table 13.4 for each mode. Then the set of identified modes is split into three mode sets $\mathcal{M}_1$, $\mathcal{M}_2$

and $\mathcal{M}_3$ containing two modes each, respectively.

Table 13.4 – Eigenvalues λ_j of beam.

Mode j	Healthy state	Damaged state	Mode set
1	$-0.55 + 28.4\text{i}$	$-1.10 + 26.1\text{i}$	$\mathcal{M}_1$
2	$-0.42 + 178.9\text{i}$	$-0.46 + 178.3\text{i}$	
3	$-0.15 + 506.2\text{i}$	$-0.15 + 505.3\text{i}$	$\mathcal{M}_2$
4	$-1.32 + 984.5\text{i}$	$-13.54 + 975.5\text{i}$	
5	$-0.71 + 1630.9\text{i}$	$-0.48 + 1605.5\text{i}$	$\mathcal{M}_3$
6	$-2.35 + 2416.0\text{i}$	$-1.33 + 2387.5\text{i}$	

13.3.4 Damage localization results

The localization results are computed at all elements from the experimental datasets in both healthy and damaged states. The computation of the stress and its covariance for the statistical evaluation in (5.15) is carried out for three different mode sets, each with s-values in the vicinity of the respective mode sets. First, one s-value is chosen for each set with $s_1^1 = -1 + 190\text{i}$ for mode set $\mathcal{M}_1$, $s_2^1 = -1 + 500\text{i}$ for $\mathcal{M}_2$ and $s_3^1 = -1 + 1700\text{i}$ for $\mathcal{M}_3$. In a second step, an additional s-value is chosen for joint evaluation for each mode set as $s_1^2 = -1 + 200\text{i}$ for $\mathcal{M}_1$, $s_2^2 = -1 + 950\text{i}$ for $\mathcal{M}_2$ and $s_3^2 = -1 + 2500\text{i}$ for $\mathcal{M}_3$. To compare the ratios of the test statistics between the healthy and damaged elements, the computed values are normalized in the figures such that the smallest value is 1.

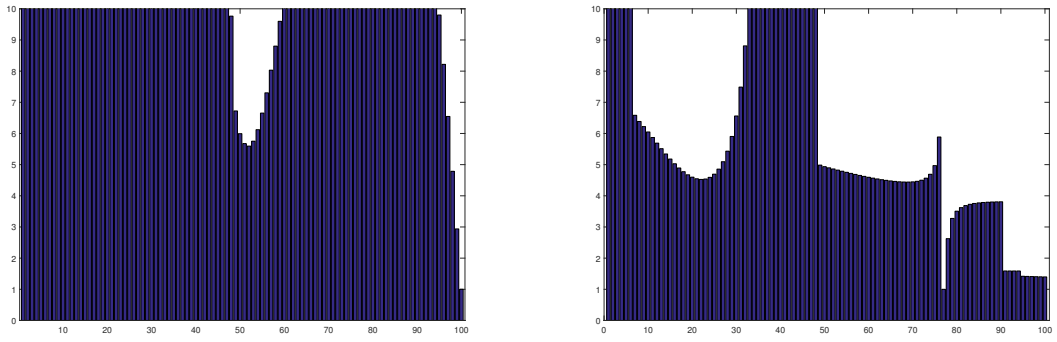

(a) Estimated stress S_t from data

(b) Test statistic s_t

Figure 13.14 – Localization results for all elements using single mode set $\mathcal{M}_1$ at $s_1^1 = -1 + 190\text{i}$ (experimental data).

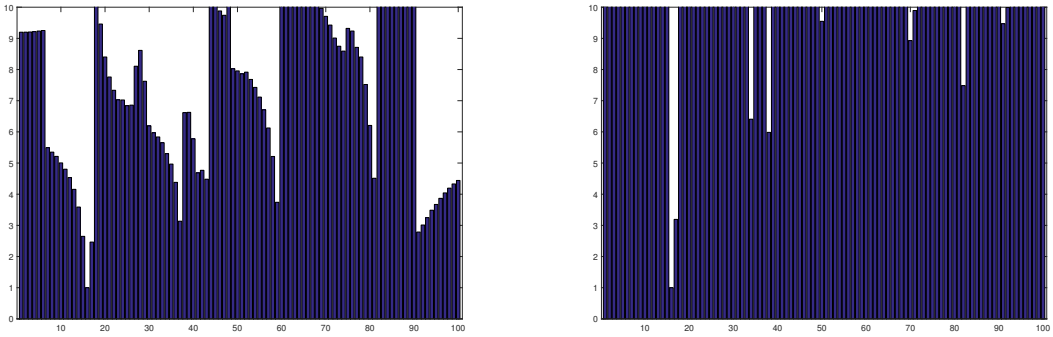

(a) 1 s-value (b) 2 s-values

Figure 13.15 – Test statistic s_t based on multiple mode sets $\mathcal{M}_1$, $\mathcal{M}_2$ and $\mathcal{M}_3$ (experimental data).

In Figures 13.14(a) and 13.14(b), the stress $S_t^1(s_1^1)$ is obtained for all 100 elements t for the single mode sets $\mathcal{M}_1$ and the respective test statistic is shown. It can be seen that neither the estimated stress nor its statistical evaluation can correctly indicate the damage at elements 16-17, which is possibly due to the modal truncation error. However, when using the joint statistical evaluation based on multiple mode sets, it is seen that damage can be localized correctly at elements 16-17 in Figures 13.15(a)-13.15(b). The use of one more s-value in Figure 13.15(b) increases the ratio to the undamaged elements compared to Figure 13.15(a), leading to a clearer localization. For the situation of multiple damages, a threshold link needs to be investigated in the future work to avoid false alarm.

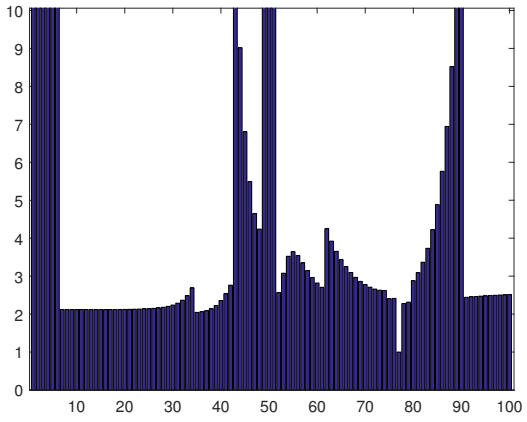

Figure 13.16 – Test statistic s_t using single mode set $\mathcal{M}_1$ at $s_1^1 = -1 + 190\mathrm{i}$ (simulated data).

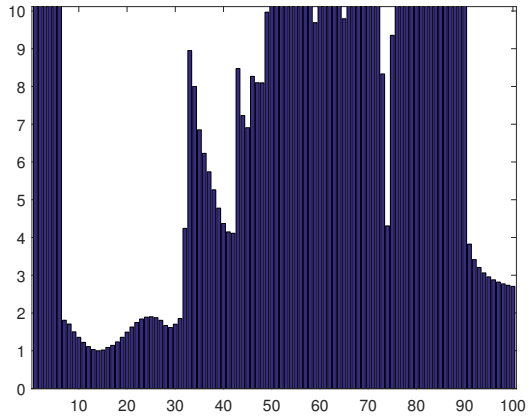

Figure 13.17 – Test statistic s_t based on multiple mode sets $\mathcal{M}_1$, $\mathcal{M}_2$ and $\mathcal{M}_3$, with 2 s-values each (simulated data).

13.3.5 Comparison to simulated data

Based on the above FE model, vibration data at the three sensor positions has been simulated from white noise excitation in both reference and damaged states, where the Young and shear modulus were reduced by 50% in elements 16 and 17 in the damaged case. White measurement noise with 5% magnitude of the simulated outputs was added. The simulated data is of length 10,000 at sampling frequency 1000 Hz after decimation, as in the previous section. From the data, the first six modes are identified and split into three mode sets as above.

The statistical evaluation using only the first mode set (as in Figure 13.14(b)) is shown in Figure 13.16, where the damage cannot be localized. Results using all mode sets with 2 s-values for each mode set (as in Figure 13.15(b)) are shown in Figure 13.17, where the lowest values of the test statistic are correctly found at the damaged elements.

13.4 Case study 3: 3D Yellow frame

In the application, both localization approaches and the quantification have been demonstrated on a four-story steel frame structure, the Yellow Frame, at the University of British Columbia, which was artificially damaged by removing of braces of the structure. The structure is described in detail in [ADVM17, All17]. The photo of the Yellow Frame structure and its schematic plan are shown in Figure 13.20. It is supposed to show a linear vibration behavior.

This structure is 3.6m high and is composed of 2 spans in each direction with the total length of 2.5m. Each floor of the structure is carrying dead loads applied to the structure by using 4 steel plates distributed on each level. The dimensions of the steel plates are 1.5×0.65m. The weight of the steel plates for the first three floors is 17.8kN per floor and for the fourth floor the weight is 13.34kN. The frame is constructed from hot rolled 300W steel members. The beams are $S75 \times 11$ sections and the columns are $B100 \times 9$ sections [ADVM17]. Four 50mm square steel tubes are used to provide in-plane stability to the diaphragm of each floor. For the lateral stability, four pairs of threaded steel rods (with diameter of 12mm) are used as braces on each side of the structure in each floor. These braces are all pretensioned by using a torque wrench. The torque moment is equal for all the braces in order to assure the same pretension force consistently throughout the structure.

In this application, the damage scenario is modeled by removing of braces at the south side of the structure on the first floor and compared to the the healthy state of the structure which is fully braced. This structure is instrumented by 15 sensors of which three are located on the base of the structure. Twelve sensors are located on the structure, three at the north, south and west side in each floor (Figure 13.20(b)). For damaged and undamaged states, acceleration data containing 219,900 and 550,000 samples, respectively, at a sampling frequency of 1000Hz were recorded.

(a) Photo of the Yellow Frame structure(south-east corner)

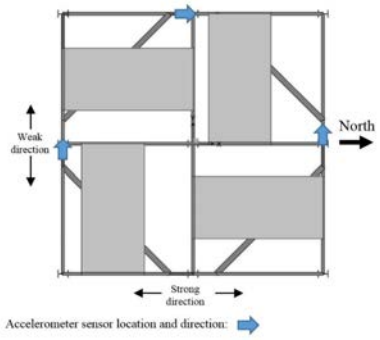

(b) Scaled plan of each level mass plates and location of sensors

Figure 13.18 – Yellow Frame structure.

13.4.1 Modal analysis and uncertainties

From the measurement data after downsampling and decimation of the data by factor 5, seven well-estimated modes were obtained in the healthy and damaged states using SSI, together with their uncertainties. The identified frequencies are shown in Table 13.5.

Table 13.5 – Identified frequencies (in Hz) of yellow frame.

Mode	healthy	damaged
1	8.1105	5.7870
2	8.7068	7.9668
3	15.5415	14.0054
4	21.4059	19.9419
5	23.7863	23.7015
6	31.1606	30.6360
7	46.4579	46.2184

13.4.2 Finite element model with Abaqus-Python

The finite element model of the Yellow frame is made by using Abaqus/CAE Student Edition 6.14-2 as depicted in Figure 13.19 (see details in Chapter 12). In this model, the properties of the sections of elements of the Yellow frame is used in modeling the beams, braces, and columns. The plates with mass are modeled as lumped mass in the four corners of each plate on the structure. Since these plates are bolted and connected with pretensioned rods to their

surrounding beams (in friction), their contribution to the stiffness of structure for ambient vibration is not negligible. Therefore these plates are also modeled as two parallel beams. The base of the structure is modeled as fixed connection to the ground. The connections of beams and columns are also modeled as fixed connection and the braces are connected as moment free hinge connections to the structure. Since each group of two braces on each floor at each span is only under axial force, they are modeled as one element with cross section area equal to the total area of both braces (see Figure 13.20). Localizing damage in one brace element indicates the possibility of damage in both of these parallel braces.

Since damage is located in the braces, we are only tested the braces element of the structure. Localizing damage in one brace element indicates the possibility of damage in both of these parallel braces.

Sensitivity of the modal parameters: In the transfer-matrix based residual, to obtain the required sensitivity matrix $\mathcal{J}_{R,\theta}$ (7.8), the derivative of the modal parameters with respect to the structural parameters is needed. Using Abaqus-Python Script in Section 12.5.2, first the FE model of the healthy structure is made and then, the sensitivities of the eigenstructure (frequencies and mode shapes) to the physical parameters (chosen in here as the stiffness of each brace) are calculated. For damage localization and quantification, the stress fields and their covariances are computed for the same or different choice of Laplace variables, s-values. Then, for each brace element, theses stress values are statistically aggregated in the χ^2_t-test. Note that highest value indicates the damaged elements in the sensitivity and minmax approaches.

L_{model} **of the structure:** For the damage localization with SDDLV approach, the L_{model} (2.2.3) of the structure are computed here with Abaqus-Python Script as depicted in Figure 12.1 and detailed in Section 12.5.1. First, the FE model of the healthy structure of Yellow Frame is made with Abaqus input file or GUI. Then the mass (M), stiffness (K) and damping (C) matrices of the model are obtained from Abaqus output database. In Matlab, G_{model} (2.23) is computed from M, C, and K matrices for a selected Laplace domain (s-value), and the displacement vectors $Z(s)$ (2.24) are computed at all DOFs after applying unit load to the model at each sensor coordinates.

In order to get the stress field, the displacement vectors are applied at the Boundary Condition (BC) of the model for each sensor position that yields stress field. The job is created for each sensor and submitted for analysis in Abaqus-Python. From Abaqus field-output requests, the output generated stress i.e. σ_{axial} at all elements are saved in a text file for each load vector. Note that L_{model} be the column of these stress resultants $S(s)_i$. In such a way, L_{model} of the structure is computed using Abaqus-Python script as illustrated in Figure 12.1. Finally, the load vector is applied to L_{model} to get the stress resultants, and for each brace element, theses stress values are statistically aggregated in the χ^2_t-test. Note that stress value close to zero indicates potentially damaged elements in the SDDLV approach.

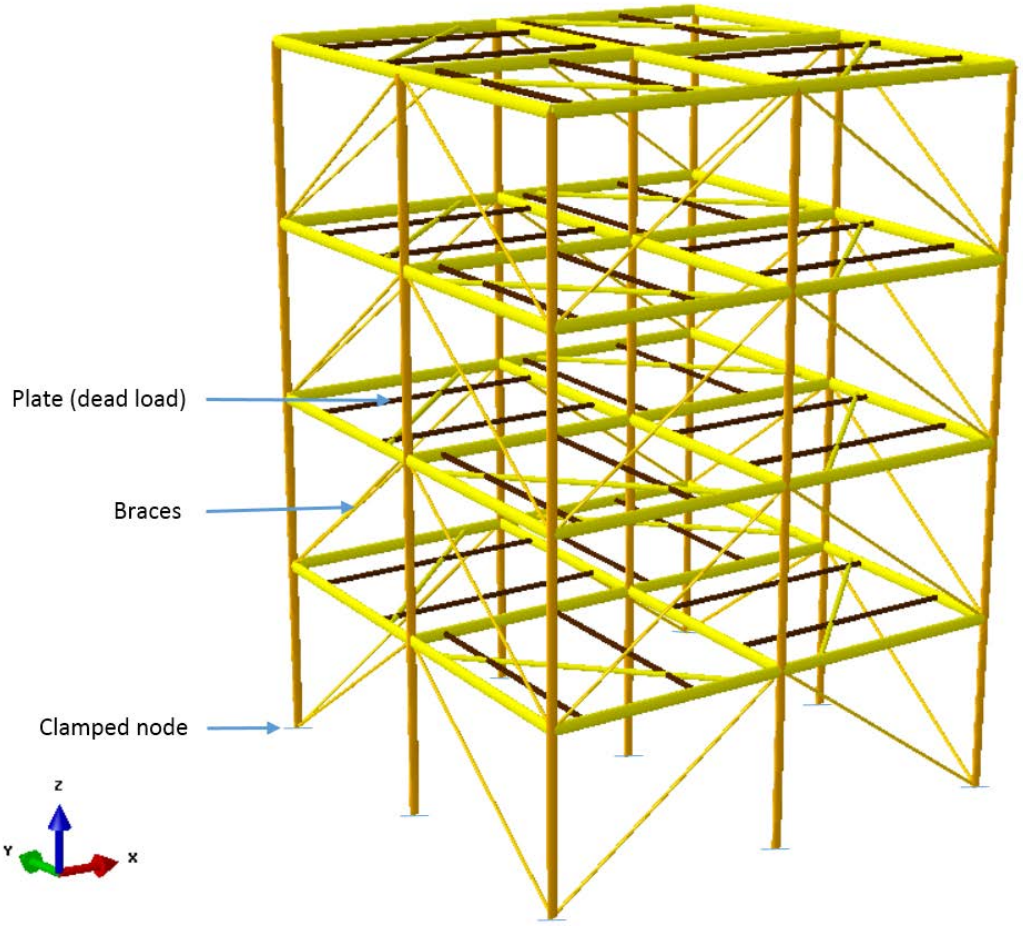

Figure 13.19 – Finite element model of the Yellow frame structure, x represents north

(a) Braces of the Yellow Frame structure (b) Braces of the Yellow frame FE model

Figure 13.20 – Braces for Yellow Frame structure.

13.4.3 SDDLV approach: localization

The localization results are computed at all brace elements from the experimental datasets in both damaged and healthy states. The computation of the stress and its uncertainties for the statistical evaluation in the χ_t^2-tests is carried out for two different sets of s-values, each in the vicinity of the respective identified poles. First, one s-value is chosen with $s_1 = -1 + 30\mathrm{i}$ and second, two s-values are chosen as $s_1 = -1 + 30\mathrm{i}$ and $s_2 = -1 + 76\mathrm{i}$ for joint evaluation. To compare the ratios of the stress values between the healthy and damaged elements, the computed values are normalized in the figures such that the smallest value of the 32 brace elements is 1.

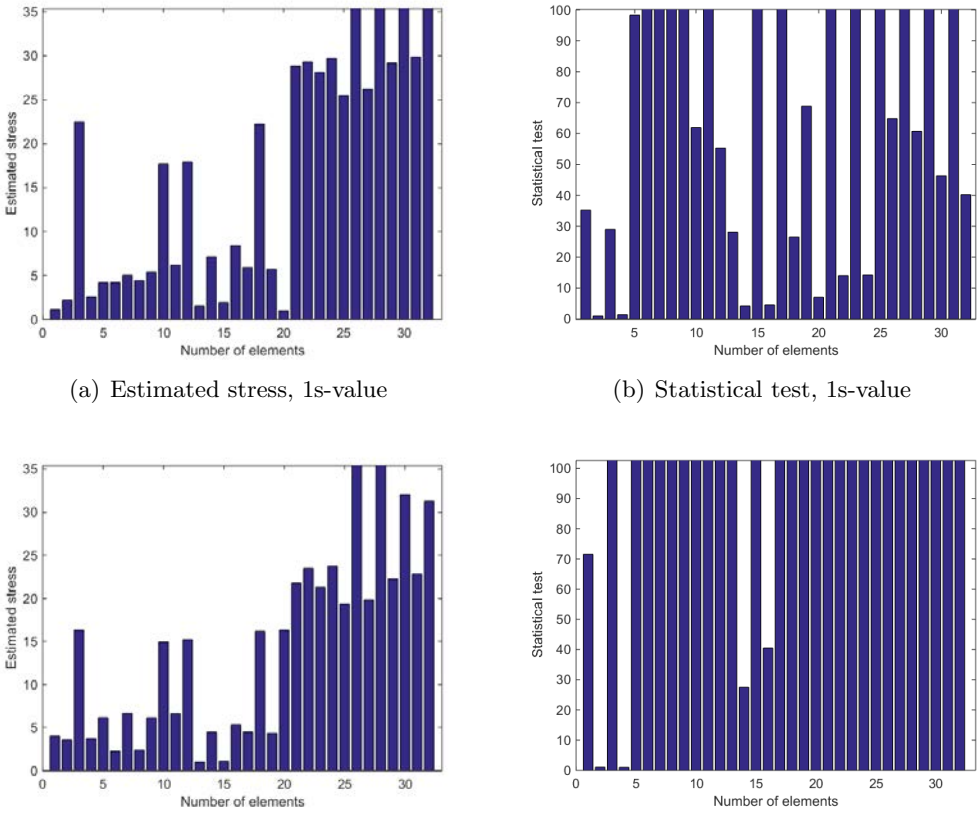

(a) Estimated stress, 1s-value

(b) Statistical test, 1s-value

(c) Estimated stress, 2s-value

(d) Statistical test, 2s-value

Figure 13.21 – Localization results for brace elements: stress computation and statistical evaluation at $1s$*-value* $(-1 + 30\mathrm{i})$ *and* $2s$*-values* $(-1 + 30\mathrm{i}, -1 + 76\mathrm{i})$ *- using 12 sensors, measurement noise, removing braces at 2 and 4.*

The estimated stress and its statistical evaluation is shown in Figures 13.21(a)-13.21(d) with considering 1s and 2s-values. It is seen that the estimated stress is unable to indicate the damage at elements 2 and 4 due to measurement noise and variance errors, while the statistical test indicates the damage elements at 2 and 4. However, by adding information through one more s-values in the same setting, the damaged elements can be correctly indicated in the joint evaluation of the statistical test in Figure 13.21(d).

13.4.4 Sensitivity-based approach: localization and quantification

The localization test statistics at all brace elements are computed using real dataset in both damaged and healthy states for one and three choices of s-values, where the damaged element is created by removing the braces at bar 2 and 4. Note that the highest value of the test indicates damage localization. The damage indicators are shown in Figures 13.22 for each tested element of the transfer-matrix based residuals. In all cases, it is seen that the test statistic at the damaged elements has the highest value, correctly localizing the damage at elements 2 and 4. Particularly in Figures 13.22(a) and 13.22(b) it can be seen that the sensitivity and minmax test reacts strongly at the undamaged elements using for 1s-value. By choosing 3s-values, in Figures 13.22(c) it can be seen that the sensitivity tests reacts still at the undamaged elements due to the violation of $\delta_b = 0$. There is also some light reaction in the undamaged elements in Figures 13.22(d) in the minmax tests. Notice that choosing three s-values, the performance is much better in Figures 13.22(c)-13.22(d).

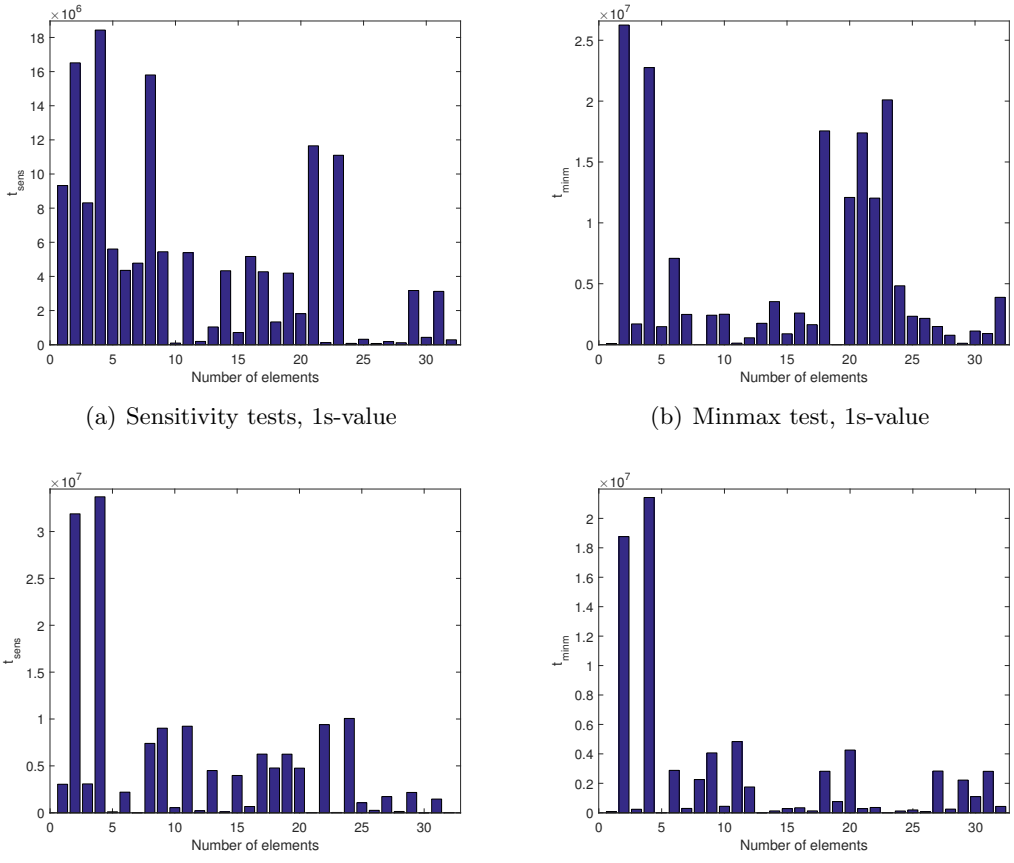

(a) Sensitivity tests, 1s-value

(b) Minmax test, 1s-value

(c) Sensitivity tests, 3s-value

(d) Minmax test, 3s-value

Figure 13.22 – Transfer matrix based localization: Sensitivity and minmax tests at at $1s$*-value* $(-1+76\mathrm{i})$ *and* $3s$*-values* $(-1+10\mathrm{i}, -1+250\mathrm{i}, -1+280\mathrm{i})$ *- using 12 sensors, measurement noise, removing braces at bar 2 and 4.*

For the quantification of the damage extent, the values of $\hat{\delta}^{sens}$ and $\hat{\delta}^{minm}$ were estimated with their standard deviation (σ) for the respective sensitivity and minmax approaches, and compared to the direct computation from $\hat{\delta} = J^{\dagger}\zeta$ as shown in Table 13.6. Since the braces are removed, the stiffness loss should be 100%. The minmax approach gets closer to this value than the sensitivity approach, as expected, however the overall quantification accuracy is not entirely satisfying, and the standard deviations on the estimates of the damage extent seem to be too low. Further work is needed to obtain more precise damage quantification estimates.

Table 13.6 – Quantification of damage extents (in '%')

Type	element 2	element 4	element 2	element 4
s-value	1s		3s	
$\hat{\delta}_{sens} \pm \sigma_{sens}$	48.16±0.79	48.65±0.78	70.92±0.79	70.00±0.79
$\hat{\delta}_{minm} \pm \sigma_{minm}$	86.01±0.02	94.18±0.02	77.12±0.02	102.22±0.02
$\hat{\delta}$	49.14	54.83	8.21	3.83

13.5 Discussion

In this chapter, the damage localization methods are demonstrated on different kinds of real case applications. First, the new approach using multiple mode sets has been applied on a damaged cantilever beam. From results, it is seen that the proposed method using multiple mode sets was able to correctly localize the damage in an experimental application on a damaged cantilever beam with a small number of sensors and using a coarse FE model. This leads to significant improvement of the localization results with the proposed method and less dependence on the particular choice of the s-values, which contributes to the applicability of the method in practice in SHM systems.

In the second real application, the method has been successfully applied to another vibration measurements of a damaged cantilever beam, where damage was also correctly localized with a small number of sensors, while the previous approach with a limited number of modes failed.

In the third real applications, two transfer matrix based localization methods have been compared and achieved similar success on a big real structure. The sensitivity based approach allows in addition the quantification of damage. The first quantification results are encouraging, however, further understanding and work is needed to obtain more precise damage quantification estimates.

Conclusions

This thesis presents vibration-based damage localization and quantification methods from output-only measurements for SHM systems. Particularly, a focus has been on improving the existing methods by considering the intrinsic uncertainty of the measurement data by covariance propagation in hypothesis tests, and using all possibly available information through multiple mode sets approach. Then, the applicability of methods was improved with fewer sensors and less dependence on the particular choice of the s-values when considering all available modes with the statistical multiple mode set strategy. In practice, the performance of these methods has been evaluated in various numerical and lab case studies, and further implementation was carried out for realistic applications with FE models in commercial software. A detailed explanation of each developed method was given in the respective contribution chapters. These developed methods can be summarized as follows:

In Chapter 5, the first theoretical contribution of this thesis is described, where the damage localization with the SDDLV approach has been extended considering multiple mode sets based on a joint statistical evaluation that takes into account the information from all identified modes of the structure. The stress computation using multiple mode sets increases the information content of the damaged or non-damaged elements of the structure, compared to evaluation from a limited number of modes due to a previous constraint of the approach on the number of modes. With the new approach using multiple mode sets, this constraint is lifted, which allows damage localization with fewer sensors at the same time. While the stress evaluation for each mode set is naturally subject to modal truncation errors that depend on the choice of the Laplace variable s, the joint statistical evaluation for several mode sets seems to mitigate these errors. Indeed, the simulation results in the numerical applications show that the effect of s-values with poor performance in single mode sets is mitigated when treating all available modes with the statistical multiple mode set strategy. This leads to significant improvement of the localization success rate with the proposed method and less dependence on the particular choice of the s-values, which contributes to the applicability of the method in practice in SHM systems. Finally, the proposed method using multiple approach has been applied in real applications to vibration measurements on two damaged cantilever beams. For both real applications, the proposed method was able to correctly localize the damage with a small number of sensors and using a coarse and fine FE model, respectively, while the previous approach with a limited number of modes failed.

In addition, the SDDLV approach has been applied on a 2D beam model with cracks. From results, it is seen that the overall performance of the method is not always satisfactory

due to the effect of large modal truncation and variance errors. However, the success rates of the damage localization in the statistical test are good compared to estimated stress. Furthermore, the success rates of the crack localization have increased, while the depth of the crack increases. It is observed that the performance of the damage localization was poor due to a small crack with compared to large crack and possibly, it happens due to the small transfer matrix difference between the healthy and damage states.

For further study, the damage localization with the SDDLV approach has been applied on a 2D beam model depending on mesh size. From results, it is seen that the performance of the method in the statistical tests is satisfactory for rough mesh in comparison to fine mesh model for large damaged area. While the success rates of the damage localization are not satisfactory at all for a small damage zone of fine mesh model due to the effect of large modal truncation and the small damage residuals in the transfer matrix differences between the healthy and damaged states. Furthermore, the results indicate that it is possible to determine zones where the probability of good localization (PGL) is larger for several sets of simulated measurement data.

In Chapter 6, the second contribution of this thesis is elaborated where the complementary ILDL approach has been extended with a statistical framework considering uncertainties. In previous works, this deterministic aggregation was only done for $s = 0$ where the uncertainty quantification was tempted. Here, the damage indicator of the ILDL is reconsidered to allow an uncertainty quantification, before deriving its statistical evaluation for damage localization for both rank 1 or arbitrary case. For rank 1, first the residual vectors with degenerate distribution, and then element-wise tests of the residual vectors are evaluated. For such an evaluation, the modal parameter covariance is propagated to the obtained damage indicators in a sensitivity-based approach. All computed values corresponding to an element are being tested for damage localization in a hypothesis test. This approach has been validated on a mass-spring chain system. From the results, it is seen that the performance of the method is satisfactory when considering modal truncation or all modes of the structure. Furthermore, parallels to the SDDLV approach have been laid out, and future investigation on the equivalence between both methods should be part of future research.

The last theoretical contribution of this thesis is described in Chapter 7, where the transfer matrix-based residual was presented in a statistical sensitivity-based output-only damage localization and quantification approach. The residual is obtained in the context of SDDLV that is based on the transfer matrix difference between the reference and damaged states. The related residual vector is statistically evaluated using the transfer matrix sensitivity with respect to structural parameters from a finite element model. Furthermore, a joint statistical evaluation of multiple mode sets approach for same or different Laplace variables has been considered for more robustness. The computation of the test values using multiple mode sets increases the information contents of the damaged or healthy elements of the structure. The proposed approach has been applied first on a mass-spring chain and then on a 2D beam model. In the applications, several experiments have been demonstrated in Monte-Carlo simulations to evaluate the success of the damage localization in dependence of the s-value, where each of the parameters corresponding to an element is tested for being non-zero in a Generalized Likelihood Ratio (GLR) test. Damage quantification corresponds to the estimates value of the changes parameter in the damaged elements. In both applications, it has been

seen that the proposed method using multiple mode sets has increased the performance of the damage localization and quantification of the damage extents compared to using a single mode set. Besides numerical applications, this approach has also been tested on a real Yellow Frame structure, where it was able to correctly localize the damage. The sensitivity-based approach allows in addition the quantification of damage. The first quantification results are encouraging, however, further understanding and work is needed to obtain more precise damage quantification estimates.

It can be concluded that several challenges were addressed in this thesis for improving the existing methods, and the proposed methods are better to locate and quantify damages under real test conditions. Therefore, the developments in this thesis contribute to the applicability of vibration-based damage localization and quantification in practice.

Recommendations for future works

In order to further improve the applicability on real structures, several recommendations were identified in this research. For future works, the following things can be considered:

- The SDDLV-based approach using multiple mode sets has been validated in both numerical simulations and on lab experiments where the results are shown promising. So, the next step should be tested on applications in the field such as real bridges and buildings.

- In this thesis, the statistical evaluation of the ILDL approach has been validated in a numerical application for rank 1 where the simulated results are promising compared to the SDDLV approach. Therefore, this approach should be investigated for arbitrary rank and real case applications in the future work.

- In the transfer-matrix sensitivity based approach for damage localization and quantification, the localization was promising, while it was not entirely satisfactory for the quantification of damage extents. Therefore, further understanding and work is needed to obtain more precise damage quantification estimates.

- In this work, no threshold was developed for the SDDLV method, ILDL or sensitivity-based methods which was not necessary for the validation of the methods and the derivation of them. The situation of multiple damages and the threshold link needs to be investigated in the future work.

- The methods in this thesis have been developed for damages that are described by stiffness reductions. They should be extended to localization and quantification of mass changes in the same framework.

- The effect of environmental nuisances like temperature changes in combination with methods needs to be investigated. These factors are important and need to be considered for real test conditions. Therefore, future works should include a detailed analysis of the performance of the localization method under these conditions in combination

with methods that remove the environmental variability on modal parameters, in order to further improve the applicability on structures in the field.

- For the practicability of this methods, the other factors such as the accuracy of FE model, optimal sensor placement, measurement length on both healthy and damaged states, and the accuracy of identification needs to be investigated carefully.

Appendix

A1: Script file for model database (mdb)

Let me walk through the code and point out to which part each line of the script belongs. Complete understanding of these lines will come with experience and exercise. However, to work in a Python environment, include these lines will import some of the Abaqus modulus used in this script file.

```
--------------------------------------------------------------------------
from part import *
from material import *
from section import *
from assembly import *
from step import *
from interaction import *
from load import *
from mesh import *
from optimization import *
from job import *
from sketch import *
from visualization import *
from connectorBehavior import *
--------------------------------------------------------------------------
```

With these following lines the sketch and part of the structure is created.

```
### Geometry of the Structure ###
mdb.models['Model-1'].ConstrainedSketch(name='__profile__', sheetSize=2.0)
mdb.models['Model-1'].sketches['__profile__'].Spot(point=(0.0, 0.0))
mdb.models['Model-1'].sketches['__profile__'].Spot(point=(1.0, 0.0))
mdb.models['Model-1'].sketches['__profile__'].Line(point1=(0.0, 0.0),
    point2=(1.0, 0.0))
mdb.models['Model-1'].sketches['__profile__'].HorizontalConstraint(
    addUndoState=False, entity=
    mdb.models['Model-1'].sketches['__profile__'].geometry[2])
```

```
mdb.models['Model-1'].Part(dimensionality=TWO_D_PLANAR, name='Part-1', type=
    DEFORMABLE_BODY)
mdb.models['Model-1'].parts['Part-1'].BaseWire(sketch=
    mdb.models['Model-1'].sketches['__profile__'])
del mdb.models['Model-1'].sketches['__profile__']
mdb.models['Model-1'].parts['Part-1'].Set(edges=
    mdb.models['Model-1'].parts['Part-1'].edges.getSequenceFromMask(('[#1 ]',
    ), ), name='Beams')
-------------------------------------------------------------------------
```

Material, profile of the section and section assignment are done with the following lines below.

```
### Material Properties  ###
mdb.models['Model-1'].Material(name='Material-1')
mdb.models['Model-1'].materials['Material-1'].Density(table=((7800.0, ), ))
mdb.models['Model-1'].materials['Material-1'].Elastic(table=((206000000000.0,
    0.3), ))
mdb.models['Model-1'].CircularProfile(name='Profile-1', r=0.015)
mdb.models['Model-1'].BeamSection(consistentMassMatrix=False, integration=
    DURING_ANALYSIS, material='Material-1', name='Section-1', poissonRatio=
    0.0, profile='Profile-1', temperatureVar=LINEAR)
mdb.models['Model-1'].parts['Part-1'].SectionAssignment(offset=0.0,
    offsetField='', offsetType=MIDDLE_SURFACE, region=
    mdb.models['Model-1'].parts['Part-1'].sets['Beams'], sectionName=
    'Section-1', thicknessAssignment=FROM_SECTION)
-------------------------------------------------------------------------
```

The assembly process is given below. Note that the word root Assembly is used and you don't have to give a name of the assembly. This is of course due to the fact that there is only one assembly.

```
mdb.models['Model-1'].rootAssembly.DatumCsysByDefault(CARTESIAN)
mdb.models['Model-1'].rootAssembly.Instance(dependent=ON, name='Part-1-1',
    part=mdb.models['Model-1'].parts['Part-1'])
-------------------------------------------------------------------------
```

These following lines will create Step, mesh control, element type and mesh.

```
### Step, mesh control, element type ###
mdb.models['Model-1'].StaticStep(name='Step-1', previous='Initial')
mdb.models['Model-1'].parts['Part-1'].seedEdgeByNumber(constraint=FINER,
edges=mdb.models['Model-1'].parts['Part-1'].edges.getSequenceFromMask
(('[#1 ]', ), ), number=5)
```

```
mdb.models['Model-1'].parts['Part-1'].setElementType(elemTypes=(ElemType
(elemCode=B23, elemLibrary=STANDARD), ), regions=(mdb.models['Model-1'].
parts['Part-1'].edges.getSequenceFromMask(('[#1 ]', ), ), ))
mdb.models['Model-1'].parts['Part-1'].generateMesh()
```

The set and getSequenceFromMask are created with the following lines. The getSequence-FromMask is a numbering system used in Abaqus. Then orientation of the Beam section and field Output Requests are also generated here.

```
mdb.models['Model-1'].parts['Part-1'].Set(name='NodeFixed', nodes=
    mdb.models['Model-1'].parts['Part-1'].nodes.getSequenceFromMask(mask=
    ( '[#1 ]', ), ))
mdb.models['Model-1'].parts['Part-1'].Set(name='Node2', nodes=
    mdb.models['Model-1'].parts['Part-1'].nodes.getSequenceFromMask(mask=
    ( '[#2 ]', ), ))
mdb.models['Model-1'].parts['Part-1'].Set(name='Node3', nodes=
    mdb.models['Model-1'].parts['Part-1'].nodes.getSequenceFromMask(mask=
    ( '[#4 ]', ), ))
mdb.models['Model-1'].parts['Part-1'].Set(name='Node4', nodes=
    mdb.models['Model-1'].parts['Part-1'].nodes.getSequenceFromMask(mask=
    ( '[#8 ]', ), ))
mdb.models['Model-1'].parts['Part-1'].Set(name='Node5', nodes=
    mdb.models['Model-1'].parts['Part-1'].nodes.getSequenceFromMask(mask=
    ( '[#10 ]', ), ))
mdb.models['Model-1'].parts['Part-1'].Set(name='Node6', nodes=
    mdb.models['Model-1'].parts['Part-1'].nodes.getSequenceFromMask(mask=
    ( '[#20 ]', ), ))
mdb.models['Model-1'].rootAssembly.regenerate()

mdb.models['Model-1'].parts['Part-1'].assignBeamSectionOrientation(method=
    N1_COSINES, n1=(0.0, 0.0, -1.0), region=
    mdb.models['Model-1'].parts['Part-1'].sets['Beams'])
del mdb.models['Model-1'].historyOutputRequests['H-Output-1']
mdb.models['Model-1'].fieldOutputRequests['F-Output-1'].setValues(variables=
('S', 'U', 'SF'))
```

A2: Script file for output database (odb)

In this section, job is created and submitted for analysis using Output Data base model(.odb)

```
# Get ABAQUS interface
from abaqus import *
```

```
from abaqusConstants import *
#from sys import path
#path='...'
#open(path)
--------------------------------------------------------------------------
```

In this section, the following displacement vectors Z(s) are computed after applying a unit load to the model at sensor coordinates. Here, each row of the Z indicates the displacement at all DOFs that are computed from the unit load at the sensor coordinate for a Laplace domain(s=0). Finally, the displacement vectors are applied at the Boundary Condition (BC) of the model within a *for loop*. Then the job is created for each loop and submitted for analysis. From field output requests, the output generated stress (Section Force (SF) and Section Moment(SM)) at all DOFs are saved as a text file for each sensor coordinate and L_{model} be the column of these stress resultants $S(s)_i$. In such a way, we can generate L_{model} of the structure using Abaqus-Python script.

```
sortie = open('stress_IntegrationPoint.txt', 'w')
sortie1 = open('stress_Centroidal.txt', 'w')
SF_SM=[]
sensors_braces = [[.1,0,0],[.3,0,0],[.5,0,0],[.7,0,0],[.9,0,0]]
number_elements = [[1],[2],[3],[4],[5]]
StressResultant_SF = [[0.12345 for x in range(len(sensors_braces))]
                                  for y in range(3*len(number_elements))]
StressResultant_SM = [[0.12345 for x in range(len(sensors_braces))]
                                   for y in range(3*len(number_elements))]

## \texit{For loop}:
k=0
ans=[]
for j in range(len(A1)):
    f=Z[j]
    mdb.models['Model-1'].DisplacementBC(amplitude=UNSET, createStepName=
    'Step-1', distributionType=UNIFORM, fieldName='', fixed=OFF, localCsys=
    None, name='BC-1', region=mdb.models['Model-1'].rootAssembly.instances
    ['Part-1-1'].sets['Node1'], u1=f[0], u2=f[1], ur3=f[2])

    mdb.models['Model-1'].DisplacementBC(amplitude=UNSET, createStepName=
    'Step-1', distributionType=UNIFORM, fieldName='', fixed=OFF, localCsys=
    None, name='BC-2', region= mdb.models['Model-1'].rootAssembly.instances
    ['Part-1-1'].sets['Node2'], u1=f[3], u2=f[4], ur3=f[5])
    mdb.models['Model-1'].DisplacementBC(amplitude=UNSET, createStepName=
    'Step-1', distributionType=UNIFORM, fieldName='', fixed=OFF, localCsys=
    None, name='BC-3', region=mdb.models['Model-1'].rootAssembly.instances
    ['Part-1-1'].sets['Node3'], u1=f[6], u2=f[7], ur3=f[8])
    mdb.models['Model-1'].DisplacementBC(amplitude=UNSET, createStepName=
```

```
    'Step-1', distributionType=UNIFORM, fieldName='', fixed=OFF, localCsys=
    None, name='BC-4', region=mdb.models['Model-1'].rootAssembly.instances
    ['Part-1-1'].sets['Node4'], u1=f[9], u2=f[10], ur3=f[11])
    mdb.models['Model-1'].DisplacementBC(amplitude=UNSET, createStepName=
    'Step-1', distributionType=UNIFORM, fieldName='', fixed=OFF, localCsys=
    None,name='BC-5', region=mdb.models['Model-1'].rootAssembly.instances
    ['Part-1-1'].sets['Node5'], u1=f[12], u2=f[13], ur3=f[14])
    mdb.models['Model-1'].DisplacementBC(amplitude=UNSET, createStepName=
    'Step-1', distributionType=UNIFORM, fieldName='', fixed=OFF, localCsys=
    None, name='BC-6', region=mdb.models['Model-1'].rootAssembly.instances
    ['Part-1-1'].sets['Node6'], u1=f[15], u2=f[16], ur3=f[17])

    mdb.Job(atTime=None, contactPrint=OFF, description='', echoPrint=OFF,
    explicitPrecision=SINGLE, getMemoryFromAnalysis=True, historyPrint=OFF,
    memory=90, memoryUnits=PERCENTAGE, model='Model-1', modelPrint=OFF,
    name='Job-1', nodalOutputPrecision=SINGLE, queue=None, resultsFormat=
    ODB, scratch='', type=ANALYSIS, userSubroutine='', waitHours=0,
    waitMinutes=0)
## Job Submit
    mdb.jobs['Job-1'].submit(consistencyChecking=OFF)
    mdb.jobs['Job-1'].waitForCompletion()
## Save Output as text file (stress.txt)
    stress=session.openOdb(r'Job-1.odb').steps['Step-1'].frames[1].
    fieldOutputs['SF']
    stress1=session.openOdb(r'Job-1.odb').steps['Step-1'].frames[1].
    fieldOutputs['SM']
    for SF, SM in zip(stress.values, stress1.values):
        sortie.write('%.10e\t\t %.10e\t\t' % (SF.data[0], SM.data[0]))

    for jj in range(0,len(stress.values)):
         StressResultant_SF[jj][k] = (stress.values[jj].data[0])
    for kk in range(0,len(stress1.values)):
         StressResultant_SM[kk][k] = (stress1.values[kk].data[0])
k += 1
mdb.models['Model-1'].rootAssembly.regenerate()

## save output results in the text file
file_output = open("StressResultant_SF.txt",'w')
for jjk in StressResultant_SF:
file_output.write("%s\n" % jjk)
file_output.close()

file_output = open("StressResultant_SM.txt",'w')
for jjkk in StressResultant_SM:
```

```
file_output.write("%s\n" % jjkk)
file_output.close()

sortie.close()
sortie1.close()
--------------------------------------------------------------------------------
```

Résumé en Français

Introduction

Contexte de la thèse

La surveillance de santé structurelle (SHM) a bénéficié d'une attention croissante dans l'ingénierie et les communautés scientifiques, car une défaillance structurelle imprévisible peut produire une perte catastrophique, économique et humaine. Il existe deux types d'évaluation, par tests destructifs et non destructifs. Plus de chercheurs se sont concentrés sur cette dernière approche en raison de l'utilité continue de rester opérationnel pour la structure, Il est donc essentiel de maintenir la sécurité et l'intégrité des structures.

Une technique prometteuse est la surveillance de santé structurelle (SHM) à base de mesures de vibrations, où les structures sont équipées, par exemple avec des capteurs d'accélération qui peuvent enregistrer en permanence des données de vibrations structurelles en présence d'excitation ambiante, puis les paramètres modaux (c'est-à-dire les fréquences naturelles, les formes de mode et les amortissement) peuvent être estimés par exemple en utilisant des méthodes de la théorie stochastique de la réalisation du système pour les systèmes linéaires. Ces paramètres sont significatifs pour la surveillance de la structure. Grâce à ces progrès dans les systèmes de détection. Il existe deux approches pour l'évaluation que l'on caractérise pleinement la structure avec l'identification du système, puis la comparaison des résultats de l'identification du système et une autre est basée sur des techniques d'évaluation des dégâts. Habituellement, le diagnostic structurel basé sur les vibrations est divisé en cinq sous-tâches de difficulté croissante: détection des dommages (niveau 1), localisation des dégâts (niveau 2), identification du type de dégâts (niveau 3), quantification de l'étendue des dégats (niveau 4) et prédiction de la durée de vie restante (niveau 5). Lors de l'exécution de ces tâches en cascade, le problème de diagnostic structurel complet est susceptible d'être résolu. Les méthodes de détection des dommages ont atteint une maturité, par exemple avec des algorithmes basés données, adaptés de la classification et du contrôle statistique des processus. Bien que la détection des dommages puisse fonctionner uniquement sur les données, en comparant l'ensemble de données actuel avec une référence, la localisation des dommages nécessite un lien entre les données et les propriétés physiques de la structure, ce qui est souvent donné par un modèle d'éléments finis (FE) structure. La quantification des dommages correspond à l'estimation des changements des paramètres physiques dans les éléments défectueux. Parmi les techniques prometteuses, le vecteur stochastique Dynamic

Damage Locating Vector (SDDLV) et Influence Lines Damage Location (ILDL) possède des capacités intéressantes puisqu'elles sont théoriquement des méthods robustes pour combiner à la fois les informations d'éléments finis et les paramètres modaux estimés à partir des données de sortie. Cela motive l'adaptation des méthodes existantes de localisation des dégâts dans cette thèse, puis l'évaluation pour la quantification des dommages dans une approche basée sensibilité.

Le but de cette thèse est de développer des méthodes de localisation et de quantification des dégâts à partir des mesures de sortie uniquement pour l'évaluation des dégâts pour les systèmes SHM en pratique.

Méthodes proposées

Les méthodes suivantes sont développées dans la contribution de cette thèse:

(1) **Localisation statistique de dégâts avec des vecteurs de charge stochastiques utilisant plusieurs jeux de modes:** La méthode de vecteur stochastique Dynamic Damage Location (SDDLV) à été étendue avec une approche statistique présont pour plusieurs ensembles de modes, surmontant la restriction sur le nombre de modes dans les travaux précédents [MDBM15]. En outre, la performance de la méthode peut varier considérablement en fonction de la variable Laplace où la fonction de transfert est évaluée. Une attention particulière est accordée à ce choix et à l'optimiser. Par conséquent, la robustesse de la localisation des dommages est obtenue en tenant compte de toutes les informations disponibles dans l'èvaluation statistique conjointe.

(2) **Prise de décision statistique pour la localisation des dégâts avec des lignes d'influence:** La méthode Influence Line Damage Location (ILDL) est complémentaire à l'approche SDDLV. Cette approche a été développée dans [Ber14] comme une approche déterministe. L'objectif est de l'étendre comme une méthode stochastique et d'étudier sa relation avec SDDLV. Par conséquent, l'approche ILDL est étendue avec un cadre statistique.

(3) **Détermination de la densité de la matrice de transfert, basée sur la sensibilité, localisation et quantification des dommages statistiques:** Alors que SDDLV et ILDL exploitent directement les propriétés de l'espace null ou de l'image de la matrice de transfert, une approche basée sur la sensibilité [DMZ16] est développée dans ce chapitre, ce qui permet en outre la quantification des dégats. On considère une approche qui fonctionne sur la différence de matrices de transfert qui est statistiquement évaluée en utilisant la sensibilité de matrice de transfert par rapport aux paramètres d'un modèle FE.

Ces approches sont dérivées en profondeur, et les propriétés théoriques sont prouvées dans les chapitres de contribution. Ils sont validés sur des données de vibration structurelle dans des applications numériques et réelles.

Chapitre 1 – L'état de l'art

Les techniques de surveillance de la santé structurale basées sur les vibrations ont été activement développées au cours des dernières décennies [FDN01, CF04, FQ11], par exemple pour la surveillance des ponts, des bêtiments ou des structures offshore. Les méthodes actuellement disponibles ne couvrent qu'une petite partie du diagnostic structurel basé sur la surveillance, qui peut être divisé en cinq sous-tâches de difficulté croissante [FW07]:

- Niveau 1: Détection des dégâts
- Niveau 2: Localisation des dégâts
- Niveau 3: Identification du type de dommage
- Niveau 4: Quantification de l'étendue des dégâts
- Niveau 5: Prévision de la durée de vie restante.

Cependant, seules les méthodes pour le niveau 1 ont atteint la maturité pour des applications réelles jusqu'à présent, par exemple avec des algorithmes basés sur les données, adaptés des champs de classification et du contrôle statistique des processus. Les niveaux 2 à 5 du diagnostic structurel sont beaucoup plus difficiles à réaliser.

Bernal [Ber10] présente une technique de localisation des dégats en utilisant à la fois des informations d'éléments finis et des paramètres modaux, à savoir l'approche Stochastic Dynamic Damage Location Vector (SDDLV). Cette approche a évolué au cours des années des systèmes déterministes d'entrée / sortie aux systèmes stochastiques uniquement de sortie [Ber02, Ber06, Ber07, Ber10]. Dans [DMBM13], l'approche SDDLV déterministe a été étendue avec un cadre statistique pour décider si un élément est endommagé, en tenant compte des incertitudes dans les données de mesure. Une robustesse supplémentaire a été obtenue grâce à une agrégation statistique des résultats pour différents paramètres de la méthode [MDBM15]. Une approche complémentaire du SDDLV est la Influence Lines Damage Localization (ILDL) [Ber14], où l'emplacement du dommage est déterminé à partir de l'angle de sous-espace de chaque position de la structure en calculant l'espace colonne du changement de flexibilité et d'un Modèle FE connu.

Cette approche nécessite une identification modale dans les états sains et endommagés.Cette thèse est axée sur les travaux de Bernal [Ber10, Ber14], décrits ci-dessus, comme base pour le développement de la localisation des dommages, et à partir du l'évaluation statistique développés dans la thèse de doctorat de Luciano Marin [Mar13].

Chapitre 2, 3, et 4 – Théorie de fond

Plusieurs méthodes de localisation des dégâts ont été décrites dans l'état de l'art à partir de la littérature [Ber02, Ber10, Ber14]. Appartenant à cette dernière catégorie, l'approche Stochastic Dynamic Damage Locating Vector (SDDLV) [Ber10] et Influence Line Damage Localization (ILDL) [Ber14] est une technique de localisation des dégâts basée sur les vibrations en utilisant à la fois des informations d'éléments finis et des paramètres modaux estimés

à partir des données de sortie. À partir des estimations des matrices du système dans les états de référence et endommagés, l'espace nul de la différence entre les matrices de transfert respectives est obtenu. Ensuite, dans le SDDLV, les dommages sont liés à un résidu dérivé de cet espace nul et situés où le résidu est proche de zéro. Une approche complémentaire du SDDLV est la Influence Lines Damage Localization (ILDL) [Ber14]. Ensuite, une approche basée sur la sensibilité a été décrite pour la localisation et la quantification des dommages qui fonctionnent sur un vecteur résiduel basé sur les données qui est statistiquement évalué à l'aide d'informations à partir d'un modèle d'éléments finis (FE) [DMZ16].

Supposons que le comportement d'une structure mécanique peut être décrit par un système dynamique linéaire (LTI)

$$M\ddot{\mathcal{X}}(t) + C\dot{\mathcal{X}}(t) + K\mathcal{X}(t) = f(t)$$

où M, C, $K \in \mathbb{R}^{d\times d}$ sont les matrices de masse, d'amortissement et de rigidité, respectivement. La force externe $f(t)$ n'est pas mesurable et modélisée comme un bruit blanc. Puisque $f(t)$ n'est pas mesuré, il peut être remplacè par une force fictive $e(t) \in \mathbb{R}^r$ n'agissant que sur les coordonnées mesurées et qui régénère la sortie mesurée. Cela conduit au modèle d'espace d'état en temps continu correspondant.

$$\begin{cases} \dot{x}(t) = A_c x(t) + B_c e(t) \\ y(t) = C_c x(t) + D_c e(t) \end{cases}$$

avec vecteur d'état $x \in \mathbb{R}^n$, vecteur de sortie $y \in \mathbb{R}^r$, la matrice de transition d'état $A_c \in \mathbb{R}^{n\times n}$ et matrice de sortie $C_c \in \mathbb{R}^{r\times n}$, où $n = 2d$ est l'ordre du système et r est le nombre de sorties. À partir de l'identification sous-espace stochastique (SSI) [VODM96, PDR99, DM12], $\widehat{A}_c$ et $\widehat{C}_c$ peuvent être obtenu à partir des mesures de sortie seulement.

Chapitre 5 –Localisation des dégâts statistiques avec des vecteurs de charge stochastiques utilisant des jeux de modes multiples

Ce chapitre présente la localisation des dommages statistiques avec le vecteur de charge stochastique en utilisant des jeux de mode multiples basés sur l'approche SDDLV du chapitre 2, qui est une technique de localisation des dommages basée sur les vibrations en utilisant à la fois des informations d'éléments finis et des paramètres modaux estimés à partir des données de sortie. Les estimations des paramètres modaux sont sujettes à des erreurs de variance. Sur la base de cette information sur l'incertitude, une extension statistique de la méthode SDDLV a été développée dans [DMBM13, MDBM15] pour décider si un élément est endommagé en utilisant une ou plusieurs valeurs s.

Dans [DMBM13, MDBM15], le nombre de modes utilisés dans le calcul ne peut pas être supérieur au nombre de capteurs situés sur la structure. Il s'agit d'une restriction lorsqu'il existe plus de modes décrivant la structure que des capteurs disponibles. Ici, la méthode SDDLV est développée avec une évaluation statistique conjointe utilisant des ensembles de mode multiples. Elle surmonte cette limitation. Il est démontré que le calcul du stress pour les

ensembles de mode multiples augmente le contenu de l'information sur les éléments endommagés ou non endommagés de la structure. Enfin, toutes les valeurs de stress correspondant à chaque élément sont testées pour détecter les dommages dans un test d'hypothèses où les contraintes calculées sont évaluées avec leur covariance jointe. Pour dériver un tel test, le calcul de la covariance du stress résultant est nécessaire. Après le chapitre 3 [DM13], le schéma de covariance nécessaire est développé et étendu pour une évaluation statistique conjointe en utilisant plusieurs ensembles de modes pour les mêmes variables ou différentes variables de Laplace.

Chapitre 6 –Prise de décision statistique pour la localisation des dégâts avec des lignes d'influence

Ce chapitre présente l'évaluation statistique avec une approche pour la localisation des dommages par les lignes d'influence (ILDL) qui est complémentaire de l'approche SDDLV. Dans l'approche ILDL, l'image de la matrice de flexibilité entre les états de référence et endommagés d'une structure est une base pour la ligne d'influence (IL) des résultats de contraintes dans les emplacements endommagés. Le dommage est donc situé aux éléments où l'angle de sous-espace entre l'image de la matrice de flexibilité et la ligne d'influence du modèle FE de la structure est nul ou petit en pratique [Ber14].

Une évaluation statistique de l'angle de sous-espace est nécessaire pour prendre une décision concernant les éléments endommagés ou en bonne santé. Pour une telle évaluation, la covariance des paramètres modaux est propagée aux angles sous-espace obtenus dans une approche basée sur la sensibilité. Ensuite, toutes les valeurs calculées correspondant à un élément sont testées pour détecter les dommages dans un test d'hypothèses où les angles de sous-espace calculés sont évalués avec leur covariance individuelle. Dans les travaux précédents [MDBM13], l'approche ILDL a été étendue dans une approche statistique pour $s = 0$, où la quantification de l'incertitude a été tentée sur l'indicateur de dommage, l'angle de sous-espace. Ici, l'indicateur de dommage de l'ILDL est considéré pour un s arbitraire puis reconsidéré pour permettre une quantification adéquate de l'incertitude et une évaluation statistique pour la localisation des dégâts. De cette manière, l'approche ILDL est étendue avec un cadre statistique.

Chapitre 7 –Transfert de la localisation et de la quantification des dégâts statistiques basés sur la matrice de transfert

On considère une approche qui fonctionne sur un vecteur résiduel basé sur les données qui est statistiquement évalué en utilisant des informations à partir d'un modèle FE [DMZ16]. Les problèmes de localisation et de quantification des dégats sont divisés en deux problèmes distincts. Tout d'abord, les éléments endommagés sont détectés dans les tests statistiques, puis les dommages ne sont quantifiés que pour les éléments endommagés. Dans ce contexte, un nouveau vecteur résiduel a été proposé qui est basé sur la différence de matrice de transfert entre états sains et endommagés, comme dans l'approche SDDLV [Ber10, DMBM13, MDBM15].

Les tests statistiques pour l'isolement des fautes et l'estimation pour la quantification des défauts sont ensuite utilisés pour effectuer la localisation et la quantification des dégâts dans les approches soi-disant sensibilité et minmax.

Chapitre 8 –Méthodologie pour les applications numériques

Ce chapitre présente les indicateurs de performance pour les méthodes développées et les modéles numériques utilisés pour les chapitres d'application 9, 10 et 11 sont décrit.

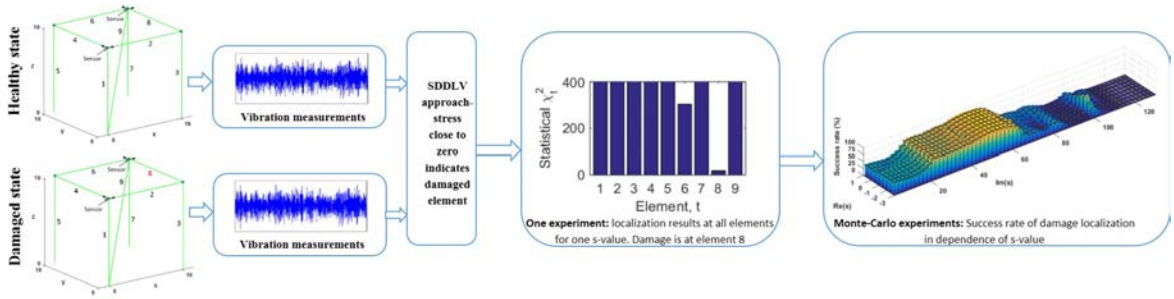

Figure 1 – Évaluation de la performance (ou taux de réussite) de la localisation des dommages en fonction de la valeur de s (x et y-axes) avec $\mathrm{Re}(s)$, $\mathrm{Im}(s)$.

Pour plus de simplicité, un exemple est illustré dans la Figure 1 pour chaque élément de la structure, où l'évaluation de la performance de la méthode proposée est illustrée. Tout seule, l'évaluation statistique avec le test χ_t^2 est obtenue à une seule valeur s en utilisant une expérience à partir des paramétres modaux estimés dans les états sains et endommagés. Rappelons que la localisation des dommages est déduite par la valeur de contrainte la plus proche de zéro. Dans l'évaluation statistique, la localisation des dommages se trouve correctement aux plus petites valeurs de χ_t^2 à l'élément de dommage. Deuxièmement, le taux de réussite de la localisation correcte des dommages est évalué pour les expériences de Monte-Carlo. Le taux de réussite (z -axis) dépend des valeurs s choisies (x et y -axes) et sert d'indicateur de performance de la méthode.

Chapitre 9 –SDDLV avec des jeux de mode unique et multiple

Dans ce chapitre, l'algorithme de localisation des dommages du chapitre 5 est appliqué sur une chaîne de masse-ressort et le modèle de cube 3D dans la Figure 2 et 6 qui permettent des simulations de Monte-Carlo pour la validation de la méthode. Figure 6 les résultat des résultats de localisation des dommages en utilisant des ensembles de mode multiples sont comparé à ceux utilisant uniquement un seul des ensembles de mode séparément.

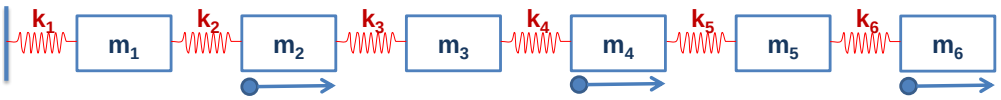

Figure 2 – Chaîne de masse-ressort (avec amortissement modal) - utilisation de trois capteurs aux éléments 2, 4 et 6.

Pour la chaîne de masse-ressort, 6 modes peuvent ètre identifiés à partir du modèle de la structure en utilisant SSI (see Table 8.2), puis divisé en deux ensembles de modes $\mathcal{M}_1$ et $\mathcal{M}_2$ de trois modes chacun pour la méthode proposée en utilisant plusieurs jeux de modes. Les résultats de la localisation des dommages à tous les éléments de la chaîne de masse-ressort sont montrés dans la Figure 3 pour l'ensemble modes unique $\mathcal{M}_1$ en utilisant une valeur s, $s = -2+51\mathrm{i}$. Rappelons que les valeurs de contraintes proches de zéro indiquent des éléments potentiellement endommagés. On peut voir que χ_t^2 dans la Figure 3(c) montre des résultats similaires à ceux du résultat théorique dans la Figure 3(a), alors que la localisation des dégâts ne peut pas être correcte indiqué pour le stress estimé dans la figure 3(b) probablement en raison d'erreurs de variance dans l'estimation à partir de données bruités.

Dans les Figures 4 et 5, les performances ou les taux de réussite de la localisation des dégats (z -axis) sont affichés pour les ensembles de modes unique et multiple en fonction du aux réel et l'imaginaire pour une partie des valeurs choisies de s (x et y -axes). Ensuite, on peut voir dans la Figure 5 que le taux de réussite de la localisation des dégats avec la nouvelle méthode a considérablement amélioré la situation partout dans le plan s, par rapport aux résultats de la Figure 4, avec des taux de réussite entre 85% et 99%.

Pour le modèle de cube 3D dans la Figure 6, les 12 premiers modes sont identifiés à partir des ensembles de données et divisés en trois jeux de modes $\mathcal{M}_1$, $\mathcal{M}_2$ and $\mathcal{M}_3$. Ensuite, une comparaison avec les taux de réussite à partir des ensembles de modes unique dans la fourchette respective de s-values est faite dans la Figure 7 pour les parties réelles fixes $\mathrm{Re}(s^1) = -3$, $\mathrm{Re}(s^2) = -9$ et $\mathrm{Re}(s^3) = -11$, où l'on voit clairement que la combinaison statistique des résultats des ensembles de modes unique améliore considérablement la localisation des dégâts et ça performance presque partout dans le plan s.

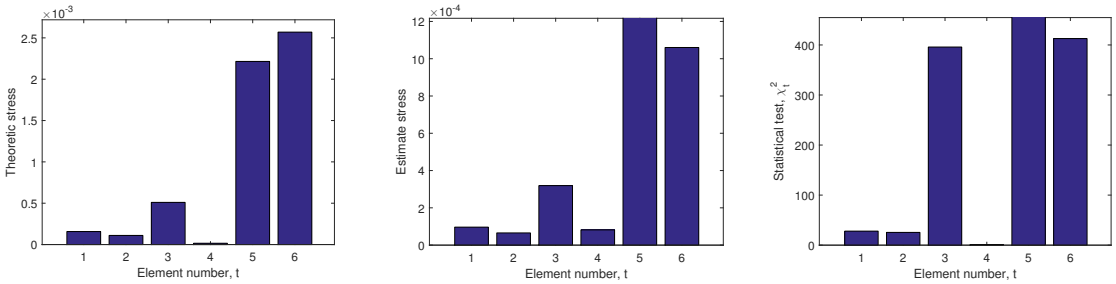

(a) SDDLV pour le stress théorique (b) SDDLV pour le stress estimé (c) S-SDDLV (test statistique)

Figure 3 – Les résultats de localisation à tous les éléments de la chaîne de masse-printemps en utilisant un ensemble de modes unique $\mathcal{M}_1$ en utilisant le calcul du stress et l'évaluation statistique à $s^1 = -2 + 51\mathrm{i}$. Le dommage est à l'élément 4.

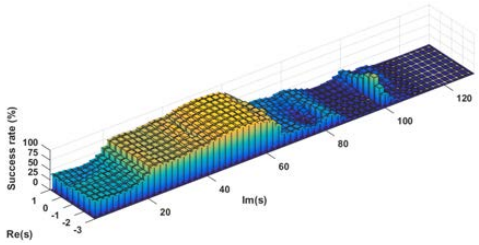

Figure 4 – Les taux de réussite du S-SDDLV à l'aide ensemble d'un mode unique, $\mathcal{M}_1$ en fonction de valeurs s, $\mathrm{Re}(s) \in [-3, 1]$ et $\mathrm{Im}(s) \in [0, 130]$

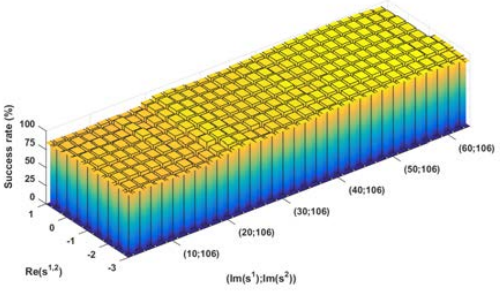

Figure 5 – Les taux de réussite du S-SDDLV à l'aide de multiples modes définissent $\mathcal{M}_1$ et $\mathcal{M}_2$, en fonction de s^1 et s^2 avec $\mathrm{Im}(s^1) \in [0, 64], \mathrm{Im}(s^2) = 106$.

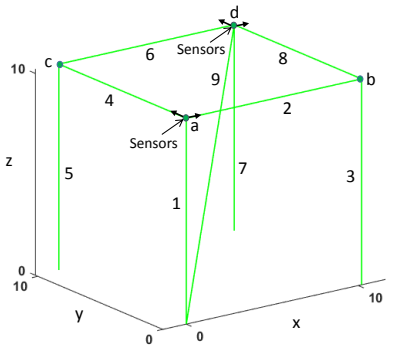

Figure 6 – Modèle Cube 3D avec éléments de poutre (24 DOFs)

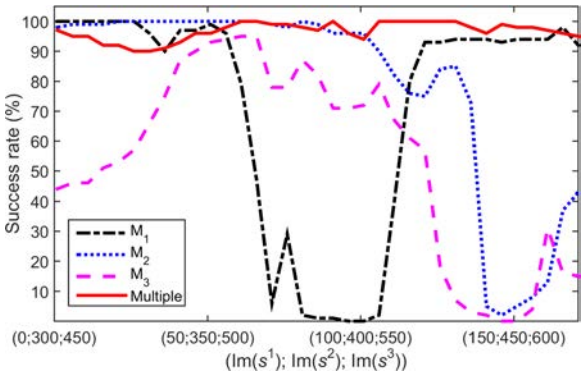

Figure 7 – Les taux de réussite du SDDLV dans les ensembles de modes unique $\mathcal{M}_1$, $\mathcal{M}_2$ et $\mathcal{M}_3$ avec s dans le voisinage des modes respectifs, par rapport au taux de réussite en utilisant conjointement les jeux de modes multiples.

Chapitre 10 –Localisation des dégâts statistiques avec l'approche ILDL

L'approche statistique de l'ILDL a été appliquée sur un système de chaîne à masse-ressort avec six DOF, comme le montre la Figure 2 à l'aide de 6 capteurs. Pour le cas complexe cas 1, deux versions sont testées en fonction du développement théorique du chapitre 6. Tout d'abord, la distribution dégénérée des vecteurs résiduels est directement prise en compte et, d'autre part, les tests élémentaires des vecteurs résiduels sont évalués séparément.

Pour l'évaluation de la performance de la méthode, les simulations de Monte-Carlo sont réalisées à l'aide de 100 ensembles de données simulées dans des états sains et endommagés pour déterminer le taux de réussite, où, dans chaque jeu de données, les modes et leurs incertitudes sont identifiés à l'aide de SSI. Dans les Figures 8 et 9, les taux de réussite des résultats de localisation sont présentés (axe z) pour la version 1 (R1v-S-ILDL) et 2 (R1e-

S-ILDL) compte tenu de tous les modes de la structure en fonction de différentes valeurs s (xy-axes). La plage entière des valeurs de s dans le voisinage des modes est $\mathrm{Re}(s) \in [-3, -1]$ et $\mathrm{Im}(s) \in [1, 130]$.

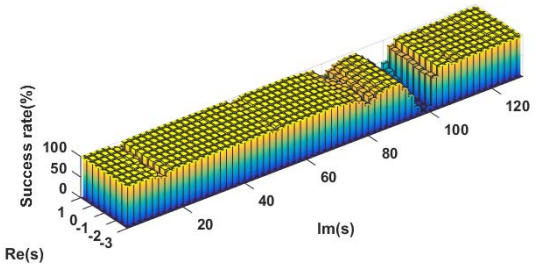

Figure 8 – Version 1: taux de réussite du R1v-S-ILDL en utilisant tous les modes en fonction des valeurs s, $\mathrm{Re}(s) \in [-3, -1]$ *et* $\mathrm{Im}(s) \in [1, 130]$.

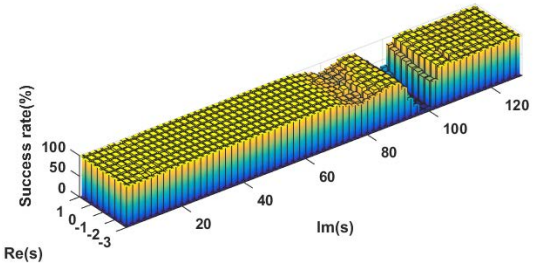

Figure 9 – Version 2: taux de réussite de la R1e-S-ILDL en utilisant tous les modes en fonction des valeurs s, $\mathrm{Re}(s) \in [-3, -1]$ *et* $\mathrm{Im}(s) \in [1, 130]$.

Chapitre 11 –Transfert de la localisation et de la quantification des dégâts statistiques basés sur la matrice de transfert

Dans cette étude, un modèle 2D Beam a été considéré dans la Figure 10 pour la localisation et la quantification des dégâts. La structure est modélisée avec 5 éléments de poutre de longueur totale 1 m. Les dommages sont simulés en diminuant la rigidité de l'élément 3 de 20 %. Dans cet exemple, 6 modes peuvent être identifiés à partir du modéle de la structure en utilisant SSI (voir Table 8.2), diviser en deux jeux de modes $\mathcal{M}_1$ and $\mathcal{M}_2$ de trois modes chacun pour la méthode proposée en utilisant plusieurs jeux de modes.

Les résultats de localisation des dommages sont indiqués pour un cas de test sur tous les éléments de la Figure 11 pour les tests de sensibilité et minmax. On voit que l'élément endommagé est correctement situé à l'élément 3. La réaction du test de sensibilité est beaucoup plus forte aux éléments non endommagés, tandis que le test minmax fonctionne très bien. Pour la quantification des dégats, les valeurs $\hat{\delta}_{sens}$ and $\hat{\delta}_{mm}$ ont été estimées, ce qui a entraîné un changement de paramétre estimé de 22.8% et 18.6%, respectivement.

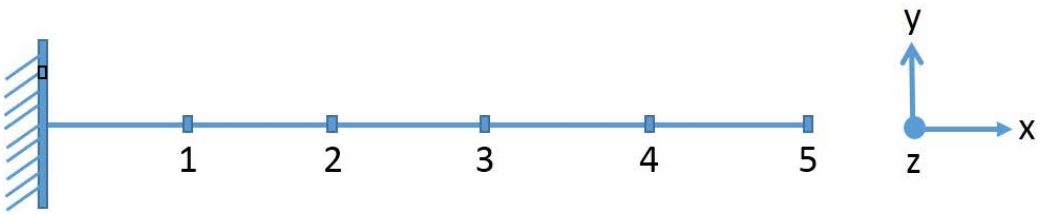

Figure 10 – Modèle 2D Poutre avec 5 éléments (15 DOFs)

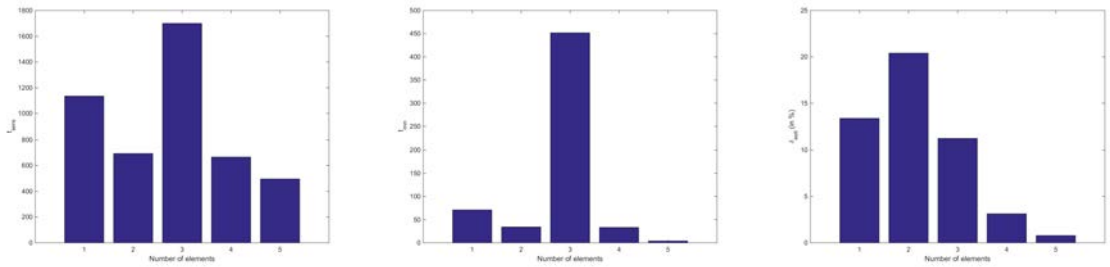

(a) tests de sensibilité (b) tests minmax (c) estimation valeur

Figure 11 – Résultats de localisation: (a) tests de sensibilité, (b) tests minmax et (c) estimation valeur à $s = -1 + 200\mathrm{i}$ *- en utilisant 5 capteurs et 5 modes, 5% bruit de sortie, 20% réduction de la rigidité à l'élément 3.*

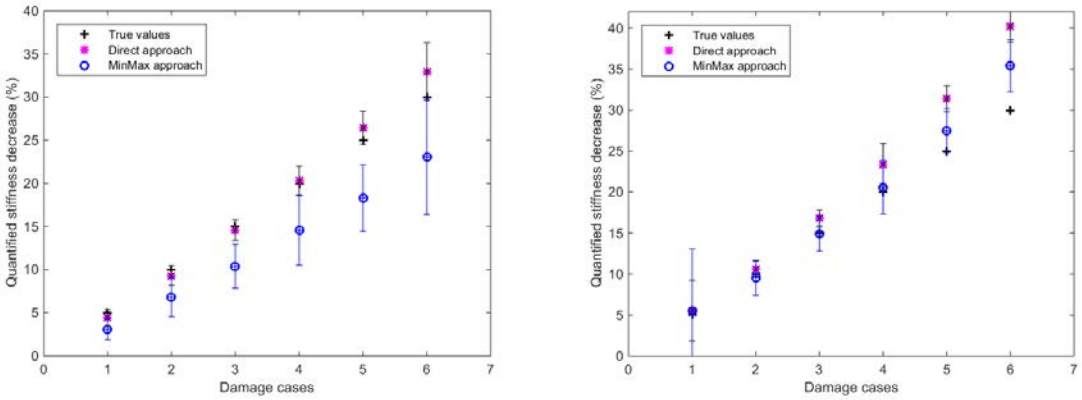

(a) 5 modes utilisant 5 capteurs (b) Ensembles de mode multiples utilisant 3 capteurs

Figure 12 – Quantification de différents dégats à partir de (a) 5 modes utilisant 5 capteurs à $s = -1 + 200\mathrm{i}$ *(à gauche) et (b) jeux de mode multiples utilisant 3 capteurs à* $s = [-1 + 200\mathrm{i}; -1 + 2600\mathrm{i}]$ *(droite) - 5% de bruit de sortie, 1% rapport d'amortissement, endommagé à l'élément 3.*

Sur la base de 100 jeux de données simulées, respectivement pour différents degrés d'endommagement entre 5% et 30% du dommage dans l'élément 3, les résultats de la quantification des dommages sont représentés sur les Figures 12(a) et 12(b). L'approche de la sensibilité surestime et l'approche minmax sous-estime l'étendue des dégâts. Les deux chiffres montrent que l'erreur augmente pour les grandes étendues de dégat qui peuvent être attendues puisque la matrice de sensibilité est calculée dans l'état de référence et n'est donc plus précise pour les changements importants. D'autres sources d'erreurs sont la troncature modale.

Chapitre 12 –Implémentation numérique

Ce chapitre présente l'implémentation numérique de la localisation des dégâts et des méthodes de quantification en utilisant le logiciel Abaqus. Les deux méthodes des chapitres 5 et 7 sont testés pour la localisation et la quantification d'un modèle de poutre en porte à faux comme le montre la Figure 13.

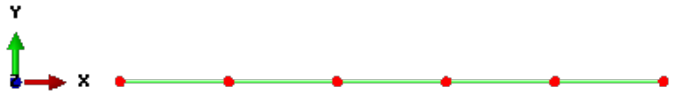

Figure 13 – Modèle 2D Poutre avec 5 éléments (15 DOFs) -en utilisant Abaqus/CAD Student Edition 6.14-2

Approche SDDLV: résultats de localisation à tous les éléments

Les résultats de la localisation à tous les éléments sont calculés à l'aide d'un des jeux de données dans les deux états sains et endommagés. Le calcul de toutes les contraintes se fait à $s_1 = -1+200\text{i}$ pour l'évaluation théorique, estimée et statistique de χ_t^2-tests en chiffres 14(a), 14(b) et 14(c), respectivement. Toutes les valeurs de stress correspondant à des éléments sains et endommagés sont présentés, tandis que la valeur de plus petite contrainte est correctement située pour l'élément endommagé 3.

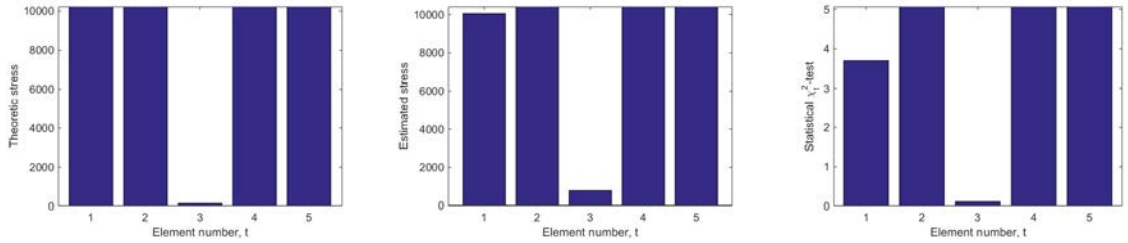

(a) SDDLV pour le stress théorique (b) SDDLV pour le stress estimé (c) S-SDDLV (Statistique χ_t^2-test)

Figure 14 – localisation des dégâts à base de SDDLV: calcul des contraintes et une évaluation statistique $s_1 = -1+200\text{i}$ *-en utilisant des modes 5 et 5 capteurs, 5% de bruit de sortie, 20% de réduction de la rigidité à l'element 3.*

Approche basée sensibilité: localisation des dégâts et la quantification

les résultats de la localisation des dommages sont présentés pour un cas d'essai à tous les éléments. Rappelons qu'un valeur élevée indique les éléments endommagés dans la sensibilité et les approches minmax. Des tests sensibilité et des tests minmax dans la Figure 15, on voit que l'élément endommagé est correctement placé à l'élément 3. La réaction du test de sensibilité est beaucoup plus forte au niveau des éléments en bon état, alors que les minmax réagissent très bien. Pour la quantification des dommages, les valeurs $\hat{\delta}_{sens}$, $\hat{\delta}_{mm}$ et $\hat{\delta}_{esti}$

ont été estimés, ce qui conduit à un changement de paramètre estimé de 23.17%, 20.10% et 13.99% dans l'élément endommagé.

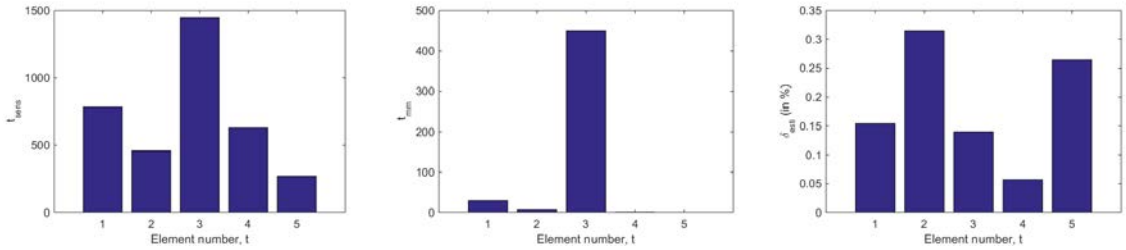

(a) tests de sensibilité (b) tests minmax (c) estimation valeur

Figure 15 – Approche basée sensibilité résultats de localisation: (a) tests de sensibilité, (b) tests minmax et (c) estimation valeur à $s = -1 + 200\mathrm{i}$ *- en utilisant 5 capteurs et 5 modes, 5% bruit de sortie, 20% réduction de la rigidité à l'element 3.*

Chapitre 13 –Applications réelles

Les méthodes de localisation et de quantification ont été appliquées sur une structure de cadre en acier de quatre étages, le "Yellow Frame" (Figure 16), à l'Université de British Columbia. La structure est décrite en détail dans [ADVM17, All17]. Il est censé montrer un comportement de vibration linéaire. Douze capteurs sont situés sur la structure, trois au nord, au sud et à l'ouest dans chaque étage (Figure 16(b)). Pour les états endommagés et non endommagés, des données d'accélération contenant 219,900 and 550,000 échantillon, respectivement, à une fréquence d'échantillonnage de 1000Hz ont été enregistrés. Les dégâts sont introduits en supprimant les élements numéro 2 et 4 du côté sud de la structure au premier étage.

Approche SDDLV: localisation

Les résultats de localisation sont calculés à tous les éléments de renfort à partir des ensembles de données expérimentaux dans des états endommagés et en bonne santé. Le calcul du stress et ses incertitudes pour l'évaluation statistique sont présentés dans les Figures 17(a)-17(b) en considérant la valeur de $s_1 = -1 + 76\mathrm{i}$ à proximité des pôles identifiés. Pour comparer les rapports des valeurs de stress entre les éléments sains et endommagés, les valeurs calculées sont normalisées dans les figures de telle sorte que la plus petite valeur des 32 éléments de renfort soit 1. On constate que le stress estimé est incapable d'indiquer le dommage aux les éléments 2 et 4 en raison des erreurs de bruit de mesure et de variance, tandis que le test statistique indique de dégâts les éléments aux 2 et 4.

(a) Photo de la structure du Yellow Frame (coin sud-est)

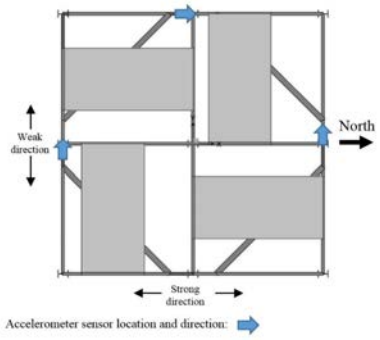

(b) Plan à l'échelle scaled de masse de niveau et l'emplacement des capteurs

Figure 16 – Structure de Yellow Frame.

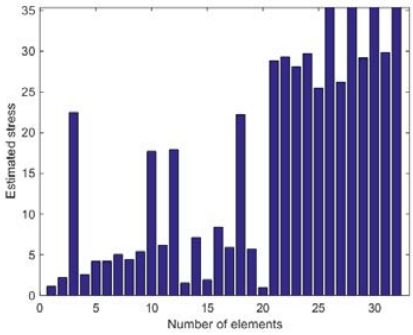

(a) Estimez le stress, 1s-value

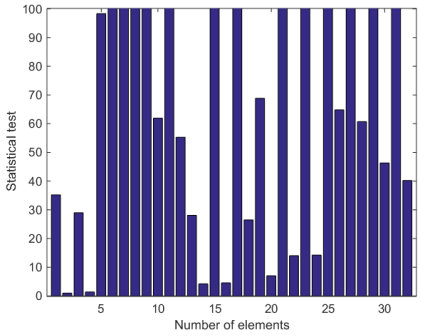

(b) Test statistique, 1s-value

Figure 17 – Résultats de localisation des dégâts basés sur SDDLV pour les éléments de renfort: calcul du stress et évaluation statistique au valeur $s = (-1 + 30\mathrm{i})$ -utilisant douze capteurs, mesure du bruit, enlevant les renforts à l'élement 2 et 4.

Approche basée sur la sensibilité à la matrice de transfert: localisation et quantification

Les indicateurs de dégâts sont présentés dans les Figures 18(a) et 18(b) pour chaque élément testé en utilisant trois choix de valeurs s de Laplace. On voit que la statistique de test aux éléments endommagés a la valeur la plus élevée, localisant correctement les dégâts aux éléments 2 et 4. Les tests de sensibilité réagissent aux éléments non endommagés, et il y a

également une légère réaction dans les éléments non endommagés dans ça Figure 18(b) pour les tests minmax.

Pour la quantification de l'étendue des dégats, les valeurs de $\hat{\delta}^{sens}$ et $\hat{\delta}^{mm}$ ont été estimées pour les approches de sensibilité et minmax respectives, et sont présentées dans l'onglet Table 1. Comme les renforts sont enlevées, la perte de rigidité devrait être de 100%. L'approche minmax s'approche de cette valeur mieux que l'approche de sensibilité, mais la précision globale de la quantification n'est pas entièrement satisfaisante.

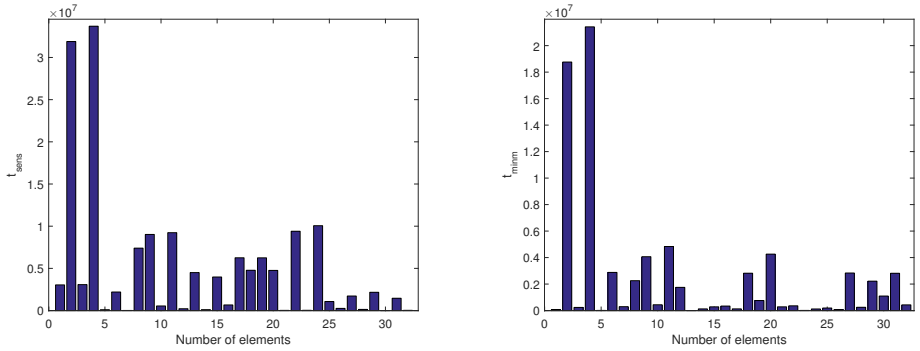

(a) tests de sensibilité, 3s-value (b) tests minmax, 3s-value

Figure 18 – Résultats de localisation de la matrice de transfert pour les éléments de renfort: Essais de sensibilité et minmax pour 3 valeurs de s de $(-1+10\mathrm{i}, -1+250\mathrm{i}, -1+280\mathrm{i})$ -utilisation de douze capteurs, mesure du bruit, enlèvement des renforts à l'élement 2 et 4.

Table 1 – Quantification des étendues de dégâts (in '%')

Type	élément 2	élément 4	élément 2	élément 4
s-value	1s		3s	
$\hat{\delta}_{sens}$	48.1571	48.6543	70.9265	70.0090
$\hat{\delta}_{minm}$	86.0142	94.1883	77.1299	102.2274
$\hat{\delta}$	49.1438	54.8310	8.2173	3.8317

Conclusions

Cette thèse présente des méthodes de localisation et de quantification des dégâts basés sur les vibrations à partir des mesures donnée de sortie pour les systèmes la surveillance de santé structurelle (SHM). En particulier, l'accent a été mis sur l'amélioration des méthodes existantes en considérant l'incertitude intrinsèque des données de mesure par propagation de la covariance dans les tests d'hypothèses et en utilisant toutes les informations éventuellement disponibles grâce à une approche de jeux de données multiples. Ensuite, l'applicabilité des méthodes a été améliorée avec moins de capteurs et moins de dépendance vis-à-vis du choix particulier des valeurs de s lorsque l'on considère tous les modes disponibles avec la stratégie

statistique définie en modes multiple. Dans la pratique, la performance de ces méthodes a été évaluée dans diverses études de cas numériques et de laboratoire, et une mise en œuvre supplémentaire a été réalisée pour des applications réalistes avec des modèles FE dans des logiciels commerciaux. Les méthodes proposées sont préférables pour localiser et quantifier les dommages dans des conditions de test réelles. Par conséquent, les développements de cette thèse contribuent à l'applicabilité de la localisation et de la quantification des dégâts basés sur les vibrations.

Bibliography

[AA16] O. Abdeljaber and O. Avci. Nonparametric structural damage detection algorithm for ambient vibration response: Utilizing artificial neural networks and self-organizing maps. *Journal of Architectural Engineering*, 22(2):04016004, 2016.

[AAK+17] O. Abdeljaber, O. Avci, S. Kiranyaz, M. Gabbouj, and D. J. Inman. Real-time vibration-based structural damage detection using one-dimensional convolutional neural networks. *Journal of Sound and Vibration*, 388:154–170, 2017.

[AB65] K.J. Aström and T. Bohlin. Numerical identification of linear dynamic systems from normal operating records. In *Proc. IFAC Symposium on Self Adaptive Systems*, Teddington, UK, 1965.

[AB82] R.J. Allemang and D.L. Brown. A correlation coefficient for modal vector analysis. In *In Proceedings of the 1st SEM International Modal Analysis Conference, Orlando, FL, USA*, 8-10 November 1982.

[AB01] Y. Aoki and O.I. Byon. Damage detection of cfrp pipes and shells by using localized flexibility method. *Advanced Composite Materials*, 10(2-3):189–198, 2001.

[ACPS78] R. D. Adams, P. Cawley, C. J. Pye, and B. J. Stone. A vibration technique for nondestructively assessing the integrity of structures. *Journal of Mechanical Engineering Science*, 1(23):1959–1982, 1978.

[ADVM17] S. Allahdadian, M. Döhler, C. Ventura, and L. Mevel. Damage localization of a real structure using the statistical subspace damage localization method. In *Proc. 11th International Workshop on Structural Health Monitoring (IWSHM)*, Stanford, CA, USA, 2017.

[Akç10] H. Akçay. An insight into instrumental variable frequency-domain subspace identification. *Automatica*, 46(2):375–382, 2010.

[Aka74] H. Akaike. Stochastic theory of minimal realization. *IEEE Transactions on Automatic Control*, 19(6):667–674, 1974.

[Aka75] H. Akaike. Markovian representation of stochastic processes by canonical variables. *SIAM Journal on Control*, 13:162–173, 1975.

[All17] S. Allahdadian. *Robust Statistical Subspace-Based Damage Assessment*. PhD thesis, University of British Columbia, Vancouver, Canada, 2017.

[ART] ARTeMIS Modal Pro - Damage Detection Plugin. Structural Vibration Solutions A/S, Aalborg, Denmark. www.svibs.com/products/ARTeMIS_Modal_Features/Damage_Detection.aspx.

[BAB00] M. Basseville, M. Abdelghani, and A. Benveniste. Subspace-based fault detection algorithms for vibration monitoring. *Automatica*, 36(1):101–109, 2000.

[BAD+SA] M.D.H. Bhuyan, S. Allahdadian, M. Döhler, Y. Lecieux, L. Mevel, F. Schoefs, and C. Ventura. Transfer matrices-based output-only statistical damage localization and quantification. In *11th International Workshop on Structural Health Monitoring (IWSHM)*, September 12-14, 2017, Stanford, CA, USA.

[Bak11] P.G. Bakir. Automation of the stabilization diagrams for subspace based system identification. *Expert Systems with Applications*, 38(12):14390–14397, 2011.

[Bas97] M. Basseville. Information criteria for residual generation and fault detection and isolation. *Automatica*, 33(5):783–803, 1997.

[Bat] Klaus-Jürgen Bathe. *Finite Element Procedures*. Cambridge.

[BAZM79] D.L. Brown, R.J. Allemang, R.D. Zimmerman, and M. Mergeay. Parameter estimation techniques for modal analysis. *SAE Transactions*, 88:828–846, 1979. SAE Paper Number 689110.

[BBA14] M. Billmaier, C. Bucher, and C. Adam. Selective sensitive finite element model updating: an improved approach. *Structural Control and Health Monitoring*, 21(8):1170–1192, 2014.

[BBM87] A. Benveniste, M. Basseville, and G.V. Moustakides. The asymptotic local approach to change detection and model validation. *IEEE Transactions on Automatic Control*, 32(7):583–592, 1987.

[BBM+08] É. Balmès, M. Basseville, L. Mevel, H. Nasser, and W. Zhou. Statistical model-based damage localization: a combined subspace-based and substructuring approach. *Structural Control and Health Monitoring*, 15(6):857–875, 2008.

[BDL+17] M.D.H. Bhuyan, M. Döhler, Y. Lecieux, L. Mevel, and F. Schoefs. Statistical damage localization with stochastic load vectors using multiple mode sets.

International Journal of Structural Health Monitoring (IJSHM), 16(5):518–535, 2017.

[BDMin] M.D.H. Bhuyan, M. Döhler, and L. Mevel. Statistical damage localization with stochastic load vectors using multiple mode sets. In *8th European Workshop on Structural Health Monitoring (EWSHM)*, July 4-7, 2016, Bilbao, Spain.

[Ber02] D. Bernal. Load vectors for damage localization. *Journal of Engineering Mechanics*, 128(1):7–14, 2002.

[Ber06] D. Bernal. Flexibility-based damage localization from stochastic realization results. *Journal of Engineering Mechanics*, 132(6):651–658, 2006.

[Ber07] D. Bernal. Damage localization from the null space of changes in the transfer matrix. *AIAA Journal*, 45(2):374–381, 2007.

[Ber10] D. Bernal. Load vectors for damage location in systems identified from operational loads. *Journal of Engineering Mechanics*, 136(1):31–39, 2010.

[Ber13] D. Bernal. Kalman filter damage detection in the presence of changing process and measurement noise. *Mechanical Systems and Signal Processing*, 39(1-2):361–371, 2013.

[Ber14] D. Bernal. Damage localization and quantification from the image of changes in flexibility. *Journal of Engineering Mechanics*, 140(2):279–286, 2014.

[BF85] A. Benveniste and J.-J. Fuchs. Single sample modal identification of a non-stationary stochastic process. *IEEE Transactions on Automatic Control*, AC-30(1):66–74, 1985.

[BFG06] D. Balageas, C.-P. Fritzen, and A. Güemes. *Structural Health Monitoring*. London, UK, 2006.

[BG63] R.E.D. Bishop and G.M.L. Gladwell. An investigation into the theory of resonance testing. *Philosophical Transactions of the Royal Society A: Mathematical and Physical Sciences*, 255(1055):241–280, 1963.

[BGD$^+$ce] M.D.H. Bhuyan, G. Gautier, M. Döhler, L. Mevel, Y. Lecieux, and F. Schoefs. Statistical damage localization in mechanical systems based on load vectors. In *International Federation of Automatic Control (IFAC), World Congress*, 9-14 July, 2017, Toulouse, France.

[BM07] A. Benveniste and L. Mevel. Nonstationary consistency of subspace methods. *IEEE Transactions on Automatic Control*, AC-52(6):974–984, 2007.

[BMCC10] J.M.W. Brownjohn, F. Magalhães, E. Caetano, and Á. Cunha. Ambient vibration re-testing and operational modal analysis of the Humber Bridge. *Engineering Structures*, 32(8):2003–2018, 2010.

[BMG04] M. Basseville, L. Mevel, and M. Goursat. Statistical model-based damage detection and localization: subspace-based residuals and damage-to-noise sensitivity ratios. *Journal of Sound and Vibration*, 275(3):769–794, 2004.

[BN93] M. Basseville and I. Nikiforov. *Detection of Abrupt Changes - Theory and Applications*. Prentice Hall, Englewood Cliffs, NJ, 1993.

[BP93] J.S. Bendat and A.G. Piersol. *Engineering Applications of Correlation and Spectral Analysis*. John Wiley & Sons, New York, USA, 2nd edition, 1993.

[BRA+15] J.M.W. Brownjohn, P. Reynolds, S.K. Au, D. Hester, and M. Bocian. Experimental modal analysis of civil structures: State of the art. In *SHMII - 7th International Conference on Structural Health Monitoring of Intelligent Infrastructure at Torino, Italy*, 2015.

[BVA01] R. Brincker, C.E. Ventura, and P. Andersen. Damping estimation by frequency domain decomposition. In *Proc. 19th International Modal Analysis Conference*, Kissimmee, FL, USA, 2001.

[BVD+ny] M.D.H. Bhuyan, E. Viefhues, M. Döhler, Y. Lecieux, L. Mevel, F. Hille, and F. Schoefs. Output-only subspace and transfer matrix-based damage localization and quantification. In *7th International Operational Modal Analysis Conference (IOMAC'2017)*, May 10-12, 2017, Ingolstadt, Germany.

[BXHX01] J. M. W. Brownjohn, Pin-Qi Xia, Hong Hao, and Yong Xia. Civil structure condition assessment by FE model updating: methodology and case studies. *Finite Elements in Analysis and Design*, 37(10):761–775, 2001.

[BZA01] R. Brincker, L. Zhang, and P. Andersen. Modal identification of output-only systems using frequency domain decomposition. *Smart Materials and Structures*, 10(3):441–445, 2001.

[CA79] P. Cawley and R.D. Adams. The location of defects in structures from measurements of natural frequencies. *Journal of Strain Analysis for Engineering Design*, 14:49–57, 1979.

[CB02] G. Casella and R.L. Berger. *Statistical inference*. Duxbury Press, 2002.

[CDF99] P. Cornwell, S. W. Doebling, and C. R. Farrar. Application of the strain energy damage detection method to plate-like structures. *Journal of Sound and Vibration*, 224(2):359–374, 1999.

[CF04] E.P. Carden and P. Fanning. Vibration based condition monitoring: a review. *Structural Health Monitoring*, 3(4):355–377, 2004.

[CGPV06] B. Cauberghe, P. Guillaume, R. Pintelon, and P. Verboven. Frequency-domain subspace identification using FRF data from arbitrary signals. *Journal of Sound and Vibration*, 290(3-5):555–571, 2006.

[CGV+05] B. Cauberghe, P. Guillaume, P. Verboven, S. Vanlanduit, and E. Parloo. On the influence of the parameter constraint on the stability of the poles and the discrimination capabilities of the stabilisation diagrams. *Mechanical Systems and Signal Processing*, 19(5):989–1014, 2005.

[CJ10] T.G. Carne and G.H. III. James. The inception of oma in the development of modal testing technology for wind turbines. *Mechanical Systems and Signal Processing*, 24(5):1213–1226, 2010.

[CPH03] C.V. Camp, S. Pezeshk, and H. Hansson. Flexural design of reinforced concrete frames using a genetic algorithm. *Journal of Structural Engineering*, 129(1):105–115, 2003.

[CSC11] H. Clarke, J. Stainsby, and E.P. Carden. Operational modal analysis of resiliently mounted marine diesel generator/alternator. In *In Proceedings of the 29th international modal analysis conference series*, 2011.

[CSQLSHYL17] W. C. Su, T. Q. Le, C. S. Huang, and P. Y. Lin. Locating damaged storeys in a structure based on its identified modal parameters in cauchy wavelet domain. *Applied Mathematical Modelling*, 000:1–19, 2017.

[DBAPS17] M. Diakhate, E. Bastidas-Arteagab, R.M. Pitti, and F. Schoefs. Cluster analysis of acoustic emission activity within wood material: Towards a real-time monitoring of crack tip propagation. *Engineering Fracture Mechanics*, 180:254–267, 2017.

[DDSG10] C. Devriendt, G. De Sitter, and P. Guillaume. An operational modal analysis approach based on parametrically identified multivariable transmissibilities. *Mechanical Systems and Signal Processing*, 24(5):1250–1259, 2010. Special Issue: Operational Modal Analysis.

[DFG97] S. W. Doebling, C. R. Farrar, and R. S. Goodman. Effects of measurement statistics on the detection of damage in the alamosa canyon bridge. In *Proceedings 15th International Modal Analysis Conference, Orlando, FL, pp. 919-929.*, 1997.

[DHMR14] M. Döhler, F. Hille, L. Mevel, and W. Rücker. Structural health monitoring with statistical methods during progressive damage test of S101 Bridge. *Engineering Structures*, 69:183–193, 2014.

[DKD09] A.D. Der Kiureghian and O. Ditlevsen. Aleatory or epistemic? does it matter? *Structural Safety*, 31:105–112, 2009.

[DLM13] M. Döhler, X.-B. Lam, and L. Mevel. Uncertainty quantification for modal parameters from stochastic subspace identification on multi-setup measurements. *Mechanical Systems and Signal Processing*, 36(2):562–581, 2013.

[DLT03] E. Douka, S. Loutridis, and A. Trochidis. Crack identification in beams using wavelet analysis. *International Journal of Solid and Structures*, 40:3557–3569, 2003.

[DM12] M. Döhler and L. Mevel. Fast multi-order computation of system matrices in subspace-based system identification. *Control Engineering Practice*, 20(9):882–894, 2012.

[DM13] M. Döhler and L. Mevel. Efficient multi-order uncertainty computation for stochastic subspace identification. *Mechanical Systems and Signal Processing*, 38(2):346–366, 2013.

[DMBM13] M. Döhler, L. Marin, D. Bernal, and L. Mevel. Statistical decision making for damage localization with stochastic load vectors. *Mechanical Systems and Signal Processing*, 39(1-2):426–440, 2013.

[DMH14] M. Döhler, L. Mevel, and F. Hille. Subspace-based damage detection under changes in the ambient excitation statistics. *Mechanical Systems and Signal Processing*, 45(1):207–224, 2014.

[DMZ16] M. Döhler, L. Mevel, and Q. Zhang. Fault detection, isolation and quantification from gaussian residuals with application to structural damage diagnosis. *Annual Reviews in Control*, 42:244–256, 2016.

[DRDRK08] A. Deraemaeker, E. Reynders, G. De Roeck, and J. Kullaa. Vibration-based structural health monitoring using output-only measurements under changing environment. *Mechanical Systems and Signal Processing*, 22(1):34–56, 2008.

[Ewi84] D.J. Ewins. *Modal testing: theory and practice*. Research Studies Press Ltd., Letchworth, Hertfordshire, UK, 1984.

[Ewi00] D. J. Ewins. Basics and state-of-the-art of modal testing. *Sadhana*, 25(3):207–220, 2000.

[FAMGA16] R. Farokhzad, G.G. Amiri, B. Mohebi, and M. Ghafory-Ashtiany. Multi-damage detection for steel beam structures. *Journal of Rehabilitation in Civil Engineering*, 4-2:25–44, 2016.

[FAP17] R. Frans, Y. Arfiadi, and H. Parung. Comparative study of mode shapes curvature and damage locating vector methods for damage detection of structures. *Procedia Engineering*, 171:1263–1271, 2017.

[FDN01] C.R. Farrar, S.W. Doebling, and D.A. Nix. Vibration-based structural damage identification. *Philosophical Transactions of the Royal Society A: Mathematical, Physical and Engineering Science*, 359(1778):131–149, 2001.

[FJI97] C.R. Farrar and G.H. James III. System identification from ambient vibration measurements on a bridge. *Journal of Sound and Vibration*, 205(1):1–18, 1997.

[FP97] M. I. Friswell and J. E. T. Penny. Is damage location using vibration measurements practical? *In DAMAS 97, Structural Damage Assessment using Advanced Signal Processing Procedures*, 1997.

[FQ09] W. Fan and P. Qiao. A 2-d continuous wavelet transform of mode shape data for damage detection of plate structures. *International Journal of Solids and Structures*, 46:4379–4395, 2009.

[FQ11] W. Fan and P. Qiao. Vibration-based damage identification methods: a review and comparative study. *Structural Health Monitoring*, 10(1):83–111, 2011.

[Fri07] M.I. Friswell. Damage identification using inverse methods. *Philosophical Transactions of the Royal Society A: Mathematical, Physical and Engineering Sciences*, 365:393–410, 2007.

[FW07] C.R. Farrar and K. Worden. An introduction to structural health monitoring. *Philosophical Transactions of the Royal Society A: Mathematical, Physical and Engineering Sciences*, 365(1851):303–315, 2007.

[GBDMia] G. Gautier, M.D.H. Bhuyan, M. Döhler, and L. Mevel. Comparison of damage localization in mechanical systems based on stochastic subspace identication method. In *European Geosciences Union, General Assembly*, 23-28 April, 2017, Vienna, Austria.

[Gev06] M. Gevers. A personal view of the development of system identification. *IEEE Control Systems Magazine*, 26(6):93–105, 2006.

[GGB+13a] M. Gonzalez, C. Gogu, N. Binaud, C. Espinosa, J. Morlier, and S. Quoniam. Towards a consideration of the uncertainties in flight loads. In *5th EUCASS*, 2013.

[GGB+13b] M. Gonzalez, C. Gogu, N. Binaud, C. Espinosa, J. Morlier, and S. Quoniam. Uncertainty quantification in aircraft load calibration. In *10th World Congress on Structural and Multidisciplinary Optimization*, 2013.

[GM03] A. Gentile and A. Messina. On the continuous wavelet transforms applied to discrete vibrational data for detecting open cracks in damaged beams. *International Journal of Solid and Structures*, 40:295–315, 2003.

[GNW+17] G.R. Gillich, J.L. Ntakpe, M. Abdel. Wahab, Z.I. Praisach, and M.C. Mimis. Damage detection in multi-span beams based on the analysis of frequency changes. In *12th International Conference on Damage Assessment of Structures*, 2017.

[Gol89] D.E. Goldberg. *Genetic algorithms in search, optimization and machine learning*. Addison-Wesley Professional, 1989.

[Gra75] D. Graupe. *Identification of Systems*. Krieger, Malabar, FL, 1975.

[GS08] H.M. Gomes and N.R.S. Silva. Some comparisons for damage detection on structures using genetic algorithms and modal sensitivity method. *Applied Mathematical Modelling*, 32(11):2216–2232, 2008.

[Gud82] P. Gudmundson. Eigenfrequency changes of structures due to cracks, notches or other geometrical changes. *Journal of the Mechanics and Physics of Solids*, 30(5):339–353, 1982.

[GVC+03] P. Guillaume, P. Verboven, B. Cauberghe, S. Vanlanduit, E. Parloo, and G. De Sitter. Frequency-domain system identification techniques for experimental and operational modal analysis. In *Proc. 13th IFAC Symposium on System Identification*, Rotterdam, The Netherlands, 2003.

[GVL96] G.H. Golub and C.F. Van Loan. *Matrix computations*. Johns Hopkins University Press, 3rd edition, 1996.

[GVV98] P. Guillaume, P. Verboven, and S. Vanlanduit. Frequency-domain maximum likelihood identification of modal parameters with confidence intervals. In *Proc. 24th International Seminar on Modal Analysis (ISMA)*, 1998.

[GVV+03] P. Guillaume, P. Verboven, S. Vanlanduit, H. Van der Auweraer, and B. Peeters. A poly-reference implementation of the least-squares complex frequency-domain estimator. In *Proc. 21th International Modal Analysis Conference*, Kissimmee, FL, USA, 2003.

[GZ08] M.P. González and J.L. Zapico. Seismic damage identification in buildings using neural networks and modal data. *Computers & Structures*, 86(3-5):416–426, 2008.

[Han70] E.J. Hannan. *Multiple time series*. Wiley New York, 1970.

[HF11] H. Hein and L. Feklistova. Computationally efficient delamination detection in composite beams using haar wavelets. *Mechanical Systems and Signal Processing*, 25(6):2257–2270, 2011.

[HK66] B.L. Ho and R.E. Kalman. Effective construction of linear state-variable models from input/output functions. *Regelungstechnik*, 14(12):545–548, 1966.

[HKLL02] J.C. Hong, Y.Y. Kim, H.C. Lee, and Y.W. Lee. Damage detection using lipschitz exponent estimated by the wavelet transform: applications to vibration modes of beam. *International Journal of Solid and Structures*, 39:1803–1846, 2002.

[HLS98] W. Heylen, S. Lammens, and P. Sas. *Modal Analysis Theory and Testing*. Katholieke Universiteit Leuven, Belgium, 1998.

[Hol92] J.H. Holland. *Adaptation in natural and artificial systems: an introductory analysis with applications to biology, control, and artificial intelligence*. A Bradford Book, 1992.

[HR14] S.J.S. Hakim and A.H. Razak. Modal parameters based structural damage detection using artificial neural networks- a review. *Smart Structures and Systems*, 14(2):159–189, 2014.

[HRR15] S.J.S. Hakim, A.H. Razak, and S.A. Ravanfar. Ensemble neural networks for structural damage identification using modal data. *International Journal of Damage Mechanics*, 25(3):400–430, 2015.

[HT91] G. Hearn and R. B. Testa. Modal analysis for damage detection in structures. *Journal of Structural Engineering*, 117(10):3042–3063, 1991.

[HVdA99] L. Hermans and H. Van der Auweraer. Modal testing and analysis of structures under operational conditions: industrial application. *Mechanical Systems and Signal Processing*, 13(2):193–216, 1999.

[HWLS06] H. Hu, B. Wang, C. Lee, and J. Su. Damage detection of surface cracks in composite laminates using modal analysis and strain energy method. *Composite Structures*, 74:399–405, 2006.

[Jam03] G.H. III. James. Modal parameter estimation from space shuttle flight data. In *In Proceedings of the 21st international modal analysis conference*, 2003.

[JICL95] G.H. James III, T.G. Carne, and J.P. Lauffer. The natural excitation technique (NExT) for modal parameter extraction from operating structures. *Modal Analysis - The International Journal of Analytical and Experimental Modal Analysis*, 10:260–277, 1995.

[JMRC17] J. J. Moughty and J. R. Casas. A state of the art review of modal-based damage detection in bridges: Development, challenges, and solutions. *Applied sciences, MDPI*, 1:1–24, 2017.

[JNJ04] Minh Q. Phan Jer-Nan Juang. *Identification and control of mechanical systems*. Cambridge, 2004.

[JP85] J.-N. Juang and R.S. Pappa. Eigensystem realization algorithm for modal parameter identification and model reduction. *Journal of Guidance, Control and Dynamics*, 8(5):620–627, 1985.

[JR05] B. Jaishi and W.X. Ren. Structural finite element model updating using ambient vibration test results. *Journal of Structural Engineering*, 131(4):617–628, 2005.

[JR06] B. Jaishi and W.X. Ren. Damage detection by finite element model updating using modal flexibility residual. *Journal of Sound and Vibration*, 290(1):369–387, 2006.

[JRWC17] R. Janeliukstis, S. Rucevskis, M. Wesolowski, and A. Chate. Experimental structural damage localization in beam structure using spatial continuous wavelet transform and mode shape curvature methods. *Measurement*, 102:253–270, 2017.

[Jua94] J.-N. Juang. *Applied System Identification*. Prentice-Hall, Englewood Cliffs, NJ, 1994.

[Kat15] A. Katunin. Nondestructive damage assessment of composite structures based on wavelet analysis of modal curvatures: State-of-the-art review and description of wavelet-based damage assessment benchmark. *Shock and Vibration*, 735219:1–19, 2015.

[KCL03] C.G. Koh, Y.F. Chen, and C.Y. Liaw. A hybrid computational strategy for identification of structural parameters. *Computers and Structures*, 81(2):107–117, 2003.

[KJL92] J.H. Kim, H.S. Jeon, and C.W. Lee. Application of the modal assurance criteria for detecting and locating structural faults. *In Proceedings of the 10th International Modal Analysis Conference, San Diego, CA, USA*, pages 536–540, 3-7 February 1992.

[KKL14] A.N. Kim, H. Kim, and Jaehong. Lee. Damage detection of truss structures using two-stage optimization based on micro genetic algorithm. *Journal of Mechanical Science and Technology*, 28(9):3687–3695, 2014.

[KM04] H. Kim and H. Melhem. Damage detection of structures by wavelet analysis. *Engineering Structures*, 26(3):347–362, 2004.

[KRCS03] J.T. Kim, Y.S. Ryu, H.M. Cho, and N. Stubbs. Damage identification in beam-type structures: frequency-based method vs. mode-shape based method. *Engineering Structures*, 25(1):57–67, 2003.

[Kri95] C. S. Krishnamoorthy. *Finite Element Analysis: Theory and Programming*. Tata McGraw-Hill Education, 1995.

[KS86] M. Kato and S. Shimada. Vibration of pc bridge during failure process. *Journal of Structural Engineering*, 112(7):1692–1703, 1986.

[Kul03] J. Kullaa. Damage detection of the z24 bridge using control charts. *Mechanical Systems and Signal Processing*, 17(1):163–170, 2003.

[Kun78] S.Y. Kung. A new identification and model reduction algorithm via singular value decomposition. In *Proc. 12th Asilomar Conference on Circuits, Systems, and Computers*, pages 705–714, Pacific Grove, CA, USA, 1978.

[Lar83] W.E. Larimore. System identification, reduced order filters and modelling via canonical variate analysis. In *Proc. American Control Conference*, pages 445–451, San Francisco, 1983.

[LC79] L. Ljung and P.E. Caines. Asymptotic normality of prediction error estimators for approximate system models. *Stochastics – An International Journal of Probability and Stochastic Processes*, 3(1):29–46, 1979.

[LC00] Y.S. Lee and M.J. Chung. A study on crack detection using eigenfrequency test data. *Computers & Structures*, 77(3):327–342., 2000.

[LCD+16] M.P. Limongelli, E. Chatzi, M. Döhler, G. Lombaert, and E. Reynders. Towards extraction of vibration-based damage indicators. In *Proc. 8th European Workshop on Structural Health Monitoring*, 2016.

[LCDLP+16] V. Le Cam, M. Döhler, M. Le Pen, I. Guéguen, and L. Mevel. Embedded subspace-based modal analysis and uncertainty quantification on wireless sensor platform PEGASE. In *8th European Workshop on Structural Health Monitoring*, 2016.

[LDD07] H. Lia, X. Dengb, and H. Dai. Structural damage detection using the combination method of emd and wavelet analysis. *Mechanical Systems and Signal Processing*, 21:298–306, 2007.

[Li11] P. Li. Structural damage localization using probabilistic neural networks. *Mathematical and Computer Modelling*, 54:965–969, 2011.

[Lju78] L. Ljung. Convergence analysis of parametric identification methods. *IEEE Transactions on Automatic Control*, 23(5):770–783, 1978.

[Lju87] L. Ljung. *System Identification: Theory for the User*. Prentice-Hall, Englewood Cliffs, NJ, 1987.

[Lju99] L. Ljung. *System identification: theory for the user*. Prentice Hall, Englewood Cliffs, NJ, USA, 1999.

[LK94] T.W. Lim and A.L. Kashangaki. Structural damage detection of space truss structures using best achievable eigenvectors. *American Institute of Aeronautics and Astronautics*, 32:1049–1057, 1994.

[LLM08] J. Liu, X. Liu, and X. Ma. First-order perturbation analysis of singular vectors in singular value decomposition. *IEEE Transactions on Signal Processing*, 56:3044–3049, 2008.

[LRZ02] Q. Lu, G. Ren, and Y. Zhao. Multiple damage location with flexibility curvature and relative frequency change for beam structures. *Journal of Sound and Vibration*, 253(5):1101–1114, 2002.

[LW98] K.M. Liew and Q. Wang. Application of wavelet theory for crack identification in structures. *Journal of Engineering Mechanics*, 124(2):152–157, 1998.

[LZL+17] G. Liua, Y. Zhaia, D. Lenga, X. Tiana, and W. Mua. Research on structural damage detection of offshore platforms based on grouping modal strain energy. *Ocean Engineering*, 140:43–49, 2017.

[MAL96] T. McKelvey, H. Akçay, and L. Ljung. Subspace-based multivariable system identification from frequency response data. *IEEE Transactions on Automatic Control*, 41(7):960–979, 1996.

[Mar13] L. Marin. *Statistical decision making for stochastic damage localization approaches*. PhD thesis, Inria, Rennes, 2013.

[MBB+06] L. Mevel, A. Benveniste, M. Basseville, M. Goursat, B. Peeters, H. Van der Auweraer, and A. Vecchio. Input/output versus output-only data processing for structural identification - application to in-flight data analysis. *Journal of Sound and Vibration*, 295(3):531–552, 2006.

[MBG03] L. Mevel, M. Basseville, and M. Goursat. Stochastic subspace-based structural identification and damage detection - Application to the steel-quake benchmark. *Mechanical Systems and Signal Processing*, 17(1):91–101, 2003. Special issue on COST F3 Benchmarks.

[MBR90] J. Mazars, Y. Berthaud, and S. Ramtani. The unilateral behaviour of damaged concrete. *Engineering Fracture Mechanics*, 35:629–635, 1990.

[MCC12] F. Magalhães, A. Cunha, and E. Caetano. Vibration based structural health monitoring of an arch bridge: From automated OMA to damage detection. *Mechanical Systems and Signal Processing*, 28:212–228, 2012.

[MDBM13] L. Marin, M. Döhler, D. Bernal, and L. Mevel. Statistical based decision making for damage localization with influence lines. In *Proc. 9th International Workshop on Structural Health Monitoring*, Stanford, CA, USA, 2013.

[MDBM15] L. Marin, M. Döhler, D. Bernal, and L. Mevel. Robust statistical damage localization with stochastic load vectors. *Structural Control and Health Monitoring*, 22:557–573, 2015.

[MGB03] L. Mevel, M. Goursat, and M. Basseville. Stochastic subspace-based structural identification and damage detection and localization - Application to the Z24 Bridge benchmark. *Mechanical Systems and Signal Processing*, 17(1):143–151, 2003. Special issue on COST F3 Benchmarks.

[MH99] T. Marwala and H.E.M. Hunt. Fault identification using finite element models and neural networks. *Mechanical Systems and Signal Processing*, 13(3):475–490, 1999.

[MJ00] Kanti V. Mardia and Peter E. Jupp. *Directional Statistics*. John Wiley & Sons, Ltd, 2000.

[MKGA13] M. Mehrjoo, N. Khaji, and M. Ghafory-Ashtiany. Application of genetic algorithm in crack detection of beam-like structures using a new cracked euler−bernoulli beam element. *Applied Soft Computing*, 13:867–880, 2013.

[MKMB08] M. Mehrjoo, N. Khaji, H. Moharrami, and A. Bahreininejad. Damage detection of truss bridge joints using artificial neural networks. *Expert Systems with Applications*, 35:1122–1131, 2008.

[MPC89] J. Mazars and G Pijaudier-Cabot. Continuum damage theory - application to concrete. *Journal of Engineering Mechanics*, 115, No. 2:345–365, 1989.

[MS97] N.M. Maia and J.M. Silva. *Theoretical and Experimental Modal Analysis*. John Wiley & Sons, 1997.

[MS14] M. Montazer and S.M. Seyedpoor. A new flexibility based damage index for damage detection of truss structures. *Shock and Vibration*, 2:1–12, 2014.

[MWC98] A. Messina, E.J. Williams, and T. Contursi. Structural damage detection by a sensitivity and statistical-based method. *Journal of Sound and Vibration*, 216(5):791–808, 1998.

[NS13] M. Nobahari and SM. Seyedpoor. An efficient method for structural damage localization based on the concepts of flexibility matrix and strain energy of a structure. *Structural Engineering and Mechanics*, 46(2):231–244, 2013.

[OKC02] W. Ostachowicz, M. Krawczuk, and M. Cartmell. The location of a concentrated mass on rectangular plates from measurements of natural vibrations. *Computers & Structures*, 80(16-17):1419–1428, 2002.

[OS04] A.V. Ovanesova and L.E. Suarez. Application of wavelet transform to damage detection in frame structures. *Engineering Structures*, 26:39–49, 2004.

[PB94] A.K. Pandey and M. Biswas. Damage detection in structures using changes in flexibility. *Journal of Sound and Vibration*, 169(1):3–17, 1994.

[PBS91] A.K. Pandey, M. Biswas, and M.M. Samman. Damage detection from changes in curvature mode shapes. *Journal of Sound and Vibration*, 145(2):321–332, 1991.

[PCM09] A.H. Panigrahi, S. Chakraverty, and B.K. Mishra. Vibration based damage detection in a uniform strength beam using genetic algorithm. *Meccanica*, 44:697–710, 2009.

[PD87] C.A. Papadopoulos and A.D. Dimarogonas. Coupled longitudinal and bending vibrations of a rotating shaft with an open crack. *Journal of Sound and Vibration*, 117(1):81–93, 1987.

[PDR99] B. Peeters and G. De Roeck. Reference-based stochastic subspace identification for output-only modal analysis. *Mechanical Systems and Signal Processing*, 13(6):855–878, 1999.

[PDR01] B. Peeters and G. De Roeck. Stochastic system identification for operational modal analysis: a review. *Journal of Dynamic Systems, Measurement, and Control*, 123(4):659–667, 2001.

[Pee00] B. Peeters. *System identification and damage detection in civil engineering.* PhD thesis, Katholieke Universiteit Leuven, 2000.

[PGS07] R. Pintelon, P. Guillaume, and J. Schoukens. Uncertainty calculation in (operational) modal analysis. *Mechanical Systems and Signal Processing*, 21(6):2359–2373, 2007.

[Pin02] R. Pintelon. Frequency-domain subspace system identification using non-parametric noise models. *Automatica*, 38(8):1295–1311, 2002.

[POB+91] M. Prevosto, M. Olagnon, A. Benveniste, M. Basseville, and G. Le Vey. State-space formulation, a solution to modal parameter estimation. *Journal of Sound and Vibration*, 148(2):329–342, 1991.

[PRM07] R. Perera, A. Ruiz, and Manzano. An evolutionary multiobjective framework for structural damage localization and quantification. *Engineering Structures*, 29:2540–2550, 2007.

[PT06] R. Perera and R. Torres. Structural damage detection via modal data with genetic algorithms. *Journal of Structural Engineering*, 132(9), 2006.

[PVdAGL04] B. Peeters, H. Van der Auweraer, P. Guillaume, and J. Leuridan. The PolyMAX frequency-domain method: a new standard for modal parameter estimation? *Shock and Vibration*, 11(3-4):395–409, 2004.

[QWZA01] S.T. Quek, Q. Wang, L. Zhang, and K.K. Ang. Sensitivity analysis of crack detection in beams by wavelet technique. *International Journal of Mechanical Science*, 43:2899–291, 2001.

[Rak17] Waldemar. Rakowski. Wavelet approach to damage detection of mechanical systems and structures. *Procedia Engineering*, 182:594–601, 2017.

[RDR08] E. Reynders and G. De Roeck. Reference-based combined deterministic-stochastic subspace identification for experimental and operational modal analysis. *Mechanical Systems and Signal Processing*, 22(3):617–637, 2008.

[RDR10] E. Reynders and G. De Roeck. A local flexibility method for vibration-based damage localization and quantification. *Journal of Sound and Vibration*, 329(12):2367–2383, 2010.

[RM71] C.R. Rao and S.K. Mitra. *Generalized inverse of a matrix and its applications*. J. Wiley, New York, 1971.

[RML+10] L.F. Ramos, L. Marques, P.B. Lourenço, G. De Roeck, A. Campos-Costa, and J. Roque. Monitoring historical masonry structures with operational modal analysis: Two case studies. *Mechanical Systems and Signal Processing*, 24(5):1291–1305, 2010. Special Issue: Operational Modal Analysis.

[RPDR08] E. Reynders, R. Pintelon, and G. De Roeck. Uncertainty bounds on modal parameters obtained from stochastic subspace identification. *Mechanical Systems and Signal Processing*, 22(4):948–969, 2008.

[RS03] A. Rouhan and F. Schoefs. Probabilistic modeling of inspection results for offshore structures. *Structural Safety*, 25:379–399, 2003.

[RV05] S. Rajasekaran and S.P. Varghese. Damage detection in beams and plates using wavelet transforms. *Computers and Concrete*, 2(6):481–498., 2005.

[RW06] M. Rucka and K. Wilde. Application of continuous wavelet transform in vibration based damage detection method for beams and plates. *Journal of Sound and Vibration*, 297:536–550, 2006.

[Sal97] O. S. Salawu. Detection of structural damage through changes in frequency: a review. *Engineering Structures*, 19(9):718–723, 1997.

[SBBRPF11] F. S. Buezas, M. B. Rosales, and C. P. Filipich. Damage detection with genetic algorithms taking into account a crack contact model. *Engineering Fracture Mechanics*, 78:695–712, 2011.

[SCB17] V. Shahsavari, L. Chouinard, and J. Bastien. Wavelet-based analysis of mode shapes for statistical detection and localization of damage in beams using likelihood ratio test. *Engineering Structures*, 132:494–507, 2017.

[SCRL06] R. Salgado, P.J.S. Cruz, L.F. Ramos, and P.B. Lourenco. Comparison between damage detection methods applied to beam structures. In *In Proceedings of the IABMAS'06, Porto, PT, USA*, 16-19 July 2006.

[SDRL15a] E. Simoen, G. De Roeck, and G. Lombaert. Dealing with uncertainty in model updating for damage assessment: A review. *Mechanical Systems and Signal Processing*, 56-57(0):123 – 149, 2015.

[SDRL15b] Ellen Simoen, Guido De Roeck, and Geert Lombaert. Dealing with uncertainty in model updating for damage assessment: A review. *Mechanical Systems and Signal Processing*, 56:123–149, 2015.

[Sek83] A.S. Sekhar. Vibration characteristics of a cracked rotor with two open cracks. *Journal of Sound and Vibration*, 223(4):583–593, 1983.

[Sey12] S.M. Seyedpoor. A two stage method for structural damage detection using a modal strain energy based index and particle swarm optimization. *International Journal of Non-Linear Mechanics*, 47:1–8, 2012.

[SIBA15] K. Samir, R. Idir, B. Brahim, and A. Aicha. Genetic algorithm based objective functions comparative study for damage detection and localization in beam structures. In *11th International Conference on Damage Assessment of Structures*, 2015.

[SK96] N. Stubbs and J.T. Kim. Damage localization in structures without baseline modal parameters. *AIAA Journal*, 34(8):1644–1649, 1996.

[SK05] E. Sazonova and P. Klinkhachorn. Optimal spatial sampling interval for damage detection by curvature or strain energy mode shapes. *Journal of Sound and Vibration*, 285:783–801, 2005.

[SKGH03] E.S. Sazonov, P. Klinkhachorn, H.V.S. GangaRao, and U.B. Halabe. Non-baseline damage detection from changes in strain energy mode shapes experiments on armored vehicle launched bridge. In *Inproceedings of 29th annual review of progress in quantitative nondestructive evaluation (QNDE), Bellingham, pp: 1415-1422*, 2003.

[SLL88] W. T. Springer, K. L. Lawrence, and T. J. Lawley. Damage assessment based on the structural frequency-response function. *Experimental Mechanics, Kluwer Academic Publishers*, 28(1):34–37, 1988.

[SLZ98] Z.Y. Shi, S.S. Law, and L.M. Zhang. Structural damage localization from modal strain energy change. *Journal of Sound and Vibration*, 218(5):825–844, 1998.

[SLZ00] Z.Y. Shi, S.S. Law, and L.M. Zhang. Damage localization by directly using incomplete mode shapes. *Journal of Engineering Mechanics*, 126(6):656–660, 2000.

[SMV10] K. Saeed, N. Mechbal, and M. Vergé. Subspace-based damage localization using artificial neural network. *18th Mediterranean Conference on Control and Automation*, 2010.

[SP92] A.S. Sekhar and B.S. Prabhu. Crack detection and vibration characteristics of cracked shafts. *Journal of Sound and Vibration*, 157(2):375–381, 1992.

[SR99] E.I. Shifrin and R. Ruotolo. Natural frequencies of a beam with an arbitrary number of cracks. *Journal of Sound and Vibration*, 222:409–423, 1999.

[SS03] M. Sahin and R.A. Shenoi. Quantification and localisation of damage in beamlike structures by using artificial neural networks with experimental validation. *Engineering Structures*, 25:1785–1802, 2003.

[STAB88] C.Y. Shih, Y.G. Tsuei, R.J. Allemang, and D.L. Brown. Complex mode indication function and its applications to spatial domain parameter estimation. *Mechanical Systems and Signal Processing*, 2(4):367–377, 1988.

[STC09] H. Shih, D. Thambiratnam, and T. Chan. Vibration based structural damage detection in flexural members using multi-criteria approach. *Journal of Sound and Vibration*, 323(3):645–661, 2009.

[SW95] O.S. Salawu and C. Williams. Bridge assessment using forced-vibration testing. *Journal of Structural Engineering*, 121:161–173, 1995.

[TMDR02] A. Teughels, J. Maeck, and G. De Roeck. Damage assessment by FE model updating using damage functions. *Computers & Structures*, 80(25):1869–1879, 2002.

[TPI00] H. Tada, P.C. Paris, and G.R. Irwin. *The Stress Analysis of Cracks Handbook*. ASME Press, New York, 2000.

[TTCAR17] Z.X. Tana, D.P. Thambiratnama, T.H.T. Chana, and H. Abdul Razakb. Detecting damage in steel beams using modal strain energy based damage index and artificial neural network. *Engineering Failure Analysis*, 79:253–262, 2017.

[UTDR06] J.F. Unger, A. Teughels, and G. De Roeck. System identification and damage detection of a prestressed concrete beam. *Journal of Structural Engineering*, 132(11):1691–1698, 2006.

[UTG05] J.F. Unger, A. Teughels, and G.De Roeck. Damage detection of a prestressed concrete beam using modal strains. *Journal of Structural Engineering*, 131(9):1456–1463, 2005.

[VdAGVV01] H. Van der Auweraer, P. Guillaume, P. Verboven, and S. Vanlanduit. Application of a fast-stabilizing frequency domain parameter estimation method. *ASME Journal of Dynamic Systems, Measurement, and Control*, 123(4):651–658, 2001.

[VDHHDT+16] T. Vo-Duya, V. Ho-Huuc, H. Dang-Trunga, D. Dinh-Cong, and T Nguyen-Thoi. Damage detection in laminated composite plates using modal strain energy and improved differential evolution algorithm. *Procedia Engineering*, 142:182 –189, 2016.

[Ver94] M. Verhaegen. Identification of the deterministic part of MIMO state space models given in innovations form from input-output data. *Automatica*, 30(1):61–74, 1994. Special issue on statistical signal processing and control.

[Vib95] M. Viberg. Subspace-based methods for the identification of linear time-invariant systems. *Automatica*, 31(12):1835–1851, 1995.

[VODM94] P. Van Overschee and B. De Moor. N4SID: Subspace algorithms for the identification of combined deterministic-stochastic systems. *Automatica*, 30(1):75–93, 1994.

[VODM96] P. Van Overschee and B. De Moor. *Subspace Identification for Linear Systems: Theory, Implementation, Applications*. Kluwer, 1996.

[VODMDS97] P. Van Overschee, B. De Moor, W. Dehandschutter, and J. Swevers. A subspace algorithm for the identification of discrete time frequency domain power spectra. *Automatica*, 33(12):2147–2157, 1997.

[WB01] K. Worden and A.P. Burrows. Optimal sensor placement for fault detection. *Engineering Structures*, 23:885–901, 2001.

[WL04] D. Wu and S.S. Law. Damage localization in plate structures from uniform load surface curvature. *Journal of Sound and Vibration*, 276:227–244, 2004.

[WMF00] K. Worden, G. Manson, and N.R.J. Fieller. Damage detection using outlier analysis. *Journal of Sound and Vibration*, 229(3):647–667, 2000.

[WZ01] Z. Waszczyszyn and L. Ziemiański. Neural networks in mechanics of structures and materials-new results and prospects of applications. *Computers & Structures*, 79(22-25):2261–2276, 2001.

[XZ17] Y.F. Xu and S.A. Zhu, W.D.and Smith. Non-model-based damage identification of plates using principal,mean and gaussian curvature mode shapes. *Journal of Sound and Vibration*, 400:626–659, 2017.

[YCWY07] Y.J. Yan, L. Cheng, Z.Y. Wua, and L.H. Yam. Development in vibration-based structural damage detection technique. *Mechanical Systems and Signal Processing*, 21:2198–2211, 2007.

[YDBG04] A.M. Yan, P. De Boe, and J.C. Golinval. Structural damage diagnosis by Kalman model based on stochastic subspace identification. *Structural Health Monitoring*, 3(2):103–119, 2004.

[YG05] A.-M. Yan and J.-C. Golinval. Structural damage localization by combining flexibility and stiffness methods. *Engineering Structures*, 27(12):1752–1761, 2005.

[YK11] K.V. Yuen and S.C. Kuok. Bayesian methods for updating dynamic models. *Applied Mechanics Reviews*, 64(1), 2011.

[YKK99] S.H. Yoo, H.K. Kwak, and B.S. Kim. Detection and location of a crack in a plate using modal analysis. In *International Modal Analysis Conference (IMAC-XVII)*, Orlando, FL, 1999.

[YO17] C. Yang and S.O. Oyadiji. Damage detection using modal frequency curve and squared residual wavelet coefficients-based damage indicator. *Mechanical Systems and Signal Processing*, 83:385–405, 2017.

[YRKO17a] Zhi-Bo. Yang, M. Radzienski, P. Kudela, and W. Ostachowicz. Damage detection in beam-like composite structures via chebyshev pseudo spectral modal curvature. *Composite Structures*, 168:1–12, 2017.

[YRKO17b] Zhi-Bo. Yang, M. Radzienski, P. Kudela, and W. Ostachowicz. Fourier spectral-based modal curvature analysis and its application to damage detection in beams. *Mechanical Systems and Signal Processing*, 84:763–781, 2017.

[YYB01] C. B. Yun, J. H. Yi, and E. Y. Bahng. Joint damage assessment of framed structures using a neural networks technique. *Engineering Structures*, 23(5):425–435, 2001.

[YYJ03] L. H. Yam, Y. J. Yan, and J. S. Jiang. Vibration-based damage detection for composite structures using wavelet transform and neural network identification. *Composite Structures*, 60(4):403–412, 2003.

[ZA98] Z. Zhang and A.E. Aktan. Application of modal flexibility and its derivatives in structural identification. *Research in Nondestructive Evaluation*, 10(1):43–61, 1998.

[Zab05] V. Zabel. A wavelet-based approach for damage detection on civil engineering structures. In *Proc. 23rd International Modal Analysis Conference*, Orlando, FL, USA, 2005.

[ZF01] D.Y. Zheng and S.C. Fan. Natural frequency changes of a cracked timoshenko beam by modified fourier series. *Journal of Sound and Vibration*, 246(2):297–317, 2001.

[ZK04] D.Y. Zheng and N.J. Kessissoglou. Free vibration analysis of a cracked beam by finite element method. *Journal of Sound and Vibration, Elsevier*, 273:457–475, 2004.

[ZWD+17] X. Zhou, D. Wang, M. Duan, J. Gu, and Y. Liu. Numerical study on mode curvature for damage detection of a drilling riser using transfer matrix technique. *Applied Ocean Research*, 63:65–75, 2017.

Résumé

La localisation de dégâts basée sur les mesures de vibrations est devenue un axe de recherche important pour la surveillance de la santé structurale (SHM). En particulier, la Stochastic Dynamic Damage Locating Vector (SDDLV) est une méthode de localisation des dégâts basée sur le couplage entre un modèle aux éléments finis (FE) de la structure et des paramètres modaux estimés à partir des mesures dynamiques en excitation ambiante dans les états structuraux sain et endommagé, interrogant les changements dans la matrice de transfert. Dans la première contribution, la méthode SDDLV est étendue avec une approche statistique conjointe utilisant plusieur ensembles de modes, surmontant la limitation théorique sur le nombre minimal de paramètres. Un autre problème traité est la performance de la méthode en fonction du choix de la variable de Laplace où la fonction de transfert est évaluée. Une attention particulière est accordée à ce choix et a son optimisation. Dans la deuxième contribution, l'approche Influence Line Damage Location (ILDL), complémentaire à l'approche SDDLV est étendue avec un cadre statistique. Dans la dernière contribution, une approche de sensibilité pour les petits dommages est développée en fonction de la différence dees matrices de transfert, permettant la localisation des dommages par des tests statistiques dans un cadre gaussien, et en plus la quantification des dommages dans une deuxième étape. Enfin, les méthodes proposées sont validées sur des simulations numériques et leurs performances sont testées dans de nombreuses études de cas sur des expériences de laboratoire.

Abstract

Vibration-based damage localization has become an important issue for Structural Health Monitoring (SHM). Particularly, the Stochastic Dynamic Damage Locating Vector (SDDLV) method is an output-only damage localization method based on both a Finite Element (FE) model of the structure and modal parameters estimated from output-only measurements in the reference and damaged states of the system, interrogating changes in the transfer matrix. Firstly, the SDDLV method has been extended with a joint statistical approach for multiple mode sets, overcoming the theoretical limitation on the number of modes in previous works. Another problem is that the performance of the method can change considerably depending on the Laplace variable where the transfer function is evaluated. Particular attention is given to this choice and how to optimize it. Secondly, the Influence Line Damage Location (ILDL) approach which is complementary to the SDDLV approach has been extended with a statistical framework. Thirdly, a sensitivity approach for small damages has been developed based on the transfer matrix difference, allowing damage localization through statistical tests in a Gaussian framework, and in addition the quantification of the damage in a second step. Finally, the proposed methods are validated on numerical simulations and their performances are tested extensively in numerous case studies on lab experiments.